Reconstruction of $B^- \to D^{*0} e^- \overline{\nu}_e$ Decays and Determination of $|V_{cb}|$

Jens Schubert

SLAC-Report-876

SLAC, Stanford University, Stanford, CA 94025

Reconstruction of $B^- \to D^{*0}e^-\overline{\nu}_e$ Decays and Determination of $|V_{cb}|$

D I S S E R T A T I O N

zur Erlangung des akademischen Grades

Doctor rerum naturalium
(Dr.rer.nat.)

vorgelegt der Fakultät Mathematik und Naturwissenschaften
der Technischen Universität Dresden

von
Diplom-Physiker Jens Schubert
geboren am 11.03.1977 in Pirna

Abstract

In this analysis the decay $B^- \to D^{*0}e^-\overline{\nu}_e$ is measured. The underlying data sample consists of about 226 million $B\overline{B}$-pairs accumulated on the $\Upsilon(4S)$ resonance by the *BABAR* detector at the asymmetric e^+e^- collider PEP-II. The reconstruction of the decay uses the channels $D^{*0} \to D^0\pi^0$, $D^0 \to K^-\pi^+$ and $\pi^0 \to \gamma\gamma$. The neutrino is not reconstructed. Since the rest frame of the B meson is unknown, the boost w of the D^{*0} meson in the B meson rest frame is estimated by $\tilde{w}$. The $\tilde{w}$ spectrum of the data is described in terms of the partial decay width $\mathrm{d}\Gamma/\mathrm{d}w$ given by theory and the detector simulation translating each spectrum $\mathrm{d}\Gamma/\mathrm{d}w$ into an expectation of the measured $\tilde{w}$ spectrum. $\mathrm{d}\Gamma/\mathrm{d}w$ depends on a form factor $F(w)$ parameterizing the strong interaction in the decay process. To find the best descriptive $\mathrm{d}\Gamma/\mathrm{d}w$ a fit to the data determines the following two parameters of $\mathrm{d}\Gamma/\mathrm{d}w$: (i) $F(1)|V_{cb}|$, the product between F at zero D^{*0}-recoil and the CKM matrix element $|V_{cb}|$; (ii) $\rho_{A_1}^2$, a parameter of the form factor $F(w)$. The former parameter scales the height of $\mathrm{d}\Gamma/\mathrm{d}w$ and $\rho_{A_1}^2$ varies the shape of it. The determined values of $F(1)|V_{cb}|$, $\rho_{A_1}^2$ and $\mathcal{B}\left(B^- \to D^{*0}e^-\overline{\nu}_e\right)$ are

$$F(1)|V_{cb}| = (35.8 \pm 0.5 \ \pm 1.5 \ ) \times 10^{-3},$$
$$\rho_{A_1}^2 = (1.08 \pm 0.05 \pm 0.09) \quad \text{and}$$
$$\mathcal{B}\left(B^- \to D^{*0}e^-\overline{\nu}_e\right) = (5.60 \pm 0.08 \pm 0.42)\%,$$

where the uncertainties are statistical and systematic, respectively. The value of $\mathcal{B}\left(B^- \to D^{*0}e^-\overline{\nu}_e\right)$ has been determined by an integration of $\mathrm{d}\Gamma/\mathrm{d}w$ over the allowed w range using the fitted values of $F(1)|V_{cb}|$ and $\rho_{A_1}^2$.

Kurzfassung

In dieser Analyse wird der Zerfall $B^- \to D^{*0}e^-\overline{\nu}_e$ gemessen. Der zugrundeliegende Datensatz umfasst ca. 226 Millionen $B\overline{B}$-Paare, die im Prozess $\Upsilon(4S) \to B\overline{B}$ am asymmetrischen e^+e^--Speicherring PEP-II erzeugt und vom *BABAR*-Detektor gemessen wurden. Der analysierte Zerfall wird in den Kanälen $D^{*0} \to D^0\pi^0$, $D^0 \to K^-\pi^+$ und $\pi^0 \to \gamma\gamma$ rekonstruiert. Das Neutrino wird nicht rekonstruiert. Da das B-Ruhesystem unbekannt ist, muss der Boost w vom D^{*0}-Meson im B-Ruhesystem durch $\tilde{w}$ abgeschätzt werden. Das $\tilde{w}$-Spektrum der Daten wird beschrieben durch die aus der Theorie bekannte partielle Zerfallsbreite $\mathrm{d}\Gamma/\mathrm{d}w$ und durch die Detektorsimulation, die jedes $\mathrm{d}\Gamma/\mathrm{d}w$ in eine Erwartung für die gemessenen $\tilde{w}$-Spektren übersetzen kann. $\mathrm{d}\Gamma/\mathrm{d}w$ hängt von einem Formfaktor $F(w)$ ab, welcher die starke Wechselwirkung im Zerfallsprozess parametrisiert. Um das am besten beschreibende $\mathrm{d}\Gamma/\mathrm{d}w$ zu finden, bestimmt eine Funktionsanpassung an die Daten folgende zwei Parameter von $\mathrm{d}\Gamma/\mathrm{d}w$: (i) $F(1)|V_{cb}|$, das Produkt zwischen F bei minimalem D^{*0}-Rückstoß und dem CKM-Matrixelement $|V_{cb}|$; (ii) $\rho_{A_1}^2$, ein Parameter des Formfaktors $F(w)$. Der erstgenannte Parameter skaliert die Höhe von $\mathrm{d}\Gamma/\mathrm{d}w$ und $\rho_{A_1}^2$ variiert die Form. Für $F(1)|V_{cb}|$, $\rho_{A_1}^2$ und $\mathcal{B}\left(B^- \to D^{*0}e^-\overline{\nu}_e\right)$ wurden die Werte

$$F(1)|V_{cb}| = (35.8 \pm 0.5 \ \pm 1.5 \ ) \times 10^{-3},$$
$$\rho_{A_1}^2 = (1.08 \pm 0.05 \pm 0.09) \quad \text{und}$$
$$\mathcal{B}\left(B^- \to D^{*0}e^-\overline{\nu}_e\right) = (5.60 \pm 0.08 \pm 0.42)\%$$

bestimmt, wobei die Unsicherheiten statistisch und systematisch sind. Der Wert für $\mathcal{B}\left(B^- \to D^{*0}e^-\overline{\nu}_e\right)$ ist aus der Integration von $\mathrm{d}\Gamma/\mathrm{d}w$ über den erlaubten w-Bereich unter Benutzung der gefundenen Werte für $F(1)|V_{cb}|$ und $\rho_{A_1}^2$ bestimmt worden.

Contents

Chapter 1

Outline

Chapter two and three help to understand the environment which this work is embedded in. The environment regarded from a theoretical point of view is given in chapter two. It contains a brief introduction to the *Standard Model of Particle Physics* with focus on the coupling between quarks and the W boson. And it derives a description for the signal decay $B^- \to D^{*0}e^-\overline{\nu}_e$ in the framework of Heavy Quark Effective Theory. The experimental situation is summarized in chapter three. The storage ring and the B-meson generation are described briefly – the main focus of chapter three is set on structure, functionality and performance of the *BABAR* detector. The chapters four and five are the largest. They describe the entire machinery necessary to obtain the quantities of interest from the data. Starting point is the definition of tracks and clusters from the detector response to charged and neutral particles. Based on a set of simulated physics events the selection cuts are developed with the aim to enhance the fraction of $B^- \to D^{*0}e^-\overline{\nu}_e$ events. Chapter four also contains detailed discussions about variables discriminating signal and background, and about variables interesting for the theoretical description of the signal. In chapter five the step-by-step composition of a fit function is documented. At the end of the chapter there is a fit procedure directly applicable to a signal-enhanced sample. Before the result of the fit on data is presented in the second part of chapter six, a validation of the fit procedure preludes chapter six. Extensive checks on the systematic uncertainties are documented in the seventh chapter. In the last chapter all results are summarized. The document closes with a comparison to former measurements.

Chapter 2

Theory

2.1 The Standard Model of Particle Physics

The *Standard Model of Particle Physics* (SM) summarizes today's knowledge of the fundamental particles. It is a quantum field theory and a gauge field theory describing three of the currently known four fundamental interactions, namely the strong, the weak and the electromagnetic interaction. A higher theory additionally describing the gravitational interaction is searched but its formulation is not yet successful. The consideration of symmetries was essential for the creation of the SM. *Emmy Noether* is one of the pioneers of the symmetry considerations. In 1918 she proved that there are conserved observables for each of nature's symmetries. A very important symmetry of the SM is the $SU(3)_C \times SU(2)_L \times U(1)_Y$ gauge symmetry leading to the three fundamental SM interactions. The subscripts C, L and Y indicate that the $SU(3)$ gauge symmetry appears within the group of **C**olor-charged particles, the $SU(2)$ gauge symmetry leads to the coupling between **L**eft-handed fermions and the $U(1)_Y$ gauge symmetry is not the electromagnetic $U(1)_Q$ gauge symmetry but is related to the weak hypercharge **Y**.

The fundamental particles of the SM are ordered into three families (also called generations) of fermions and 12 bosons for the mediation of the interaction between the fermions (see table 2.1 and 2.2). All fermions have a spin $s = \frac{1}{2}$ whereas the bosons have integer-spin. The fermions build up the visible matter known to us [1] and for each particle there is also a corresponding anti-particle with opposite intrinsic parity. Each fermion family contains two flavors of quarks and two flavors of leptons, and all of them have been observed experimentally. The quarks (u, d, s, c, b, t) are the only strongly-interacting fermions; the left-handed parts of all fermions participate in the weak interaction; and all fermions beside the neutrinos (ν_e, ν_μ, ν_τ) interact electromagnetically. The three generations of fermions appear to be equal in all of their quantum numbers[2] and to differ only in their masses. The increase of the fermion masses from one generation to the next is called the *mass hierarchy* of the SM. Each particle of the first family has a heavier partner in the second family and a still heavier copy in the third family. Within the SM the neutrinos were handled as massless particles for a long time. Since the 'Solar Neutrino Problem' observed by the Homestake experiment has been solved by finding consistency between a neutrino oscillation model and the data of the *Super-Kamiokande* experiment we know that also neutrinos have masses [1, 2].

---

[1]Since the results of the WMAP experiment[3] we assume that SM matter make only about 4% of the entire mass of the universe and that the remaining 96% are made of dark matter (23%) and dark energy (73%), both not explained by the SM.

[2]exactly spoken: all of their quantum numbers except strangeness, charm, beauty and topness

Table 2.1: Fermions of the SM together with their quantum numbers and the underlying gauge symmetries. Subscripts L and R denotes left- and right-handed fields, respectively. The listed quantum numbers are the weak isospin (T), the third component of the weak isospin (T_3), the weak hypercharge (Y), the electric charge (Q) and the color charge (C). The electric charge Q is a dependent quantum number, $Q = T_3 + Y$.

			interaction→		electroweak			strong
			gauge group→		$SU(2)_L \times U(1)_Y$			$SU(3)_C$
			quantum number→	T	T_3	Y	Q	C
quarks:								
$Q_1 = \begin{pmatrix} u \\ d' \end{pmatrix}_L$	$Q_2 = \begin{pmatrix} c \\ s' \end{pmatrix}_L$	$Q_3 = \begin{pmatrix} t \\ b' \end{pmatrix}_L$		1/2	+1/2 −1/2	+1/6	+2/3 −1/3	r,g,b
u_R	c_R	t_R		0	0	+2/3	+2/3	
d_R	s_R	b_R		0	0	−1/3	−1/3	
leptons:								
$L_1 = \begin{pmatrix} \nu_e \\ e \end{pmatrix}_L$	$L_2 = \begin{pmatrix} \nu_\mu \\ \mu \end{pmatrix}_L$	$L_3 = \begin{pmatrix} \nu_\tau \\ \tau \end{pmatrix}_L$		1/2	+1/2 −1/2	−1/2	0 −1	white
e_R	μ_R	τ_R		0	0	−1	−1	
ν_{eR}	$\nu_{\mu R}$	$\nu_{\tau R}$		0	0	0	0	

Table 2.2: The gauge bosons in the SM.

interaction	mediating gauge boson
electromagnetic	γ (photon)
weak	W^+, W^-, Z^0
strong	$g_1, \ldots, g_8$ (gluons)

A very important part of the SM concerns the masses of all fermions and the masses of the only massive interaction bosons W^+, W^- and Z^0. The SM-Lagrangian's mass terms describing the fermion masses have the structure $m_f \bar{\Psi}_f \Psi_f$, where m_f and Ψ_f are the mass and the Dirac-spinor of the fermion f, respectively. Because a simple by-hand-addition of the mass term to the Lagrangian would destroy the local $SU(2)$ gauge invariance one needs a more tricky way to obtain mass terms. The SM solution of the problem is the *Higgs* mechanism named after Peter Higgs who first suggested this mechanism [4]. It introduces a scalar, weakly-interacting Higgs-doublet with a potential allowing for spontaneous breakdown of the $SU(2)_L \times U(1)_Y$ symmetry. However, the Higgs-Boson defined within this mechanism is not yet observed experimentally. The main goal of the soon starting LHC[3]-experiments is to compare the Higgs mechanism's predictions with the measurements in order to verify or to rule out the Higgs mechanism. The observation of the Higgs-Boson is the central point for the verification.

2.1.1 The Electroweak Interaction and the Higgs Mechanism

The unification of the electromagnetic and the weak interaction to the so-called electroweak interaction is mainly attributed to *Glashow*, *Weinberg* and *Salam* (see Nobel lectures [5, 6, 7]). Their theory unifies the $SU(2)_L$ gauge group with the $U(1)_Q$ gauge group to the $SU(2)_L \times U(1)_Y$ elec-

---

[3]LHC is an abbreviation for the *Large Hadron Collider* currently under construction at the *Conseil Européen pour la Recherche Nucléaire* (CERN).

troweak gauge group. If the fundamental gauge fields of $SU(2)_L$ are W_1, W_2 and W_3 and that of $U(1)_Y$ is B then the physical fields of the electroweak interaction are given by

$$
\begin{aligned}
W^\pm &= \frac{1}{\sqrt{2}}\left(W_1 \mp iW_2\right) \\
Z &= \cos\theta_W W_3 - \sin\theta_W B \\
A &= \sin\theta_W W_3 + \cos\theta_W B \quad,
\end{aligned}
\tag{2.1}
$$

where θ_W is the Weinberg angle, $\sin^2\theta_W \approx 0.231$ [8]. The Lagrangian's electroweak interaction term $\mathcal{L}_{EW}$ between the gauge bosons and the fermions is divided into a charged current part $\mathcal{L}_{CC}$ (describing the coupling of W^+ and W^- to the fermions) and a neutral current part $\mathcal{L}_{NC}$ (describing the coupling of fermions to the Photon field A and the Z), $\mathcal{L}_{EW} = \mathcal{L}_{NC} + \mathcal{L}_{CC}$. The charged current part is divided into a leptonic part, $\mathcal{L}_{CC}^l$, and a quark part, $\mathcal{L}_{CC}^q$:

$$
\mathcal{L}_{CC} = \mathcal{L}_{CC}^q + \mathcal{L}_{CC}^l
\tag{2.2a}
$$

$$
\mathcal{L}_{CC}^q = -\frac{1}{\sqrt{2}}g\left(\bar{u}'_{Li}\gamma^\mu d'_{Li}W_\mu^+ + \bar{d}'_{Li}\gamma^\mu u'_{Li}W_\mu^-\right)
\tag{2.2b}
$$

$$
\mathcal{L}_{CC}^l = -\frac{1}{\sqrt{2}}g\left(\bar{\nu}_{Li}\gamma^\mu e_{Li}W_\mu^+ + \bar{e}_{Li}\gamma^\mu \nu_{Li}W_\mu^-\right) .
\tag{2.2c}
$$

In these equations, g is the weak coupling constant, the prime ($'$) denotes a quark state to be the eigenstate of the electroweak interaction (in contrast to the mass eigenstate) and the index i runs over the families ($i = 1, 2, 3$). The u_i and the d_i are the up-type and the down-type quark states, respectively, with $\boldsymbol{u} = (u, c, t)$ and $\boldsymbol{d} = (d, s, b)$. The corresponding symbols in the leptonic part, ν_i and e_i, denote the neutrino and the charged lepton states, respectively, with $\boldsymbol{\nu} = (\nu_e, \nu_\mu, \nu_\tau)$ and $\boldsymbol{e} = (e^-, \mu^-, \tau^-)$. The index L indicates an fermion state f to be the left-handed part f_L of the fermion,

$$
f_L = \frac{1 - \gamma_5}{2}f \qquad \text{with } f = u_i, d_i, e_i, \nu_i \quad (i = 1, 2, 3).
\tag{2.3}
$$

Two further important terms of the SM-Lagrangian are the Higgs term $\mathcal{L}_{Higgs}$ and the Higgs-fermion-coupling *Yukawa*-term $\mathcal{L}_Y$. Both terms contain the weak interacting Higgs-doublet $\Phi = \binom{\Phi_1}{\Phi_2}$. The Higgs term is given by

$$
\mathcal{L}_{Higgs} = (\partial^\alpha \Phi^\dagger)(\partial_\alpha \Phi) + V(\Phi) \quad, \text{with} \quad V(\Phi) = -\mu^2 \Phi^\dagger \Phi + \lambda^2 \left(\Phi^\dagger \Phi\right)^2 .
\tag{2.4}
$$

Due to $\mu^2 > 0$ and $\lambda^2 > 0$ the potential $V(\Phi)$ has a Mexican Hat shape resulting in a non-zero vacuum expectation value with $\sqrt{\Phi^\dagger \Phi} = \frac{v}{\sqrt{2}} = \frac{\mu}{\sqrt{2}\lambda}$ for the ground state of Φ. The Yukawa-term $\mathcal{L}_Y$ describes the coupling of left-handed fermion-doublets, Higgs-doublet and right handed fermions, where the fermions are either leptons or quarks. In the end $\mathcal{L}_Y$ produces the mass terms in the SM-Lagrangian. With $\tilde{\Phi} = \binom{\Phi_2}{-\Phi_1^*}$, the Lagrangian $\mathcal{L}_Y$ is given by

$$
\mathcal{L}_Y = \mathcal{L}_Y^q + \mathcal{L}_Y^l \quad \text{with}
\tag{2.5a}
$$

$$
\mathcal{L}_Y^q = -\Lambda_{ij}^u \bar{Q}'_{Li}\tilde{\Phi}u'_{Rj} - \Lambda_{ij}^d \bar{Q}'_{Li}\Phi d'_{Rj} \;+\; (h.c.) \quad \text{and}
\tag{2.5b}
$$

$$
\mathcal{L}_Y^l = -\Lambda_{ij}^e \bar{L}_{Li}\Phi e_{Rj} - \Lambda_{ij}^\nu \bar{L}_{Li}\Phi \nu_{Rj} \;+\; (h.c.)
\tag{2.5c}
$$

The fermion doublets Q_{Li} and L_{Li} are defined in table 2.1. Λ_{ij}^e, Λ_{ij}^ν, Λ_{ij}^u and Λ_{ij}^d are the Yukawa coupling constants which are in general complex numbers. They are the only source of *CP* violation in the SM.

The remaining part of this section focuses on the quark sector. Only at the end of this section a short comment to the difference between equation 2.5b and 2.5c is appended. After the spontaneous symmetry breaking the Higgs-doublet can be written as

$$\Phi(x) = \frac{1}{\sqrt{2}} \begin{pmatrix} 0 \\ v + h(x) \end{pmatrix}. \tag{2.6}$$

Thereby the Yukawa term from equation 2.5b simplifies to

$$\mathcal{L}_Y^q = \mathcal{L}_{mass}^q + \mathcal{L}_{h(x)}^q \tag{2.7}$$

$$\mathcal{L}_{mass}^q = -m_{ij}^u \overline{u}'_{Li} u'_{Rj} - m_{ij}^d \overline{d}'_{Li} d'_{Rj} + \text{h.c.} \tag{2.8}$$

with

$$m_{ij}^u = \Lambda_{ij}^u \frac{v}{\sqrt{2}} \qquad m_{ij}^d = \Lambda_{ij}^d \frac{v}{\sqrt{2}} \tag{2.9}$$

and $\mathcal{L}_{h(x)}^q$ containing interaction processes between quarks and the effective Higgs-field $h(x)$. By unitary transformation matrices $\boldsymbol{V}_L^u$, $\boldsymbol{V}_R^u$, $\boldsymbol{V}_L^d$ and $\boldsymbol{V}_R^d$ one can diagonalize the mass matrices $\boldsymbol{m}^u$ and $\boldsymbol{m}^d$:

$$(\boldsymbol{V}_L^u)^\dagger \boldsymbol{m}^u \boldsymbol{V}_R^u = \begin{pmatrix} m_u & 0 & 0 \\ 0 & m_c & 0 \\ 0 & 0 & m_t \end{pmatrix} \quad , \quad (\boldsymbol{V}_L^d)^\dagger \boldsymbol{m}^d \boldsymbol{V}_R^d = \begin{pmatrix} m_d & 0 & 0 \\ 0 & m_s & 0 \\ 0 & 0 & m_b \end{pmatrix}. \tag{2.10}$$

Because there are no restrictions to the choice of the mass matrices $\boldsymbol{m}^u$ and $\boldsymbol{m}^d$ the diagonalizing matrices for up-type and down-type quarks are, in general, different

$$\boldsymbol{V}_L^u \neq \boldsymbol{V}_L^d \quad , \quad \boldsymbol{V}_R^u \neq \boldsymbol{V}_R^d. \tag{2.11}$$

The electroweak interaction eigenstates u_i' (d_i') and the mass eigenstates u_i (d_i) are related by

$$\begin{aligned} u'_{Li} &= V_{Lij}^u u_{Lj} & d'_{Li} &= V_{Lij}^d d_{Lj} \\ u'_{Ri} &= V_{Rij}^u u_{Rj} & d'_{Ri} &= V_{Rij}^d d_{Rj}. \end{aligned} \tag{2.12}$$

The transformation of equation 2.2b to an expression with mass eigenstates instead of weak interaction eigenstates results in

$$\mathcal{L}_{CC}^q = -\frac{1}{\sqrt{2}} g \left(\overline{u}_{Li} \gamma^\mu V_{ij} d_{Lj} W_\mu^+ + \text{h.c.} \right), \tag{2.13}$$

where the appearing matrix $\boldsymbol{V} = (V_{ij})$ is defined by

$$\boldsymbol{V} = (\boldsymbol{V}_L^u)^\dagger \boldsymbol{V}_L^d. \tag{2.14}$$

$\boldsymbol{V}$ is called *Cabibbo-Kobayashi-Maskawa* matrix (CKM matrix) and is discussed in more detail in the next section.

But what happens to $\mathcal{L}_{NC}$ after the renotation using the mass eigenstates instead of the interaction eigenstates? In case of $\mathcal{L}_{CC}^q$ it was just shown that the diagonalizing matrices appear within the charged current interaction term $\mathcal{L}_{CC}^q$. The situation is different for the neutral current interaction term $\mathcal{L}_{NC}$. In $\mathcal{L}_{NC}$ the renotation ends with the cancellation of the diagonalizing matrices.

2.1.2 The CKM Matrix

The matrix $\boldsymbol{V}$ from equation 2.13 transforms down-type quarks from a basis of mass eigenstates to a basis of weak interaction eigenstates:[4]

$$
\begin{pmatrix} d' \\ s' \\ b' \end{pmatrix}_L = \underbrace{\begin{pmatrix} V_{ud} & V_{us} & V_{ub} \\ V_{cd} & V_{cs} & V_{cb} \\ V_{td} & V_{ts} & V_{tb} \end{pmatrix}}_{=\boldsymbol{V}} \begin{pmatrix} d \\ s \\ b \end{pmatrix}_L \qquad . \tag{2.15}
$$

In honor for its originators it is called *Cabibbo-Kobayashi-Maskawa* matrix (CKM matrix). In 1973 Kobayashi and Maskawa extended Cabibbo's idea of quark mixing from two families to three families[9, 10] in order to explain the *CP* violation observed in the neutral kaon system in 1964 [11]. As is shown below, the three-family-mixing-mechanism leads to non-removable complex elements of $\boldsymbol{V}$ responsible for SM *CP* violation. In the two-family-case the matrix could be written without complex elements and therefore would not cause *CP* violation. The idea of Kobayashi and Maskawa successfully predicted an entire third family at a time when even the first two families were not completely experimentally observed.

Let us now study the structure of the CKM matrix. Because $\boldsymbol{V}$ is a complex 3×3 matrix it could contain eighteen real parameters. But these parameters can not be completely independent because $\boldsymbol{V}$ is a product of unitary matrices and therefore has to be unitary itself:

$$
\boldsymbol{V}^\dagger \boldsymbol{V} = 1, \tag{2.16}
$$

or in index notation

$$
\sum_{k=1}^{3} V_{ki} V_{kj}^* = \delta_{ij} \qquad \text{for } i, j = 1, 2, 3 . \tag{2.17}
$$

The former equation sets nine constraints to the eighteen elements. That leaves $\boldsymbol{V}$ with nine independent parameters which can be implemented as three mixing angles and six phases. Consider now the transformation

$$
\boldsymbol{V} \rightarrow \begin{pmatrix} e^{-i\alpha_1^u} & 0 & 0 \\ 0 & e^{-i\alpha_2^u} & 0 \\ 0 & 0 & e^{-i\alpha_3^u} \end{pmatrix} \boldsymbol{V} \begin{pmatrix} e^{i\alpha_1^d} & 0 & 0 \\ 0 & e^{i\alpha_2^d} & 0 \\ 0 & 0 & e^{i\alpha_3^d} \end{pmatrix} \tag{2.18}
$$

with the real numbers α_i^q. On the one hand it leaves the Lagrangian $\mathcal{L}_{CC}$ of equation 2.13 invariant because it is equivalent to the allowed redefinition of quark phases,

$$
q_j \rightarrow e^{i\alpha_j^q} q_j \qquad (q = u, d; j = 1, 2, 3) . \tag{2.19}
$$

On the other hand the phase differences among the $e^{i\alpha_j^q}$ terms can be chosen so that the transformation 2.18 eliminates five of the six independent phase parameters of $\boldsymbol{V}$. A further simplification of $\boldsymbol{V}$ is not possible so that it retains four parameters: three angles and one phase which, if not equal to zero or π, forbids that $\boldsymbol{V}$ has a representation with only real elements.

---

[4]As one can see by equation 2.13 this is equivalent with transforming the up-type quarks by the matrix $\boldsymbol{V}^\dagger$.

The *Standard Representation* of V [8] is constructed by three real rotation matrices with the phase parameter additionally inserted in one of them:

$$
\begin{aligned}
V &= \begin{pmatrix} 1 & 0 & 0 \\ 0 & c_{23} & s_{23} \\ 0 & -s_{23} & c_{23} \end{pmatrix} \begin{pmatrix} c_{13} & 0 & s_{13}e^{-i\delta} \\ 0 & 1 & 0 \\ -s_{13}e^{-i\delta} & 0 & c_{13} \end{pmatrix} \begin{pmatrix} c_{12} & s_{12} & 0 \\ -s_{12} & c_{12} & 0 \\ 0 & 0 & 1 \end{pmatrix} \\
&= \begin{pmatrix} c_{12}c_{13} & s_{12}c_{13} & s_{13}e^{-i\delta} \\ -s_{12}c_{23}-c_{12}s_{23}s_{13}e^{i\delta} & c_{12}c_{23}-s_{12}s_{23}s_{13}e^{i\delta} & s_{23}c_{13} \\ s_{12}s_{23}-c_{12}c_{23}s_{13}e^{i\delta} & -c_{12}s_{23}-s_{12}c_{23}s_{13}e^{i\delta} & c_{23}c_{13} \end{pmatrix}.
\end{aligned}
\qquad (2.20)
$$

All factors are unitary, so the product V is also unitary. The matrix contains only the mixing angles θ_{12}, θ_{23}, and θ_{13} and the Kobayashi-Maskawa-phase δ. Together, they are four of the 25 independent parameters of the SM. The used abbreviations for equation 2.20 are $c_{ij} = \cos\theta_{ij}$ and $s_{ij} = \sin\theta_{ij}$.

To understand the representation of V suggested by *Lincoln Wolfenstein* [12] one firstly needs to know the approximate size of the CKM matrix elements. Measurements show that their order of magnitude can be expressed by powers of λ, with $\lambda = \sin\theta_{12}$:

- The diagonal matrix elements are of order one ($\sim \lambda^0$).

- The off-diagonal elements $|V_{us}|$ and $|V_{cd}|$ are of order 0.227 ($\sim \lambda^1$).

- The off-diagonal elements $|V_{cb}|$ and $|V_{ts}|$ are of order 0.040 ($\sim \lambda^2$).

- The remaining elements $|V_{ub}|$ and $|V_{td}|$ are of order 0.005 ($\sim \lambda^3$).

The *Wolfenstein approximation* [12] exploits this natural hierarchy in the size of matrix elements and with the definitions

$$\sin\theta_{12} = \lambda\,, \qquad (2.21a)$$

$$\sin\theta_{23} = \lambda^2 A \quad \text{and} \qquad (2.21b)$$

$$\sin\theta_{13}\, e^{i\delta} = \lambda^3 A(\rho + i\eta) \qquad (2.21c)$$

it is given by

$$
V = \begin{pmatrix} 1 - \lambda^2/2 & \lambda & A\lambda^3(\rho - i\eta) \\ -\lambda & 1 - \lambda^2/2 & A\lambda^2 \\ A\lambda^3(1 - \rho - i\eta) & -A\lambda^2 & 1 \end{pmatrix} + \mathcal{O}(\lambda^4)\,.
\qquad (2.22)
$$

This parametrization is obtained by expansions of the cosine terms in the standard representation (equ. 2.20). In equation 2.22 the expansion is broken off at λ^4 terms. The definition of the parameter set (λ, A, ρ, η) is divided into one part defining the order-of-magnitude-scale for the matrix elements (λ) and into another part defining the fine-tuning-parameters for the matrix elements (A, ρ, η). A and $\sqrt{\rho^2 + \eta^2}$ are of order 1. From the numbers of powers in λ one easily gets the order of magnitude of any CKM term.

A further advantage of the definition of (λ, A, ρ, η) is that the Wolfenstein approximation can be improved to be accurate up to $\mathcal{O}(\lambda^6)$ without big expense [14]. In this case a parameter set (λ, A, $\bar{\rho}$, $\bar{\eta}$) with $\bar{\rho} = \rho(1 - \lambda^2/2)$ and $\bar{\eta} = \eta(1 - \lambda^2/2)$ is used to parametrize V. The approximate values of the CKM matrix parameters are $\lambda \approx 0.227$, $A \approx 0.818$, $\bar{\rho} \approx 0.221$ and $\bar{\eta} \approx 0.340$ [8].
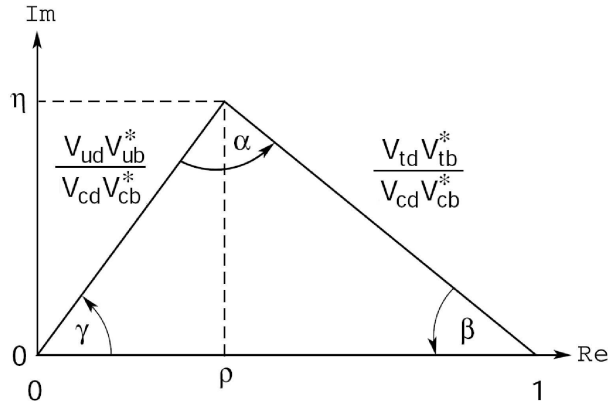
Figure 2.1: The Unitarity Triangle.

Relation 2.17 for $i \neq j$ gives three equations, each summing up three complex numbers to zero. The three equations can be represented by three triangles in the complex plain. Using the Wolfenstein parametrization (WP) one can easily see by counting of λ-powers that two equations sum up terms of different magnitude ($i = 1, 3; j = 2$) whereas one sums up terms of comparable magnitude ($i = 1; j = 3$). The latter case in a non-compressed notation reads

$$V_{ud}V_{ub}^* \;+\; V_{cd}V_{cb}^* \;+\; V_{td}V_{tb}^* \;= 0 \tag{2.23a}$$

$$(\text{ in WP: } \quad A\lambda^3(\rho + i\eta) \;-\; A\lambda^3 \;+\; A\lambda^3(1 - \rho - i\eta) \;= 0 \text{)}. \tag{2.23b}$$

After the division of this equation by its second term one obtains

$$\frac{V_{ud}V_{ub}^*}{V_{cd}V_{cb}^*} \;+\; 1 \;+\; \frac{V_{td}V_{tb}^*}{V_{cd}V_{cb}^*} \;= 0 \tag{2.24a}$$

$$(\text{ in WP: } \quad (\rho + i\eta) \;-\; 1 \;+\; (1 - \rho - i\eta) \;= 0 \text{)}\quad . \tag{2.24b}$$

The corresponding triangle which is shown in figure 2.1 is called the *Unitarity Triangle* (UT). It depends only on the CKM parameters ρ and η. The angles of the triangle are given by

$$\alpha = \arg\left[-\frac{V_{td}V_{tb}^*}{V_{ud}V_{ub}^*}\right], \qquad \beta = \arg\left[-\frac{V_{cd}V_{cb}^*}{V_{td}V_{tb}^*}\right] \qquad \text{and} \qquad \gamma = \arg\left[-\frac{V_{ud}V_{ub}^*}{V_{cd}V_{cb}^*}\right] = \pi - \alpha - \beta \tag{2.25}$$

and the side lengths of the triangle can be read from equation 2.24. A very important property of the UT is that all of its side lengths and angles can be determined from B meson observations alone [14]. *BABAR*'s main goal is to perform the necessary measurements as precisely as possible. This set of measurements could principally be inconsistent with the CKM formalism resulting in a non-closing UT. The quality of the $|V_{cb}|$ measurement is important for the determination of ρ and η since $|V_{cb}|$ acts as a scale for the two upper UT sides.

More generally spoken: All measurements of CKM matrix elements or combinations of CKM matrix elements (such as α, β, γ) which are predicted in dependence on the four CKM matrix parameters help to further constrain λ, A, ρ and η. The measurement of $|V_{cb}|$ gives constraints on all CKM terms containing $A\lambda^2$-expressions. The current agreement between measurements and CKM formalism is very good as also shown e.g. by the *CKMFitter* group [13].

2.1.3 The Strong Interaction

The theory of strong interaction is the *Quantum Chromo Dynamics* (QCD). It arises from the $SU(3)_C$ gauge symmetry.

The fermions participating in QCD are the quarks. Each quark carries one of three different strong color-charges which are named *red*, *green* and *blue*. Anti-quarks are charged *anti-red*, *anti-green* or *anti-blue*. However, color-charged objects have not been observed in nature – only color-neutral objects were observed. That means that in nature the quarks need to occur in bound *white*[5] states which are named *hadrons*. The two simplest combinations forming such hadrons are:

qqq: The *baryons* which bind one red, one green and one blue quark. The most popular representatives are the proton and the neutron.

$q\bar{q}$: The *mesons* which bind a quark q_1 and an anti-quark $\bar{q}_2$ carrying the anti-color of q_1. Examples are the π-, K-, D- and B-meson.

Also other compositions with vanishing total color-charge are possible ($qq\bar{q}\bar{q}$, $qqqq\bar{q}$, ...) but their existence is not yet clear. The non-existence of free quarks is also called *confinement* – meant is the confinement of quarks in hadrons.

The gauge bosons of the strong interaction are called *gluons*. Due to $SU(3)$ gauge field theory being a non-abelian theory the eight gluons are color-charged themselves and therefore they are allowed to couple to each other.

A very important property of QCD is the running of the strong coupling constant α_s. At very high momenta k^2 (as can be found at low distances, like in hadrons) the coupling constant goes to very low values, $\alpha_s \ll 1$. This feature allows to apply perturbation theory in the high momentum range and is also known as *asymptotic freedom* of quarks. The quark-gluon coupling tends to grow as the momentum scale decreases which results in very strong interactions at energies below $\sim 0.5\,\text{GeV}$ (or distances above the typical hadron dimension of $\sim 1\,\text{fm}$). In contrast to the high momentum range the perturbation theory can not be applied in this low momentum range. Alternative methods for the calculation of the interaction processes have to be found.

There are several calculation techniques. *Lattice QCD* (LQCD) summarizes the procedures to solve the QCD equations directly and numerically by simulations on a discrete space-time-lattice. In principle it could reproduce all features of QCD with arbitrary accuracy, but due to its huge needs of computing power the results have limited precision. The technique called *QCD Sum Rules* uses quark-hadron duality to relate hadronic matrix elements to transition amplitudes of quarks and gluons. The *Heavy Quark Symmetry* (HQS) exploits symmetries from the limit of infinitely heavy quarks, namely spin- and flavor-symmetries. For the calculation of QCD-involved Feynman-diagrams mostly combinations of such techniques are used. For the effective description of exclusive QCD-involved processes, such as $B^- \to D^{*0}e^-\overline{\nu}_e$, one uses the method of form factors.

2.2 The Decay $B^- \to D^{*0}e^-\overline{\nu}_e$

This section contains the most important considerations and formulas to describe the signal decay $B^- \to D^{*0}e^-\overline{\nu}_e$. As a motivation of the analysis, subsection 2.2.1 clarifies why semileptonic decays

---

[5]In analogy to optical theory, color-neutral objects are *white*.

are appropriate to determine $|V_{cb}|$. The *Heavy Quark Symmetry* (HQS) is discussed in subsection 2.2.2 because it is fundamental for the formulas describing the signal decay. Subsections 2.2.3 and 2.2.4 are the core parts of this section, since they derive the partial decay width of the signal decay and go through the relevant items concerning the form factors used in this analysis.

2.2.1 Why Semileptonic Decays

To extract the values of the CKM matrix elements one needs to analyze processes containing the coupling of quarks to the W boson. The corresponding Lagrangian $\mathcal{L}_{CC}^q$ was already given in equation 2.13. For the determination of $|V_{cb}|$ only the terms $V_{cb}\bar{c}_L\gamma^\mu b_L W_\mu^+$ and $V_{cb}^*\bar{b}_L\gamma^\mu c_L W_\mu^-$ are interesting. At the end of this subsection, it should be clear (i) why semileptonic B decays are appropriate for the extraction of $|V_{cb}|$ and (ii) how the strong interaction complicates this extraction. Figures 2.2a to 2.2d give the outline of the current subsection.

Semileptonic Decay on the Quark Level

If there would be no confinement of quarks in hadrons, $|V_{cb}|$ could be determined by analyzing the weak decay of a b quark into a c quark and a lepton pair (see figure 2.2a). The corresponding formulas describing this decay are simple because there are no strong interaction effects to be taken into account. The decay amplitude $\mathcal{M}(b \to c\ell^-\overline{\nu}_\ell)$ would simply be a product of propagator terms for quarks (Q_μ), leptons (L_μ) and W boson ($P^{\mu\nu}(q)$),

$$\mathcal{M}(b \to c\ell^-\overline{\nu}_\ell) = -i\frac{G_F}{\sqrt{2}}V_{cb}L^\mu Q_\mu \,, \tag{2.26}$$

where

$$Q_\mu = \bar{c}\gamma_\mu(1 - \gamma_5)b \,, \tag{2.27}$$

$$L_\mu = \bar{\ell}\gamma_\mu(1 - \gamma_5)\nu \text{ and} \tag{2.28}$$

$$P_{\mu\kappa}(q) = \frac{-i(g_{\mu\kappa} - q_\mu q_\kappa/M_W^2)}{q^2 - M_W^2} \approx i\frac{g_{\mu\kappa}}{M_W^2}. \tag{2.29}$$

In equation 2.26 the approximation of 2.29 has been used. This approximation is valid for little momentum transfers q^μ from the quark current to the lepton current, $q^2 \ll M_W^2$. In this momentum range it is common to use the Fermi-constant G_F instead of the W mass M_W. (Both are connected by $G_F/\sqrt{2} = g^2/8M_W^2$.) At the end of this paragraph it should be re-emphasized: There are no complicated calculations necessary to determine $\mathcal{M}(b \to c\ell^-\overline{\nu}_\ell)$ because the strong interaction is neglected. $\mathcal{M}(b \to c\ell^-\overline{\nu}_\ell)$ is calculable as easy as $\mathcal{M}(\mu^- \to e^-\overline{\nu}_e\nu_\mu)$ for the muon decay.

Semileptonic Decay on the Hadron Level

However, because there is confinement one has to deal with quarks bound in hadrons and one has to deal with QCD. There is still the b quark's semileptonic decay described above, but instead of an initial b and a final c quark state the decay has to be described in dependence of an initial X_b and a final X_c hadron state. That is, because the hadrons are the observed particles — not the quarks. Principally, the translation from the quark-decay-scenario to the hadron-decay-scenario gives the desired decay amplitude $\mathcal{M}(X_b \to X_c\ell^-\overline{\nu}_\ell)$, but for this translation one needs an exact and computable description of quarks within hadrons. Unfortunately, the dynamics within hadrons are given by QCD whose equations are not perturbatively solvable for the quark's typical momentum
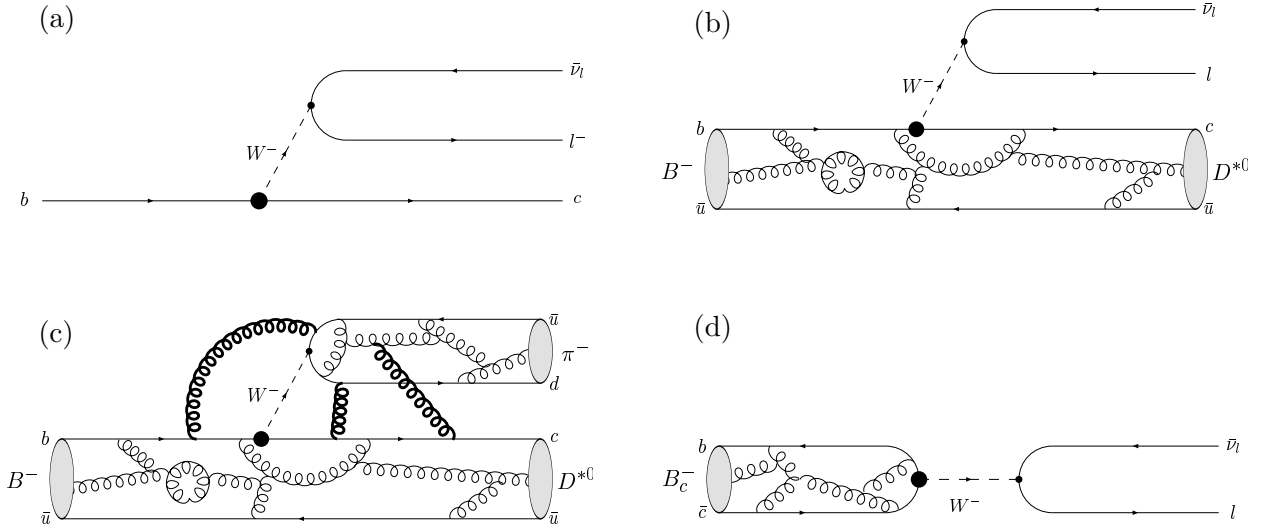
Figure 2.2: Feynman diagrams for weak decays containing the quark transition $b \to cW^-$. The interesting vertex where V_{cb} enters the decay is drawn bigger. **(a,b)** Due to the strong interaction within hadrons, the theoretical description of $B^- \to D^{*0}\ell^-\overline{\nu}_\ell$ is not as simple as the underlying decay on quark level . **(c)** In comparison to the semileptonic B decay, there is an additional exchange of gluons within the hadronic decay $B^- \to D^{*0}\pi^-$. As illustrated by the boldly-drawn gluons , this interaction modifies the coupling between the fermion currents and finally destroys the factorization of the decay amplitude (see text). **(d)** The leptonic meson decay does not have the problems shown in (b) and (c) but its description also depends on the precision limits of QCD calculations.

range within the hadron. Figure 2.2b shows the semileptonic decay on the hadron level. The sketched gluons indicate that complicated QCD dynamics are responsible for the b quark state within the hadron. These gluons destroy the simplicity of the description of the weak decay.

However, the decay $X_b \to X_c\ell^-\overline{\nu}_\ell$ has also pleasant features: The leptonic current coupling to the W boson does not strongly interact with the hadronic current. Therefore, the QCD calculations necessary for the quark-to-hadron translation of the weak decay are limited to the hadronic current. This feature leaves the product structure of equation 2.26 unchanged and therefore it is also called *factorization of hadronic current* (H_μ) *and leptonic current* (L_μ). For the quark-to-hadron translation of equation 2.26 one only needs to replace the quark current Q_μ by the hadron current H_μ and obtains

$$\mathcal{M}(X_b \to X_c\ell^-\overline{\nu}_\ell) = -i\frac{G_F}{\sqrt{2}}V_{cb}L^\mu H_\mu \,, \tag{2.30}$$

for the amplitude of the X_b decay. The leptonic current is still given by equation 2.28. The hadronic current H_μ is connected to the quark current Q_μ,

$$H_\mu = \langle X_c|\overline{c}\gamma_\mu(1-\gamma_5)b|X_b\rangle = \langle X_c|Q_\mu|X_b\rangle \,, \, \tag{2.31}$$

but can not be calculated in a simple manner. The complicated QCD part of H_μ is expressed by form factors. For the decay $B^- \to D^{*0}e^-\overline{\nu}_e$, where Heavy Quark Effective Theory (HQET) is applicable, these form factors can be related to each other. This is shown in detail in section 2.2.3.

Weak Hadronic Decay

The replacement of the leptonic current by a second hadronic current illustrates the advantages

of semileptonic decays for the $|V_{cb}|$ determination (see figure 2.2c). To express the resulting decay amplitude it is not enough to replace L_μ by a term similar to the H_μ term defined in equation 2.31. Besides the strong interaction *within* the hadrons, there is also strong interaction *between* the two hadronic currents. This destroys the factorization of the decay amplitude of the weak decay. In figure 2.2c, this is emphasized by the bold drawn gluon lines.

At this point the importance of semileptonic decays should become clear: There is not only the advantage to express the decay amplitude $\mathcal{M}(X_b \to X_c \ell^- \overline{\nu}_\ell)$ as a product. There is also the possibility to learn more about the states of quarks in hadrons. In the quark-to-hadron transition of semileptonic decays, all changes not explained by phase space effects should be assigned to effects arising from the QCD *within* hadrons. In contrast to semileptonic decays, within weak hadronic decays there is the occurrence of strong interaction (i) within each of the hadrons and (ii) between the hadrons.

Leptonic Meson Decay

For completeness one should mention leptonic meson decays (see figure 2.2d). Are they more appropriate for the determination of CKM matrix elements since they do not show the disturbing QCD effects of weak hadronic and semileptonic decays? The difficulties to perform precise QCD calculations enter also the analyses of leptonic decays. The leptonic decay rate of a meson M is proportional to $f_M^2 |V_{q_1 q_2}|^2$ where $|V_{q_1 q_2}|$ is the corresponding CKM matrix element and f_M is the meson decay constant giving the overlap probability of the quarks q_1 and $\bar{q}_2$ within the meson M. To determine $|V_{q_1 q_2}|$ from a measurement of the meson decay rate one has to give an input value for f_M. But this input is (mostly) only available by less-precise QCD calculations. Therefore, a convincing determination of $|V_{q_1 q_2}|$ is not possible from leptonic decays, but there are other interesting issues for leptonic decays [14].

However, for a determination of $|V_{cb}|$ from leptonic decays one would need to experiment with B_c mesons. This is obviously not convenient.

2.2.2 Heavy Quark Symmetry and Isgur-Wise Function

If the b and the c quark masses are much larger then the other constituents of the X_b and the X_c hadrons, $m_b \approx m_{X_b}$ and $m_c \approx m_{X_c}$, then for an effective description of $X_b \to X_c \ell^- \overline{\nu}_\ell$ one can use the *Heavy Quark Symmetry* (HQS). This description is obtained in two steps. Firstly, the hadronic current H_μ defined in equation 2.31 is regarded in the limit $m_b, m_c \to \infty$. This leads directly to the symmetries summarized by the name Heavy Quark Symmetry and to the existence of the *Isgur-Wise function*. Secondly, the corrections of HQS due to the finite masses of b and c quarks are performed by the *Heavy Quark Effective Theory* (HQET).

Heavy Quark Symmetry

Assuming $m_b \approx m_{X_b}$ and $m_c \approx m_{X_c}$, the essential feature for the description of $X_b \to X_c \ell^- \overline{\nu}_\ell$ is a separation of the length scales within the hadrons. There are the two scales R_{had} and λ_Q. The former gives the typical size of a hadron, $R_{\text{had}} \sim 1/\Lambda_{\text{QCD}} \sim 1\,\text{fm}$, where Λ_{QCD} is the typical momentum transfer between the light constituents and the heavy quark Q of the hadron. The second scale within a hadron, λ_Q, is the Compton wavelength of the heavy quark. Since its value is much smaller then the typical hadron size ($\lambda_Q \sim 1/m_Q \sim (0.04\ldots0.1)\,\text{fm} \ll 1\,\text{fm}$) to resolve the quantum numbers of the heavy quark would require a hard probe. The gluons exchanged between the hadron's light constituents and the hadron's heavy quark can only resolve distances much larger
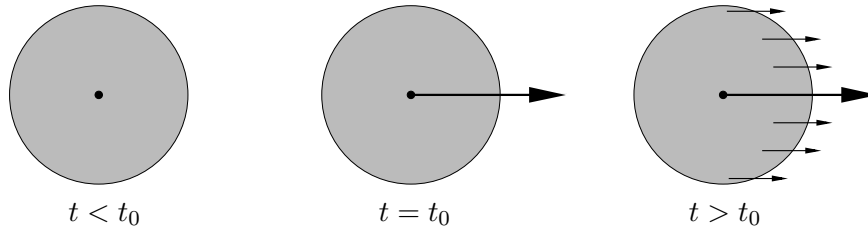
Figure 2.3: The elastic transition of the B meson. After the velocity of the heavy quark (centered dot) changes at $t = t_0$ the meson's light degrees of freedom (grey area) have to be rearranged (see text).

then λ_Q. Therefore, they do not directly interact with the heavy quark but experience its color field extending over distances large compared to λ_Q. In fact, only the heavy quark's electric color field is important and its relativistic effects such as color magnetism vanish in the limit $m_Q \to \infty$. Since the heavy quark spin only participates in interactions through such relativistic effects, it decouples. Summarizing, one often says that the hadron's light degrees of freedom are blind to the flavor (mass) and the spin of the heavy quark. More precisely spoken: In the limit $m_Q \to \infty$, hadronic systems which differ only in the flavor or spin of the heavy quark have the same configuration of light degrees of freedom. These symmetries are commonly called Heavy Quark Symmetry.

Isgur-Wise Function

The (hadron-internal) strong interaction in the decay $X_b \to X_c \ell^- \overline{\nu}_\ell$ is expressed by form factors (see section 2.2.3 and [17]). In the HQS limit all of these form factors converge at one single function, the *Isgur-Wise function* $\xi(v \cdot v')$ where v and v' are the initial and the final four velocity of the hadron system, respectively, and the product $w = v \cdot v'$ is the boost of the X_c hadron in the X_b rest frame. HQS helps to relate the form factors to each other but can not predict their absolute values. The only known absolute value is that of $\xi(w = 1)$ — a fact playing an important role for the determination of $|V_{cb}|$. At this interesting point in the decay's phase space ($w = 1$) the hadron is minimally disturbed and the normalization of the Isgur-Wise function is given by $\xi(1) = 1$.

To demonstrate the use and the origin of the Isgur-Wise function it is common to consider the elastic scattering of a B meson, $B(v) \to B(v')$, induced by a vector current coupled to the b quark.[6] What happens within the B meson during the scattering process? The initial situation is the following: Due to $m_b \approx m_B$, the b quark and B meson have the same average velocity v. Therefore, the heavy quark is nothing else but a static source of color charge in the meson rest frame. The meson's light degrees of freedom (LDF) orbit around the b quark. At a time t_0 the meson's heavy quark b_v is instantaneously replaced by another b quark ($b_{v'}$) moving with velocity v' (see figure 2.3). For $t > t_0$ the LDF have to interact with a moving color source instead with a static one. To 'repair' the meson disordered by the b quark replacement, an exchange of soft gluons between the heavy quark and the LDF is needed. This exchange re-establishes the old situation within the B meson, i.e. the LDF within the rest frame of the initial B meson at $t < t_0$ have to look like the LDF within the rest frame of the final B meson at $t > t_0$. As the difference between v and v' grows the probability to successfully rearrange the LDF decreases — there is a form factor suppression of the elastic scattering. In the HQS limit the probability amplitude ξ of this elastic scattering is found to depend only on the boost $w = v \cdot v'$ between the rest frame's of the initial and the final B meson. In honor for its originators [15, 16], the probability amplitude $\xi(w)$ is also

---

[6]From this point on, the discussion considers only the case where X_b and X_c are mesons (e.g. $X_b = B$ and $X_c = D^*$), although it is identical for the baryonic case (such as $X_b = \Lambda_b$ and $X_c = \Lambda_c$).

called the Isgur-Wise function. For $v = v'$ (which is equal to $w = 1$) there is no real scattering process. Thus, the probability of a 'successful rearrangement' within the B meson should be one, $\xi(1) = 1$.

How does these considerations help to describe the process $B \to D^* \ell \overline{\nu}_\ell$? The conclusions of the described elastic B scattering do not change ...

- ... if the heavy bottom quark b_v is replaced by a heavy charm quark $c_{v'}$ (instead of replacement by a heavy bottom quark $b_{v'}$) or

- ... if an additional spin rotation is performed in the heavy quark replacement, i.e. if the heavy bottom quark $b_v^{\Uparrow}$ with spin up is replaced by the heavy charm quark $c_{v'}^{\Downarrow}$ with spin down.

These statements are due to flavor and spin symmetry, respectively. Since (i) the replacement of $b_v^{\Uparrow}$ by $c_{v'}^{\Downarrow}$ transforms the B meson into a D^* meson and (ii) the vector current giving the kick to the heavy quark could be a W boson, the conclusions of the elastic B scattering can directly be applied to the decay $B \to D^* \ell \overline{\nu}_\ell$. All of these statements are only true in the HQS limit, i.e. $m_b, m_c \to \infty$.

Heavy Quark Effective Theory

Since the b and the c quark mass are finite, it is not correct to describe the meson in the HQS limit. But it can be described by means of an effective theory where the HQS is broken. Within the framework of this theory it should be easy to examine the limit $m_b, m_c \to \infty$ and to use the existence of the Isgur-Wise function in this limit. Such a theory is called Heavy Quark Effective Theory (HQET). HQET systematically expands the QCD Lagrangian in terms of Λ_{QCD}/m_Q and in terms of $\alpha_s(m_Q)$ where $m_Q = m_b$ or m_c, and α_s is the strong coupling constant. The HQS-breaking correction terms $\alpha_s^n(m_Q)$ can be calculated order by order by perturbation theory, whereas the determination of the terms $(\Lambda_{\text{QCD}}/m_Q)^n$ is more difficult. Section 2.2.4 contains a discussion of these corrections.

2.2.3 The Partial Decay Width of $B^- \to D^{*0} e^- \overline{\nu}_e$

Usually, the amplitude of a process $X \to Y W^\pm$ is expressed by the four-momentum transfer $q^2 = (p_X - p_Y)^2$, where p_X and p_Y are the four momenta of the fermions X and Y coupling to the W boson. However, for the HQET description of $X_b \to X_c \ell^- \overline{\nu}_\ell$ it is more convenient to use the four velocities of the X_b hadron (v) and the X_c hadron (v') instead of their corresponding momenta. This statement becomes plausible if one argues like this: The mass of the light constituents of the X_b hadron is of order Λ_{QCD}. Therefore, the square of the four momentum transferred to these constituents during the decay must be $\sim \Lambda_{\text{QCD}}^2 (v - v')^2 = 2\Lambda_{\text{QCD}}^2 (1 - v \cdot v')$, independent of the heavy quark mass. But, four velocities are not only appropriate variables to describe the QCD dynamics in the hadron transition. Since the velocity and the mass of a particle are independent the HQS limit ($m_b, m_c \to \infty$) can be easily performed, simultaneously checking the small HQS-breaking terms.

Kinematic Range

Within the next lines the semileptonic decay $B^- \to D^{*0} e^- \overline{\nu}_e$ is regarded (see figure 2.2b) which is a special case of the previously discussed general case $X_b \to X_c \ell^- \overline{\nu}_\ell$. A already mentioned, the product w of the D^{*0}'s and the B's four velocity,

$$w = v_B \cdot v_{D^{*0}}, \tag{2.32}$$

plays an important role in HQET. Within the rest frame of the B meson the product can be identified with the relativistic boost $\gamma_{D^{*0}}$ of the D^{*0} meson,

$$w = \begin{pmatrix} 1 \\ \vec{0} \end{pmatrix} \begin{pmatrix} \gamma_{D^{*0}} \\ \gamma_{D^{*0}}\vec{\beta}_{D^{*0}} \end{pmatrix} = \gamma_{D^{*0}}. \tag{2.33}$$

The boost w and the momentum transfer $q^\mu = p_B^\mu - p_{D^{*0}}^\mu$ from the hadron to the lepton system are connected by

$$w = \frac{m_B^2 + m_{D^{*0}}^2 - q^2}{2m_B m_{D^{*0}}}. \tag{2.34}$$

Setting $w = 1$ gives $q_{\max}^2$ in the 'zero-recoil' situation, and setting $q^2 = 0$ gives $w_{\max}$ in the situation of maximum momentum transfer to the D^{*0} meson:

$$w = w_{\min} = 1 \qquad \Rightarrow \qquad q_{\max}^2 = (m_B - m_{D^{*0}})^2 = 10.71 \,\text{GeV}^2 \tag{2.35a}$$

$$q^2 = q_{\min}^2 = 0 \qquad \Rightarrow \qquad w_{\max} = \frac{m_B^2 + m_{D^{*0}}^2}{2m_B m_{D^{*0}}} = 1.5054. \tag{2.35b}$$

Zero-recoil means, that there is no momentum transfer from the B meson to the D^{*0} meson. The daughter meson rests in its mother's rest frame. Due to HQS, the meson system remains nearly undisturbed at this interesting phase space point. Section 2.2.4 shows that this is important for the $|V_{cb}|$ determination. As also shown in this section, the small kinematic w-range of the decay ($\Delta w = w_{\max} - w_{\min} \approx 0.5$) helps to approximate the w dependence of the form factor.

Traditional Form Factors

In section 2.2.1, there was already given the decay amplitude $\mathcal{M}$ for semileptonic decays. For reasons of clarity it is rewritten here. For the decay of a meson $M_{Q\bar{q}}$ to a meson $X_{q'\bar{q}}$ and a lepton pair $\ell^-\bar{\nu}_\ell$ it is given by

$$\mathcal{M}(M_{Q\bar{q}} \rightarrow X_{q'\bar{q}}\ell^-\bar{\nu}_\ell) = -i\frac{G_F}{\sqrt{2}}V_{q'Q}L^\mu H_\mu, \tag{2.36}$$

with the leptonic and hadronic currents

$$L^\mu = \bar{\ell}\gamma^\mu(1-\gamma_5)\nu \quad \text{and} \tag{2.37}$$

$$H_\mu = \langle X|\bar{q}'\gamma_\mu(1-\gamma_5)Q|M\rangle. \tag{2.38}$$

The meson $M_{Q\bar{q}}$ is composed by a heavy quark Q and a light quark $\bar{q}$, the meson $X_{q'\bar{q}}$ is composed by a heavy quark q' and the previous light quark $\bar{q}$. For a semileptonic decay of a pseudoscalar meson P ($= M_{Q\bar{q}}$) to an vector meson V ($= X_{q'\bar{q}}$) the most general form of the hadronic current must be linear in the vector meson's polarization vector ε.[7] It is given by a set of traditional form factors $V(q^2)$ and $A_i(q^2)$ with $i = 0, 1, 2, 3$ [17]:

$$\begin{aligned} H^\mu &= \langle V(p',\varepsilon)|V^\mu - A^\mu|P(p)\rangle \\ &= \frac{2i\epsilon^{\mu\nu\alpha\beta}}{M+m}\varepsilon_\nu^* p'_\alpha p_\beta V(q^2) \;-\; (M+m)\varepsilon^{*\mu}A_1(q^2) \\ &\quad + \frac{\varepsilon^* \cdot q}{M+m}(p+p')^\mu A_2(q^2) \;+\; 2m\frac{\varepsilon^* \cdot q}{q^2}q^\mu A_3(q^2) \;-\; 2m\frac{\varepsilon^* \cdot q}{q^2}q^\mu A_0(q^2), \end{aligned} \tag{2.39}$$

---

[7]The polarization vector ε of a meson with velocity v satisfies the equations $\varepsilon \cdot v = 0$ and $\varepsilon \cdot \varepsilon^* = -1$, as well as $\sum_{\text{pol.}} \varepsilon^\mu \varepsilon^{*\nu} = v^\mu v^\nu - g^{\mu\nu}$. It can be written as sum of three orthonormal vectors e^i that are orthogonal to v: $\varepsilon^\mu = \vec{a}\vec{e}^\mu$ [18].

where $V^\mu = \bar{q}'\gamma^\mu Q$ and $A^\mu = \bar{q}'\gamma^\mu\gamma_5 Q$, and A_3 is an abbreviation,

$$A_3(q^2) = \frac{M+m}{2m}A_1(q^2) - \frac{M-m}{2m}A_2(q^2) \tag{2.40}$$

$$A_3(0) = A_0(0). \tag{2.41}$$

The total anti-symmetric tensor $\epsilon^{\mu\nu\alpha\beta}$ fulfills the relation $\epsilon^{0123} = -\epsilon_{0123} = -1$. The variables M and m are the masses of the P and the V meson, p and p' are their four-momenta, respectively. $q = p - p'$ defines the four-momentum transfer to the lepton pair. Since the term $q^\mu L_\mu$ vanishes in the limit $m_\ell \to 0$ [18] the relevant hadronic current for $\ell \neq \tau$ can be written in terms of the three form factors:

$$\langle V(p',\varepsilon)|V^\mu - A^\mu|P(p)\rangle = \frac{2i\epsilon^{\mu\nu\alpha\beta}}{M+m}\varepsilon_\nu^* p'_\alpha p_\beta V(q^2)$$
$$- (M+m)\varepsilon^{*\mu}A_1(q^2) - \frac{\varepsilon^* \cdot q}{M+m}(p+p')^\mu A_2(q^2). \tag{2.42}$$

The form factors $A_1(q^2)$ and $A_2(q^2)$ can be associated with the exchange of a particle with quantum numbers $J^P = 1^+$, whereas $V(q^2)$ is associated with $J^P = 1^-$.

Helicity Form Factors
Instead to express the hadronic current H_μ in terms of axial vector fractions (A_i terms) and vector fractions (V term) it can be reordered in terms of helicity fractions. The reordered expression of H_μ contains the form factors H_0, H_+ and H_- corresponding to the possible helicities $0, +1$ and -1 of the vector meson V, respectively. The helicity form factors are defined by

$$H_0(q^2) = \frac{1}{2m\sqrt{q^2}}\left[(M^2 - m^2 - q^2)(M+m)A_1(q^2) - 4\frac{M^2|\vec{p}'|^2}{M+m}A_2(q^2)\right] \quad \text{and} \tag{2.43a}$$

$$H_\pm(q^2) = (M+m)A_1(q^2) \mp \frac{2M|\vec{p}'|^2}{M+m}V(q^2), \tag{2.43b}$$

where $\vec{p}'$ is the momentum three-vector of the vector meson in the rest frame of P. Its magnitude is $|\vec{p}'| = m\sqrt{w^2 - 1}$. (In general all q^2 dependent expressions can be noted by w instead of q^2.) In the definition of H_+, H_- and H_0 one can see that A_1 dominates all three helicity form factors in the range of high q^2 values (range with $w \approx 1$). This becomes important in section 2.2.4 where the q^2 dependence of the form factors is parametrized.

At this point, the resulting expression for H_μ would still contain the polarization vector ε of the vector meson V. If V decays into two pseudoscalars, $V \to P_1 P_2$, then ε is determined by the orientation of the $V \to P_1 P_2$ decay relative to the $P \to V\ell^-\bar{\nu}_\ell$ decay. In this case the differential decay width resulting from equations 2.36 and 2.42 can be expressed in terms of the four kinematic
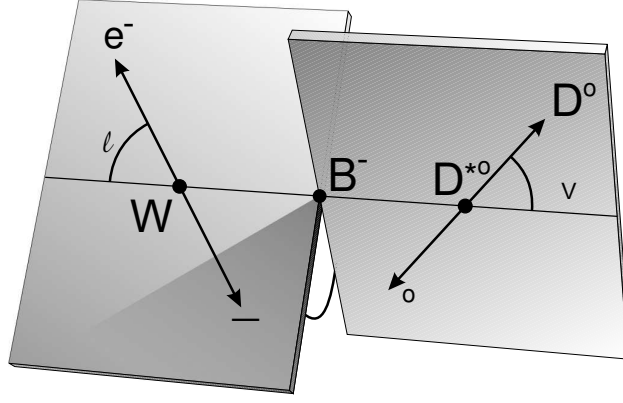
Figure 2.4: The definition of the decay angles θ_ℓ, θ_V and χ is illustrated for the decay $B^- \to D^{*0} e^- \bar{\nu}_e$, $D^{*0} \to D^0 \pi^0$. The daughters of the W boson and the D^{*0} are drawn back-to-back because the angles θ_ℓ and θ_V are defined in the corresponding B daughter rest frames.

variables θ_ℓ, θ_V, χ, and w as

$$
\begin{aligned}
\frac{\mathrm{d}\Gamma(P \to V\ell^- \bar{\nu}_\ell, V \to P_1 P_2)}{\mathrm{d}w \, \mathrm{d}\cos\theta_V \, \mathrm{d}\cos\theta_\ell \, \mathrm{d}\chi} = {} & \frac{6}{8(4\pi)^4} G_F^2 \left| V_{q'Q} \right|^2 M^3 r^2 \sqrt{w^2 - 1}(1 - 2wr + r^2)\mathcal{B}(V \to P_1 P_2) \\
& \times \Big[(1 - \eta\cos\theta_\ell)^2 \sin^2\theta_V \left| H_+(w) \right|^2 \\
& + \; (1 + \eta\cos\theta_\ell)^2 \sin^2\theta_V \left| H_-(w) \right|^2 \\
& + \; 4\sin^2\theta_\ell \cos^2\theta_V \left| H_0(w) \right|^2 \\
& - \; 4\eta\sin\theta_\ell(1 - \eta\cos\theta_\ell)\sin\theta_V \cos\theta_V \cos\chi H_+(w)H_0(w) \\
& + \; 4\eta\sin\theta_\ell(1 + \eta\cos\theta_\ell)\sin\theta_V \cos\theta_V \cos\chi H_-(w)H_0(w) \\
& - \; 2\sin^2\theta_\ell \sin^2\theta_V \cos 2\chi H_+(w)H_-(w) \Big] .
\end{aligned}
$$

$$(2.44)$$

Figure 2.4 illustrates the relevant decay angles. It shows the decay for a special choice of particles, $B^- \to D^{*0} e^- \bar{\nu}_e$, $D^{*0} \to D^0 \pi^0$. The angle between the charged lepton and the opposite direction of the vector meson has to be measured within the $\ell^- \bar{\nu}_\ell$ rest frame to define θ_ℓ. Similarly, θ_V is the angle between the directions of V and P_1 meson as measured in the rest frame of V. The angle χ is defined as the angle between the momentum vector projection of P_1 meson and charged lepton onto the plane perpendicular to the direction of V in the P rest frame. If the heavy quark of the P meson is a b quark then $\eta = +1$, if it is a c quark then $\eta = -1$. The variable r is an abbreviation for the ratio of the V and P meson mass, $r = m/M$. Since the mother meson P has spin zero, the vector meson V and the exchanged W boson must have the same helicity. Thus, the derivation of the differential decay rate is simplified by using form factors in the helicity notation.

HQET Form Factors
So far, two sets of form factors have been introduced. Each is appropriate for a certain task. The traditional form factor set is momentum related. It allows for an easy division of the matrix element $\mathcal{M}$ into an axial-vector-coupled interaction part and a vector-coupled interaction part, helpful to discuss physics. The helicity form factor set is appropriate to translate the decay amplitude into a differential decay rate of clean structure.

The definition of a third set of form factors starts with the renotation of H_μ in terms of velocities rather then momenta,

$$
\begin{aligned}
\langle V(v',\varepsilon)|V^\mu - A^\mu|P(v)\rangle = \sqrt{Mm} \Big[& ih_V(w)\epsilon^{\mu\nu\alpha\beta}\varepsilon^*_\nu v'_\alpha v_\beta \\
& - h_{A_1}(w)\varepsilon^{*\mu}(w+1) \ + \ h_{A_2}(w)v^\mu\varepsilon^* \cdot v \\
& + h_{A_3}(w)v'^\mu\varepsilon^* \cdot v \Big],
\end{aligned}
\tag{2.45}
$$

where $w = v \cdot v'$. The comparison with equation 2.42 shows how the traditional form factors V, A_1, A_2 and A_3 are connected to the HQET form factors h_V, h_{A_1}, h_{A_2} and h_{A_3}:

$$
R^* V(q^2) = h_V(w) \tag{2.46a}
$$

$$
R^{*-1} A_1(q^2) = \frac{w+1}{2}h_{A_1}(w) \tag{2.46b}
$$

$$
R^* A_2(q^2) = h_{A_3}(w) + \frac{m}{M}h_{A_2}(w). \tag{2.46c}
$$

Thereby, R^* is an abbreviation for the ratio between geometric and arithmetic mean of the V and the P meson mass, $R^* = 2\sqrt{Mm}/(M+m)$, and q^2 and w are connected by equation 2.34. One important feature of the HQET notation is the simplification in the HQS limit $(m_Q, m_{q'} \to \infty)$ [15, 16],

$$
h_V(w) = h_{A_1}(w) = h_{A_3}(w) = \xi(w) \quad \text{and} \tag{2.47a}
$$

$$
h_{A_2}(w) = 0, \tag{2.47b}
$$

where $\xi(w)$ is the already discussed Isgur-Wise function. The heavier the Q and the q' quark are, the closer are the HQET form factors to the Isgur-Wise function. The form factor ratios R_1 and R_2, defined by

$$
R_1(w) = \frac{h_V(w)}{h_{A_1}(w)} = \left[1 - \frac{q^2}{m+M}\right]\frac{V(q^2)}{A_1(q^2)} \quad \text{and} \tag{2.48a}
$$

$$
R_2(w) = \frac{h_{A_3}(w) + \frac{m}{M}h_{A_2}(w)}{h_{A_1}(w)} = \left[1 - \frac{q^2}{m+M}\right]\frac{A_2(q^2)}{A_1(q^2)}, \tag{2.48b}
$$

have a smaller w dependence at higher Q and q' quark masses. At very high masses these ratios become nearly constant, and in the HQS limit there is even $R_1(1) = R_2(1) = 1$.

At this point one should emphasize the big benefit of the HQET form factor notation. In general, to calculate the q^2 dependence of a semileptonic decay one needs the q^2 dependence of the form factors. Starting from the traditional form factors (equ. 2.42) one would need to feed the calculations by q^2 dependencies of V, A_1 and A_2 – these are three different functions one has to 'guess'. Using the HQET form factors one only has to 'guess' the w dependence (or q^2 dependence) of one single form factor. The other two form factors are expressed by R_1 and R_2 whose w dependence is very mild or even negligible.[8] As already mentioned before, in HQET one calculates HQS-breaking corrections. Also due to equations 2.47, h_{A_1}, R_1 and R_2 are the most-appropriate functions for the calculation of these corrections. This discussion is continued in section 2.2.4.

---

[8]As for most statements within section 2.2, this is only true if the HQET assumptions are truly given. HQET makes only sense for mesons composed by a heavy and a light quark.

Partial Decay Rate dΓ/dw

In order to relate the formulas of this chapter to the entire document, the particles of the discussed semileptonic decay $P \to V\ell^-\overline{\nu}_\ell, V \to P_1 P_2$ are concretized by the decay $B^- \to D^{*0}e^-\overline{\nu}_e, D^{*0} \to D^0\pi^0$. After the integration of equation 2.44 over the three decay angles θ_ℓ, θ_V and χ one obtains the differential decay rate dΓ/dw depending on a form factor $F(w)$:

$$\frac{\mathrm{d}\Gamma\left(B^- \to D^{*0}e^-\overline{\nu}_e\right)}{\mathrm{d}w} = \frac{G_F^2}{48\pi^3}\left(m_B - m_{D^*}\right)^2 m_{D^*}^3 \sqrt{w^2-1}\,(w+1)^2$$
$$\times \left[1 + \frac{4w}{w+1}\frac{m_B^2 - 2wm_Bm_{D^*} + m_{D^*}^2}{(m_B - m_{D^*})^2}\right] \quad (2.49)$$
$$\times F(w)^2 \left|V_{cb}\right|^2.$$

The form factor $F(w)$ can be expressed in terms of $h_{A_1}(w)$, $R_1(w)$ and $R_2(w)$:

$$F(w) = |h_{A_1}(w)|^2 \left[1 + \frac{4w}{w+1}\frac{m_B^2 - 2wm_Bm_{D^*} + m_{D^*}^2}{(m_B - m_{D^*})^2}\right]^{-1} \sum_{i=0,+,-}\left|\tilde{H}_i(w)\right|^2 \quad (2.50\mathrm{a})$$

$$\left|\tilde{H}_0(w)\right|^2 = \left[1 + \frac{w-1}{1-r}\left(1 - R_2(w)\right)\right]^2 \quad (2.50\mathrm{b})$$

$$\left|\tilde{H}_\pm(w)\right|^2 = \frac{1 - 2wr + r^2}{(1-r)^2}\left[1 \mp \sqrt{\frac{w-1}{w+1}}R_1(w)\right]^2. \quad (2.50\mathrm{c})$$

In the literature the $\tilde{H}_i(w)$ expressions are also called 'reduced helicity amplitudes' because they are related to the helicity amplitudes by [19]

$$\tilde{H}_i(w) = \frac{H_i(w)}{(m_B - m_{D^{*0}})\sqrt{m_B m_{D^{*0}}/q^2(w)}(w+1)h_{A_1}(w)} \quad (i = 0, +, -). \quad (2.51)$$

Branching Fraction

From the integration of dΓ/dw over the allowed w range one obtains the branching fraction $\mathcal{B}\left(B^- \to D^{*0}e^-\overline{\nu}_e\right)$,

$$\mathcal{B}\left(B^- \to D^{*0}e^-\overline{\nu}_e\right) = \tau_{B^-} \int_{w_{\min}}^{w_{\max}} \frac{\mathrm{d}\Gamma}{\mathrm{d}w}\mathrm{d}w, \quad (2.52)$$

where τ_{B^-} is the lifetime of charged B mesons, and $w_{\min}$ and $w_{\max}$ are given by equations 2.35.

2.2.4 $|V_{cb}|$ Determination

Basic Idea

As can be seen in equation 2.49, the differential decay rate dΓ/dw of the $B^- \to D^{*0}e^-\overline{\nu}_e$ decay is proportional to $[F(w)|V_{cb}|]^2$. As discussed later in this section, theory can calculate the form factor F at zero-recoil ($w = 1$) with a precision which is higher then at any other point in the phase space ($w > 1$). Consequently, from a measurement of dΓ/dw at $w = 1$ one could obtain $[F(1)|V_{cb}|]^2$, and due to the high precision of $F(1)$ this measurement would also give a precise value of $|V_{cb}|$. However, since dΓ/dw is proportional to the factor $\sqrt{w^2-1}$ the phase space is empty at
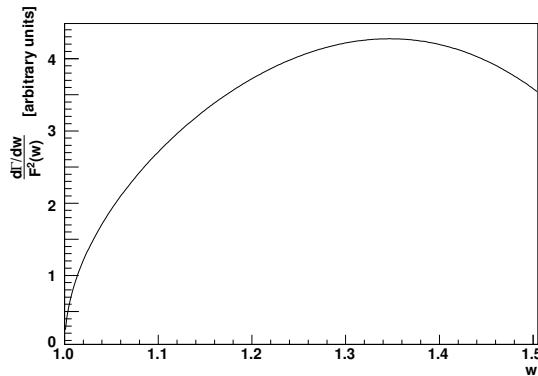
Figure 2.5: The phase space fraction of $\mathrm{d}\Gamma/\mathrm{d}w(B^- \to D^{*0}e^-\overline{\nu}_e)$ from equation 2.49. One can see that the phase space is empty at $w = 1$. This complicates the $|V_{cb}|$ extraction.

$w = 1$ (see figure 2.5). The solution is to measure $\mathrm{d}\Gamma/\mathrm{d}w$ as a function of w and to extract $|V_{cb}|$ from an extrapolation of this function to $w = 1$. For the extrapolation one needs the shape of the form factor F in the neighborhood of $w = 1$. Since HQET gives no predictions for the shape of h_{A_1}, the principle shape of F remains also unconfined. There are different models predicting the shape. One of the simplest models is the linear dependence $h_{A_1}(w) = h_{A_1}(1)[1 - \tilde{\rho}^2(w - 1)]$ with one single parameter $\tilde{\rho}^2$ which is also implemented in the *BABAR* simulation (see sec. 5.3.1.2). For a comparison of various $|V_{cb}|$ determinations, all following the strategy described above but basing on different h_{A_1} models or different data samples, one uses an expansion of the form factor F around $w = 1$:

$$F(w) = F(1) \left[1 \ - \ \rho_F^2(w - 1) \ + \ c_F(w - 1)^2 \ + \ \dots \right]. \tag{2.53}$$

The parameters ρ_F^2 and c_F are the negative slope and the curvature of the form factor F at zero-recoil – they are the important parameters for the $|V_{cb}|$ determining extrapolation. The small allowed w-range of the $B^- \to D^{*0}e^-\overline{\nu}_e$ decay ranging only from $w = 1$ up to $w \approx 1.5$, and the very mild w dependence of the form factor ratios R_1 and R_2 (see equ. 2.64), both facts motivate the expansion ansatz of $F(w)$. In case of very big data samples one may be sensitive to higher order terms , but so far the first two coefficients in equation 2.53 are enough.

Normalization of $F(w)$

In the HQS limit one finds $F(w) = \xi(w)$. Due to the normalization of the Isgur-Wise function at zero-recoil, $\xi(1) = 1$, one also knows the corresponding value of $F(1)$ in the HQS limit,

$$\lim_{m_Q \to \infty} F(1) = 1. \tag{2.54}$$

Outside the HQS limit one has to install corrections to this value. The principle structure of the corrected form factor at $w = 1$ is mostly expressed like this [8]:

$$F(1) \ = \ \eta_{\mathrm{QED}} \ \eta_{\mathrm{QCD}} \left[1 \ + \ \cancel{\delta_{1/m}} \ + \ \delta_{1/m^2} \ + \ \dots \right], \tag{2.55}$$

where η_{QED} and η_{QCD} are the short-distance radiative corrections of QED [20] and QCD [21],

$$\eta_{\mathrm{QED}} = 1.007 \quad \text{and} \tag{2.56}$$

$$\eta_{\mathrm{QCD}} = 0.960 \pm 0.007. \tag{2.57}$$

The terms δ_{1/m^n} represent the non-perturbative $(1/m_b)^n$ and $(1/m_c)^n$ corrections $(n = 1, 2, \ldots)$. For $n = 2$ the correction is given by [22]

$$\delta_{1/m^2} = -0.055 \pm 0.025. \tag{2.58}$$

A combination of all contributions to the form factor value gives

$$F(1) = 0.914 \pm 0.026. \tag{2.59}$$

This result is in agreement with recent results from lattice QCD calculations [23],

$$F(1) = 0.919^{-0.030}_{+0.035}. \tag{2.60}$$

The non-perturbative correction term $\delta_{1/m}$ in equation 2.55 is canceled due to *Luke*'s theorem [24]. Luke's theorem states that $1/m$ corrections vanish for the form factor h_{A_1} at zero-recoil ($w = 1$). The form factors h_{A_2}, h_{A_3} and h_V do have $1/m$ corrections. From equations 2.43 and 2.46b one can recognize that only h_{A_1} contributes to the decay rate at $w = 1$. The consequence is a form factor F whose $1/m$ corrections vanish at $w = 1$. As one can see now, it has been useful to express F in dependence on h_{A_1} than in dependence on any other h_x form factor. As can be seen from equations 2.50, the form factors h_{A_1} and F are equal at zero-recoil, $F(1) = h_{A_1}(1)$.

Shape of $F(w)$

Constraints on the shape of $F(w)$ are highly desirable because they improve the $|V_{cb}|$-determining extrapolation. A suitable framework to derive such constraints is a dispersion technique proposed some time ago [25, 26]. This technique has also been applied to heavy-meson form factors by authors like Rafael and Taron [27, 28], or Boyd, Grinstein and Lebed [29, 30, 31]. As briefly described in [32], the dispersion technique bases on first principles: the analyticity properties of QCD two-point functions of local currents and the positivity of the corresponding hadronic spectral function. From relations between the two-point function and the spectral function one obtains boundaries arising from the positivity of the spectral function. Consequently, these bounds set constraints on the form factors of the regarded states. Briefly said, the dispersion technique is a special type of the 'QCD Sum Rules' already mentioned in section 2.1.3.

Caprini, Lellouch and Neubert [32] apply the dispersion technique by fully exploiting the spin symmetry of $B^{(*)}$ and $D^{(*)}$ mesons. They investigate all spin-parity channels ($J^P = 0^+, 0^-, 1^+$ and 1^-) relevant for $B^{(*)} \to D^{(*)}$ transitions. This results in four inequalities giving constraints to the allowed range of the parameters of the corresponding twenty form factors. Since the form factors can be related to each other, strong constraints can be given also to h_{A_1}. One of the results of their work is a one-parameter description of the form factor $h_{A_1}(w)$ describing the shape within the relevant semileptonic region with an accuracy better then 2%[9]:

$$\begin{aligned}
\frac{h_{A_1}(w)}{h_{A_1}(1)} &= 1 - 8\rho_{A_1}^2 z + \left(53\rho_{A_1}^2 - 15\right) z^2 - \left(231\rho_{A_1}^2 - 91\right) z^3 \\
&\text{with} \quad z = \frac{\sqrt{w+1} - \sqrt{2}}{\sqrt{w+1} + \sqrt{2}}.
\end{aligned} \tag{2.61}$$

---

[9]In formulas (35) and (38) of reference [32] the form factor function has been called $A_1(w)$ instead of $h_{A_1}(w)$. However, here the notation usually found in literature [18, 23, 33] is used.
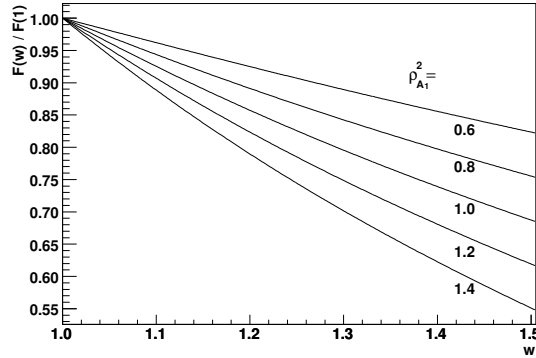
Figure 2.6: Form factor $F(w)$ for the model of Caprini, Lellouch and Neubert [32]. The form factor is shown for the $\rho_{A_1}^2$ values 0.6, 0.8, 1.0, 1.2 and 1.4, respectively from top function to bottom function.

The parametrization of $h_{A_1}(w)$ is constructed in a way that its only parameter $\rho_{A_1}^2$ is the negative slope of $h_{A_1}(w)$ at zero-recoil,

$$\left.\frac{\mathrm{d}h_{A_1}(w)}{\mathrm{d}w}\right|_{w=1} = -\rho_{A_1}^2. \tag{2.62}$$

From the found dispersive bounds also follow an upper and a lower limit on $\rho_{A_1}^2$,

$$-0.14 < \rho_{A_1}^2 < 1.54. \tag{2.63}$$

For applying this parametrization to the differential decay rate in equation 2.49, Caprini, Lellouch and Neubert give also the form factor ratio parametrization,

$$R_1(w) = R_1(1) - 0.12(w-1) + 0.05(w-1)^2 \quad \text{and} \tag{2.64a}$$
$$R_2(w) = R_2(1) + 0.11(w-1) - 0.06(w-1)^2. \tag{2.64b}$$

Instead of their calculated values for $w = 1$,

$$R_1(1) = 1.27 \qquad\qquad R_2(1) = 0.80, \tag{2.65}$$

for the $|V_{cb}|$ determination in this analysis the form factor ratios obtained from a *BABAR* measurement [33] are used,

$$R_1(1) = 1.396 \pm 0.075 \qquad\qquad R_2(1) = 0.885 \pm 0.047, \tag{2.66}$$

where the uncertainties stated in [33] have been added in quadrature. The resulting form factor $F(w)$ in the model of Caprini, Lellouch and Neubert is shown for different values of $\rho_{A_1}^2$ in figure 2.6.

Chapter 3

The *BABAR* Experiment

The *BABAR* experiment is located at the Stanford Linear Accelerator Center (SLAC) in California, USA. Its primary goal is the measurement of time-dependent *CP*-violating asymmetries in the decay of neutral B mesons to *CP* eigenstates. Secondary goals are precision measurements of decays of bottom and charm mesons and τ leptons as well as studies of rare B decays. More generally said, the *BABAR* experiment has been built up to perform precision tests on the CKM sector of the Standard Model.

The information of this chapter is divided in two parts. The first part gives an overview about PEP-II and the B meson production at *BABAR* in general. The second section is a description of the *BABAR* detector. More detailed information about the detector and the physics at the *BABAR* experiment can be found in [14, 34].

3.1 B Meson production at the e^+e^- Storage Ring PEP-II

The linear accelerator (LINAC) and the PEP-II[1] storage ring system, they both together form the "*B*-meson factory" at the Stanford Linear Accelerator Center. In the LINAC electrons and positrons are accelerated to an energy of $9.0\,\text{GeV}$ and $3.1\,\text{GeV}$, respectively, before being injected into the high energy e^- ring (HER) and the low energy e^+ ring (LER) of PEP-II. The HER beam and the LER beam are collided head on within the *BABAR* detector in the interaction region two of PEP-II. A schematic sketch of the "*B*-meson factory" is shown in figure 3.1.

The PEP-II beam energies result in a center-of-mass energy $\sqrt{s} = 10.58\,\text{GeV}$ which corresponds to the rest-energy of the $\Upsilon(4S)$ resonance, the lightest $b\bar{b}$ resonance above the $B\bar{B}$ production threshold. The $\Upsilon(4S)$ decays to about 50% into B^+B^- and to about 50% into $B^0\bar{B}^0$ meson pairs.

A big advantage of the B-meson production by the process $e^+e^- \to \Upsilon(4S) \to B\bar{B}$ is the very clean environment compared to hadronic production processes. The cross sections of the background processes $e^+e^- \to q\bar{q}(q = u, d, s, c), \tau^+\tau^-$ are of the same order as the cross section

---

[1] PEP-II for Positron Electron Project II

Table 3.1: Production cross sections at $\sqrt{s} = 10.58\,\text{GeV}$. For $e^+e^- \to e^+e^-$ the $\cos\theta$ integral of the detector is given.

$e^+e^- \to$	$b\bar{b}$	$c\bar{c}$	$s\bar{s}$	$u\bar{u}$	$d\bar{d}$	$\tau^+\tau^-$	$\mu^+\mu^-$	e^+e^-
cross section (nb)	1.05	1.30	0.35	1.39	0.35	0.94	1.16	$\sim$40
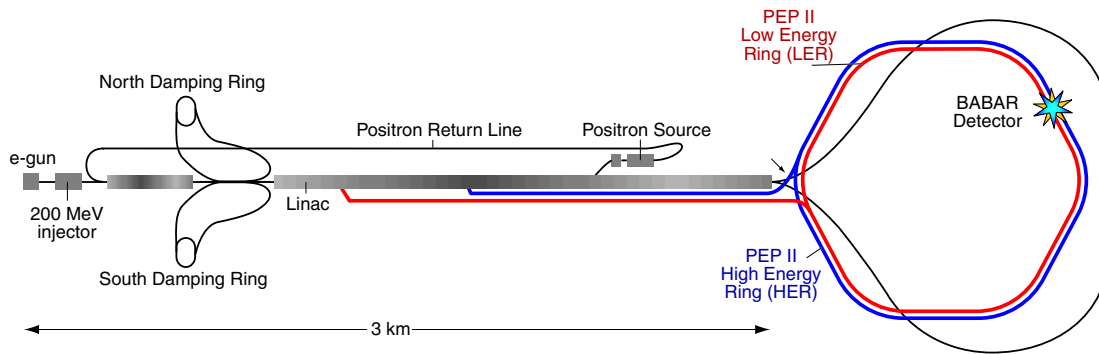
Figure 3.1: Shown is the *B*-meson factory at SLAC. After electrons and positrons have been accelerated in the LINAC bunches of them are stored in the PEP-II ring system. The beams are collided in the *BABAR* detector in the interaction region two of PEP-II.

of the *B*-meson production process (see table 3.1). Data taken at a center-of-mass energy $\sqrt{s} = 10.54\,\text{GeV}$, which is below the $B\bar{B}$ production threshold, allow to study these background processes at nearly unchanged kinematic conditions. Because these data are taken outside of the $\Upsilon(4S)$ peak region they are also called *off-peak data*. Accordingly, data taken at $\sqrt{s} = 10.58\,\text{GeV}$ are called *on-peak data*.

The asymmetry of the PEP-II beam energies is one of the novel and most important design features for observing time-dependent *CP* violation in the neutral *B*-meson system. The asymmetry leads to a Lorentz boost $\beta\gamma = 0.56$ of the $\Upsilon(4S)$ system against the laboratory system. Thereby, the desired separation between the decay vertices of two sister *B*-mesons is significantly enlarged (compared to the situation with symmetric beam energies) and becomes observable by polished vertex tracker techniques.

The data recorded by *BABAR* till July 2006 comprises a sample of ∼340 million $B\bar{B}$ pairs and ∼34 fb^{-1} off-peak data. Figure 3.2 shows how the integrated luminosity grows with time. The design luminosity of $3 \cdot 10^{33}\,\text{cm}^{-2}\text{s}^{-1}$ has been surpassed by a record peak luminosity of $12.1 \cdot 10^{33}\,\text{cm}^{-2}\text{s}^{-1}$.

3.2 The *BABAR* Detector

The BABAR detector is a typical high energy physics detector. Figure 3.3 gives an overview to its structure and the arrangement of its major components. Also shown is the *BABAR* coordinate system. The detector is symmetric in the azimuthal angle ϕ but because of the boost of the e^+e^- system against the laboratory system there is no mirror symmetry between the forward part (positive z coordinates) and the backward part (negative z coordinates) of the detector. Instead of this a boost-adapted design is necessary for an optimal acceptance of the detector along the polar angle θ. The average angular acceptance of the components is 91% in the rest frame of the beam system.

The order of the main subdetectors from the interaction point outwards together with their major tasks is given in the following:

1. The innermost detector is the *Silicon Vertex Tracker (SVT)*. Its task is to measure positions and angles of charged particles just outside the beam pipe.
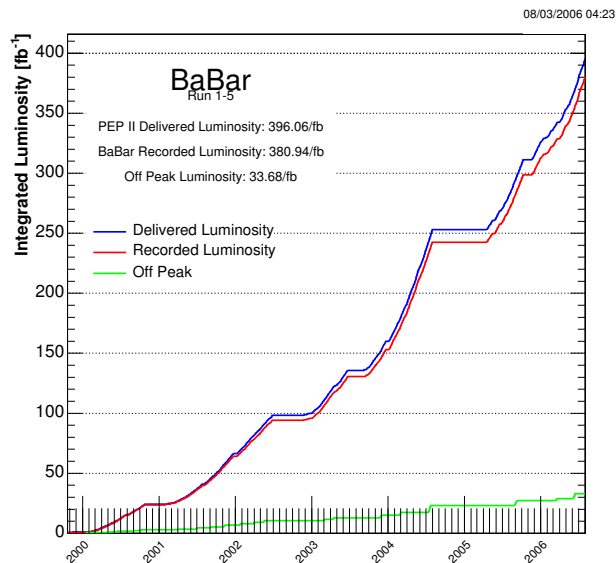
Figure 3.2: The integrated luminosity delivered by PEP-II and recorded by the *BABAR* detector between November 1999 and July 2006. This analysis uses the data taken until July 2004.

2. The *Drift Chamber (DCH)* together with the SVT forms the charged particle tracking system. It measures the momentum of charged particles. Its dE/dx measurements are important for the identification of charged particles.

3. The *Detector of Internally Reflected Cherenkov Light (DIRC)* is important for the identification of charged particles, especially for the kaon-pion-separation.

4. The *Electromagnetic Calorimeter (EMC)* measures electromagnetic showers, mainly for the reconstruction of photons and neutral π- and η-mesons. It is fundamental for the pion-electron-separation.

5. The *Superconducting Solenoid* produces a magnetic field of 1.5 Tesla. This enables the DCH and the SVT to measure the momentum of charged particles.

6. The *Instrumented Flux Return (IFR)* returns the magnetic flux outside the solenoid and provides information for the identification of muons and neutral hadrons.

The success of this analysis depends strongly on the quality of the detector performance. The most-crucial points are covered by the *BABAR* detector:

- Since the reconstruction of the analyzed decay includes three tracks and two photons for the π^0 meson one needs a high angular acceptance. It turns out that the 91% within the beam rest frame are sufficient for the analysis.

- Also the π^0 reconstruction efficiency of about 95% within this acceptance range ensures a high total reconstruction efficiency for the analyzed decay.
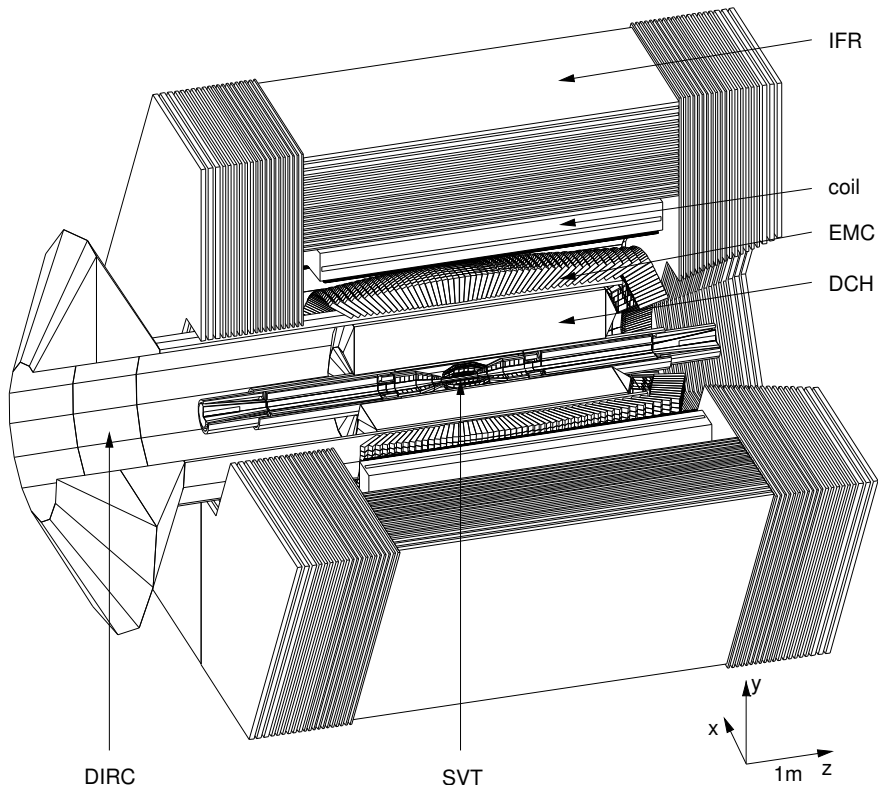
Figure 3.3: The *BABAR* detector with its main subdetectors. The electron beam comes from the left side and the positron beam comes from right side. The *BABAR* coordinate system has its origin in the center of the detector but for clarity the it is drawn outside the detector.

(a)   (b)
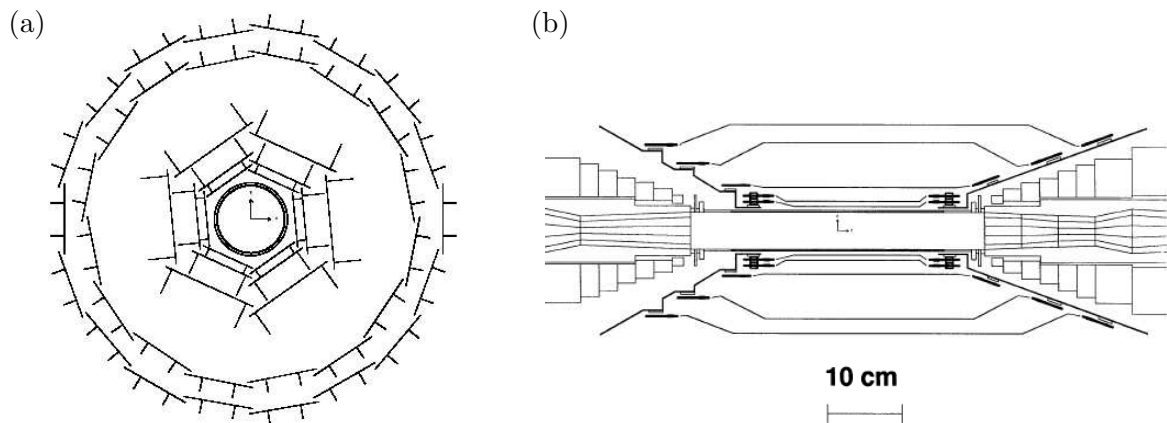
Figure 3.4: Cross-sectional view of the SVT: (a) in a plane orthogonal to the beam axis; (b) in a plane containing the beam axis.

- The high granularity of the EMC provides a good angular resolution in the reconstruction of electromagnetic showers. The high EMC energy-resolution is reached due to the little amount of material in front of the EMC. Both features are important for a narrow mass distribution of correctly reconstructed π^0 mesons and therefore they are very helpful for the background suppression.

- The previously mentioned angular and energy resolution properties are also important for the clean identification of electrons. The EMC is not only there to measure photon energies but also to identify electrons.

- The DIRC provides excellent particle identifying information, primarily used for the kaon-pion-separation. This is extremely useful because there are about five times more pion tracks then kaon tracks in an event. So the DIRC drastically reduces the combinatorial background in the D^0 reconstruction. The DIRC plays also an important role for the electron-pion-separation.

3.2.1   The Silicon Vertex Tracker

The SVT is located in a 4.5 m long support tube. It consists of five layers of double sided silicon micro strip detectors covering about 90% of the solid angle in the center-of-mass system. The three inner layers are cylindrical and very close to the beam pipe at radii $r = 32\,\text{mm}, 40\,\text{mm}, 54\,\text{mm}$. That allows for good spatial resolution of track trajectories near the interaction point. The two outer layers are arch-shaped and are located at radii $r = 109\,\text{mm}, 129\,\text{mm}$. They are important for the merging of DCH tracks and SVT tracks as well as for the SVT-stand-alone tracking of particles not reaching the DCH (transversal momentum p_T between $50\,\text{MeV}/c$ and $100\,\text{MeV}/c$). Two cross-sectional views of the SVT are shown in figure 3.4. The outer sides of the silicon layers contain stripes parallel to the z axis allowing for precise ϕ measurements. They are called ϕ stripes. The stripes on the inner sides are aligned perpendicular to the ϕ stripes which allows for precise z measurement. These stripes are called z stripes. The spatial resolution for the vertex of a B meson decay is about $70\,\mu\text{m}$ to $140\,\mu\text{m}$. This makes it possible to measure the distance between the decay vertices of two sister B-mesons (approximately $\sim 240\,\mu\text{m}$). The measurement of this distance is required for one of *BABAR*'s primary goals,e.g. the $\sin 2\beta$ measurement [35].

(a)

(b)

Figure 3.5: (a) Longitudinal section of the DCH with its principal dimensions (lengths in mm, angles in degree). (b) Schematic layout of drift cells for the four innermost superlayers. Lines have been added between field wires to aid in visualization of the cell boundaries. The number on the right side gives the stereo angles (in mrad) of wires in each layer.

3.2.2 The Drift Chamber

The principal dimensions of the DCH are shown in figure 3.5. The DCH is a multi-wire chamber. It contains a gas mixture with 80% helium and 20% isobutane. Its volume is divided in 7104 hexagonal drift cells. These cells are arranged in ten superlayers of four layers each. There are superlayers with wires parallel to the z axis (A) and there are superlayers with a positive small stereo angle (U) or a negative small stereo angle (V) between the wires and the z axis. The order of the superlayer wire alignment is AUVAUVAUVA. This alternation has been designed to achieve an optimal spatial resolution of a trajectory. Figure 3.5b shows a part of the cross section of the four innermost superlayers and lists the values of the corresponding stereo angles. In this figure one can also see the arrangement of field wires and sense wires. Field wires are on ground potential, the operating voltage for the sense wires is +1930V.

A charged particle flying through the DCH ionizes gas molecules along its track. The resulting negative charges drift to the next neighboring sense wires and produce a signal in these wires. The signal in one cell is called a DCH hit. All hits being consistent with the trajectory of a particle are grouped to a track. (For more details see sec. 4.2.) The transverse momentum of a charged particle is reconstructed from the radius of its track. Together with the z information of the track hits the momentum vector of the track is accessible. A charged particle's energy loss dE/dx provides primary input for the particle identification, especially for the K/π separation below $700\,\text{MeV}/c$.

3.2.3 The Detector of Internally Reflected Cherenkov Light

The DIRC was designed for the identification of charged particles with momentum above $700\,\text{MeV}/c$, the momentum limit where the K/π separation power of the DCH breaks down. The DIRC provides an excellent K/π separation for tracks with momentum between $0.5\,\text{GeV}/c$ and $2.0\,\text{GeV}/c$ (better then 5σ K/π separation) and has still good separation up to the kinematic limit of $4.5\,\text{GeV}/c$ (better then 2.5σ K/π separation). To achieve this performance with a material thickness of only 20% of

Figure 3.6: This schematic view shows the structure of the DIRC including the barrel, the standoff cone and the photo multiplier tubes (PMT).

a radiation length X_0 makes the DIRC to an outstanding particle identification device.

Figure 3.6 shows the structure of the DIRC. The active detector component of the Cherenkov detector consists of 144 bars of fused silica. The bars are $4.9\,\mathrm{m}$ long and have a $(1.7 \times 3.5)\,\mathrm{cm}^2$ cross section. They are grouped in bar boxes with 12 bars per box. The 12 boxes are arranged parallel to the z axis forming a 12-sided polygonal barrel around the DCH. Due to little gaps between the bar boxes the azimuthal coverage of the bars is 94%. The polar angle coverage within the center-of-mass system is 83%.

Figure 3.7 illustrates how the DIRC works. If a charged particle flies through one of the bars with a velocity $\beta > \frac{1}{n}$ then it produces Cherenkov light (refraction index of the bars $n = 1.473$). The Cherenkov photons are emitted at an angle θ_C relatively to the direction of the particle. The Cherenkov angle θ_C depends on mass and momentum of the particle and on the refraction index n of the silica bars:

$$\cos\theta_\mathrm{C} = \frac{\sqrt{1 + \left(\frac{m}{p}\right)^2}}{n} = \frac{1}{\beta n} \quad . \tag{3.1}$$

Inside the bars the Cherenkov photons are reflected many times until they enter the standoff box at the rear side of the detector. While the backward-going Cherenkov photons are reflected more ore less directly towards the standoff box, the forward-going Cherenkov light is reflected at the front side mirror of the silica bars before being reflected towards the standoff box. This box is filled with about 6000 liters of purified water and its rear is equipped with nearly 11000 photo multiplier tubes (PMT) to detect the Cherenkov photons. After the reflections of the photons towards the PMTs the information about the θ_C value is not lost but only modified by the refraction between the silica and the water. Thus parts of a Cherenkov ring are imaged on the PMT array. Starting from reconstructed DCH tracks going through the silica bars one can calculate the expected image on the PMT array as a function of photons arrival time. This leads to the discriminating probabilities for different mass hypothesis. The separation power of θ_C can bee seen in figure 3.8.

29
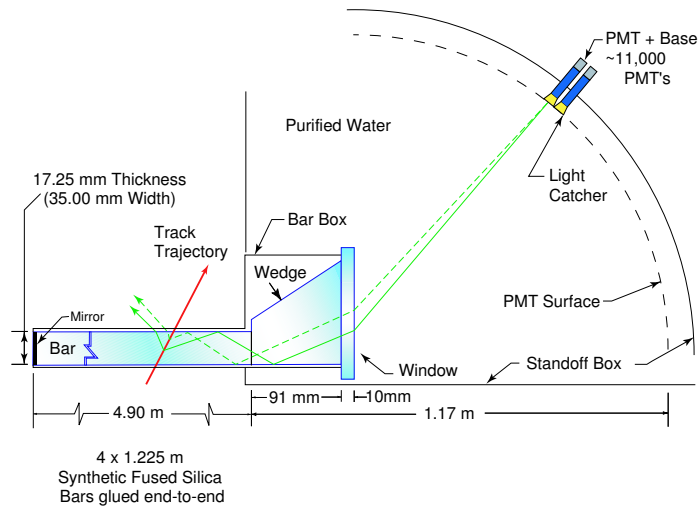
Figure 3.7: This schematic view of the DIRC illustrates the operation of the DIRC when a charged particle flies through the bars.
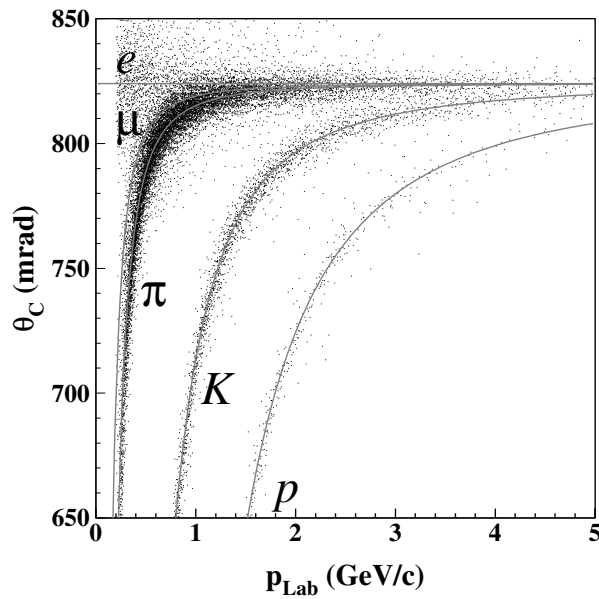
Figure 3.8: The fitted Cherenkov angle of tracks from an inclusive sample of multi-hadron events plotted against the momentum of the tracks at the entrance to the DIRC bar box. The grey lines are the predicted values of the θ_C for the different particle species. The excellent K-π-separation is clearly visible. [36]

30
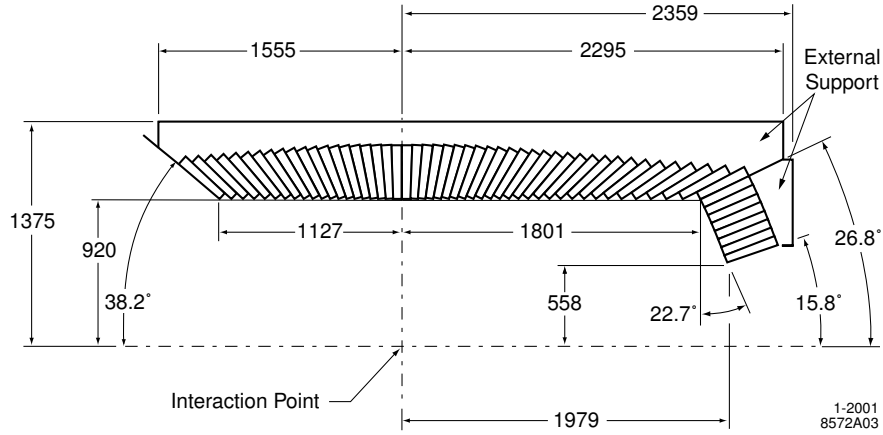
Figure 3.9: This cross-sectional view of the EMC indicates the arrangement of the crystal rings along polar angle θ. (The principal dimensions are in mm.)

Table 3.2: Properties of the EMC crystal material

Parameter	Values
Radiation length X_0	1.85 cm
Molière Radius	3.8 cm
Density	4.53 g cm^3
Light Yield	50,000γ/ MeV
Lied Yield Temp. Coeff.	0.28%/°C
Peak Emission $\lambda_{\max}$	565 nm
Refraction Index ($\lambda_{\max}$)	1.80

3.2.4 The Electromagnetic Calorimeter

The Electromagnetic Calorimeter (EMC) was designed to measure electromagnetic showers with excellent efficiency, angle resolution and energy resolution over the energy range from 20 MeV to 9 GeV. The two major contributions of the EMC to this analysis are (i) measurements used for the e/π separation leading to a very clean sample of electrons (see section 4.2.2) and (ii) the efficient selection of the soft π^0-mesons produced in D^* decays. The energy resolution σ_E/E and the angular resolutions σ_ϕ and σ_θ of the EMC are determined to be:

$$\frac{\sigma_E}{E} = \frac{(2.32 \pm 0.30)\%}{\sqrt[4]{E(\,\mathrm{GeV})}} \oplus (1.85 \pm 0.12)\% \tag{3.2}$$

$$\sigma_\phi = \sigma_\theta = \left(\frac{3.87 \pm 0.07}{\sqrt{E(\,\mathrm{GeV})}} + 0.00 \pm 0.04\right) \mathrm{mrad} \tag{3.3}$$

Figure 3.9 shows a longitudinal cross section of the EMC with its principal dimensions. The EMC is divided into a barrel component and a forward endcap component containing 5760 and 820 crystals, respectively. The crystals are operating as scintillation detectors made of thallium-doped caesium iodide. Some important material properties are listed in table 3.2. The crystals of the barrel are arranged in 48 rings of 120 crystals for each ring. The endcap is composed of three 120-crystal-rings, three 100-crystal-rings and two 80-crystal-rings. The tapered trapezoidal crystal cross

section varies between $(4.7 \times 4.7)\,\text{cm}^2$ and $(6.0 \times 6.1)\,\text{cm}^2$ which is in the order of the Molière radius to optimize between angle resolution and segmentation expense. The trapezoidal cross section ensures hermetic coverage. The crystal length varies between $29.6\,\text{cm}$ (backward detector side) and $32.4\,\text{cm}$ (forward detector side) which translates into a 16-fold till 17.5-fold length of one radiation length X_0 and allows the deposition of the entire energy of photons, electrons and positrons.

Photons entering a crystal convert into e^+e^- pairs by interacting with the crystal material. The so created electrons and positrons produce bremsstrahlung photons. The positron can also produce two photons by an annihilation with an electron. Then the process is repeated many times with the just created photons and the total process is the called development of an electromagnetic shower. Interactions of the moving shower charges with the crystal material lead to atomic excitations followed by the emission of scintillation light. Two $(2 \times 1)\,\text{cm}^2$ silicon photo-diodes are glued onto the rear side of the crystals to read out the light.

An electromagnetic shower is mostly distributed over more then one crystal, where the number of crystals belonging to the shower depends on energy and impact point of the primary shower particle.

The reconstruction procedure searches for groups of neighboring crystals with deposited energy. Such a group is called a *cluster*. Roughly spoken, it contains only neighboring crystals (i) with deposed energy $E_{\text{dep}} > 1\,\text{MeV}$ per crystal, (ii) with at least one crystal with $E_{\text{dep}} > 10\,\text{MeV}$ and (iii) with a total energy $E_{\text{cluster}} > 20\,\text{MeV}$. If a cluster contains more then one E_{dep} maximum then it is likely that it has been created by superimposed showers of different particles and therefore the cluster is divided in so called *bumps*. The bumps remaining after the matching between EMC-bumps and DCH-tracks are called *neutral candidates* of an event. (Section 4.3 contains a more detailed description of the reconstruction in the EMC.)

Because the crystals change their behavior during their permanent irradiation they have to be calibrated regularly. For the calibration in the high energy range non-radiative Bhabha events are used. For the calibration in the low energy range the source calibration is used, where the EMC is exposed to the radiation of the $6.13\,\text{MeV}$ photons from the reaction $^{16}O^* \rightarrow^{16} O\gamma$. The $^{16}O^*$ is produced after the neutron-irradiation of ^{19}F via $^{19}F + n \rightarrow^{16} N + \alpha$ and $^{16}N+ \rightarrow^{16} O^* + \beta^-$, and is pumped through a system of small aluminum pipes passing the front of the inner EMC surface. The crystal energy calibration is performed by an interpolation between the Bhabha calibration and the source calibration.

3.2.5 The Superconducting Solenoid and the Instrumented Flux Return

The EMC is surrounded by a toroidal superconducting coil creating a magnetic field of strength $1.5\,\text{T}$. Due to the Lorentz force on moved charges in magnetic fields the tracks of charged particles in the field are curved. The measurement of the curvature is translated into a momentum measurement.

The outermost detector is the Instrumented Flux Return (IFR). It deals with two tasks: (i) It has to return the magnetic flux outside the coil and (ii) it has to identify muons as well as neutral hadrons such as K_L^0 mesons.

The IFR is divided into one barrel part and two end door parts as shown in figure 3.10. Each of the three parts is segmented in 18 steel layers with gaps of about $3.2\,\text{cm}$ thickness inbetween. The steel layers have increasing thickness from $2\,\text{cm}$ for the innermost layers to $10\,\text{cm}$ for the outermost layers. This is a compromise between the demands of the muon identification and the neutral hadron identification. The total thickness of the layers sums up to $65\,\text{cm}$. The gaps of the barrel part (end door parts) have originally been instrumented with 19 (18) layers of Resistive Plate
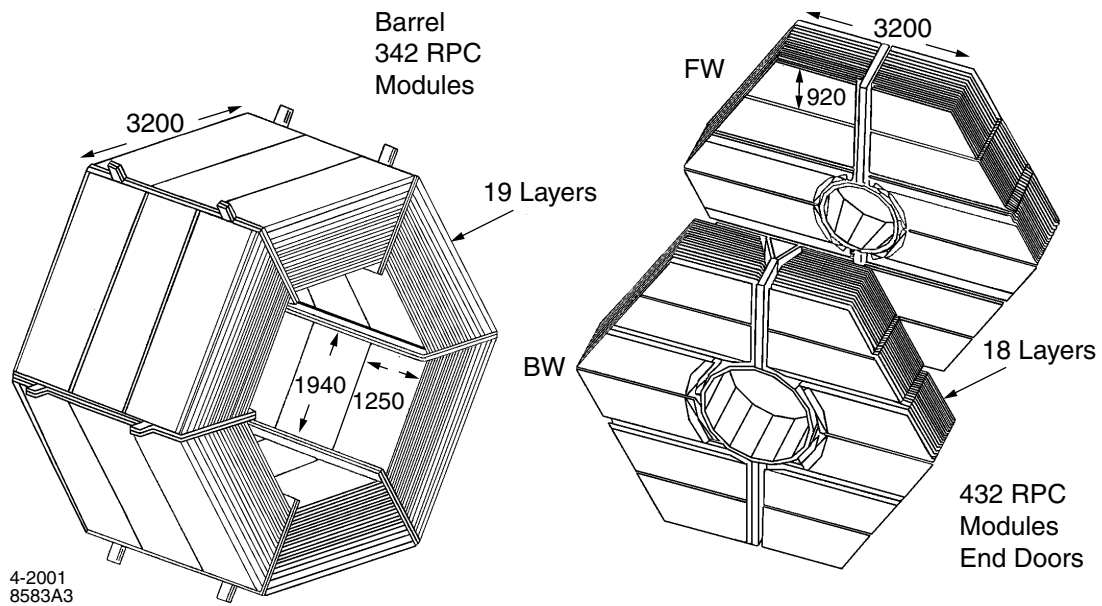
Figure 3.10: The barrel sector (left) and the forward (FW) and backward (BW) end doors (right) of the IFR. (The principal dimensions are given in mm.)

Chambers (RPC) [37] resulting in a total of 342 (216) RPC modules. The RPCs detect streamers from ionizing particles via capacitive read out stripes. There are $\tilde{x}$ stripes and orthogonally arranged $\tilde{y}$ stripes measuring the $\tilde{x}$-$\tilde{y}$-coordinates of the track-layer-intersection within the $\tilde{x}$-$\tilde{y}$-layer-plane. The Chambers are filled with a gas mixture of approximately equal fractions of argon and freon and a small fraction of isobutane.

Due to problems with the linseed oil used in the RPC-manufacturing the efficienies of the RPCs were significantly decreased year by year. For that reason it has been decided to replace the RPCs step by step by so called Limited Streamer Tubes (LST) [38]. A first replacement of the detectors in the barrel top sextant and the barrel bottom sextant was successfully done during August and September 2004. The next four sextants are planned to be replaced in the Summer of 2006.

33

Chapter 4

Candidate Selection

The major goal of this analysis is to reconstruct $B^- \to D^{*0} e^- \overline{\nu}_e$ events in order to determine

- the CKM matrix element product $F(1)|V_{cb}|$,

- the branching fraction $\mathcal{B}(B^- \to D^{*0} e^- \overline{\nu}_e)$ and

- the form factor parameter $\rho_{A_1}^2$.

The three definitions and the connections between the three values are given in chapter 2. The current chapter documents everything concerning the reconstruction and the selection of the desired events. Chapter 5 describes the sophisticated fit directly giving $F(1)|V_{cb}|$ and $\rho_{A_1}^2$ when being applied to the data sample resulting from the reconstruction and the selection of chapter 4.

The Reconstruction Chain
The B meson is reconstructed in the decay chain

$$
\begin{aligned}
B^- &\to D^{*0} e^- \overline{\nu}_e & (6.5 \pm 0.5) \\
D^{*0} &\to D^0 \pi^0 & (61.9 \pm 2.9) \\
D^0 &\to K^- \pi^+ & (3.80 \pm 0.07) \\
\pi^0 &\to \gamma\gamma \,, & (98.798 \pm 0.032)
\end{aligned}
\qquad (4.1)
$$

where the numbers on the right side are the branching fractions in percent reported by the Particle Data Group [8]. Except for the neutrino, all particles of the decay chain are reconstructed. As a general naming convention the $D^{*0} e^-$ combination is called Y and the high-energetic (low-energetic) photon wrt. the laboratory frame is called γ_1 (γ_2), with $E_{\gamma_1} > E_{\gamma_2}$.

The D^{*0} reconstruction channel $D^{*0} \to D^0 \pi^0$ has been chosen because it has an advantage over the only alternative channel $D^{*0} \to D^0 \gamma$. If one exploits the fact that the reconstructed $\gamma\gamma$ mass should be the true π^0 mass then one can obtain a nearly five times smaller Δm[1] distribution for correctly reconstructed D^{*0} particles (see section 4.5.2). That helps a lot because then the number of correctly reconstructed D^{*0} particles is determinable with a significantly higher accuracy. This narrowing of the Δm distribution is not possible for the channel $D^{*0} \to D^0 \gamma$ and therefore this channel is not considered in this analysis. A further advantage of the $D^{*0} \to D^0 \pi^0$ channel is the

---

[1]Δm is the mass difference between the D^{*0} candidate and the D^0 candidate, $\Delta m = m_{K\pi\pi^0} - m_{K\pi}$, as defined in the later section 4.5.2.

Table 4.1: The amount of *BABAR* Monte Carlo (BMC) and data is given for each run period.

run	$N_{B\bar{B}}^{\mathrm{BMC}}$ / 10^6	$N_{c\bar{c}}^{\mathrm{BMC}}$ / 10^6	$N_{B\bar{B}}^{\mathrm{Data}}$ / 10^6	$\mathcal{L}_{\mathrm{on}}$ / fb^{-1}	$\mathcal{L}_{\mathrm{off}}$ / fb^{-1}
1	48.492	21.346	21.2	19.45	2.32
2	238.712	100.076	66.4	60.26	6.93
3	122.620	57.700	34.1	31.06	2.40
4	658.751	238.798	104.3	94.56	4.39
$1-4$	1,068.575	417.920	226.0	205.35	16.06

two times higher decay rate compared to the alternative decay. The advantage to have the $\gamma\gamma$ mass as an additional selection criterion cancels the disadvantage of combinatorial $\gamma\gamma$ background.

For the D^0 reconstruction only the mode $D^0 \to K^-\pi^+$ is used because it is the cleanest compared to the alternative practicable modes $D^0 \to K^-\pi^+\pi^+\pi^-$ ($\mathcal{B} = (7.71 \pm 0.28)\%$) and $D^0 \to K^-\pi^+\pi^0$ ($\mathcal{B} = (14.1 \pm 0.5)\%$) which have higher combinatorial background and contain the less exactly reconstructible π^0. The branching fraction of the chosen D^0 channel is the one with the lowest uncertainty ($\frac{\Delta\mathcal{B}}{\mathcal{B}} = 1.8\%$). There are only 3.80% decaying into $K^-\pi^+$ but the data sample is large enough so that the analysis can be performed with the $K^-\pi^+$ mode only.

From a theoretical point of view, the $B^- \to D^{*0}\,\mu^-\,\bar{\nu}_\mu$ events could have been included in the analysis, but the electron channel has two practical advantages compared to the muon channel: **(i)** The particle identification (PID) efficiency of electron tracks is stable with time. Due to the linseed oil problem in the RPCs (see section 3.2.5) the PID efficiency of muon IFR-tracks is significantly decreasing with time of data taking and its simulation has a significantly bigger uncertainty compared to electron tracks. **(ii)** The selection of electrons is cleaner and more efficient. The electron selector used in this analysis is about 92% efficient in the interessting kinematic range and acceptance range and has a pion fake rate below 0.2% (see figure 4.2 and [66]). This compares to clearly worse muon selector values of 73% efficiency at 3% pion fake rate [66].

Computing Frameworks
Two computing frameworks have been used to perform this analysis. In the first analysis part the release version 14.5.5 of the *BABAR* software *Beta* with all its recommended bug fixes is used. A package obtained by editing the *BetaMiniUser* package composes the particle candidates and performs geometric candidate-by-candidate fits. It also applies very loose selection criteria and stores the result in big ntuples. For the second step I wrote the *ROOT* [39] based framework `VcbFit` which applies the final selection cuts and performs a fit (see chapter 5) extracting the three desired values with their statistical uncertainties. It allows to vary the cuts and the fit options in a clear and friendly way and provides automatic html- and plot-generation. The automatically generated summaries are very helpful for making extensive checks of the fit performance [40].

4.1 The Data Sample

The data used for this analysis is listed in table 4.1. Generally, there are the data recorded by the *BABAR* detector and there are the simulated *BABAR* Monte Carlo data (BMC). Both are briefly commented on the following two subsections.

4.1.1   Data Events

The data events used by this analysis have been recorded by the *BABAR* detector between May 1999 and July 2004. The data sample contains 205.35 fb^{-1} *on-peak* data taken at an e^+e^- center-of-mass energy of about 10.58 MeV corresponding to the mass of the $\Upsilon(4S)$ resonance. It also contains 16.06 fb^{-1} *off-peak* data taken at a e^+e^- center-of-mass energy of about 10.54 MeV which is 20 MeV below the $B\bar{B}$ production threshold. Since the off-peak data only contain the unwanted background-events $e^+e^- \to q\bar{q}$ ($q = u, d, s, c$) they are used to describe the amount of those $q\bar{q}$ events in the on-peak data (see equation 5.20).

The number of $B\bar{B}$ events in the analyzed data sample, $N_{B\bar{B}}^{\text{Data}} = (226.0 \pm 2.5) \cdot 10^6$, has been reported by *BbkLumi* [42] which is a bookkeeping tool of the *BABAR* computing model 2 (CM2). The BbkLumi-reported value for $N_{B\bar{B}}^{\text{Data}}$ has been determined as described in [41]. The number of multi-hadron events is determined on a run-by-run[2] basis in the on-peak data as well as in the off-peak data. The subtraction of the luminosity-scaled numbers gives the excess of multi-hadron events in the on-peak data. Assuming that the $\Upsilon(4S)$ resonance decays in 100% into B meson pairs[3], the excess of multi-hadron events is completely caused by $\Upsilon(4S) \to B\bar{B}$ decays and the subtraction gives the number of B meson pairs ($N_{B\bar{B}}^{\text{Data}}$).

The luminosities are determined from $e^+e^- \to e^+e^-(\gamma), \mu^+\mu^-(\gamma), \gamma\gamma$ events and have systematic errors of about 1% [44, 45].

The entire data has been divided into four data subsets, namely *run1* till *run4*, to group all those data that has been commonly taken between two big *shut downs*[4].

4.1.2   Monte Carlo Events

A very central point of the analysis strategy is to use simulated events, the so called Monte Carlo events (MC). The simulation of a MC event is performed in four steps:

Generation of the physics event: In a first step the *BABAR* software package *EvtGen* [46] generates the events. The events used for this analysis are $\Upsilon(4S) \to B\bar{B}$ and $e^+e^- \to c\bar{c}$. EvtGen describes about 60% of the B meson decays by exclusive decay models. The remaining 40% and the $c\bar{c}$ events are handed to *JetSet* [47] to be described by an inclusive technique.

Particle transport and GHits: In a second step each generated event is traversed through the *BABAR* detector model. This task is performed by the *GEANT4* [48] based software package *BOGUS* in a step-by-step technique where after each step the particles are allowed to decay, to deposit energy, to produce secondaries or to perform multiple scattering. When the particles are passed through the sensitive detector regions the information of their position and their energy deposit is stored in so called *GHits*.

Detector response and background mixing: The task of the *BABAR* software package *SimApp* is to transform these idealized GHits into raw detector signals (called *digis*) that mimic the real detector electronics. The detector answer to a physics event is generated by also using real-data background events, which makes the simulation more realistic. Because the conditions

---

[2]The data recorded within a time window of approximately one up to three hours is called a *run*.

[3]The CLEO collaboration measured $\mathcal{B}\left(\Upsilon(4S) \to B\bar{B}\right) > 96\%$ with a confidence level of 95% [43].

[4]Normally the detector takes data around the clock, aside from smaller breaks necessary for slight maintenance work or caused by technical failures. However, about one time each year there is a bigger *shut down* for about one or two months where the PEP-II operation is down. During these shut downs time-consuming upgrades and reparations at the detector and the machine are performed.

of the detector and the machine change with time there has to be a dedicated set of simulated events for each run period.

Reconstruction: The last step applies the reconstruction procedure resulting in DCH tracks, EMC clusters and so on. The procedure applied on the digis of simulated events is identical to the one applied on the true-data digis.

Each MC event contains two types of information: The *reco-side* and the *truth-side*. The reco-side contains all the information that is also available in true-data events, i.e. the DCH tracks, the EMC clusters and further reconstruction information. The truth-side consists of the *MC-truth list* and the GHits, where the MC-truth list is nothing else but the decay tree with the momentum four-vectors of all participating particles as generated by EvtGen.

The first easily-understandable advantage of the MC simulation is that one can study what the reco-side looks like for a given truth-side, i.e. for interesting decays such as signal or important background events. That means one can learn the following: What will the real detector approximately answer if it is confronted with a special type of physics event? For example, in the early stages of this analysis the so called *Signal MC* was studied. Signal MC contains $B\overline{B}$ events where one B meson decays generically and the other B meson decays as given by equation 4.1. This technique uses the fact that for each truth-side there is an assigned reco-side. It is a unambiguous assignment of the whole truth-part to the whole reco-part of an event.

A second very useful advantage is that one can successfully ask for the causal reason of a reconstructed object (such as a DCH track or an EMC cluster): Which particle of the MC-truth list is responsible for the existence of the reconstructed object? The answer is given by using a technique called *MC-truth matching* which exploits the GHits of the event. The MC-truth matching determines which particle of the MC-truth list caused a detector signal and is therefore responsible for a certain reconstructed object. But sometimes this assignment is ambiguous. Since in special cases more than one single MC-truth particle may be responsible for, e.g. a cluster in the EMC, the matching between MC-truth particles and reconstructed objects is not one-to-one. For each particle of the MC-truth list there is a weight for having contributed to the reconstructed object. Fortunately, in most of the matching processes there is one MC-truth particle whose weight clearly dominates.

The full simulation of the *BABAR* MC requires a lot of computing power and therefore it is performed centrally by the *Simulation Production Group* [49]. For run1-3 there is the SP5 MC and for run4 there is the SP6 MC, which are the fifth and the sixth revision of the *BABAR* simulation production, respectively.

The used amount of MC events of generically decayed B mesons is listed in table 4.1. For each of the four runs an equal amount of $\Upsilon(4S) \to B^+B^-$ and $\Upsilon(4S) \to B^0\overline{B}^0$ events has been used. This so called 'generic $B\overline{B}$ MC' includes a comprehensive cocktail of measured and expected B meson decays. Because this analysis reconstructs the decay $B^- \to D^{*0}e^-\overline{\nu}_e$ all other semileptonic charmed B decays are important and dominant background sources, especially those decays that contain true D^{*0} mesons in their decay chain. The EvtGen branching fractions of all such $b \to c\ell^-\overline{\nu}_\ell$ decays are listed in table 4.2. The decay model of Goity and Roberts [52] describes all listed modes with two hadrons in the final state.[5] If there is only one hadron in the final state then the decay is described by the ISGW2 decay model [53], an update of a model developed by Isgur, Scora,

---

[5]Citation from the EvtGen documentation [46]: 'This is not exactly what was published by Goity and Roberts, partly due to errors in the paper and because the D^* had to be removed from the $D\pi$ non-resonant.'

Table 4.2: Listed are the branching fractions $\mathcal{B}$ of all EvtGen decay modes where a B meson goes into a lepton, a neutrino and a charmed hadronic system X_c. If the decays $B \to X_c \ell \nu_\ell$ (with $\ell = e, \mu$) and $B \to X_c \tau \nu_\tau$ contain true D^{*0} mesons directly within the X_c system or in a subsequent decay of X_c then they are of type 1; otherwise they are type 2 events. Since only events with correctly reconstructed D^{*0} mesons can contribute to reconstructed signal events (see end of section 5.1) the events assigned to type 1 are a critical background for this analysis.

Type	$B^0 \to$	$\mathcal{B}$ (%)	Type	$B^- \to$	$\mathcal{B}$ (%)
2	$D^{*+}\ \ell^-\ \overline{\nu}_\ell$	5.60	Signal	$D^{*0}\ \ell^-\ \overline{\nu}_\ell$	5.60
2	$D^+\ \ell^-\ \overline{\nu}_\ell$	2.10	2	$D^0\ \ell^-\ \overline{\nu}_\ell$	2.10
1	$D_1^+\ell^-\ \overline{\nu}_\ell$	0.56	1	$D_1^0\ell^-\ \overline{\nu}_\ell$	0.56
2	$D_0^{*+}\ell^-\ \overline{\nu}_\ell$	0.20	2	$D_0^{*0}\ell^-\ \overline{\nu}_\ell$	0.20
1	$D_1'^+\ell^-\ \overline{\nu}_\ell$	0.37	1	$D_1'^0\ell^-\ \overline{\nu}_\ell$	0.37
1	$D_2^{*+}\ell^-\ \overline{\nu}_\ell$	0.37	1	$D_2^{*0}\ell^-\ \overline{\nu}_\ell$	0.37
2	$D^{*+}\ \pi^0\ \ell^-\ \overline{\nu}_\ell$	0.10	2	$D^{*+}\ \pi^-\ \ell^-\ \overline{\nu}_\ell$	0.20
1	$D^{*0}\ \pi^+\ \ell^-\ \overline{\nu}_\ell$	0.20	1	$D^{*0}\ \pi^0\ \ell^-\ \overline{\nu}_\ell$	0.10
2	$D^+\ \pi^0\ \ell^-\ \overline{\nu}_\ell$	0.30	2	$D^+\ \pi^-\ \ell^-\ \overline{\nu}_\ell$	0.60
2	$D^0\ \pi^+\ \ell^-\ \overline{\nu}_\ell$	0.60	2	$D^0\ \pi^0\ \ell^-\ \overline{\nu}_\ell$	0.30
	total $X_c\ell^-\ \overline{\nu}_\ell$	10.40		total $X_c\ell^-\ \overline{\nu}_\ell$	10.40
2	$D^{*+}\ \tau^-\ \overline{\nu}_\tau$	1.60	1	$D^{*0}\ \tau^-\ \overline{\nu}_\tau$	1.60
2	$D^+\ \tau^-\ \overline{\nu}_\tau$	0.70	2	$D^0\ \tau^-\ \overline{\nu}_\tau$	0.70
1	$D_1^+\tau^-\ \overline{\nu}_\tau$	0.13	1	$D_1^0\tau^-\ \overline{\nu}_\tau$	0.13
1	$D_1'^+\tau^-\ \overline{\nu}_\tau$	0.20	1	$D_1'^0\tau^-\ \overline{\nu}_\tau$	0.20
1	$D_2^{*+}\tau^-\ \overline{\nu}_\tau$	0.20	1	$D_2^{*0}\tau^-\ \overline{\nu}_\tau$	0.20
	total $X_c\tau^-\ \overline{\nu}_\tau$	2.96		total $X_c\tau^-\ \overline{\nu}_\tau$	2.96

Grinstein and Wise [54]. The only exceptions are the decays $B^- \to D^{*0}e^-\overline{\nu}_e$ and $\overline{B}^0 \to D^{*+}e^-\overline{\nu}_e$, which are described by an HQET inspired model (see sections 5.3.1 and 5.3.1.2).

Last but not least it is important to mention that EvtGen uses the *PHOTOS* algorithm [51] for performing QED photon radiative corrections.

4.2 The Reconstruction of Charged Particles

4.2.1 The Reconstruction of a Track

The DCH and the SVT provide the information for the reconstruction of a *charged track*. Because of the magnetic field $\vec{B}$ inside the detector a charged track has the shape of a helix. The parameter set $(d_0, \phi_0, z_0, \kappa, \tan \lambda)$ and the associated covariance matrix define the charged track. The parameters are determined at the point of closest approach (POCA) to the z axis. From the values of the first three parameters one can read off the absolute position of the helix: The distance of the helix to the origin of the coordinate system in z direction is given by z_0 and the corresponding distance in the x-y-plane sets the parameter d_0; the azimuth of the track is given by ϕ_0. The helix curvature is expressed by κ and is connected to the particle's transversal momentum p_T by $\kappa = Q/p_T$. The sign of the variable depends on the particle's charge Q. κ is connected to the radius ρ of the helix by $\rho = \frac{1}{|\vec{B}|\kappa} = \frac{p_T}{Q|\vec{B}|}$. Together with λ — the dip angle of the track into the x-y-plane — one obtains

the particle momentum $p = \frac{p_T}{\cos \lambda}$. However, the raw DCH data are not directly translated into the helix parameters but into so called *DCH hits*. (The same is true for the SVT.) A DCH hit appears for these DCH cells whose collected charge exceeds a certain threshold value. From the DCH and SVT hits the tracks are found and fitted by the Kalman filter algorithm [55]. Thereby the full map of the magnetic field and the detailed distribution of material in the detector is taken into account. Firstly, a reconstruction with only DCH hits is performed. Secondly, if there are SVT hits which consistently belong to the found DCH tracks, then they are assigned to the corresponding DCH tracks. At the end of this step all tracks are checked whether some of them could have been created by the same primary particle — if yes then the corresponding tracks are merged. After that, the *BABAR* tracking algorithm tries to reconstruct tracks that have only hits in the SVT, the so called SVT only tracks. Finally, DCH hits consistent with an SVT only track are added to this SVT only track. If there is a DCH track consistent with a SVT only track then both tracks are merged.

All charged particles in this analysis are required to have tracks fulfilling the *BABAR Good Tracks Loose* (GTL) selection criteria:

- The polar angle θ ($= 90° - \lambda$) must be within the acceptance range: $23.5° < \theta < 145.5°$.

- The distance of the helix's POCA to the z axis must be low enough: $d_0 < 1.5\,\text{cm}$.

- Similarly there is a criterion for the distance in z direction: $|z_0| < 10\,\text{cm}$.

- The momentum must be lower than $10\,\text{GeV}/c$.

- The track must have a minimum transverse momentum: $p_T > 0.1\,\text{GeV}/c$.

- Tracks with very few DCH hits are not selected: $N^{\text{DCH}} \geq 12$.

The tracking algorithm and the GTL selection criteria lead to the event-specific lists of available tracks used in this analysis. Nearly 100% of all measured tracks stem from pions, kaons, electrons, protons and muons. In generic $B\bar{B}$ events, the ratio of the average number of expected pion, kaon, electron and proton tracks is about $N_\pi : N_K : N_e : N_p = 5 : 1 : 1 : 0.2$ (see also section 4.2.2). Thus the biggest contribution comes from pions. To have a purer signal sample after the combination to $B^- \to D^{*0} e^- \overline{\nu}_e$ candidates it is recommendable to require particle identification (PID) from the particle candidates associated with the tracks. The electron purity and the kaon purity can be increased significantly without big efficiency loss by applying PID selection criteria. The corresponding criteria used in this analysis are briefly discussed in the next two subsections. A tighter pion selection would reduce the combinatorial background not as much as in the electron and kaon case but would introduce further systematic uncertainties. Therefore no extra pion identification is applied but all tracks of an event remaining after the kaon and the electron selection are used as pions.

4.2.2 The Electron Identification

The electrons for the reconstruction of the $B^- \to D^{*0} e^- \overline{\nu}_e$ candidates are selected by the *PidLHElectrons* selector [56] which is a standard selector provided by the *BABAR* software. Its decision to select or reject a track is made by cutting on the likelihood ratio R,

$$R = \frac{A_e L_e(t)}{A_e L_e(t) + A_\pi L_\pi(t) + A_K L_K(t) + A_p L_p(t)} \tag{4.2}$$

$$A_e : A_\pi : A_K : A_p = 1 : 5 : 1 : 0.2 \,, \tag{4.3}$$

where A_i are *a priori* probabilities of the appearance of an i-track ($i = e, \pi, K, p$) in the event and L_i are the likelihoods of track t to originate from an i-particle. Muons are excluded by requiring that the track-associated EMC-cluster must have more than five crystals. All tracks with $R < 0.95$ are rejected by the *PidLHElectrons* selector. The likelihoods L_i rely on five variables obtained from the major detector components DCH, DIRC and EMC. The variables are the following:

E/p – the ratio between the energy E deposited in the EMC-cluster associated with the track t and the momentum p measured in the DCH. Because the used electrons are very relativistic particles ($\frac{E}{m} \approx 2000$) and deposit nearly all their energy in the EMC they have a narrow E/p distribution peaking slightly below one. The biggest e-track background comes from π mesons. Because they are less relativistic ($\frac{E}{m} \approx 7$) and often transverse the EMC with depositing only a part of their energy the resulting E/p distribution is broader and shifted to lower values. The situation for kaons and protons is similar.

$\Delta\Phi$ – the angle between the EMC cluster center and the intersection of the track with the EMC surface with respect to the origin of coordinates. Hadrons produce electromagnetic showers penetrating deeper into the EMC than those produced by electrons. Because the tracks enter the EMC under a non-zero angle the variable $\Delta\Phi$ contains information about the length of the shower and therefore provides discrimination power.

LAT – the lateral shower shape of the track-associated EMC-cluster defined by

$$LAT = \frac{\sum_{j=3}^{N} E_j r_j^2}{\sum_{j=1}^{N} E_j r_j^2} \tag{4.4}$$

where j, E_j and r_j are the index of the crystal within the EMC cluster, the crystal energy and the distance of the crystal center to the cluster center, respectively. E_1 and E_2 must be the two biggest crystal energies in the cluster. By definition, LAT has values between zero and one. Low values result from concentrated energy deposition in the EMC cluster — high values come from clusters where the energy is deposited less compactly. Electrons (and also photons) have a LAT distribution peaking between 0.2 and 0.4 whereas hadrons have a nearly flat LAT distribution.

dE/dx – the specific energy loss in the DCH. The ionization energy loss of the DCH-transversing charged particle within a DCH cell is proportional to the ratio Q/l with l and Q being the track's path length through the cell and the charge collected during the DCH hit. The 80% truncated mean of the DCH-hit individual energy losses gives the DCH's dE/dx of a track. The expectation of the dE/dx is given by the *Bethe-Bloch* formula [8].

θ_C – the Cherenkov angle, measured in the DIRC. If less than six Cherenkov photons are measured then this variable is excluded from the likelihoods.

Some of these variables are illustrated in figure 4.1. The selector has an excellent electron efficiency at a very low hadron misidentification rate as can be seen in figure 4.2.

4.2.3 The Kaon Identification

The kaons for the reconstruction of the D^0 candidates are selected by the *KMicroVeryLoose* selector [59], which is a standard selector provided by the *BABAR* software. Its decision to select or reject
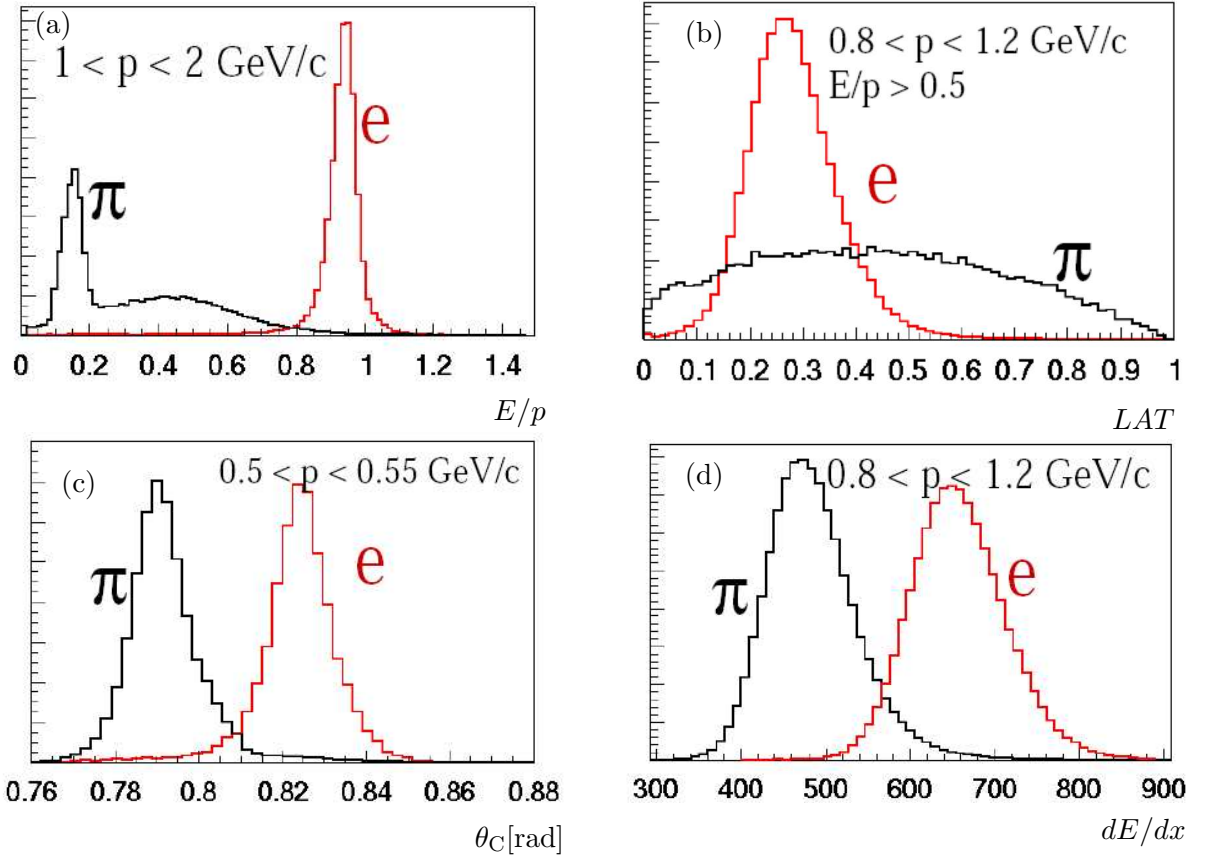
Figure 4.1: The distributions of the discriminating variables of the used electron selector illustrate the separation power between electrons (in red) and pions (in black). The graphics are taken from [57] and were obtained from data samples of nearly pure electron tracks (radiative Bhabha events) and nearly pure pion tracks ($K_S^0 \rightarrow \pi\pi$ events) [58].
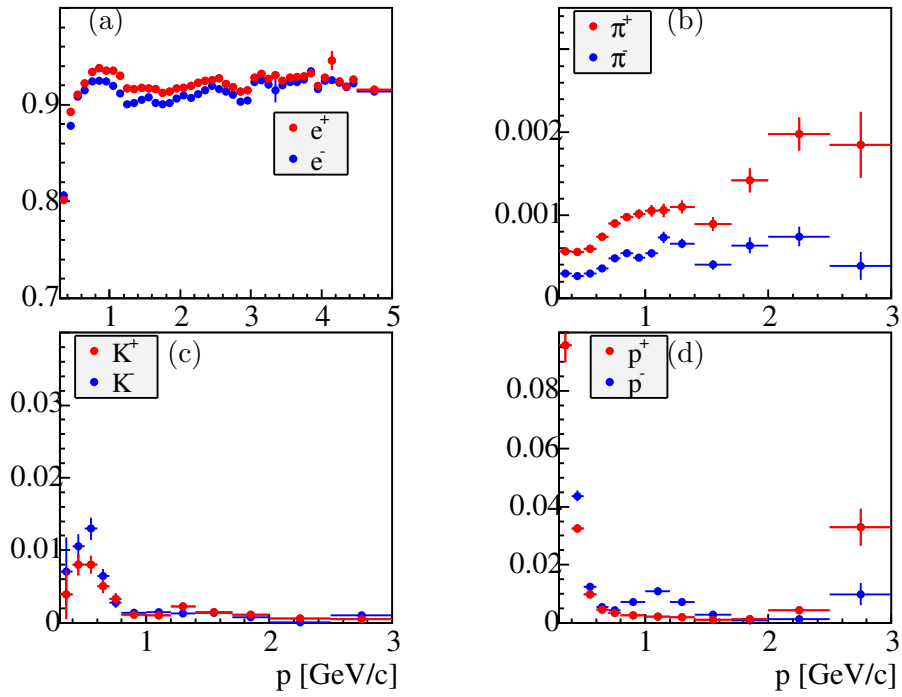
Figure 4.2: The selection rates of the *PidLHElectrons* selector are shown in dependence of the track momentum p: (a) the electron efficiency for tracks reaching the backward part of the EMC barrel $(71.53° < \theta < 141.72°)$; (b)-(d) the misidentification rates for pions, kaons and protons for tracks reaching the backward part of the EMC barrel $(77.42° < \theta < 137.38°)$. The PID group [66] created the plots. The numbers were obtained from data samples containing only tracks of the corresponding particle type [58].
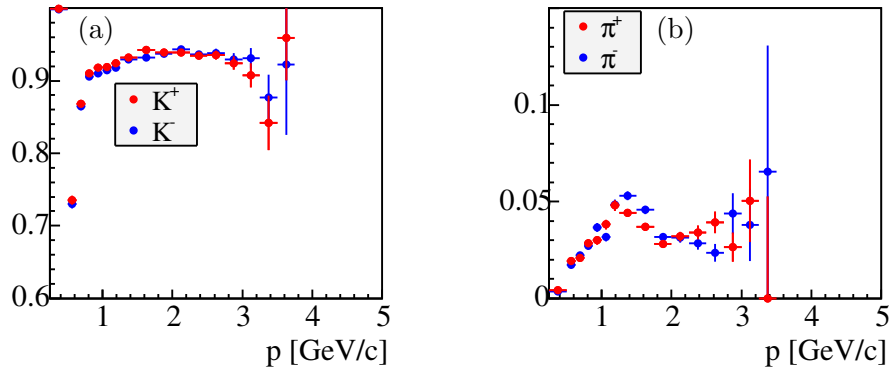
Figure 4.3: The selection rates of the *KMicroVeryLoose* selector are shown as a function of the track momentum p for tracks reaching the backward part of the DIRC barrel ($95.0° < \theta < 146.1°$): (a) The kaon efficiency and (b) the misidentification rate for pions. The PID group [66] created the plots from data samples containing only tracks of the corresponding particle type [58].

a track is made by cutting on the neural net output of a K-NET [60]. The net input variables are the track's momentum and three individual likelihood ratios R_x,

$$R_x = \frac{L_{Kx}}{L_{Kx} + L_{\pi x}}, \tag{4.5}$$

with $x =$DCH, SVT, DIRC. The ratios are limited to only kaons and pions and do not include electron and proton terms. The variables used for the likelihoods L_x are:

dE/dx: The $(dE/dx)_{\mathrm{DCH}}$ is used for the likelihood L_{DCH} and the $(dE/dx)_{\mathrm{SVT}}$ is used for L_{SVT}.

θ_C: The Cherenkov angle and the number of Cherenkov photons, both measured in the DIRC, are used for the L_{DIRC} calculation.

The performance of the *KMicroVeryLoose* selector is shown in figure 4.3. In the K momentum range below $0.7\,\mathrm{GeV}/c$, the separation power comes mainly from the DCH and is better than 2σ. For the momentum range between $0.7\,\mathrm{GeV}/c$ and $3.0\,\mathrm{GeV}/c$ the DIRC provides a K-π-separation better than 4σ. Figure 4.4 shows the kaon momentum distribution for kaons coming from D^0 mesons of the signal decay (equation 4.1).

4.3 The Reconstruction of Neutral π Mesons

A π^0 meson is reconstructed from two photon candidates of the event as described below. Because this analysis uses the π^0 efficiencies provided by [61] the π^0 reconstruction has to be exactly equal to one of the *BABAR* standard π^0 selectors.[6] Before the definition of π^0 candidates is given one needs to know how a photon is reconstructed in the EMC.

---

[6]The analysis described in [61] determines the π^0 efficiency with respect to the π^0 standard selectors defined in the *BABAR* software.
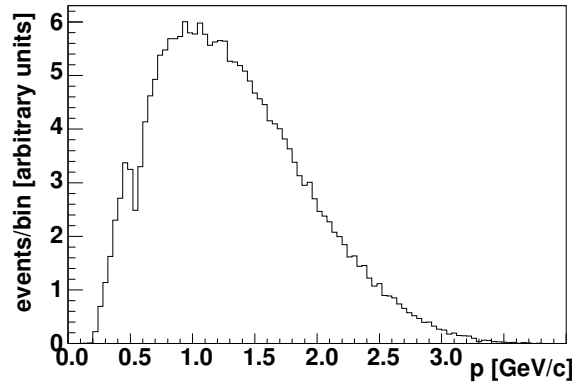
Figure 4.4: The momentum distribution of kaons stemming from signal decays (equation 4.1) measured for MC events in the laboratory frame. The little dent between $0.5\,\text{GeV}/c$ and $0.6\,\text{GeV}/c$ is caused by the fact that the separation power of the DCH already decreases but the DIRC separation power is not yet high enough. In the rest of the spectrum the DIRC and the DCH allow for a good K-π-separation.

EMC Clusters

The definition of a photon candidate bases on the EMC cluster objects. A group of contiguous neighboring crystals in the EMC having the following properties is called a cluster:

- The crystal group must contain at least one seed crystal with a deposed energy $E_{\text{dep}} > 10\,\text{MeV}$.

- Each cluster crystals must have an energy $E_{\text{dep}} > 1\,\text{MeV}$.

- Each cluster crystal with $E_{\text{dep}} < 3\,\text{MeV}$ must have at least one contiguous neighbor with energy $E_{\text{dep}} > 3\,\text{MeV}$.

- The total energy of all crystals contributing to the cluster, E_{cluster}, has to be greater than $20\,\text{MeV}$.

In principal, a lower threshold on the single crystal energy would improve the energy resolution because the fluctuations in the energy loss at the shower edges would be smaller. However, the value $1\,\text{MeV}$ is necessary to keep the EMC data volume at an acceptable level. The main contributors to the low energy background are electronics noise and beam-generated background. The beam-generated background rises dramatically more when going to lower crystal energies (see figure 4.5). The $20\,\text{MeV}$ cluster energy requirement reduces this background.

EMC Bumps

Since it is possible that a cluster is a superposition of electromagnetic showers generated by more than one primary particle a search for the number of local energy maxima within the cluster is performed. After that the cluster is split into as many bumps as it has maxima. To be a local energy maximum, the corresponding crystal must (i) have an energy E_{LocMax} greater than the energy of each of its neighbors and (ii) it must satisfy the condition $(N - 2.5)/2 > E_{N\text{max}}/E_{\text{LocMax}}$, where $E_{N\text{max}}$ is the highest energy of any of the neighboring N crystals with an energy above $2\,\text{MeV}$.
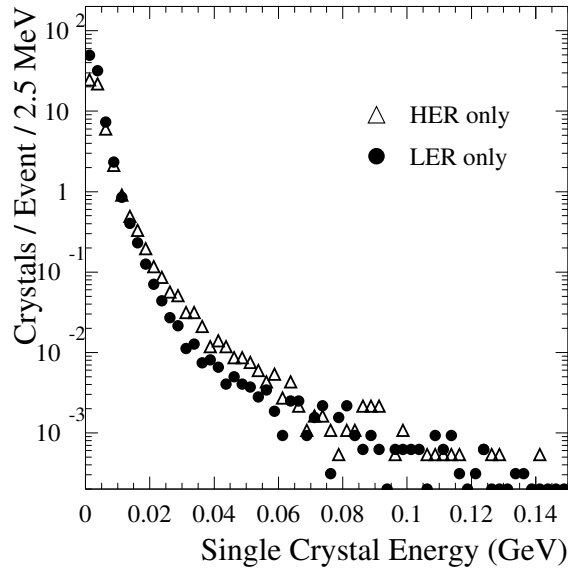
Figure 4.5: The energy spectrum of photons recorded in the EMC by random triggers with single beams at typical operating currents, LER at 1.1A and HER at 0.7A. The electronics noise has been subtracted. [34]

The splitting of a cluster consisting of N_{crys} crystals into N_{bump} bumps is realized by giving weights w_{ik} to each crystal so that the energy of the kth bump of a cluster is calculated

$$E_{\text{bump}\,k} = \sum_{i=1}^{N_{\text{crys}}} w_{ik}\, E_i \,. \tag{4.6}$$

Thereby the index i runs over all crystals of the cluster and E_i is the energy deposed in the ith crystal. Trivially, for a cluster with one single bump all weights are one, $w_{i1} = 1$. For $N_{\text{bump}} > 1$ the crystal weights are calculated in an iterative process together with the position of the bump centroid. In a first step the bump centroid positions

$$\vec{r}_{\text{bump}\,k} = \frac{\sum_{i=1}^{N_{\text{crys}}} \hat{E}_{ik} \vec{r}_i}{\sum_{i=1}^{N_{\text{crys}}} \hat{E}_{ik}} \tag{4.7}$$

are calculated, in a second step the crystal weights

$$w_{ik} = \frac{E_i \exp\left(-2.5 r_{ik}/r_{\text{M}}\right)}{\sum_{j=1}^{N_{\text{bump}}} E_j \exp\left(-2.5 r_{ij}/r_{\text{M}}\right)} \tag{4.8}$$

are calculated, and after this the two steps are iteratively repeated until the centroid positions are stable to within a tolerance of 1 mm. In equation 4.8, r_{M} is the Molière radius and r_{ik} is the distance between the ith cluster crystal and the kth bump centroid, $r_{ik} = |\vec{r}_i - \vec{r}_{\text{bump}\,k}|$. For each crystal i, the point $\vec{r}_i$ is situated 12.5 cm deep inside the crystal on the longitudinal crystal axis.[7]

---

[7]In earlier software releases the inner EMC surface was used. The change shifts the bump centroid into the crystals and thereby improves the track-bump matching described below [62].

In the calculation of the bump centroids the crystal energies are weighted logarithmically

$$\hat{E}_{ik} = \max\left(0,\, a + \ln\frac{w_{ik}E_{ik}}{E_{\mathrm{bump}\,k}}\right), \qquad (4.9)$$

where a is a cutoff parameter ($a \approx 4$).

Track-Bump Matching
At this stage of event reconstruction there are EMC bumps. In a next step one tries to match the EMC bumps to the DCH tracks. The track-bump matching algorithm takes two things into account:

- Spatial track-bump location: One can define the azimuthal and polar angle differences between (i) a point on the EMC-extrapolated track trajectory being 12.5 cm deep inside the EMC and (ii) the EMC bump centroid. Both angle differences are used to calculate significance levels.

- Energy of EMC crystal and DCH track: A significance level is also calculated from the ratio of the energy of the struck EMC crystal to that of the track using the pion hypothesis.

A cut on the combined consistency separates the EMC bumps into matched and non-matched bumps. The list of bumps remaining non-matched is called *CalorNeutral* in the *BABAR* language. A newer documentation of the track-bump matching algorithm can be found in [62], older maybe more detailed but not so up-to-date information can be obtained from [63, 64].

Photon Candidates
The photon candidates used to reconstruct π^0 mesons are members of the CalorNeutral list and must survive the following two selection cuts predefined by the π^0 efficiency analysis [61]:

- The lateral momentum *LAT* defined in equation 4.4 must be lower than 0.8 to reject non-compact bumps mainly produced by hadrons.

- The energy of the bump must be greater than 30 MeV.

Photon candidates satisfying these requirements are called *GoodPhotonsLoose* photons in the *BABAR* language.

π^0 Candidates
Again, the π^0 selection criteria are predefined by the chosen standard π^0 selector whose efficiency is given by the study described in [61]. Because the phase space of the decay $D^{*0} \to D^0\pi^0$ is very small the momentum spectrum of the π^0 is very soft – a π^0 coming from a D^{*0} decay is also called *soft* π^0 (see figure 4.6a). As a result, an appropriate π^0 list should contain low-energetic π^0 candidates. The *pi0SoftDefaultMass* list has been chosen as the most appropriate list for this analysis because it is the list with the lowest π^0 energies accompanied with the lowest combinatorial background. Each π^0 candidate of this list is composed by two *GoodPhotonsLoose* photon candidates. The detailed π^0 selection requirements are:

- The invariant two-photon mass satisfies the condition $0.115\,\mathrm{GeV}/c^2 < m_{\gamma\gamma} < 0.150\,\mathrm{GeV}/c^2$ (see figure 4.6b).

46
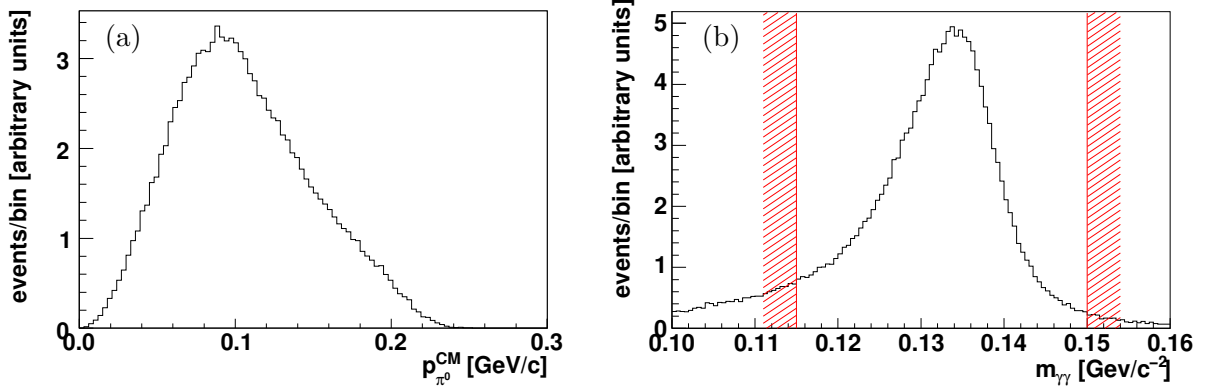
Figure 4.6: The plots show properties of unfitted π^0 candidates correctly matched to a signal decay (see equation 4.1): **(a)** the $\gamma\gamma$ momentum distribution within the $\Upsilon(4S)$ rest frame; **(b)** the $\gamma\gamma$ mass distribution. The $m_{\gamma\gamma}$ selection criterion is plotted too.

- The π^0 momentum calculated in the $\Upsilon(4S)$ rest frame, $p_{\pi^0}^{\mathrm{CM}}$, must be lower than $0.45\,\mathrm{GeV}/c$.

Each selected π^0 candidate is fitted by a *VtxFitterOper* object of the *BABAR* software package *VtxFitter*. Thereby the photon energies are varied within their uncertainties and $m_{\gamma\gamma}$ is constrained to the value $134.976\,\mathrm{MeV}/c^2$. The fit procedure is called π^0-mass-constrained-fit and improves the energy resolution of the photons, $\Delta E_\gamma = E_{\gamma\mathrm{truth}} - E_{\gamma\mathrm{reco}}$, where $E_{\gamma\mathrm{truth}}$ and $E_{\gamma\mathrm{reco}}$ are the true and the reconstructed photon energy. The improvement of ΔE_γ is shown in figure 4.7.

4.4 Efficiency Differences between Data and MC

Since this analysis tries to determine the absolute number of $B^- \to D^{*0} e^- \overline{\nu}_e$ events in the data sample — detected **and** undetected events — one needs to know the detector efficiency $\varepsilon_{\mathrm{sig}}$ for such decays as precisely as possible. To first order this efficiency is taken from the MC simulated events (sec. 4.1.2) as the ratio of measured signal events $\check{N}_{\mathrm{sig}}^{\mathrm{m}}$ relative to the number of generated signal events $\check{N}_{\mathrm{sig}}^{\mathrm{tot}}$:

$$\frac{N_{\mathrm{sig}}^{\mathrm{m}}}{N_{\mathrm{sig}}^{\mathrm{tot}}} = \varepsilon_{\mathrm{sig}} \quad \approx \quad \check{\varepsilon}_{\mathrm{sig}} = \frac{\check{N}_{\mathrm{sig}}^{\mathrm{m}}}{\check{N}_{\mathrm{sig}}^{\mathrm{tot}}} \;. \tag{4.10}$$

A symbol with (without) tilde on top is meant with respect to the simulated MC sample (true-data sample). Equation 4.10 is a good approximation but $\check{\varepsilon}_{\mathrm{sig}}$ can still be improved by tuning it with true data: After one applies some efficiency corrections to the MC, the signal efficiency $\check{\varepsilon}_{\mathrm{sig}}$ is transformed into an improved signal efficiency $\check{\varepsilon}'_{\mathrm{sig}}$. To explain the transformation one needs to express $\check{\varepsilon}_{\mathrm{sig}}$ as a product,

$$\check{\varepsilon}_{\mathrm{sig}} = \check{\varepsilon}^* \prod_{i=e,K,\pi,\pi^0} \check{\varepsilon}_i \quad, \tag{4.11}$$

where $\check{\varepsilon}_i$ is the efficiency to detect a particle i within a special range of acceptance (θ_i, ϕ_i), momentum (p_i), transversal momentum (p_{Ti}) and event's track multiplicity (M). The $\check{\varepsilon}^*$ takes into account the correlations between the four particles. It acts as a correction to the product ansatz in
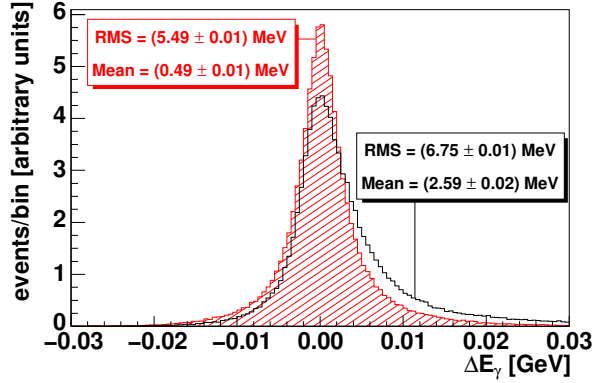
Figure 4.7: The distribution $\Delta E_\gamma = E_{\gamma\text{truth}} - E_{\gamma\text{reco}}$ is plotted for the lower-energy photons of the π^0 candidates correctly matched to a signal decay (see equ. 4.1). The distribution obtained after the π^0-mass-constrained-fit (red hatched) shows a significant improvement to the distribution obtained without the fit (black).

4.11 and remains untuned. The tuning transforms $\check{\varepsilon}_i$ by a multiplication with a data-MC correction factor R_i into an efficiency $\check{\varepsilon}_i'$,

$$\check{\varepsilon}_i \quad \longmapsto \quad \check{\varepsilon}_i' = \check{\varepsilon}_i R_i \,, \tag{4.12}$$

so that the best estimate of the signal efficiency in data is given by

$$\check{\varepsilon}_{\text{sig}}' = \check{\varepsilon}^* \prod_{i=e,K,\pi,\pi^0} \check{\varepsilon}_i' \quad . \tag{4.13}$$

The value of R_i for charged particles is divided into two factors. The first factor, R_i^{Track}, is the ratio of the track-finding efficiency for the used GTL tracks in data ($\varepsilon_i^{\text{Track}}$) and in MC ($\check{\varepsilon}_i^{\text{Track}}$). The second factor, R_i^{Pid}, is the ratio of the particle-identification efficiency for the i-particle-selector to select an i-particle from the GTL track-list in data ($\varepsilon_i^{\text{Pid}}$) and in MC ($\check{\varepsilon}_i^{\text{Pid}}$):

$$
\begin{aligned}
R_i &= R_i^{\text{Track}} R_i^{\text{Pid}} \\
&= \frac{\varepsilon_i^{\text{Track}}}{\check{\varepsilon}_i^{\text{Track}}} \frac{\varepsilon_i^{\text{Pid}}}{\check{\varepsilon}_i^{\text{Pid}}} \qquad\qquad (i = e, K, \pi)
\end{aligned}
\tag{4.14}
$$

Because particle-identifying criteria are only applied to the electron and the kaon candidates but not to the pion candidates we have $\varepsilon_\pi^{\text{Pid}} = \check{\varepsilon}_\pi^{\text{Pid}} = 1$ and therefore $R_\pi = R_\pi^{\text{Track}}$. More detailed information on the track finding efficiency (particle identification efficiency) can be found in subsection 4.4.1 (4.4.2).

The value of the data-MC correction factor R_{π^0} is the ratio of the π^0 reconstruction efficiency in data (ε_{π^0}) and in MC ($\check{\varepsilon}_{\pi^0}$) and is determined from $e^+e^- \to \tau^+\tau^-$ events [61]. Details on that are discussed in section 4.4.3.

In practice, the analysis uses a reweighting technique not requiring the explicit calculation of the signal efficiency (see chapter 5). Nevertheless, one can calculate the total signal efficiency $\check{\varepsilon}_{\text{sig}}'$ effectively applied in this analysis. This efficiency is given later in table 4.3.
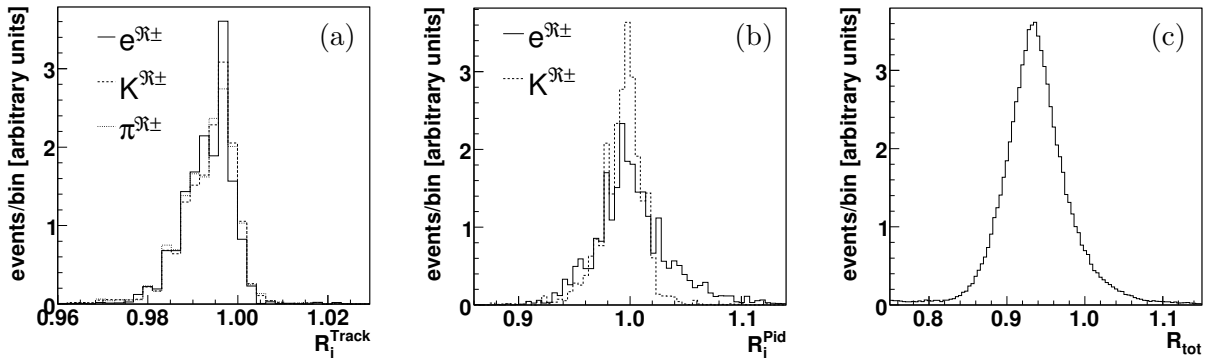
Figure 4.8: The tracking correction factors R_i^{Track} for $i = e, K, \pi$ are applied to the MC to obtain an equal track reconstruction efficiency in data and MC **(a)**. To correct the different selection efficiencies of the PID selectors the MC is also tuned by the correction factors R_i^{Pid} for $i = e, K$ **(b)**. The final correction factors applied to each Y candidate reconstructed in MC is the product R_{tot} of all correction factors, $R_{\mathrm{tot}} = R_e \cdot R_K \cdot R_\pi \cdot R_{\pi^0}$. The distribution of R_{tot} for Y candidates correctly matched to a signal decay is shown in subfigure **(c)**.

4.4.1 The Tracking Efficiency

Reference [65] summarizes the information about the tracking efficiency. The probability to reconstruct a GTL track along a particle's trajectory is called track-finding efficiency or also tracking efficiency. The ratio of its value in data and MC is R^{Track} and has been determined and tabulated in bins of the following track properties: (i) transverse momentum p_T, (ii) polar angle θ, (iii) azimuthal angle ϕ and (iv) track multiplicity M of the event the track is reconstructed in. For each single track used in the reconstruction of the MC signal-candidates the analysis looks up the table and assigns the corresponding weight to the track. Technically, the weights are applied as described by the formulas 4.12 to 4.14 and formula 5.14. But how are these ratios R^{Track} determined?

For the determination of the tracking efficiency the independence of the two *BABAR* tracking devices, SVT and DCH, is exploited. If a track is reconstructed in the SVT and has a transverse momentum $p_T > 0.1\,\mathrm{GeV}/c$ then the DCH should have seen it. Assume that from the N_{svt} tracks reconstructed in the SVT a number of N_{dch} tracks is also reconstructed by the DCH. After subtracting the N_{f} tracks which are falsely reconstructed in the SVT (so called SVT ghost tracks whose number is estimated from Bhabha events) one gets an estimate for the tracking efficiency, $\varepsilon^{\mathrm{Track}} = N_{\mathrm{dch}}/(N_{\mathrm{svt}} - N_{\mathrm{f}})$. The determination of this ratio in data and MC leads to the double ratio $R^{\mathrm{Track}} = \varepsilon^{\mathrm{Track}}/\check{\varepsilon}^{\mathrm{Track}}$ where many systematic uncertainties of $\varepsilon^{\mathrm{Track}}$ and $\check{\varepsilon}^{\mathrm{Track}}$ cancel out. The main contribution to the systematic uncertainty of R^{Track} springs from the fact that the *BABAR* track finding does not exclusively rely on the DCH alone (see section 4.2.1). Altogether the systematic uncertainty on R^{Track} is 0.8%. Figure 4.8a shows the distributions of the tracking correction factors R_i^{Track}.

4.4.2 The Particle Identification Efficiency for Charged Particles

Besides the tracking efficiency, also the efficiency of the applied PID selectors for electrons and kaons could significantly differ between data and MC. Assume that starting from a pure sample of N^{tot} x-particle's GTL-tracks the x-selector would select N^{sel} tracks ($x = e, K$). The resulting x-particle

identification efficiencies in data and MC are $\varepsilon^{\mathrm{Pid}} = N^{\mathrm{sel}}/N^{\mathrm{tot}}$ and $\check{\varepsilon}^{\mathrm{Pid}} = \check{N}^{\mathrm{sel}}/\check{N}^{\mathrm{tot}}$, respectively. The electron and the kaon efficiencies are determined and tabulated in bins of momentum, polar angle and run range. For each single MC signal candidate the analysis looks up the corresponding table and assigns the weight $R_e^{\mathrm{Pid}} \cdot R_K^{\mathrm{Pid}} = (\varepsilon_e^{\mathrm{Pid}}/\check{\varepsilon}_e^{\mathrm{Pid}}) \cdot (\varepsilon_K^{\mathrm{Pid}}/\check{\varepsilon}_K^{\mathrm{Pid}})$ improving the data-MC-agreement.

But the samples of pure electron and kaon GTL-tracks, how are they defined? This is documented in [58]. There are no PID cuts performed to create the two samples because that would fake the desired efficiencies. Only kinematic and topological cuts are allowed.

Electrons: Starting from events with exactly two tracks belonging to oppositely charged particles, a sample of radiative Bhabha events is created. The number of counted tracks before (N_e^{tot}) and after (N_e^{sel}) the electron selector is applied gives the selector's efficiency $\varepsilon_e^{\mathrm{Pid}} = N_e^{\mathrm{sel}}/N_e^{\mathrm{tot}}$. From the two tracks of an event only the low-energetic one is used.

Kaons: For the kaon efficiency one uses cuts to select $D^{*+} \to D^0(K^-\pi^+)\pi^+$ candidates from multi-hadron events. A fit to the D^0 mass determines the number of kaon GTL-tracks. N_K^{tot} is this number before the kaon selector is applied and N_K^{sel} is this number after it is applied. From both one easily determines the kaon efficiency, $\varepsilon_K^{\mathrm{Pid}} = N_K^{\mathrm{sel}}/N_K^{\mathrm{tot}}$.

Further information about the PID tables is available in [66] and [67]. Figure 4.8b shows the distributions of the tracking correction factors R_i^{Pid}.

4.4.3 The Neutral Pion Reconstruction Efficiency

The data-MC-disagreement in the π^0 reconstruction efficiency is corrected by using the correction factor R_{π^0} as given by the result of the τ analysis [61]. In the τ analysis result, R_{π^0} is given as a function of the magnitude of the π^0 laboratory momentum ($\vec{p}_{\pi^0}$) and as a function of the used π^0 selector[8]. For the π^0 selector used in the semileptonic analysis (*pi0SoftDefaultMass*) the correction factor is given by the function [61]

$$R_{\pi^0} = a + b \cdot \frac{|\vec{p}_{\pi^0}|}{\mathrm{GeV}/c}, \tag{4.15}$$

with

$$a = 0.9597 \qquad \text{and} \qquad b = 7.636 \cdot 10^{-3}. \tag{4.16}$$

To improve the data-MC-agreement, each single signal candidate of the MC is weighted by $|\vec{p}_{\pi^0}|$, according to equation 4.15. The π^0 efficiency needs a bit more discussion than the tracking and the PID efficiency, because an *extrapolation* of the result of the τ analysis is used. It is an extrapolation because the parametrization 4.15 is validated by the τ analysis for a momentum range from $0.3\,\mathrm{GeV}/c$ to $\sim 5.0\,\mathrm{GeV}/c$ only, but the π^0 mesons of the signal decay have momenta between $0.0\,\mathrm{GeV}/c$ and $0.35\,\mathrm{GeV}/c$ (see figure 4.9). As can also be seen in figure 4.11, in spite of the lower limit of the validated momentum range ($0.3\,\mathrm{GeV}/c$), the τ analysis determined R_{π^0} down to $0.1\,\mathrm{GeV}/c$.

After presenting the basic ideas of the τ analysis, a few sentences give insight into the τ event selection. Subsequently, the main sources of the data-MC-disagreement (low-energy photon-background, hadronic split-offs) are briefly explained. The section closes with an argumentation for the extrapolation of equation 4.15 into the π^0 momentum range of the $D^{*0}e\nu$ signal candidates.

---

[8] π^0-selector properties, such as allowed $\gamma\gamma$-mass-range or γ-energy-range (where γ is a π^0 daughter) influence the π^0 efficiency.
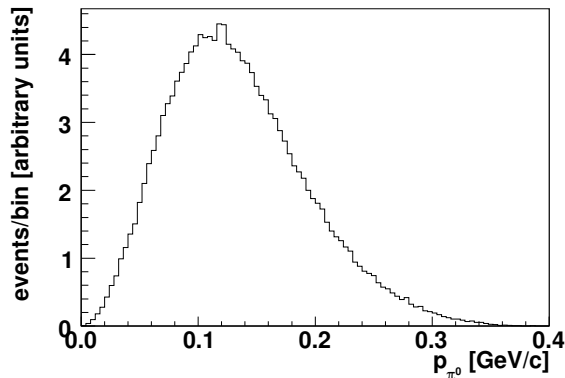
Figure 4.9: The π^0 momentum distribution within the laboratory system, plotted for π^0 candidates correctly matched to a signal decay (see equ. 4.1). The momentum range is situated at the boarder of the validated range of the τ analysis.

4.4.3.1 Introduction of the τ Analysis

The τ analysis studies $e^+e^- \to \tau^+\tau^-$ events, where one τ is reconstructed in the decay channel $\tau^\pm \to e^\pm \nu \bar{\nu}$ and the other τ is reconstructed in the decay channel (i) $\tau^\pm \to \pi^\pm \nu$ or (ii) $\tau^\pm \to \rho^\pm \nu \to \pi^\pm \pi^0 \nu$. The selection and reconstruction of the events is described in more detail in [61] and in appendix A.1. From the selected events one can determine ε'_{π^0} and $\breve{\varepsilon}'_{\pi^0}$, which are proportional to the π^0 efficiency in data (ε_{π^0}) and in MC ($\breve{\varepsilon}_{\pi^0}$), respectively. One can define

$$\varepsilon_{\pi^0} \propto \varepsilon'_{\pi^0} = \frac{N^{\text{sel}}}{N^{\text{tot}}} \tag{4.17a}$$

$$\breve{\varepsilon}_{\pi^0} \propto \breve{\varepsilon}'_{\pi^0} = \frac{\breve{N}^{\text{sel}}}{\breve{N}^{\text{tot}}}, \tag{4.17b}$$

where N^{sel}, N^{tot}, $\breve{N}^{\text{sel}}$ and $\breve{N}^{\text{tot}}$ are numbers of counted events obtained from the data and the MC sample[9], respectively. The proportionality factors and the large systematic uncertainties of ε'_{π^0} and $\breve{\varepsilon}'_{\pi^0}$ cancel in the ratio

$$R_{\pi^0} = \frac{\varepsilon_{\pi^0}}{\breve{\varepsilon}_{\pi^0}} = \frac{\varepsilon'_{\pi^0}}{\breve{\varepsilon}'_{\pi^0}} = \frac{N^{\text{sel}}/N^{\text{tot}}}{\breve{N}^{\text{sel}}/\breve{N}^{\text{tot}}}. \tag{4.18}$$

In principle, the authors of [61] determine the numbers N^{sel}, N^{tot}, $\breve{N}^{\text{sel}}$ and $\breve{N}^{\text{tot}}$ in two different ways leading to two values of the double ratio R_{π^0}:

(a) The first way of R_{π^0} determination is performed for all π^0 standard lists of the *BABAR* software. Due to its procedure it uses a special case where $\varepsilon_{\pi^0} = \varepsilon'_{\pi^0}$ and $\breve{\varepsilon}_{\pi^0} = \breve{\varepsilon}'_{\pi^0}$. The strategy is to use the MC-truth matching described on page 37. The denominator of equation 4.17b is determined by

$$\breve{N}^{\text{tot}} = \breve{A} - \breve{B}, \tag{4.19}$$

---

[9] The numbers corresponding to the MC sample are not only counted but also luminosity-weighted. Thus, they give a direct estimate for the numbers observed in the data sample.

where $\check{A}$ is the total number of all selected MC events containing a π^0 candidate, and $\check{B}$ is the number of all MC background-events, i.e. all MC events where the π^0 candidate was not successfully MC-truth matched to a π^0 meson of the MC-truth list. The corresponding numerator of equation 4.17b is calculated by

$$\check{N}_{(x)}^{\text{sel}} = \check{A}_x - \check{B}_x,\tag{4.20}$$

where the definitions of $\check{A}_x$ and $\check{B}_x$ are like before, but the events must be selected by the *BABAR* standard π^0 selector x (x = pi0VeryLoose, pi0Loose, pi0SoftDefaultMass, ...). The definition of the data corresponding numbers N^{tot} and N^{sel} is obtained similarly,

$$N^{\text{tot}} = A - B \quad \text{and}\tag{4.21}$$

$$N_{(x)}^{\text{sel}} = A_x - B_x,\tag{4.22}$$

where A and A_x are defined as before but with respect to the data sample instead of the MC sample. The B and the B_x are taken from MC ($B = \check{B}$ and $B_x = \check{B}_x$). Altogether, the π^0 efficiency correcting factor $R_{\pi^0}^x$ for a π^0 selector x is defined by:

$$R_{\pi^0}^x = \frac{\varepsilon_{\pi^0}^x}{\check{\varepsilon}_{\pi^0}^x} = \frac{\left(\check{A}_x - \check{B}_x\right)/\left(\check{A} - \check{B}\right)}{\left(A_x - B_x\right)/\left(A - B\right)}.\tag{4.23}$$

(b) The second type of R_{π^0} determination can be interpreted as a detailed check for the $R_{\pi^0}^x$ result of (a). This time, the denominator of equation 4.17b is the number ($\check{N}^\pi$) of selected MC events that have been assigned to $\tau \to \pi\nu$ decays. Correspondingly, the numerator of 4.17b is the number ($\check{N}^\rho$) of selected MC events assigned to $\tau \to \rho\nu$ decays. Due to

$$\frac{\check{N}^\rho}{\check{N}^\pi} \propto \frac{\check{\varepsilon}_{\pi^0}\check{\varepsilon}_\pi \mathcal{B}\left(\tau \to \rho\nu\right)\check{\varepsilon}_e \mathcal{B}\left(\tau \to e\nu\bar{\nu}\right)}{\check{\varepsilon}_\pi \mathcal{B}\left(\tau \to \pi\nu\right)\check{\varepsilon}_e \mathcal{B}\left(\tau \to e\nu\bar{\nu}\right)}\tag{4.24}$$

the ratio $\check{N}^\rho/\check{N}^\pi$ is proportional to the π^0 efficiency $\check{\varepsilon}_{\pi^0}$. Similarly defining the numbers of data events assigned to the $\tau \to \pi\nu$ and $\tau \to \rho\nu$ decays (N^π and N^ρ, respectively), one gets the factor $R_{\pi^0}^x$ corresponding to the π^0 selector x (x = pi0VeryLoose, pi0Loose, ...):

$$R_{\pi^0}^x = \frac{\varepsilon_{\pi^0}^x}{\check{\varepsilon}_{\pi^0}^x} = \frac{N^\rho{}_x/N^\pi}{\check{N}_x^\rho/\check{N}^\pi}.\tag{4.25}$$

The two subscripts x in the right side of the equation indicate that each of the number of events is taken after the π^0 candidates were required to pass the selector x. One important feature of strategy (b) compared to strategy (a) is that it does not rely on MC-truth matching.

The two types of R_{π^0} determination are consistent within a broad π^0 momentum range as shown in figure 4.11. The disagreement in the two low-momentum bins of figure 4.11 is discussed in section 4.4.3.3. The important parametrization 4.15 has been obtained using method (a) for the π^0 selector *pi0SoftDefaultMass*, where the requirement on the π^0 momentum ($p_{\pi^0}^{\text{CM}} < 0.45\,\text{GeV}/c$) was omitted. The corresponding dependence of the MC-correction-factor R_{π^0} on the π^0 momentum is shown in figure 4.10. Once again, the unphysical steep rise in the low-momentum bins is explained in section 4.4.3.3.
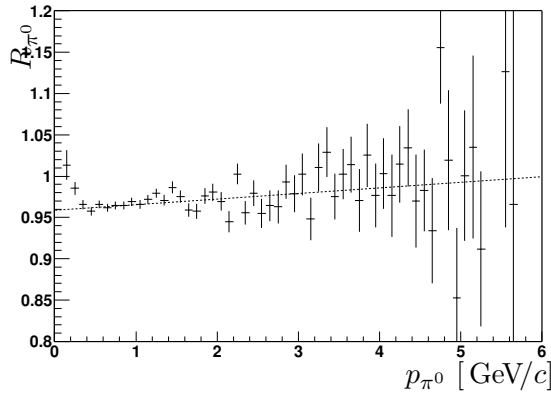
Figure 4.10: Measurement of R_{π^0} by the τ analysis using the MC-truth-matching method. The measured values are shown for the selector *pi0SoftDefaultMass*. Also plotted is the obtained parametrization (dotted), given in equation 4.15.
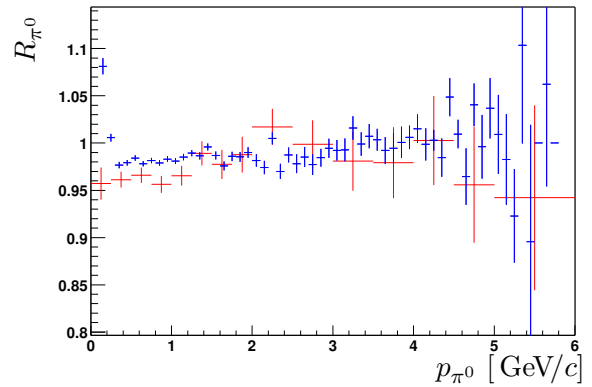
Figure 4.11: Overlay of the correction factors R_{π^0} for method (a)(blue) and (b)(red) of the τ analysis. The correction factor is shown for the π^0 selector *pi0VeryLoose*. The disagreement in the low-momentum range is discussed in the text. From the level of agreement between the two methods, the authors of the τ analysis state a systematic error $\Delta R_{\pi^0} = 3\%$.

4.4.3.2 Main Differences between Data and MC

There are two effects giving the dominant contribution to the difference between data and MC, where 'difference' is mentioned in view of the reconstruction in the EMC. The listed effects do not influence the π^0 efficiency itself, but they complicate the determination of the π^0 efficiency:

1.) **Low-Energy Photon Background** As can be seen in figure 4.5, the low-energy photon background from the machine rises dramatically when going to lower energies. This behavior is modeled in the MC by also using real data (see page 36). More generally, the simulation of the (low-energy) photon background does not exclusively rely on first principles. It also bases on empiric models trying to match the distributions of various EMC-variables. However, as is also shown in the τ analysis (see figure 4.12), the MC overestimates the amount of low-energy photons.

2.) **Hadronic Split-offs** A hadron (e.g. a pion) interacts with the EMC material by electromagnetic and hadronic interaction processes. As a result of the hadronic interaction, secondary hadrons can be generated. If these secondary particles have (i) a large enough lifetime and (ii) a very small probability to deposit energy in the EMC, then they can produce secondary EMC clusters, separated from the primary EMC cluster. Such a secondary cluster is called *hadronic split-off*. The true cause of the improper split-off description in MC is a bad description of the EMC-internal hadronic interaction processes.

For method (b) explained on page 52, the τ analysis performs corrections accounting for the split-offs and the low-energy photon background.
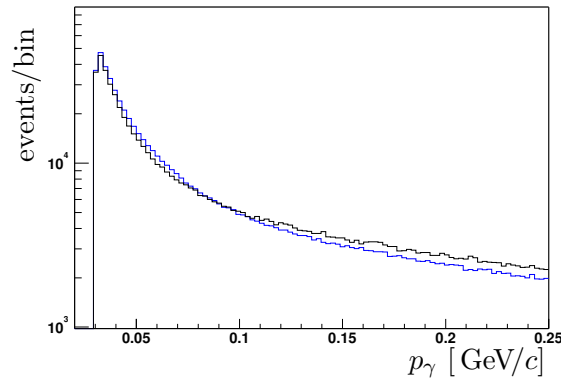
Figure 4.12: Distribution of photon momentum for the events selected by the τ analysis. In a comparison of data (black) and MC (blue) one can see an increase in the number of MC photons at low energies. (As already mentioned on page 51, the MC is scaled to the same luminosity like data.)

4.4.3.3 Argumentation for an Extrapolation of the τ Analysis Result

At the beginning of the argumentation one should mention that the R_{π^0} results of the τ analysis are recommended by the *Neutral Reconstruction Working Group* of *BABAR* [68]. The results are consistent to other *BABAR*-internal studies about π^0 efficiency [69]. However, there is no completed study giving the π^0 efficiency with an acceptable uncertainty ($\sim 3\%$) for the desired momentum range of π^0 mesons coming from D^* mesons.

Since the effects dominantly contributing to the data-MC-disagreement concern the π^0 background and not the true π^0 mesons, there are good arguments to use an extrapolation of the τ analysis result:

- First of all, the result of the semileptonic analysis is checked against systematic uncertainties arising from the extrapolation by systematically cutting on the π^0 momentum (see section 7.1.3).

- Second, how can the steep rise of R_{π^0} (MC-truth-matching method) in figures 4.11 and 4.10 be explained? Since there are too many low-energy background-photons in the MC (compared to data), the approximations used in equation 4.23 ($B = \check{B}$ and $B_x = \check{B}_x$) are not allowed in the low π^0 momentum range. In this momentum range, the assumption of equal background leads to an overestimation of the background in data. The resulting underestimation of N^{sel} and N^{tot} leads to an overestimation of R_{π^0} at low π^0 momentum. The effect should become more extreme when going from a tighter to a looser π^0 definition, because the background disagreement should grow. Indeed, in the plot with the looser π^0 definition (figure 4.11, π^0 selector = pi0VeryLoose) the R_{π^0} edge in the low momentum bins is steeper than in the plot with the tighter π^0 definition (figure 4.10, π^0 selector = pi0SoftDefaultMass).

4.5 The Selection Criteria

Due to the huge data sample, the uncertainty of the final result is not dominated by statistical uncertainties. The main uncertainties are of systematic nature. Therefore, the selection criteria increasing the signal fraction in the data sample have been optimized in a subjective way.

4.5.1 The Event Selection

The BToDlnu Skim
Since the total branching fraction of the signal decay chain (equation 4.1) is about 1.5‰ one expects only one out of 670 events to contain a signal decay.[10] Of course, there are many events looking similar to the searched events regarding the event's detector response. But still, a big fraction of the events of the analyzed data set is not interesting for this analysis and can be very easily excluded, e.g. events having fewer than three charged tracks. Since this situation is comparable to many of *BABAR*'s analyses, the *BABAR* computing model divides the total data set into subsamples called skims. A certain skim is an appropriate starting point for many similar analyses [70].

The skim used in this analysis is the *BToDlnu* skim [71]. Besides the signal decay events, the skim contains also events with reconstructed decays (i) where a semileptonic decay of a neutral *B* meson is reconstructed instead of a charged *B*, (ii) where the daughter lepton of the *B* meson is assumed to be a muon instead of an electron, and (iii) where an alternative reconstruction channel of the *D* meson is used (e.g. $D \to K\pi\pi$). This (incomplete) listing illustrates that many *BABAR* analyses can profit from the centrally created BToDlnu skim. The BToDlnu skim contains about 25% of the *AllEvents* skim, for data as well as for $B\bar{B}$ MC. Since the time-consuming steps of the analysis are not only the combinatorics corresponding to equation 4.1 but also the uploading of an event from the *BABAR* database, the use of the BToDlnu skim was very helpful to perform this analysis.

The Second Normalized Fox Wolfram Moment
The second normalized Fox Wolfram moment R_2 is defined by

$$R_2 = \frac{H_2}{H_0}, \tag{4.26}$$

with [72]

$$H_l = \sum_{i\,j} \frac{|p_i|\,|p_j|}{E_{\text{vis}}^2} P_l\left(\cos\theta_{ij}\right). \tag{4.27}$$

The double sum runs over all particles i and j of the event, where p_i is the momentum of particle i, θ_{ij} is the opening angle between the momenta of particles i and j, and P_l is the lth Legendre polynomial,

$$P_0(x) = 1 \text{ and}$$
$$P_2(x) = \frac{1}{2}\left(3x^2 - 1\right).$$

E_{vis} is the total visible energy of the event. R_2 is calculated from charged tracks and neutral clusters passing loose quality requirements. By definition, the value of R_2 ranges from zero to one. R_2 is a variable characterizing the event's momentum distribution. For events with jet structure R_2 gives higher values (due to higher $|\cos\theta_{ij}|$ and higher P_2 values) than for events with spherical structure. Accordingly, the R_2 distribution of $e^+e^- \to B\bar{B}$ events is shifted to lower values compared to the R_2 distribution of $e^+e^- \to q\bar{q}$ events ($q = uds$). In order to suppress $q\bar{q}$ events, each event with $R_2 > 0.45$ is rejected from the analysis. This selection criteria and the corresponding distributions in $B\bar{B}$ and $q\bar{q}$ events are shown in figure 4.13.

---

[10]There are two charged *B* mesons in each second $B\bar{B}$ event.
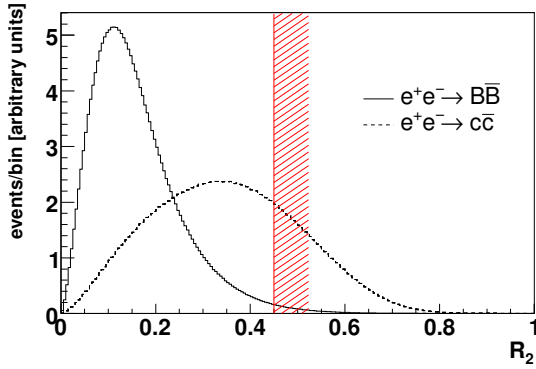
Figure 4.13: The second normalized Fox Wolfram Moment R_2 is plotted for MC events of type $e^+e^- \to B\bar{B}$ (solid) and $e^+e^- \to c\bar{c}$ (dashed). The two graphs are scaled to the same number of events. The plotted selection criteria, $R_2 < 0.45$ suppresses the $c\bar{c}$ events.
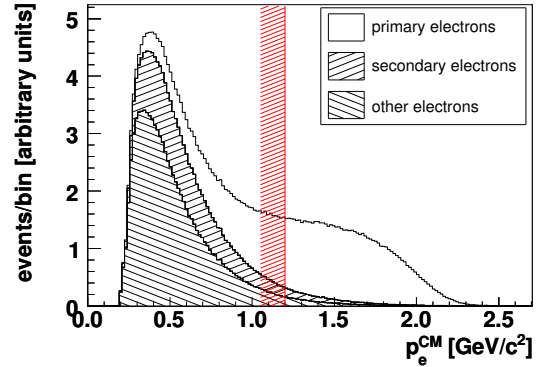
Figure 4.14: The electron momentum spectrum for $B\bar{B}$ events. Electrons directly coming from a B meson have a harder spectrum then electrons coming from a B daughter or even from another particle of the B decay chain. The requirement $p_e^{\mathrm{CM}} > 1.2\,\mathrm{GeV}/c$ increases the signal fraction in the sample. (Histograms are stacked.)

4.5.2 The Candidate Selection

In the composition of the Y candidates the charge correlation between the tracks has been taken into account. The charge of the kaon and the electron track have to be equal to each other, but opposite to the charge of the pion track.

The Electron Momentum
A very important selection criteria, even already applied in the BToDlnu skim production, is the requirement to select only candidates with high-momentum electrons. In principal, in the $B\bar{B}$ events there are

- primary electrons directly originating from a B meson,

- secondary electrons originating from a direct daughter of a B meson, and

- further electrons originating from a still longer B decay chain.

The more intermediate states between the B meson and the electron, the softer is the corresponding electron momentum spectrum. Figure 4.14 illustrates the electron momentum spectrum in $B\bar{B}$ events for different types of electron origin. The BToDlnu skim only uses electrons with $p_e^{\mathrm{CM}} > 0.8\,\mathrm{GeV}/c$. For this analysis each selected candidate needs to satisfy the condition $p_e^{\mathrm{CM}} > 1.2\,\mathrm{GeV}/c$, which increases the fraction of signal candidates in the final sample. The superscript CM marks the electron momentum (p_e^{CM}) to be measured in the $\Upsilon(4S)$ rest frame.

The Vertex Probability
For the composition of D^0, D^{*0} and Y^{11} candidates there is the possibility to simply add the four-momenta of the charged tracks and the neutral pion, corresponding to the decay chain 4.1.

---

[11] $Y = D^{*0}e^-$, as defined on page 34.
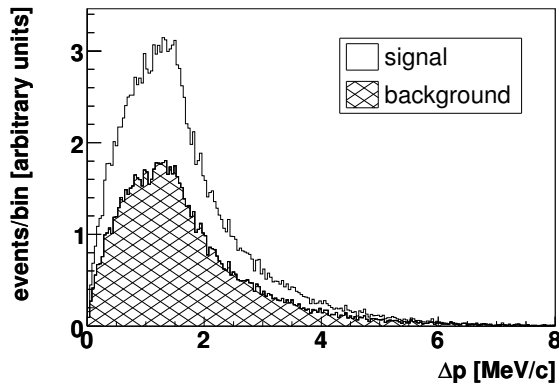
Figure 4.15: Shown is the variation of the kaon momenta in the geometrical constrained fit of the D^0 candidates surviving the cuts listed in table 4.3. The difference $\Delta p = |\vec{p} - \vec{p}_{\text{fit}}|$ is taken between the kaon momentum before the fit ($\vec{p}$) and after the fit ($\vec{p}_{\text{fit}}$). The two stacked histograms correspond to candidates from signal (background) events containing (not containing) a signal decay on the MC-truth-side (see equ. 4.1). The corresponding distribution for the pions has the same shape.

From the resulting four-momenta of the composed candidates follow mass and angular distributions providing selection criteria which increase the signal fraction in the data sample. But the detector provides more information than 'just' the momentum. It provides also the spatial information about a track. If the pion and the kaon candidate really originate from one and the same mother particle (D^0 meson) then their reconstructed tracks should overlap at the mother's decay vertex within the track parameter uncertainties. In a fit called *geometrically constrained fit*, the pion and the kaon track are forced to originate from one and the same common vertex. The fit varies the parameters of the two tracks within their uncertainties. It is performed by a *VtxFitterOper* object of the *BABAR* software package *VtxFitter* and relies on a least square method using Lagrange multipliers. The probability of obtaining a higher value then χ^2 at a given number of degrees of freedom (n) is given by $P(\chi^2, n)$,

$$P(\chi^2, n) = \int_{\chi^2}^{\infty} f(x, n)\, \mathrm{d}x \qquad \text{with} \tag{4.28a}$$

$$f(x, n) = \frac{\left(\frac{x}{2}\right)^{\frac{n}{2}-1} e^{-\frac{x}{2}}}{2\Gamma\left(\frac{n}{2}\right)}, \tag{4.28b}$$

where $\Gamma(y)$ is the standard gamma function and P satisfies the condition $0 \leq P \leq 1$ by definition. For consistent track pairs originating from one common mother vertex, P is flatly distributed in x. For inconsistent tracks χ^2 is very large and results in very low values for P. To suppress candidates with inconsistent track-fits the selected D^0 candidates are required to satisfy $P_{K\pi} > 0.01$.

Besides the consistency check the track parameter variation in the fit gives also changed momenta. The difference between momenta before and after the fit is very small (see figure 4.15). However, the VtxFitterOper package performs the fit in a way that the magnitude of the momentum vector remains unchanged ($|\vec{p}| = |\vec{p}_{\text{fit}}|$) and only the direction of the momentum vector is corrected. Therefore, the kinematic variables such as Δm and $m_{K\pi}$ remain unchanged. Nevertheless, for the rest of this document the fitted momenta are used, except if the use of unfitted momenta is pointed out. However, the main benefit from the fit is the rejection of badly matching track pairs.
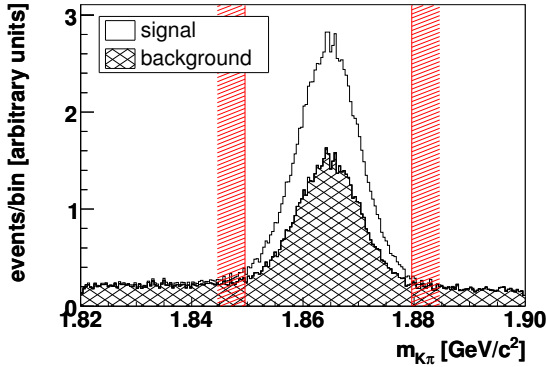
Figure 4.16: Shown is the distribution of the reconstructed K-π-mass, $m_{K\pi}$, for candidates from signal (background) events containing (not containing) a signal decay on the MC-truth-side. There are correctly reconstructed D^0 candidates in the signal and in the background events. The candidates contributing to the two stacked histograms survive all selection criteria listed in table 4.3 except for the illustrated $m_{K\pi}$ cut.
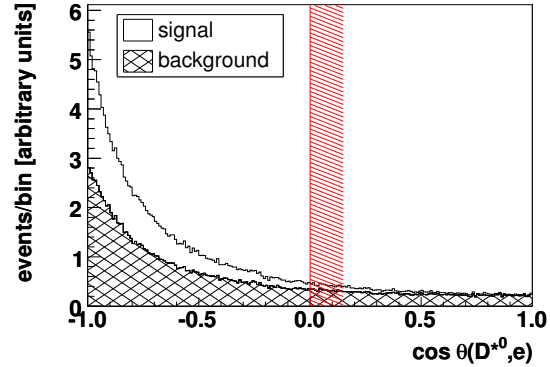
Figure 4.17: Shown is the distribution of $\cos\theta(D^{*0}, e)$, where $\theta(D^{*0}, e)$ is the angle between the momentum vectors of D^{*0} meson and electron as reconstructed in the $\Upsilon(4S)$ rest frame. The signal (background) candidates belong to events containing (not containing) a signal decay on the MC-truth-side. The candidates contributing to the two stacked histograms survive all selection criteria listed in table 4.3 except for the illustrated $\cos\theta(D^{*0}, e)$ cut. As explained in the text, the flat fraction of the distribution mainly corresponds to uncorrelated $D^{*0}e^-$ combinations.

Since the D^{*0} meson has a negligible flight length one can similarly ask for a reasonable overlap of the D^0 flight path (arising from the refitted pion and kaon momenta) and the electron track. This is also done by performing a geometrical constrained fit using the VtxFitter software package. To reject badly matching D^0-electron-pairs, signal candidates are required to satisfy $P_{D^0 e} > 0.01$.

The D^0 Mass

The mass of the D^0 candidate ($m_{K\pi}$) is required to be within a $30\,\text{MeV}/c^2$ broad mass window centered at the D^0 mass ($m_{D^0} = 1.8646\,\text{GeV}/c^2$),

$$|m_{K\pi} - m_{D^0}| < 15\,\text{MeV}/c^2. \tag{4.29}$$

The suppression of combinatorial background due to this cut is shown in figure 4.16.

The Angle between D^{*0} Meson and Electron

Due to the $V - A$ nature of the weak interaction, the D^{*0} meson and the electron, both coming from the same semileptonic B decay, preferentially fly into different hemispheres in the B rest frame. The angle between their flight directions, $\theta(D^{*0}, e)$, is calculated in the $\Upsilon(4S)$ rest frame and is shown in figure 4.17.[12] One can see the accumulation of signal events towards lower $\cos\theta(D^{*0}, e)$ values. The flat fraction in the histograms of figure 4.17 comes from wrongly reconstructed Y candidates, whose origin can be explained as follows: If the Y candidate is reconstructed in a way

---

[12]On the one hand, the B rest frame is unknown due to the unknown flight direction of the B meson in the $\Upsilon(4S)$ rest frame. On the other hand, the angle and momentum distributions are only mildly modified when changing from one rest frame to the other because the B meson has a very small momentum in the $\Upsilon(4S)$ rest frame.
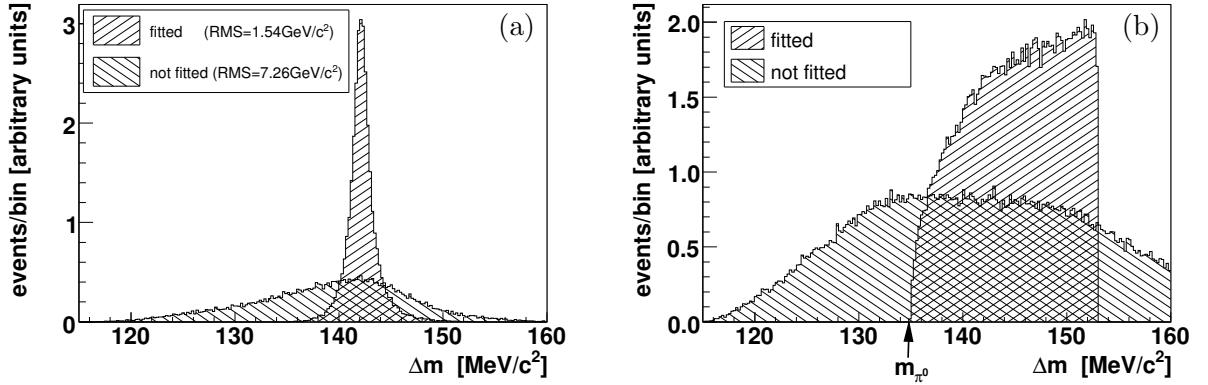
Figure 4.18: Shown are Δm distributions for candidates with: **(a)** correctly reconstructed D^{*0} meson, and **(b)** wrongly reconstructed D^{*0} meson. All of the candidates passed the selection criteria listed in table 4.3. After the π^0-mass-constrained fit, (a) the Δm distribution of correctly reconstructed D^{*0} mesons becomes about five times narrower and (b) the Δm distribution of wrongly reconstructed D^{*0} mesons gets a better parameterizable shape.

that (i) the D^{*0} comes from the one B meson of the event and (ii) the electron comes from the other B meson of the event, then there is no correlation between the flight directions of the two Y daughters; the corresponding $\cos\theta(D^{*0}, e)$ distribution is flat. To reduce this type of background events, each selected candidate has to satisfy the condition $\cos\theta(D^{*0}, e) < 0.0$.

The Mass Difference Δm

The mass difference Δm between a D^{*0} and a D^0 candidate is defined by

$$\Delta m = m_{K\pi\pi^0} - m_{K\pi}, \tag{4.30}$$

where $m_{K\pi\pi^0}$ is the mass of the D^{*0} candidate. The use of the fitted π^0 four-momentum rather than unfitted π^0 four-momentum (see π^0-mass-constrained fit on page 47) brings two essential advantages:

- For candidates with correctly reconstructed D^{*0} mesons the mass difference is narrowed by a factor 4.7. This is illustrated in figure 4.18a.

- For candidates without correctly reconstructed D^{*0} mesons the shape of the Δm distribution is better parameterizable after the π^0-mass-constrained fit. Due to the π^0-mass-constraint, the Δm value must always be greater than the π^0 mass. The corresponding distributions before and after the π^0-mass-constrained fit are shown in figure 4.18b.

Altogether, after the π^0-mass-constrained fit there is a better separation between the candidates with correctly and wrongly reconstructed D^{*0} meson. As already mentioned, the Δm distribution does not depend on using the results of the geometrical-constrained fits.

As discussed in section 5.1, the variable Δm is one of the three fundamental fit variables. It is used to determine the number of correctly reconstructed D^{*0} mesons in the samples as precisely as possible. Together with the variable $\cos\theta_{\mathrm{BY}}$ (see section 4.6) it is possible to determine the number of events that were successfully reconstructed in the decay mode 4.1.
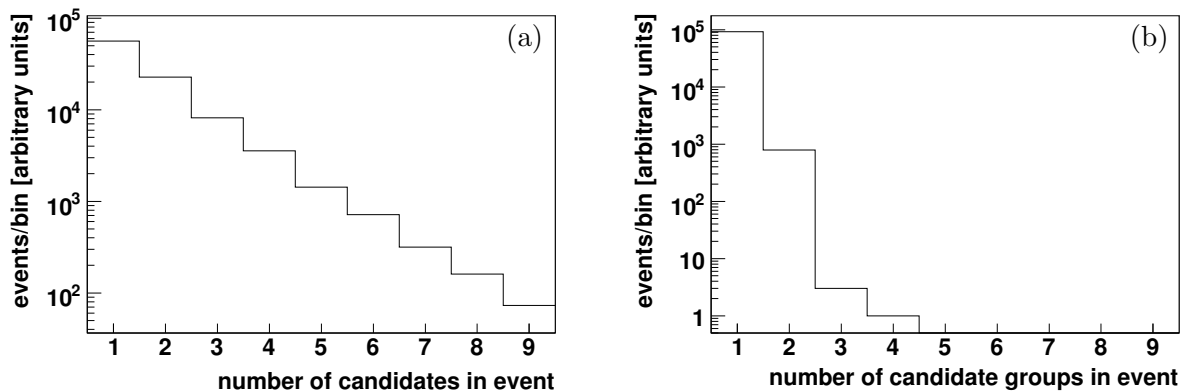
Figure 4.19: Plot (a) shows the number of MC Y candidates obtained after all selection criteria listed in sections 4.5.1 and 4.5.2 were applied. After the Y candidates with equal e-K-π-combination were grouped (see section 4.5.3) the number of candidate groups is only in few events greater than one (see plot (b)).

All candidates passing the selection are required to satisfy the condition $\Delta m < 0.153\,\text{GeV}/c^2$. This selection criteria is well visible in figure 4.18b. But how has it been chosen? There are two competitive arguments for the choice of the Δm selection cut:

- On the one hand, the Δm selection cut should be chosen tight enough to suppress as many background candidates as possible. As described below, in the case of multiple candidates per event one has to select one candidate-group — the other candidate-groups of the event must be rejected. A smaller allowed Δm range increases the probability to select a candidate-group contributing to the Δm signal-peak because the other candidate-groups not contributing to the Δm signal-peak were already rejected by the Δm selection cut.

- On the other hand, the Δm selection cut should not be too hard. If the Δm sideband becomes too small the determination of the number of correctly reconstructed D^{*0} candidates becomes less and less precise.

4.5.3 Multiple Candidates per Event

After all selection criteria listed in table 4.3 have been applied, the samples very often contain more than one candidate per event (see figure 4.19a). In the sister analysis, analyzing the B decay channel $\overline{B}^0 \to D^{*+}e^-\overline{\nu}_e$ [75], these multiple-candidate events appeared in only 1.5% of all events containing reconstructed candidates. The reason for the big difference is that in the $\overline{B}^0 \to D^{*+}e^-\overline{\nu}_e$ analysis one has to deal with *charged* soft pions, but in the $B^- \to D^{*0}e^-\overline{\nu}_e$ analysis one has to deal with *neutral* soft pions composed of two photon candidates. The combinatorial background due to wrong $\gamma\gamma$ combinations increases the number of allowed Y candidates significantly. Since there are many low-energetic (background) photons in the event most of the event's Y candidates base one the same three tracks (e-K-π combination) but use different $\gamma\gamma$ combinations. Which candidate should be selected to be the final signal-candidate of the event? The sister analysis with the semileptonic decay of a neutral B meson found a criterion defining one candidate of the event as the final signal-candidate. But this is not the best method for the $B^- \to D^{*0}e^-\overline{\nu}_e$ analysis since there are multiple candidates in about 40% of all events with reconstructed candidates (instead of

1.5%). To understand the requirements on the candidate selection in case of multiple candidates per event one should consider the following items:

- For the final fit explained in chapter 5 it is important that the efficiency for correctly reconstructed D^{*0} mesons is exactly known in data. The strategy is to use the values obtained from the $B\overline{B}$ MC simulation (corrected as described in section 4.4).[13]

- Assume that there is an (arbitrary) decision criterion for events with multiple candidates, e.g. the final candidate is randomly chosen from the candidates of the event. With such a criterion the measured efficiency of correctly reconstructed D^{*0} mesons depends on the number of candidates passing all selection criteria. If one increases the number of low-energetic photons per MC event then the number of Y candidates passing all selection criteria increases (in the MC), and the measured efficiency decreases. In other words: If the low-energetic photon spectrum[14] in the event differs between the MC sample and the data sample then the measured efficiency of correctly reconstructed D^{*0} mesons should not be applied to the data sample. The consideration remains unchanged with other selection criteria also taking one candidate of the event as the final candidate.

The multiple-candidate problem is solved by the selection of one entire candidate-group of the event. Instead of one selected final candidate there is one selected final candidate-group in each event. All members of the same candidate-group base on the same e-K-π-combination but use different $\gamma\gamma$ pairs. Members of different candidate-groups have different e-K-π-combinations. The big advantage of this selection method is that each candidate-group contains either one or no correctly reconstructed D^{*0} candidate. The resulting number of candidate-groups per event is shown in figure 4.19b. Only 8.6‰ of all events contain more then one candidate-group. In case of multiple candidate-groups in the event the candidate-group with the K-π-mass ($m_{K\pi}$) closest to the nominal D^0 mass ($m_{D^0} = 1.8646\,\mathrm{GeV}/c^2$) is selected, i.e. the candidate-group with the lowest value for

$$\left| m_{K\pi} - m_{D^0} \right|. \tag{4.31}$$

To summarize section 4.5, all applied selection cuts are listed in table 4.3. The table shows also counted MC event numbers, efficiencies and purity, all characterizing the cuts.

4.6 The Definition of $\cos\theta_{\mathrm{BY}}$ and $\tilde{w}$

In the previous section, formula 4.30 already defines the variable Δm. The aim of this section is to define two additional variables, namely $\cos\theta_{\mathrm{BY}}$ and $\tilde{w}$. The three variables are very important for this analysis because the Δm-$\cos\theta_{\mathrm{BY}}$-$\tilde{w}$ distribution of the data is used to determine $F(1)|V_{cb}|$ and $\rho_{A_1}^2$. As already mentioned, the Δm variable is necessary to determine the number of correctly reconstructed D^{*0} mesons. But not all Y candidates containing a correctly reconstructed D^{*0} meson represent a signal decay. The fraction of correctly reconstructed D^{*0} mesons coming from signal and not from background events is determined by the different $\cos\theta_{\mathrm{BY}}$ distributions of signal events and various types of background events. The third variable, $\tilde{w}$ is used to be sensitive to the parameter $\rho_{A_1}^2$, which describes the shape of the w distribution of the signal decays.

---

[13]The final fit (see chapter 5) *implicitly* uses efficiency of correctly reconstructed D^{*0} mesons.
[14]mainly the multiplicity spectrum of low-energetic photons, but also the energy spectrum

Table 4.3: The table lists the successively applied selection criteria together with information about efficiency and purity. The numbers in the columns are obtained from run1 and run3 of the *BABAR* MC.[a] The first column lists all selection criteria applied to the final samples. The second column lists the number of events surviving the cuts listed until the corresponding row (N_{tot}). The third column gives the number of events additionally containing a B meson decaying in the signal mode ($N_{\text{sig tr}}$)(see equation 4.1). In $N_{\text{sig ma}}$ of these events there is also a correctly reconstructed Y candidate that is fully matched to a signal decay on the MC-truth-side. The efficiencies ε_{tr} and ε_{ma} correspond to the numbers listed in the third and the fourth column, respectively. The purity P_{ma} of the sample is defined as the fraction of correctly reconstructed Y candidates in the sample of all Y candidates belonging to the signal region defined by $140.12\,\text{MeV}/c^2 < \Delta m < 144.12\,\text{MeV}/c^2$ and $-1 < \cos\theta_{\text{BY}} < 1$.

Selection Criterion	N_{tot}	$N_{\text{sig tr}}$	$N_{\text{sig ma}}$	ε_{tr}	ε_{ma}	P_{ma}
MC Generated	$171,112,000$	$258,473$	$-$	100.0%	$-$	$-$
Reconstructed in BToDlnu Skim	$576,029$	$69,671$	$38,271$	26.9%	14.8%	37.8%
$R_2 < 0.45$	$568,235$	$68,348$	$37,488$	26.4%	14.5%	37.6%
$p_e^{\text{CM}} > 1.2\,\text{GeV}/c$	$309,014$	$51,113$	$28,109$	19.7%	10.8%	40.1%
$P_{K\pi} > 0.01$	$273,718$	$48,802$	$26,911$	18.8%	10.4%	41.4%
$P_{D^0\pi} > 0.01$	$248,104$	$47,147$	$26,052$	18.2%	10.0%	42.4%
$|m_{K\pi} - m_{D^0}| < 15\,\text{MeV}/c^2$	$181,902$	$44,438$	$24,801$	17.1%	9.5%	46.1%
$\cos\theta(D^{*0}, e) < 0.0$	$153,910$	$41,362$	$23,016$	16.0%	8.9%	48.0%
$\Delta m < 0.153\,\text{GeV}/c^2$	$85,706$	$33,188$	$22,976$	12.8%	8.8%	48.0%
Multiple Candidate Group Selection	$85,706$	$33,188$	$22,894$	12.8%	8.8%	48.1%

---

[a]The calculation of the numbers in the table saves time if one omits the large subsamples run2 and run4. This is no problem since the numbers have only illustrating character and no influence to the final result.

Definition of $\cos\theta_{\text{BY}}$

Under the hypothesis that a Y candidate belongs to a correctly reconstructed signal decay, energy momentum conservation gives

$$p_\nu^2 = (p_B - p_Y)^2 = m_B^2 - m_Y^2 - 2(E_B E_Y - |\vec{p}_B||\vec{p}_Y|\cos\theta) = 0, \tag{4.32}$$

where θ is the angle between the momentum vector of the B meson ($\vec{p}_B$) and the $D^{*0}e$ combination ($\vec{p}_Y$). Solving for $\cos\theta$ gives the definition of the variable $\cos\theta_{\text{BY}}$,

$$\cos\theta_{\text{BY}} = \frac{2E_B^* E_Y^* - m_B^2 - m_Y^2}{2|\vec{p}_B^*||\vec{p}_Y^*|}. \tag{4.33}$$

The additional stars at the energy and momentum of the B meson ($E_B^*, \vec{p}_B^*$) and the $D^{*0}e$ combination ($E_Y^*, \vec{p}_Y^*$) indicate that the variable $\cos\theta_{\text{BY}}$ is calculated with energy and momentum values taken in the $\Upsilon(4S)$ rest frame. This is necessary because E_B and $|\vec{p}_B|$ can only be calculated in this frame,

$$E_B^* = \frac{E_{\text{cms}}}{2} \quad \text{and} \tag{4.34a}$$

$$|\vec{p}_B^*| = \sqrt{\left(\frac{E_{\text{cms}}}{2}\right)^2 - m_B^2}, \tag{4.34b}$$
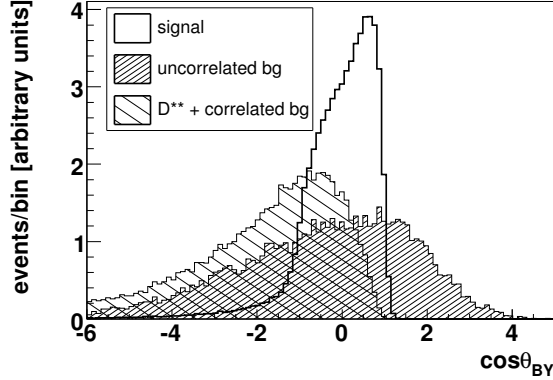
Figure 4.20: The $\cos\theta_{\mathrm{BY}}$ distributions of three different types of Y candidates are shown. The histograms are scaled to have the same area, otherwise the signal histogram would dominate the figure. The histograms are drawn for candidates passing all selection criteria listed in table 4.3. The plot clearly shows the $\cos\theta_{\mathrm{BY}}$ discrimination power between signal and background candidates.

where E_{cms} is the center-of-mass energy determined from the PEP-II collider conditions. In other frames the $\Upsilon(4S)$ resonance does not rest and thus the magnitude of the B meson momentum is variable and can not be determined. E_Y^* and $\vec{p}_Y^*$ are the reconstructed energy and momentum of the $D^{*0}e$ combination.

The calculation of $\cos\theta_{\mathrm{BY}}$ neglects the spread of the beam energies, which is of the order of $5\,\mathrm{MeV}$. A possible uncertainty in the mean of the beam energies results in an uncertainty of $|\vec{p}_B^*|$ and E_B^* and thus $\cos\theta_{\mathrm{BY}}$ has also a bias. As described in section 5.2.3.1, this effect is taken into account by an additional parameter in the final fit to the data sample.

At the end of this paragraph the discrimination power of $\cos\theta_{\mathrm{BY}}$ is illustrated. All Y candidates with correctly reconstructed D^{*0} meson and correctly identified electron track belong to one of the following three candidate classes (for more detail see table 5.1):

- If the D^{*0} and the electron of the Y candidate are matched to a decay $B^- \to D^{*0}e^-\overline{\nu}_e$, then the Y candidate belongs to the 'signal' class.

- If the electron comes from one B meson of the event and the D^{*0} meson comes from the other B meson of the event, then the Y candidate belongs to the 'uncorrelated bg' class.

- If the electron and the D^{*0} meson come from the same B meson decay but the decay was not a signal decay, then the Y candidate is assigned to the 'D^{**} bg'[15] class or to the 'correlated bg'[16] class.

The $\cos\theta_{\mathrm{BY}}$ distributions of these three types of Y candidates are compared in figure 4.20. The Y candidates belonging to the signal have a $\cos\theta_{\mathrm{BY}}$ distribution mainly occupying the allowed range between -1 and $+1$. Due to resolution effects of the detector there is a small fraction of Y

---

[15]If the true B meson decay is $B \to D^{*0}\pi\ell\nu_\ell$ or $B \to D^{**}\ell\nu_\ell$ where D^{**} is an higher excited charmed meson $(D_2^{*0}, D_1^{'0}, \dots)$ and the reconstructed D^{*0} and e are matched to the decay products of this true B meson decay, then the reconstructed Y candidate is assigned to the 'D^{**} bg' class.

[16]If the D^{*0} and the e of a Y candidate are matched to particles coming from the decay cascade of the same B meson and the Y candidate was not assigned to 'D^{**} bg', then the Y candidate is assigned to the 'correlated bg' class.
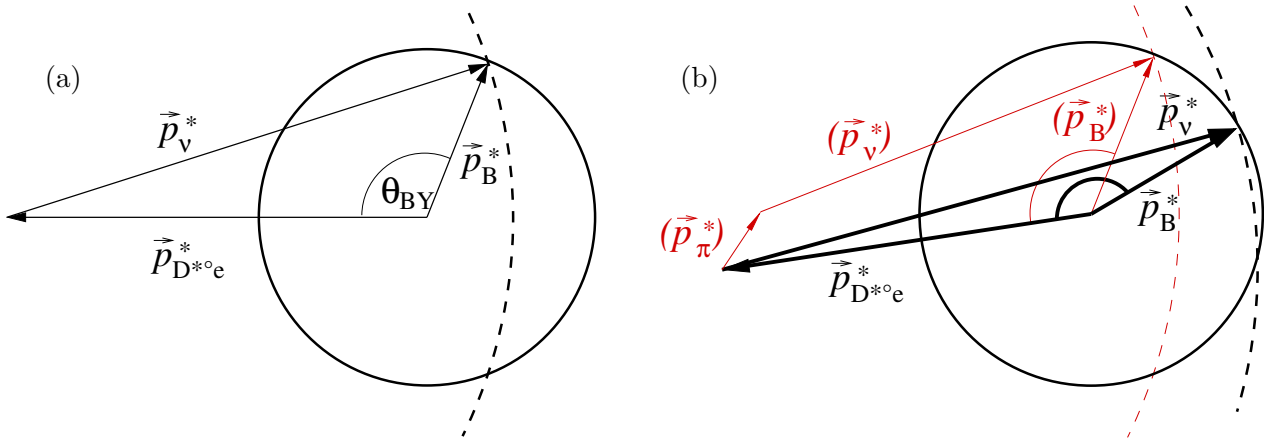
Figure 4.21: Momentum triangles of semileptonic B decays: **(a)** $B^- \to D^{*0}e^-\overline{\nu}_e$; **(b)** $B \to D^{*0}\pi e^-\overline{\nu}_e$. Consider subfigure (a): Starting from the $\Upsilon(4S)$ rest frame, the endpoints of all possible momentum vectors $\vec{p}_B^*$ of the B meson form the surface of a sphere (solid circle). The radius is given by equation 4.34b. Since the D^{*0}-e-combination is fully reconstructed one can calculate the neutrino energy, $E_\nu^* = E_B^* - E_{D^{*0}e}^*$, which is the radius of a second sphere (dashed circle). The intersection of both spheres defines the angle θ_{BY}. (The intersection is visible as two points in the sketch, but in truth it is a circle.) In subfigure (b) the true decay $B \to D^{*0}\pi e^-\overline{\nu}_e$ is reconstructed in the decay mode $B^- \to D^{*0}e^-\overline{\nu}_e$. The true momenta of the participating particles are sketched as thin red arrows. The reconstructed momenta are sketched with bold lines. Since the energy of the not reconstructed pion is assigned to the reconstructed neutrino momentum ($E_\nu^* = E_B^* - E_{D^{*0}e}^*$), the neutrino momentum is overestimated. Thus, the reconstructed variable $\cos\theta_{BY}$ is is shifted to lower values. If the reconstructed neutrino momentum gets too big then the circle lines do not cross and $\cos\theta_{BY}$ has values below -1.

signal-candidates with $\cos\theta_{BY} > +1$. The long tail below $\cos\theta_{BY} < -1$ arises from energy loss of the Y candidates, e.g. due to bremsstrahlung of the electron. Appendix A.2 contains a calculation showing why $\cos\theta_{BY}$ can have values below -1 if the energy and the momentum of the Y candidate were measured too low. This calculation can also be used to explain the allowed $\cos\theta_{BY}$ range for D^{**} bg and for correlated bg ($\cos\theta_{BY} < 1$). The calculation is illustrated in figure 4.21. Since the electron and the D^{*0} meson of Y candidates of the uncorrelated bg class come from different B mesons, a restriction of $\cos\theta_{BY}$ similar to that of the other candidate classes is not possible.
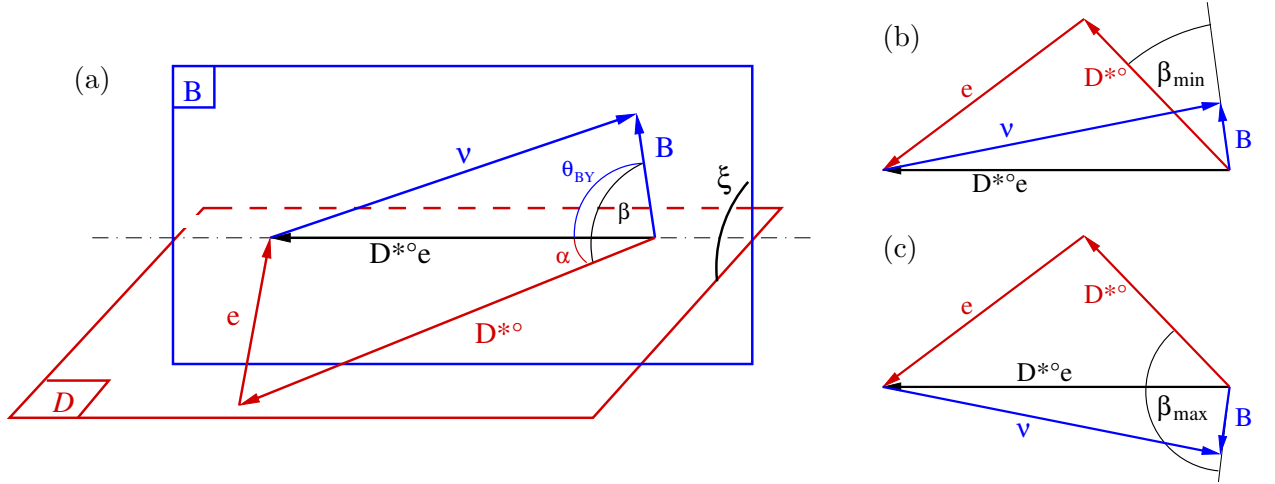
Figure 4.22: (a) Shown are the momentum vectors of various particles participating at a signal decay. Plane D is defined by particles that can be reconstructed (D^{*0}, e). Plane B is defined by the non-reconstructed particles (B, ν). Since the direction of the B meson is unknown, the angle ξ between the two planes is unknown too. Assuming $\xi = 0°$ defines $\beta_{\min}$ and is illustrated in subfigure **(b)**. Assuming the other extreme case $\xi = 180°$ defines $\beta_{\max}$ and is illustrated in subfigure **(c)**.

Definition of $\tilde{w}$

As explained in section 2.2.4, for the determination of $F(1)|V_{cb}|$ one has to take into account the shape of the w spectrum of the signal decays. However, to reconstruct w one needs to know the angle β between the momenta of the B and the D^{*0} meson because w is given by

$$w(\beta) = v_B v_{D^{*0}} = \frac{p_B p_{D^{*0}}}{m_B m_{D^{*0}}}$$
$$= \frac{\left(E_B^* E_{D^{*0}}^* - |\vec{p}_B^*|\,|\vec{p}_{D^{*0}}^*| \cos\beta\right)}{m_B m_{D^{*0}}}. \tag{4.35}$$

But since the direction of the B momentum vector is unknown, w can not be reconstructed. Because $|\vec{p}_B^*|$ has small values (compared to the other variables of equation 4.35) one could replace $\cos\beta$ by its average value, $\cos\beta = 0$, to obtain a rough estimation $\tilde{w}'$ of the true value of w,

$$\tilde{w}' = \frac{E_B E_{D^{*0}}}{m_B m_{D^{*0}}}. \tag{4.36}$$

The value of $\tilde{w}'$ is calculable from reconstructed particle properties only, but one can define a more consistent estimator $\tilde{w}$. Using information from θ_{BY} and α, where α is the angle between the D^{*0} meson and the D^{*0}-e combination, it is possible to find better limits for the unknown angle β: $\beta_{\min} = \alpha - \theta_{BY}$ and $\beta_{\max} = \alpha + \theta_{BY}$. This is illustrated in figure 4.22. Using this restriction one can define another estimator $\tilde{w}$,

$$\tilde{w} = \frac{1}{2}\left(w\left(\beta_{\min}\right) + w\left(\beta_{\max}\right)\right). \tag{4.37}$$

Using a cosine relation, this can be simplified to

$$\tilde{w} = \frac{1}{m_B m_{D^{*0}}}\left(E_B E_{D^{*0}} - |\vec{p}_B|\,|\vec{p}_{D^{*0}}| \cos\alpha \,\cos\theta_{BY}\right). \tag{4.38}$$
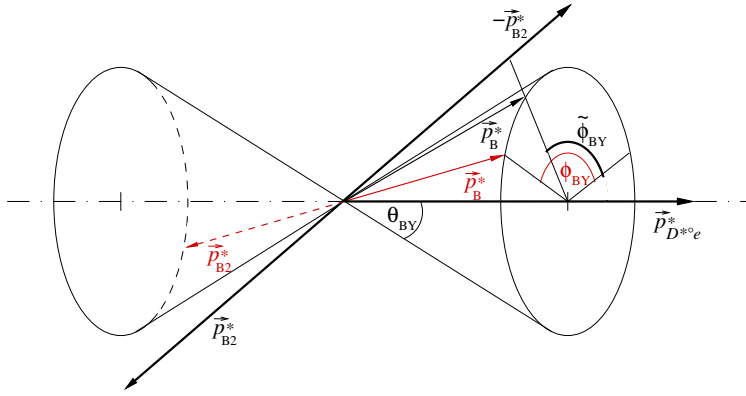
Figure 4.23: The sketch illustrates how the direction of the B meson momentum vector is obtained. The direction is needed to calculate $\tilde{w}''$. True momentum vectors and angles are drawn in red. Reconstructed momentum vectors and angles are drawn in black. For more details see text.
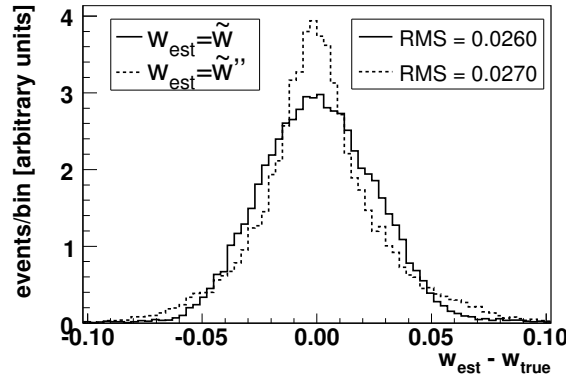
Figure 4.24: The plot shows the resolution $w_{\text{est}} - w_{\text{true}}$ for the two different estimators $\tilde{w}$ and $\tilde{w}''$. The two histograms were created from Y candidates completely correctly matched to a signal decay.

Figure 4.23 illustrates a third possibility to get a well estimated w. After the reconstruction of $\cos\theta_{\text{BY}}$ the momentum vector $\vec{p}_B^*$ of the B meson is restricted to lay on the girthed area of a cone (in the $\Upsilon(4S)$ rest frame). If one would know the direction of the second B meson of the event then one could determine an azimuthal angle ϕ_{BY} giving the direction of the hypothetic signal B meson the Y candidate belongs to. The sum of the momentum vectors of the particle candidates remaining in the event and not contributing to the Y candidate (unmatched EMC clusters with photon hypothesis, DCH tracks with PID) give an estimate for the momentum vector $\vec{p}_{B2}^*$ of the second B meson of the event. As illustrated in figure 4.23, the projection of $-\vec{p}_{B2}^*$ onto the cone area defines an estimated angle $\tilde{\phi}_{BY}$. From $\tilde{\phi}_{BY}$ and the reconstructed $\cos\theta_{\text{BY}}$ the momentum vector $\vec{p}_B^*$ is unambiguously defined. The use of this momentum vector $\vec{p}_B^*$ in equation 4.35 defines the estimator $\tilde{w}''$.

Figure 4.24 shows a comparison of the resolutions $R = \tilde{w} - w_{\text{true}}$ and $R'' = \tilde{w}'' - w_{\text{true}}$. The estimator $\tilde{w}'$ is not considered since it has a worse resolution than $\tilde{w}$ by definition. The two shown resolutions have similar distributions. Their root mean square (RMS) is about the twentieth part of the totally allowed w range, which principally allows for a successful determination of the w shape

of $B^- \rightarrow D^{*0}e^-\overline{\nu}_e$ decays. The distribution of R'' shows a sharper peak than the distribution of R, but it has also longer tails to bad resolution values. This shape is an indicator for the fact that either the $\tilde{w}''$ estimates clearly better than $\tilde{w}$ (sharper peak) or it estimates clearly worse than $\tilde{w}$ (long tails). However,

- the RMS of the R-distribution (0.0260) is slightly better than the RMS of the R''-distribution (0.0270) and

- the consideration of the entire event brings additional systematic uncertainties.

Due to these two reasons, for the rest of the analysis $\tilde{w}$ is used as estimator of w.

Chapter 5

Fit Method

5.1 Introduction

This chapter explains how the two parameters $F(1)|V_{cb}|$ and $\rho^2_{A_1}$ are extracted. The abbreviations

$$V = F(1)|V_{cb}| \qquad \text{and} \tag{5.1a}$$
$$\rho^2 = \rho^2_{A_1} \tag{5.1b}$$

are used too keep the text and the complex formulas of this chapter readable. Before the details are given the main features of the fit method are briefly summarized in the following.

First of all: For extracting V and ρ^2 there is only **one single three-dimensional fit** of weighted and corrected Monte Carlo distributions to the selected data. The three variables are: Δm, $\cos\theta_{\mathrm{BY}}$, and $\tilde{w}$. Their definition was already given, but it is rewritten later in this section (equations 5.2 to 5.4) The fit is performed directly to the candidates surviving the selection criteria described in chapter 4. It is a **binned log-likelihood fit**. In contrast to that, earlier analyses [73, 74, 75] were performed in two steps. After a division of data into $\tilde{w}$ bins their strategy was (1) Determination of the amount of signal for each $\tilde{w}$ bin (mostly by fitting Δm and $\cos\theta_{\mathrm{BY}}$ distributions) and (2) Extraction of V and ρ^2 from this $\tilde{w}$ dependent amount of signal by fitting the $\tilde{w}$ distribution. For those analyses the amount of signal in the single $\tilde{w}$ bins remains unchanged when determining V and ρ^2. The analysis described in this document performs the two steps simultaneously. So the amount of signal per $\tilde{w}$ bin and the values of V and ρ^2 are varied in one single common fit.

A second important feature of the V-ρ^2 extraction method is that the full MC simulation is varied by a **reweighting technique** presented in section 5.3. This reweighting technique changes the actually inflexible MC simulation into a flexible one depending on the parameters V and ρ^2. The reweighting uses only generator level information and nothing coming from reconstruction. The reweighting technique thus avoids uncertainties coming from the description of the w resolution function. It also avoids to determine the signal efficiency explicitly; a corrected MC signal efficiency is used automatically. Reweighting includes normalization of the MC expectation and therefore the fit determines not only ρ^2 but also V.

The third important main feature of the V-ρ^2 extraction method is the structure of the PDFs used in the fit. To model the Δm-$\cos\theta_{\mathrm{BY}}$-$\tilde{w}$ distribution of the selected MC candidates I group them into $\tilde{w}$ bins and subclasses whose **distributions factorize in $\boldsymbol{\Delta m}$ and $\cos\boldsymbol{\theta_{\mathrm{BY}}}$**.

The observables Δm, $\cos\theta_{\mathrm{BY}}$, and $\tilde{w}$ are defined by the following equations:

$$\Delta m = m_{\mathrm{K}\pi\pi^0} - m_{\mathrm{K}\pi} \tag{5.2}$$

$$\cos\theta_{\mathrm{BY}} = \frac{2E_{\mathrm{B}}^* E_{\mathrm{Y}}^* - m_{\mathrm{B}}^2 - m_{\mathrm{Y}}^2}{2|\vec{p}_{\mathrm{B}}^*||\vec{p}_{\mathrm{Y}}^*|} \tag{5.3}$$

$$\tilde{w} = \frac{1}{m_{\mathrm{D}^{*0}}\, m_{\mathrm{B}}} \left(E_{\mathrm{B}}^*\, E_{\mathrm{D}^{*0}}^* - |\vec{p}_{\mathrm{B}}^*||\vec{p}_{\mathrm{D}^{*0}}^*|x \right) \tag{5.4}$$

$$x = \cos\theta_{Y\, D^{*0}}\, \cos\theta_{\mathrm{BY}}$$

- The variable Δm is just the mass difference between the D^{*0} candidate and the D^0 candidate.

- For correctly reconstructed signal candidates the variable $\cos\theta_{\mathrm{BY}}$ gives the cosine of the angle between the momenta of the B meson and the Y. Both momenta and energies are taken in the $\Upsilon(4S)$ rest system.

- The variable $\tilde{w}$ is an estimator for the relativistic boost w of the D^{*0} in the B meson rest frame. The D^{*0} boost w can also be written as the product of the four velocities of B and D^{*0} meson. Because of that, x from equation 5.4 should be equal to $\cos\theta_{BD^{*0}}$. But the B meson flight direction is unknown and therefore $\cos\theta_{BD^{*0}}$ is not determinable. In principle one could assume the mean value of $\cos\theta_{BD^{*0}}$. But the estimator given by x of equation 5.4 is more efficient [75].

The task of the first two fit variables (Δm and $\cos\theta_{\mathrm{BY}}$) is to enable the fit to determine the number of correctly reconstructed signal candidates very precisely (see decay chain 4.1). Thereby, Δm determines the number of events containing a correctly reconstructed D^{*0} candidate. The signal fraction within these events is determined using the variable $\cos\theta_{\mathrm{BY}}$. The third fit variable ($\tilde{w}$) is not good for signal-background-separation. The task of $\tilde{w}$ is to enable the fit to measure the signal's w-shape-parameter $\rho_{A_1}^2$. As has been emphasized in section 2.2.4, this is important for the determination of $F(1)|V_{cb}|$ because it defines the form factor extrapolation to the zero-recoil scenario where the meson system is minimally disturbed.

5.2 The Fit Function

At the beginning of this section a few comments are given concerning the notation used. Most of the equations of this section apply to the ith $\tilde{w}$ bin. Index name i is exclusively reserved for the $\tilde{w}$ bin number of mathematical objects. Similarly the index name j is exclusively reserved for the code number of the candidate class. The third convention is, that all functions X with a hat ($\hat{X}$) are PDFs[1]. As all PDFs, $\hat{X}$ is normalized to the corresponding subrange of the later defined fit range. A fourth point concerns the meaning of the indices 'BMC', 'RMC' and 'Exp'. Most of the functions and numbers of this chapter are assigned

- either to the *BABAR* MC simulation (BMC),

- or to the reweighted *BABAR* MC simulation (RMC),

- or to the expectations for the data (Exp).

---

[1]PDF is an abbreviation for probability density function.

These functions and numbers are indexed accordingly with either BMC, RMC, or Exp, respectively.

After these comments on the notation let me summarize the general purpose of this section. This section should answer the question: How is the function built that is fitted to the data? The roadmap for the extraction of the fit function is divided into three parts.

1. The selected BMC events are reweighted and used to produce continuous distribution functions. This production is done by fits of functions f_{RMC} to the RMC events.

2. The RMC functions f_{RMC} are transformed to expectation functions f_{Exp}. On the one hand in the f_{Exp} functions all parameters are fixed which were still floating in the f_{RMC} function extraction. On the other hand the functions f_{Exp} obtain additional correction parameters by taking into account characteristic and significant differences between data and simulation. The normalization of the expectation functions is obtained by summing up the weights of the MC events.

3. At the end all the functions f_{Exp} are put together to form the total expectation function for data. In this step further parameters are introduced and at the end there is a function that can be fitted to the data.

5.2.1 General Ansatz in the $\Delta m \cos \theta_{\text{BY}}$ Plane

5.2.1.1 Product Ansatz — the Definition Criteria for the Candidate Classes

The function $F_i^s (\Delta m, \cos \theta_{\text{BY}})$ describes the $\Delta m \cos \theta_{\text{BY}}$ distribution of all selected candidates for the ith $\tilde{w}$ bin. It can be written as

$$F_i^s (\Delta m, \cos \theta_{\text{BY}}) = N_i^s \cdot \hat{F}_i^s (\Delta m, \cos \theta_{\text{BY}}) \tag{5.5}$$

$$\begin{aligned} i &= 1, \ldots, 10 &\quad (\tilde{w} \text{ bin}) \\ s &= \text{BMC, RMC, Exp} \end{aligned}$$

where N_i^s is the number of candidates in the ith $\tilde{w}$ bin for the BMC, the RMC or the expectation on data. The allowed range of index i anticipates that the used $\tilde{w}$ binning comprises ten bins (see section 5.4). $\hat{F}_i^s (\Delta m, \cos \theta_{\text{BY}})$ is the PDF belonging to the ith $\tilde{w}$ bin. The function $F_i^s (\Delta m, \cos \theta_{\text{BY}})$ is a sum of 24 candidate classes which the sample is divided in,

$$F_i^s (\Delta m, \cos \theta_{\text{BY}}) = \sum_{j=1}^{24} N_{ij}^s \ \hat{P}_{ij}^s (\Delta m, \cos \theta_{\text{BY}}) . \tag{5.6}$$

$\hat{P}_{ij}^s (\Delta m, \cos \theta_{\text{BY}})$ and N_{ij}^s are the two-dimensional PDF and the number of candidates for the jth candidate class in the ith $\tilde{w}$ bin. Of course the N_{ij}^s have to sum up to N_i^s,

$$N_i^s = \sum_{j=1}^{24} N_{ij}^s \qquad s = \text{BMC, RMC, Exp}. \tag{5.7}$$

It would be very convenient and efficient for the calculation of function values of various $(\Delta m, \cos \theta_{\text{BY}})$ pairs during the fit if $\hat{P}_{ij}^s (\Delta m, \cos \theta_{\text{BY}})$ could be a product PDF

$$\hat{P}_{ij}^s (\Delta m, \cos \theta_{\text{BY}}) = \hat{D}_{ij}^s (\Delta m) \ \cdot \ \hat{C}_{ij}^s (\cos \theta_{\text{BY}}) \tag{5.8}$$

made of

$\hat{D}^s_{ij}\,(\Delta m)$, a PDF describing the Δm distribution of the j th candidate class in the i th $\tilde{w}$ bin and

$\hat{C}^s_{ij}\,(\cos\theta_{\mathrm{BY}})$, a PDF describing the $\cos\theta_{\mathrm{BY}}$ distribution of the j th candidate class in the i th $\tilde{w}$ bin.

At this point one should emphasize that the product structure in the $\Delta m \cos\theta_{\mathrm{BY}}$ distribution is the very basic idea of the final fit!

Now follows the explanation why the product ansatz is a good and reasonable ansatz. On the one hand Δm has a distribution strongly depending on the properties of the $\gamma\gamma$ pair. Because Δm is the distribution of the difference $\Delta m = m_{K\pi\gamma\gamma} - m_{K\pi}$ the influence of the tracks of $K\pi$ is very small but the influence of the $\gamma\gamma$ pair is very high. That is in spite of the fact that K and π are very high energetic compared to the $\gamma\gamma$ pair. On the other hand $\cos\theta_{\mathrm{BY}}$ has a distribution only weakly depending on the properties of $\gamma\gamma$ pair but strongly depending on the properties of e-, K- and π-tracks. That is because $\cos\theta_{\mathrm{BY}}$ depends directly on the kinematic properties of the Y $(= eK\pi\gamma\gamma)$ and not on differences between kinematic properties of Y candidate and the Y subcandidate $eK\pi$ (see equation 5.3). If you change the low energy of the two γs within a reasonable range then the change in the variables E_Y and $|\vec{p}_Y|$, entering $\cos\theta_{\mathrm{BY}}$, is marginal.[2] To sum up: The Δm distributions are governed by momentum and energy of the $\gamma\gamma$ pairs and $\cos\theta_{\mathrm{BY}}$ distributions are governed by momentum and energy of e-, K- and π-tracks. What one has now still to take care of is that distributions depend on the following two questions:

Q1: What are the true decays in the events of selected candidates?

Q2: How well are the various particles reconstructed (totally, partially, . . .)?

If one divides the sample of selected candidates into classes depending on the candidate-specific answer to these two questions then one ends up with the candidate classes listed in table 5.1. For these candidate classes the PDF with the product ansatz 5.8 models the two dimensional distributions with a high quality. This is shown in the quality plots of appendix B.2.

5.2.1.2 The Normalization of the Candidate Classes

The number of candidates in the j th class and the i th $\tilde{w}$ bin for the BMC, N^{BMC}_{ij}, is related to the same number for the RMC, N^{RMC}_{ij}, and to the expectation of this number in data, N^{Exp}_{ij}, by

$$N^s_{ij} \;\; = \;\; N^{\mathrm{BMC}}_{ij}\,W_{ij} \tag{5.9}$$
$$j = 1,\ldots,22 \qquad s = \mathrm{RMC}, \mathrm{Exp}.$$

The formula is only valid for $B\bar{B}$ candidate classes. The expectations for numbers of $c\bar{c}$-event candidates in the data sample, $N^{\mathrm{Exp}}_{i\,23}$ and $N^{\mathrm{Exp}}_{i\,24}$, are defined by equation 5.20. The weights W_{ij}

---

[2]There is a weak correlation between Δm and $\cos\theta_{\mathrm{BY}}$. This correlation for each of the 22 candidate classes defined in table 5.1 is listed in the appendix in table B.1.

Table 5.1: This table contains the definition of the candidate classes. Third and fourth column correspond to the questions **Q1** and **Q2** on page 71. The classes 1 to 4 contain candidates with a correctly reconstructed D^{*0} and an e candidate belonging to a true e. The classes 5 to 14 contain candidates populating mainly the region $|\cos\theta_{BY}| < 1.0$. Their e- and D^0-candidates belong to a true electron and a true D^0 meson. The candidates of the classes 17 to 22 are candidates with a wrongly reconstructed D^{*0} which are not sorted into other $B\bar{B}$ classes. There are also two candidate classes for the $c\bar{c}$ background. Signal means $B^- \to D^{*0}e^-\bar{\nu}_e; D^{*0} \to D^0(K\pi)\pi^0(\gamma\gamma)$.

j	candidate class	true decay	reconstruction
1	Sig	signal	Complete signal is correctly reconstructed.
2	$D^{**}e\nu$ (1)	$B \to D^{*0}e\nu\pi$	D^{*0} and e are correctly reconstructed.
3	Correlated	A D^{*0} and an e come from the same B meson.	D^{*0} and e are correctly reconstructed.
4	Uncorrelated	A D^{*0} and an e come from two different B mesons.	D^{*0} and e are correctly reconstructed.
5	SemiSig (1)	signal	Like 1, but the reconstructed γ_2 candidate[a] does not belong to the true γ_2.
6	SemiSig (2)	signal	Like 1, but the reconstructed γ_1 candidate[a] does not belong to the true γ_1.
7	SemiSig (3)	signal	Like 1, but both reconstructed γs do not belong to the true γs.
8	SemiSig (4)	signal	All signal decays not sorted to classes 1, 5, 6, or 7.
9	SigLike (1)	like signal but $\pi^0 \not\to \gamma\gamma$	D^0 and e are correctly reconstructed.
10	SigLike (2)	like signal but $D^{*0} \to D^0\gamma$	D^0, e and γ are correctly reconstructed.
11	SigLike (3)	like signal but $D^{*0} \to D^0\gamma$	D^0 and e are correctly reconstructed.
12	$D^{*\pm}e\nu$	$\bar{B}^0 \to D^{*+}e^-\bar{\nu};$ $D^{*+} \to D^0\pi^+$	D^0 and e are correctly reconstructed.
13	$D^0e\nu(1)$	$B \to D^0e\nu$	D^0 and e are correctly reconstructed.
14	$D^0e\nu(2)$	$B \to D^0e\nu$	D^0 and/or e are not correctly reconstructed.
15	$D^0\pi e\nu$	$B \to D^0e\nu\pi$	D^0 and e are correctly reconstructed.
16	$D^{**}e\nu(2)$	$B \to D^*e\nu\pi;$ $D^* \to D^0\pi/D^0\gamma$	D^0 and e are correctly reconstructed.
17	CombD^{*0} (1)		D^0 is correctly reconstructed. D^0 and e [b] come from same B meson.
18	CombD^{*0} (2)		D^0 and π^0 are correctly reconstructed. D^0 and e [b] come from different B mesons.
19	CombD^{*0} (3)		D^0 and π^0 are correctly and wrongly reconstructed, respectively. D^0 and e [b] come from different B mesons.
20	CombD^{*0} (4)		D^0 is wrongly reconstructed. K, π and e [b] come from same B meson.
21	CombD^{*0} (5)		D^0 and π^0 are wrongly and correctly reconstructed, respectively. K, π and e [b] come from two different B mesons.
22	CombD^{*0} (6)		D^0 and π^0 are wrongly reconstructed. K, π and e [b] come from two different B mesons.
23	$c\bar{c}$(peak)	$e^+e^- \to c\bar{c}$ event with a D^{*0}	D^{*0} is correctly reconstructed.
24	$c\bar{c}$(flat)	$e^+e^- \to c\bar{c}$ event	D^{*0} is not correctly reconstructed.

---

[a] The energy of γ_1 is greater than the energy of γ_2, $E_{\gamma_1} > E_{\gamma_2}$, w.r.t. the laboratory frame (see page 34).

[b] The e track does not need to spring from a true e.

have the structure

$$W_{ij} \quad = \quad \frac{1}{N_{ij}^{\mathrm{BMC}}} \sum_{k=1}^{N_{ij}^{\mathrm{BMC}}} W_{ijk} \tag{5.10}$$

$$W_{ijk} \quad = \quad W_{ijk}^{\mathrm{Phy}} \ \cdot \ W^{B\bar{B},\mathrm{run}(k)} \ \cdot \ W_{ijk}^{\mathrm{Cor}} \tag{5.11}$$

$$W^{B\bar{B},r} \quad = \quad \frac{N^{B\bar{B},\mathrm{Data},r}}{N^{B\bar{B},\mathrm{BMC},r}} \qquad\quad r = 1, 2, 3, 4 \tag{5.12}$$

$$W_{ijk}^{\mathrm{Cor}} \quad = \quad W_{ijk}^{\mathrm{Pid}} \ \cdot \ W_{ijk}^{\mathrm{Track}} \ \cdot \ W_{ijk}^{\pi^0} \quad . \tag{5.13}$$

The index k codes a single candidate in the jth candidate class and runs up from the first candidate ($k = 1$) to the last candidate ($k = N_{ij}^{\mathrm{BMC}}$) of this class – the weights are given on a candidate-by-candidate basis. The function run(k) gives the run period of candidate k. So run(k) returns 1, 2, 3, or 4. $N^{B\bar{B},\mathrm{Data},r}$ is the number of all analyzed $B\bar{B}$ pairs in the rth run of the data sample as listed in table 4.1. $N^{B\bar{B},\mathrm{BMC},r}$ is the number of all used $B\bar{B}$ pairs in the rth run of the BMC as listed in the same table. The three factors W_{ijk}^{Pid}, W_{ijk}^{Track} and $W_{ijk}^{\pi^0}$ are PID efficiency correcting factor obtained from PID weighting technique [66], track efficiency correcting factor [65] and π^0 efficiency correcting factor [61] for the kth candidate of the jth candidate class, respectively. These three factors and the efficiencies corrected by them are intensively discussed in section 4.4. The connection to the correction factors R_x ($x = e, K, \pi, \pi^0$) defined in section 4.4 is given by

$$W^{\mathrm{Pid}} = R_e^{\mathrm{Pid}} R_K^{\mathrm{Pid}} \qquad\quad W^{\mathrm{Track}} = R_e^{\mathrm{Track}} R_K^{\mathrm{Track}} R_\pi^{\mathrm{Track}} \qquad\quad W^{\pi^0} = R_{\pi^0} \quad , \tag{5.14}$$

where the index set ijk has been omitted for a better readability. For the weight W_{ijk}^{Phy} one has to differentiate between four different types

$$W_{ijk}^{\mathrm{Phy}} = \begin{cases} W_{ijk}^{\mathrm{Phy,Sig}} & l = 1, 5 - 11 \\ \frac{\tau_{B^0,\mathrm{BMC}}}{\tau_{B^+,\mathrm{BMC}}} W_{ijk}^{\mathrm{Phy,Sig}} & l = 12 \\ W_{ijk}^{\mathrm{Phy,D^0 e\nu}} & l = 13, 14 \\ 1 & \text{otherwise} \end{cases} \tag{5.15}$$

The weights $W_{ijk}^{\mathrm{Phy,Sig}}$ and $W_{ijk}^{\mathrm{Phy,D^0 e\nu}}$ are defined by equations 5.74 and 5.85 in section 5.3 describing the reweighting of a candidate reconstructed in a $B^- \to D^{*0} e^- \bar{\nu}_e$ or an $B^- \to D^0 e^- \bar{\nu}_e$ event.

Now follows the explanation to the factor $\frac{\tau_{B^0,\mathrm{BMC}}}{\tau_{B^+,\mathrm{BMC}}}$ in equation 5.15. If one assumes that the decays $\bar{B}^0 \to D^{*+} e^- \bar{\nu}_e$ and $B^- \to D^{*0} e^- \bar{\nu}_e$ have the same decay dynamics then one can write

$$\Gamma\left(\bar{B}^0 \to D^{*+} e^- \bar{\nu}_e\right) \quad = \quad \Gamma\left(B^- \to D^{*0} e^- \bar{\nu}_e\right) \qquad\qquad \text{and} \tag{5.16}$$

$$\frac{\mathrm{d}\Gamma}{\mathrm{d}w}\left(\bar{B}^0 \to D^{*+} e^- \bar{\nu}_e\right) \quad = \quad \frac{\mathrm{d}\Gamma}{\mathrm{d}w}\left(B^- \to D^{*0} e^- \bar{\nu}_e\right) \tag{5.17}$$

and the equations are true up to corrections arising from the approximations $m_{\pi^+} \approx m_{\pi^0}$ and $m_{D^{*+}} \approx m_{D^{*0}}$. In the BMC the following input is given

$$\begin{aligned} \mathcal{B}\left(\bar{B}^0 \to D^{*+} e^- \bar{\nu}_e\right)_{\mathrm{BMC}} &= 0.056, \\ \mathcal{B}\left(B^- \to D^{*0} e^- \bar{\nu}_e\right)_{\mathrm{BMC}} &= 0.056, \\ \tau_{B^+,\mathrm{BMC}} &= 0.502 \ \mathrm{mm}/c, \ \text{and} \\ \tau_{B^0,\mathrm{BMC}} &= 0.462 \ \mathrm{mm}/c \quad . \end{aligned} \tag{5.18}$$

That leads to the deviation

$$\Gamma\left(\bar{B}^0 \to D^{*+}e^-\bar{\nu}_e\right)_{\text{BMC}} = \frac{0.502}{0.462}\,\Gamma\left(B^- \to D^{*0}e^-\bar{\nu}_e\right)_{\text{BMC}} \tag{5.19}$$

of the two decay widths within the BMC. The factor $\frac{\tau_{B^0,\text{BMC}}}{\tau_{B^+,\text{BMC}}}$ in equation 5.15 corrects the BMC in a sense that the ratios among some of the candidate classes of RMC are based on the assumption 5.16.

The expected number of candidates for $B\bar{B}$-event candidate-classes in the data sample, N_{ij}^{Exp}, is given at the beginning of this section in formula 5.9. The expected number of $c\bar{c}$-event candidates in the on-peak data sample is calculated by scaling and correcting the number of selected candidates in the off-peak data,

$$N_{ij}^{\text{Exp}} = \frac{N_{ij}^{\text{RMC}}}{N_{i\,23}^{\text{RMC}} + N_{i\,24}^{\text{RMC}}}\;\frac{\sigma^{\text{on}}}{\sigma^{\text{off}}}\sum_{r=1}^{4} N_i^{c\bar{c}\,\text{off},r}\frac{\mathcal{L}^{\text{on},r}}{\mathcal{L}^{\text{off},r}} \tag{5.20}$$

$$j = 23, 24.$$

The first term divides the expected number of $c\bar{c}$-event candidates into a Δm peaking part ($j = 23$) and a Δm-flat part ($j = 24$). The sum term weights the number of selected candidates in the off-peak data sample of run r, $N_i^{c\bar{c}\,\text{off},r}$, with a run dependent luminosity ratio $\mathcal{L}^{\text{on},r}/\mathcal{L}^{\text{off},r}$. $\mathcal{L}^{\text{on},r}$ and $\mathcal{L}^{\text{off},r}$ are the on-peak luminosity and the off-peak luminosity of run r. The term $\sigma^{\text{on}}/\sigma^{\text{off}}$ performs an energy correction between on-peak data and off-peak data. The used values of the cross sections of $e^+e^- \to c\bar{c}$ are [14]

$$\begin{aligned} \sigma^{\text{on}} &= 1.30\,\text{nb} \qquad \text{and} \\ \sigma^{\text{off}} &= 1.31\,\text{nb}. \end{aligned} \tag{5.21}$$

5.2.2   Extraction of Δm PDFs and $\cos\theta_{\text{BY}}$ PDFs for the BMC and for the RMC

In this section the extraction of $\hat{D}_{ij}^{\text{RMC}}(\Delta m)$ and $\hat{C}_{ij}^{\text{RMC}}(\cos\theta_{\text{BY}})$ is described. There is one subsection for the PDFs of flat Δm distributions, one subsection for the PDFs of peaking Δm distributions and one subsection for the PDFs of $\cos\theta_{\text{BY}}$ distributions.

5.2.2.1 Δm PDFs for Candidate Classes with correctly reconstructed D^{*0} Candidates

In this section only candidate classes having correctly reconstructed D^{*0} candidates are regarded. For these candidate classes the PDF $\hat{D}_{ij}^{\text{RMC}}(\Delta m)$ is one and the same function, which peaks in Δm. This function is called $\hat{D}_i^{\text{peak RMC}}(\Delta m)$,

$$\hat{D}_{ij}^{\text{RMC}}(\Delta m) = \begin{cases} \hat{D}_i^{\text{peak RMC}}(\Delta m) & j = 1, 2, 3, 4, 23 \\ \hat{D}_{ij}^{\text{flat RMC}}(\Delta m) & \text{otherwise} \end{cases} \tag{5.22}$$

What is the parametrization of $\hat{D}_i^{\text{peak RMC}}(\Delta m)$? The shape of the peaking Δm distribution is asymmetric and has a tail to values bigger than the maximum. The parametrization of $\hat{D}_i^{\text{peak RMC}}(\Delta m)$ uses a sum of six half Gaussians with one common mean parameter[3] and individual widths. Three

---

[3]This 'mean parameter' gives the maximum but not the mean of the parametrization, as one could assume from the name.

of the half Gaussians describe the distribution for Δm values smaller than the mean parameter, the other three Gaussians describe the distribution for Δm values bigger than the mean parameter. There are six fraction parameters but only four of them are independent. The PDF $\hat{D}_i^{\text{peak RMC}}\left(\Delta m | \ldots\right)$ is given by

$$
\begin{aligned}
&\hat{D}_i^{\text{peak RMC}}\left(\Delta m |\, \Delta\mu_i, \sigma_i, \vec{f}_i^{\Delta m\, \text{p}}, \vec{S}_i^{\Delta m\, \text{p}}\right) \\
&= \begin{cases} N_i^{\text{left}} \;\; \sum\limits_{t=1}^{3} f_{i\,t}^{\Delta m\, \text{p}}\; G\left(\Delta m | \mu^{\text{MCtr}} - \Delta\mu_i\,,\, S_{it}^{\Delta m\, \text{p}} \cdot \sigma_i\right) & \text{for } \Delta m < \mu^{\text{MCtr}} - \Delta\mu_i \\[2mm] N_i^{\text{right}} \;\; \sum\limits_{t=4}^{6} f_{i\,t}^{\Delta m\, \text{p}}\; G\left(\Delta m | \mu^{\text{MCtr}} - \Delta\mu_i\,,\, S_{it}^{\Delta m\, \text{p}} \cdot \sigma_i\right) & \text{for } \Delta m \geq \mu^{\text{MCtr}} - \Delta\mu_i \end{cases}
\end{aligned}
\tag{5.23}
$$

with

$$
G\left(\Delta m | \mu, \sigma\right) \;\;=\;\; \frac{1}{\sqrt{2\pi}\sigma}\; e^{-\frac{(\Delta m - \mu)^2}{2\,\sigma^2}}, \tag{5.24}
$$

$$
\vec{f}_i^{\Delta m\, \text{p}} \;\;=\;\; \left(f_{i1}^{\Delta m\, \text{p}}, \ldots, f_{i6}^{\Delta m\, \text{p}}\right), \tag{5.25}
$$

$$
\vec{S}_i^{\Delta m\, \text{p}} \;\;=\;\; \left(S_{i1}^{\Delta m\, \text{p}}, \ldots, S_{i6}^{\Delta m\, \text{p}}\right) \;\; \text{and} \tag{5.26}
$$

$$
\mu^{\text{MCtr}} \;\;=\;\; m_{D^{*0}}^{\text{MCtr}} - m_{D^0}^{\text{MCtr}} = 0.14212\,\text{GeV}/c^2. \tag{5.27}
$$

The value of μ^{MCtr} is the true mass difference between the D^{*0} meson and the D^0 meson as implemented in the MC generator [46]. $\Delta\mu_i$ and σ_i are parameters for position and width of the Δm peak. To make the formulas and text better readable the index 'RMC' is omitted at the symbols $\Delta\mu_i$, σ_i, $\vec{f}_i^{\Delta m\, \text{p}}$, $\vec{S}_i^{\Delta m\, \text{p}}$, N_i^{left} and N_i^{right} within this section. The fractions $f_{i\,t}^{\Delta m\, \text{p}}$ $(t = 1, \ldots, 6)$ are only allowed to have values between 0 and 1. Not all of them are free parameters. The values of $f_{i3}^{\Delta m\, \text{p}}$ and $f_{i6}^{\Delta m\, \text{p}}$ are functions of the other components,

$$
\begin{aligned}
f_{i3}^{\Delta m\, \text{p}} &\;\;=\;\; 1 - (f_{i1}^{\Delta m\, \text{p}} + f_{i2}^{\Delta m\, \text{p}}) \quad \text{and} \\
f_{i6}^{\Delta m\, \text{p}} &\;\;=\;\; 1 - (f_{i4}^{\Delta m\, \text{p}} + f_{i5}^{\Delta m\, \text{p}}) \quad .
\end{aligned}
\tag{5.28}
$$

Also the scaler vector for the individual widths of the Gaussians, $\vec{S}_i^{\Delta m\, \text{p}}$, hasn't six degrees of freedom. Its first component is set to one,

$$
S_{i1}^{\Delta m\, \text{p}} = 1, \tag{5.29}
$$

to give a meaning to σ_i. The variables N_i^{left} and N_i^{right} are allowed to depend on all parameters of $\hat{D}_i^{\text{peak RMC}}$. Their values guarantee two things:

- $\hat{D}_i^{\text{peak RMC}}$ is continuous at $\Delta m = \mu^{\text{MCtr}} - \Delta\mu_i$.

- $\hat{D}_i^{\text{peak RMC}}$ is normalized to one over the fit range discussed in a later section.

To extract the parameters of $\hat{D}_i^{\text{peak RMC}}$ the function

$$
D_i^{\text{peak RMC}}\left(\Delta m\right) = N_i^{\Delta m\, \text{p RMC}}\; \hat{D}_i^{\text{peak RMC}}\left(\Delta m |\, \Delta\mu_i, \sigma_i, \vec{f}_i^{\Delta m\, \text{p}}, \vec{S}_i^{\Delta m\, \text{p}}\right) \tag{5.30}
$$
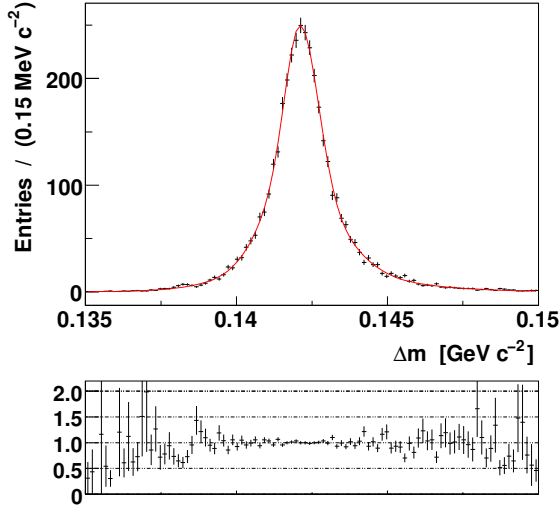
Figure 5.1: The upper plot shows the Δm distribution of the candidates with correctly reconstructed D^{*0} meson for the sixth $\tilde{w}$ bin. The function $D_6^{\text{peak RMC}}(\Delta m)$ (red line) defined in equation 5.30 has been fitted to this distribution with $\chi^2/n.d.f. = 107.4/88$. The bin-by-bin ratios between the histogram and the fitted function are shown in the lower plot.
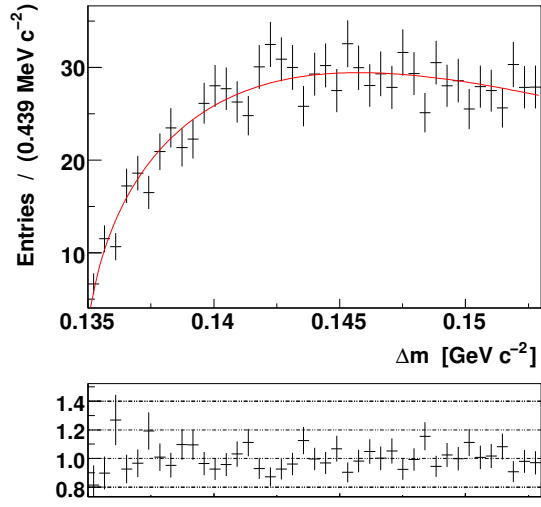
Figure 5.2: The upper plot shows the Δm distribution of the candidate class 'SemiSig(2)' ($j = 6$) for the sixth $\tilde{w}$ bin. The function $D_{66}^{\text{flat RMC}}(\Delta m)$ (red line) defined in equation 5.34 has been fitted to this distribution with $\chi^2/n.d.f. = 34.1/39$. The bin-by-bin ratios between the histogram and the fitted function are shown in the lower plot.

is fitted to the sum of the histogram $h_i^{\Delta m\,\text{p}}$. $h_i^{\Delta m\,\text{p}}$ is filled with the Δm values of RMC candidates containing correctly reconstructed D^{*0} mesons (candidate class =1, 2, 3, 4 and 23). $N_i^{\Delta m\,\text{p\,RMC}}$ is not free but a fixed number within this fit. It is the sum of the contributing candidate classes,

$$N_i^{\Delta m\,\text{p\,RMC}} = \sum_{j=1,2,3,4,23} N_{ij}^{\text{RMC}}, \tag{5.31}$$

and is equal to the integral of the fitted histogram $h_i^{\Delta m\,\text{p}}$. As an example, figure 5.1 shows the fitted function $D_6^{\text{peak RMC}}(\Delta m)$ overlayed to the histogram $h_6^{\Delta m\,\text{p}}$. Plots of all fits ($i = 1, \ldots, 10$) can be seen in [40].

5.2.2.2 Δm PDFs for Candidate Classes with wrongly reconstructed D^{*0} Candidates

This section treats the extraction of $\hat{D}_{ij}^{\text{flat RMC}}(\Delta m)$ for candidate classes containing no correctly reconstructed D^{*0} meson ($j = 5, \ldots, 22, 24$). The shape of these Δm distributions is parametrized by the threshold PDF

$$\hat{D}_{ij}^{\text{flat RMC}}(\Delta m | a_{ij}, c_{ij}) = \begin{cases} N_{ij} \cdot (\Delta m - m_{\pi^0})^{a_{ij}} \cdot e^{-c_{ij}(\Delta m - m_{\pi^0})} & \text{for } \Delta m \geq m_{\pi^0} \\ 0 & \text{for } \Delta m < m_{\pi^0} \end{cases} \tag{5.32}$$

as already mentioned in equation 5.22. (Like in the previous section the index 'RMC' is omitted for better readability. 'RMC' is omitted whenever a_{ij} and c_{ij} are used within this section.) For Δm

values above the threshold m_{π^0} the PDF is a product of a power law factor and an exponential law factor where each factor gets one parameter. These are a_{ij} and c_{ij}, respectively. N_{ij} normalizes the function in the desired Δm range to one. The threshold parameter m_{π^0} is set to

$$m_{\pi^0} = 0.13495\,\mathrm{GeV}/c^2. \tag{5.33}$$

That is because during the candidate reconstruction the mass of the $\gamma\gamma$ pair has been constrained to that value. To extract the parameters a_{ij} and c_{ij} for each candidate class and each $\tilde{w}$ bin a fit of the function

$$D_{ij}^{\mathrm{flat\,RMC}}(\Delta m) = N_{ij}^{\mathrm{RMC}}\ \hat{D}_{ij}^{\mathrm{flat\,RMC}}\left(\Delta m | a_{ij}, c_{ij}\right) \tag{5.34}$$

is performed on the histogram $h_{ij}^{\Delta m}$. $h_{ij}^{\Delta m}$ is filled with the Δm values of reweighted MC candidates (RMC) belonging to the ith $\tilde{w}$ bin and the jth candidate class. The fit has two free parameters (a_{ij} and c_{ij}). N_{ij}^{RMC} is a fixed number in this fit and is equal to the integral of the fitted histogram. As an example, figure 5.2 shows the Δm distribution of the 'SemiSig(1)' candidates ($j = 6$) of the sixth $\tilde{w}$ bin together with the fitted function $D_{66}^{\mathrm{flat\,RMC}}(\Delta m)$. Plots of all other fits ($i = 1, \ldots, 10$; $j = 1, \ldots, 22, 24$) can be seen in [40].

5.2.2.3 $\cos\theta_{\mathrm{BY}}$ PDFs

This section describes the generation of the $\cos\theta_{\mathrm{BY}}$ PDFs $\hat{C}_{ij}^{\mathrm{RMC}}$. (The index 'RMC' is suppressed at all functions and parameters in the rest of this section.) Firstly, a KEYS function[4] [79] is constructed for each candidate class. from the MC ntuple containing the $\cos\theta_{\mathrm{BY}}$ values of the corresponding candidate class. When constructing the KEYS function (RMC) for the jth candidate class the kth candidate of the class gets the weight W_{ijk} as defined in equation 5.11. After a normalization of the so constructed KEYS function one gets the PDF $\hat{C}_{ij}^{*}\left(\cos\theta_{\mathrm{BY}}\right)$. For the $\cos\theta_{\mathrm{BY}}$ peaking candidate classes

- Sig,
- $D^{**}e\nu\,(1)$,
- SemiSig (1),
- SemiSig (2),
- SemiSig (3),

- SigLike (2),
- SigLike (3),
- $\mathrm{D}^{*\pm}e\nu$,
- $D^{0}e\nu(1)$ and
- $D^{**}e\nu(2)$

the $\cos\theta_{\mathrm{BY}}$ distribution shows a steep edge at $\cos\theta_{\mathrm{BY}} \approx 1$. But the KEYS function does not satisfactorily model this edge. Due to the construction rules of a KEYS function steep edges of the true distribution are washed out. (Compare dashed line and histogram in figure 5.3.) That means for the $\cos\theta_{\mathrm{BY}}$ peaking classes one has to correct the function $\hat{C}_{ij}^{*}\left(\cos\theta_{\mathrm{BY}}\right)$:

$$\hat{C}_{ij}^{*}\left(\cos\theta_{\mathrm{BY}}\right) \mapsto \hat{C}_{ij}\left(\cos\theta_{\mathrm{BY}} | b_{ij}, r_{ij}\right) = \begin{cases} \hat{C}_{ij}^{\mathrm{Cor}}\left(\cos\theta_{\mathrm{BY}} | b_{ij}, r_{ij}\right) & \text{for } j = 1, 2, 5-7, 10-13, 16 \\ \hat{C}_{ij}^{*}\left(\cos\theta_{\mathrm{BY}}\right) & \text{otherwise.} \end{cases}$$

$$\tag{5.35}$$

---

[4]KEYS is an abbreviation for <u>K</u>ernel <u>E</u>stimating <u>Y</u>our <u>S</u>hape. A KEYS function provides an unbinned and non-parametric estimate of the PDF from which a set of data is drawn.
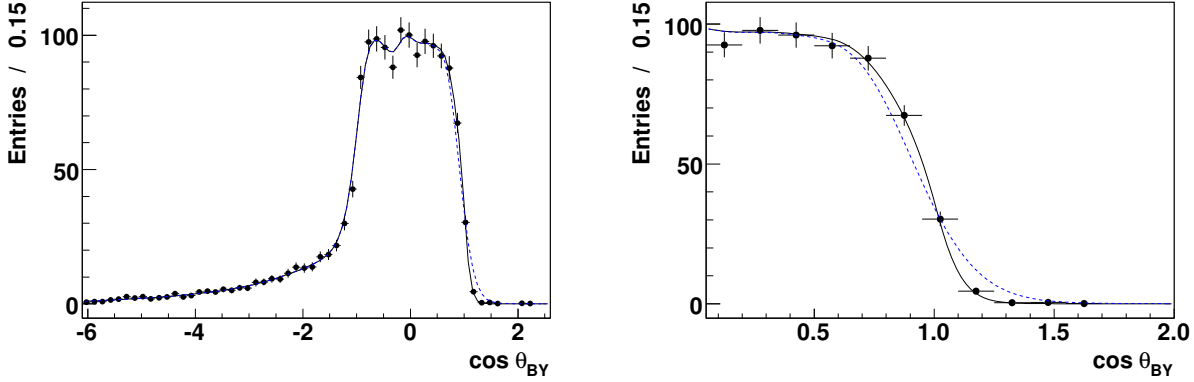
Figure 5.3: The $\cos\theta_{\mathrm{BY}}$ distribution of the candidate class 'Sig' for the first $\tilde{w}$ bin is plotted together with the two functions $C_{11}^{*\,\mathrm{RMC}}$ (dashed) and C_{11}^{RMC} (solid). The left plot shows the mainly populated $\cos\theta_{\mathrm{BY}}$ range. The right plot shows the range with the steep edge in the $\cos\theta_{\mathrm{BY}}$ distribution. The two areas enclosed by the solid and the dashed line are equal. This property is a feature of the edge correction. The fitted parameter values of C_{11}^{RMC} are $r_{11} = 1.02 \pm 0.02$ and $b_{11} = 0.50 \pm 0.06$. The correction substantially improves the edge modeling.

The allowed ranges of the indices are $i = 1, \ldots, 10$ and $j = 1, \ldots, 24$. The parameterizations of the edge-reshaped PDFs $\hat{C}_{ij}^{\mathrm{Cor}}\left(\cos\theta_{\mathrm{BY}}|b_{ij}, r_{ij}\right)$ are given by

$$
\hat{C}^{\mathrm{Cor}}\left(\cos\theta_{\mathrm{BY}}|b, r\right) = N^{\mathrm{Cor}} \cdot
\begin{cases}
L\left(\cos\theta_{\mathrm{BY}}|b, r\right) & \text{for } \cos\theta_{\mathrm{BY}} < r \\
\hat{C}^{*}\left(\cos\theta_{\mathrm{BY}}\right) & \text{for } \cos\theta_{\mathrm{BY}} = r \\
R\left(\cos\theta_{\mathrm{BY}}|b, r\right) & \text{for } \cos\theta_{\mathrm{BY}} > r
\end{cases},
$$

$$
L\left(\cos\theta_{\mathrm{BY}}|b, r\right) = \hat{C}^{*}\left(\cos\theta_{\mathrm{BY}}\right) + \left[\hat{C}^{*}\left(2\,r - \cos\theta_{\mathrm{BY}}\right) - R\left(2\,r - \cos\theta_{\mathrm{BY}}|b, r\right)\right] \quad \text{and}
$$

$$
R\left(\cos\theta_{\mathrm{BY}}|b, r\right) = \hat{C}^{*}\left(r + \frac{\cos\theta_{\mathrm{BY}} - r}{b}\right). \tag{5.36}
$$

This correction effects a sharpening of the edge in the $\cos\theta_{\mathrm{BY}}$ PDF. To keep the parametrization readable the indices i and j are omitted at the normalization factor N^{Cor}, at the parameters r and b, and at the functions $\hat{C}^{\mathrm{Cor}}$, $\hat{C}^{*}$, L and R. The parameter r is something like a fix point. It should have its value at the steep edge around $\cos\theta_{\mathrm{BY}} \approx 1$. Parameter b defines the strength of the correction and has to be positive. For $b = 1$ the function remains the same. For $b < 1$ the function gets smaller in the range $\cos\theta_{\mathrm{BY}} > r$ and bigger in the range $\cos\theta_{\mathrm{BY}} < r$. That is the desired correction. As an illustrating example, figure 5.3 shows the KEYS correction of the candidate-class 'Sig' of the first $\tilde{w}$ bin. The factor N^{Cor} makes that $\hat{C}^{\mathrm{Cor}}\left(\cos\theta_{\mathrm{BY}}|b, r\right)$ is normalized. The parameters b_{ij} and r_{ij} are determined by fits of

$$
C_{ij}^{\mathrm{Cor}}(\cos\theta_{\mathrm{BY}}) = N_{ij}^{\mathrm{cby}}\hat{C}_{ij}^{\mathrm{Cor}}\left(\cos\theta_{\mathrm{BY}}|b_{ij}, r_{ij}\right) \tag{5.37}
$$

to the histograms h_{ij}. The h_{ij} are filled with the $\cos\theta_{\mathrm{BY}}$ RMC distributions of the candidate class j within the ith $\tilde{w}$ bin. The parameter N_{ij}^{cby} is fixed to the integral of h_{ij}. For the correction typical values of r_{ij} and b_{ij} are

$$
r_{ij} = 1 \qquad \text{and} \qquad b_{ij} = 0.4 \quad .
$$

Finally one has to consider that $\hat{C}_{ij}^{\mathrm{RMC}}(\cos\theta_{\mathrm{BY}})$ depends also on $\rho_{A_1}^2$ because the weights W_{ijk} from equation 5.11 are used for the generation of $\hat{C}_{ij}^{\mathrm{RMC}}(\cos\theta_{\mathrm{BY}})$. But it turns out that the $\rho_{A_1}^2$ dependence of the $\hat{C}_{ij}^{\mathrm{RMC}}(\cos\theta_{\mathrm{BY}})$ is marginal. Strong and important is the $\rho_{A_1}^2$ dependence of the normalization factors N_{ij}^{RMC}.

5.2.3 Corrections to the Expectation on Data Relatively to the RMC

Point 1 of the roadmap from page 70 is completed. That means: (1) The *BABAR* MC has been reweighted. (2) The MC distributions have been transformed from discrete values given by the selected MC candidates to continuous shapes given by RMC PDFs. Now comes point 2 of the roadmap, the correction between PDFs for the reweighted MC and PDFs for the expectation on data.

5.2.3.1 Corrections for $\cos\theta_{\mathrm{BY}}$ PDFs

First of all let me retype the $\cos\theta_{\mathrm{BY}}$ definition:

$$\cos\theta_{\mathrm{BY}} = \frac{2E_B^* E_Y^* - m_B^2 - m_Y^2}{2|\vec{p}_B^*||\vec{p}_Y^*|} \qquad \text{with} \qquad |\vec{p}_B^*| = \sqrt{E_B^{*2} - m_B^2}. \tag{5.38}$$

On the one hand $\cos\theta_{\mathrm{BY}}$ has input values from the reconstruction. These are energy (E_Y^*), momentum ($\vec{p}_Y^*$) and mass (m_Y) of the reconstructed Y system. On the other hand it has also E_B^*, the energy of the B meson as input. The $*$ at the symbols indicates that the values are taken in the center of mass system (CMS) of the beams. For on-peak data E_B^* is half of the beam energy E_{beam}^*,

$$E_B^* = \frac{1}{2}E_{\mathrm{beam}}^*, \tag{5.39}$$

where E_{beam}^* is determined from the PEP-II collider conditions. For off-peak data equation 5.39 would result in $E_B^* < m_B^*$ and thus $|\vec{p}_B^*|$ could not be calculated. As a commonly used approximation $E_{\mathrm{beam}}^* = 10.58\,\mathrm{GeV}$ is used to calculate the value of $\cos\theta_{\mathrm{BY}}$ in off-peak data. For the MC simulation E_{beam}^* is fixed to $10.58\,\mathrm{GeV}$. For completeness one should also give the value of m_B. For MC and data the same value $m_B = 5.2791\,\mathrm{GeV}$ is used. This is the *BABAR* MC value, which is equal to the PDG value [8].

The expectation for the $\cos\theta_{\mathrm{BY}}$ distribution in data is given by

$$\hat{C}_{ij}^{\mathrm{Exp}}(\cos\theta_{\mathrm{BY}}|k_i) = \hat{C}_{ij}^{\mathrm{RMC}}\left(\frac{1}{k_i}\cdot\cos\theta_{\mathrm{BY}}\right). \tag{5.40}$$

The task of parameter k_i is to correct a wrongly assumed $|\vec{p}_B^*|$ value. Uncertainties on E_B^* and m_B affect $|\vec{p}_B^*|$ and therefore they also affect the $\cos\theta_{\mathrm{BY}}$ distribution. Because $|\vec{p}_B^*|$ is indirect proportional to $\cos\theta_{\mathrm{BY}}$ the simplest solution is to stretch or compress the $\cos\theta_{\mathrm{BY}}$ distribution along the $\cos\theta_{\mathrm{BY}}$ axis (see figure 5.4a). This has been done in equation 5.40.

In principle, the stretch parameter (k_i) should not depend on $\tilde{w}$. To check if this is true the stretch parameter is treated as a function of the $\tilde{w}$ bin (using k_i instead of k). As will be shown in section 5.2.5 the used function is a first-order polynomial. If the fit finds that the slope of this function is compatible with zero then the parameters k_i do what they are expected to do. A more intensive check is introduced in section 7.6.
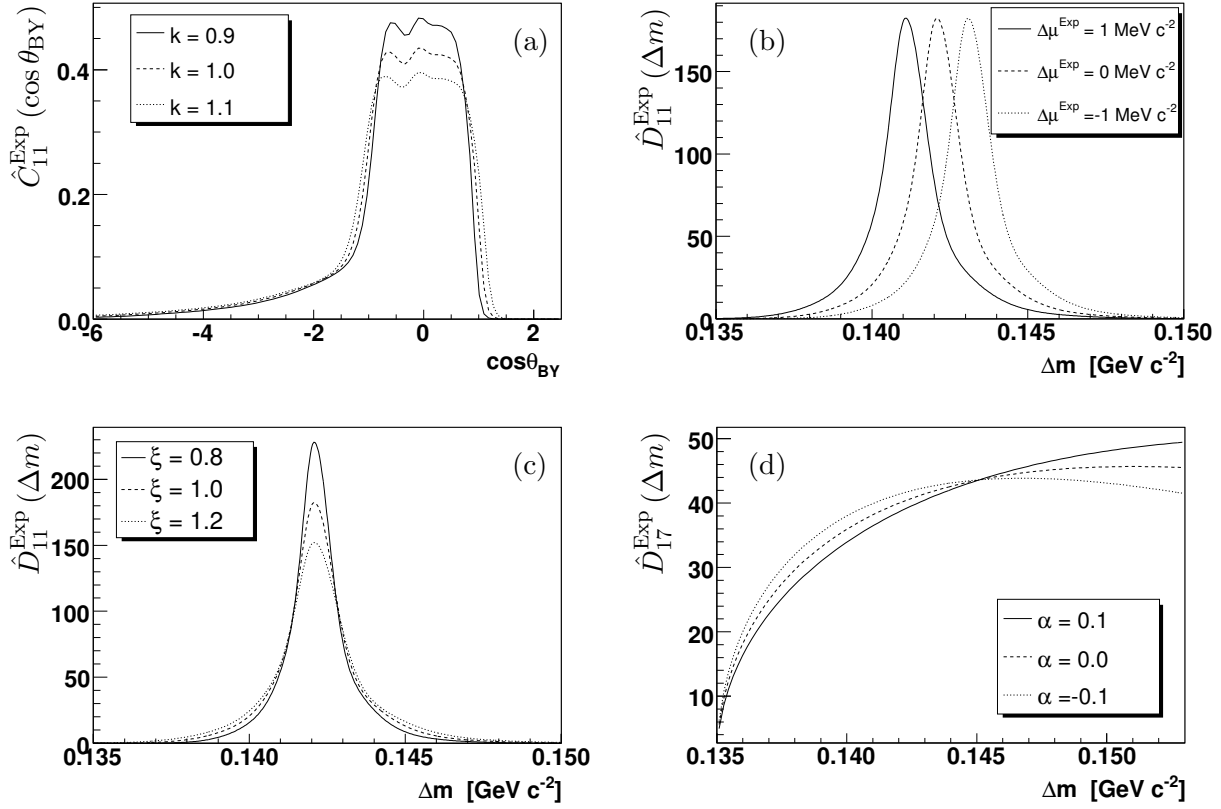
Figure 5.4: An illustration of the parameterizations correcting the RMC for a better description of the expectation on data. The illustrated parameters from subfigure **(a)** to **(d)** are k, $\Delta\mu^{\mathrm{Exp}}$, ξ and α, respectively. The plotted functions are $\hat{C}_{11}^{\mathrm{Exp}}(\cos\theta_{\mathrm{BY}})$, $\hat{D}_{11}^{\mathrm{Exp}}(\Delta m)$, $\hat{D}_{11}^{\mathrm{Exp}}(\Delta m)$ and $\hat{D}_{17}^{\mathrm{Exp}}(\Delta m)$, respectively.

5.2.3.2 Corrections for Δm PDFs

For the PDFs which describe the Δm distributions in data there are also corrections. There is one parametrization for the Δm-flat part and there is one parametrization for the Δm-peaking part,

$$\hat{D}_{ij}^{\mathrm{Exp}}\left(\Delta m|\ldots\right) = \begin{cases} \hat{D}_i^{\mathrm{peak\,Exp}}\left(\Delta m|\ldots\right) & j = 1, 2, 3, 4, 23 \\ \hat{D}_{ij}^{\mathrm{flat\,Exp}}\left(\Delta m|\ldots\right) & \text{otherwise} \end{cases}. \tag{5.41}$$

For the Δm-peaking candidate classes the following two-parameter PDFs for the expectation on data are defined,

$$\hat{D}_i^{\mathrm{peak\,Exp}}\left(\Delta m|\Delta\mu_i^{\mathrm{Exp}}, \xi_i\right) =$$
$$\hat{D}_i^{\mathrm{peak\,RMC}}\left(\Delta m|\Delta\mu_i^{\mathrm{RMC}} + \Delta\mu_i^{\mathrm{Exp}}, \xi_i \cdot \sigma_i^{\mathrm{RMC}}, \vec{f}_i^{\Delta m\,\mathrm{pRMC}}, \vec{S}_i^{\Delta m\,\mathrm{pRMC}}\right). \tag{5.42}$$

$\hat{D}_i^{\mathrm{peak\,Exp}}\left(\Delta m\right)$ has a parameter $\Delta\mu_i^{\mathrm{Exp}}$ for taking into account that the peak maximum may not be the same in data and RMC (see figure 5.4b). And it has the parameter ξ_i, a width scaler for the peak, which accounts for differences of the peak width in data and RMC (see figure 5.4c). For the Δm non-peaking candidate classes the following one-parameter PDFs for data are defined,

$$\hat{D}_{ij}^{\mathrm{flat\,Exp}}\left(\Delta m|\alpha_i\right) = \hat{D}_{ij}^{\mathrm{flat\,RMC}}\left(\Delta m|b_{ij}, c_{ij}\right) \cdot N_{ij}^{\mathrm{Cor}} \cdot \left[1 + \frac{\alpha_i}{\delta_-}\left(\Delta m - \delta_+\right)\right] \tag{5.43}$$

where δ_+ and δ_- are the center and the width of the Δm fit-range $\{\Delta m^{\mathrm{fr\,min}}, \Delta m^{\mathrm{fr\,max}}\}$,

$$\delta_\pm = \frac{\Delta m^{\mathrm{fr\,max}} \pm \Delta m^{\mathrm{fr\,min}}}{2}. \tag{5.44}$$

The factor N_{ij}^{Cor} takes care of the normalization. The parametrization $\hat{D}_{ij}^{\mathrm{flat\,Exp}}\left(\Delta m\right)$ allows to perform small corrections to the Δm shape expected in data without varying the individual b_{ij} and c_{ij} obtained from RMC (see figure 5.4d). Due to the excess of low-energetic photons in the simulation compared to the data (see figure 4.12) the shape of the Δm distribution in RMC is expected to rise faster than in data. A parameter value $\alpha_i < 0$ could compensate this effect.

It should be emphasized that there are only three parameters $(\Delta\mu_i^{\mathrm{Exp}}, \xi_i, \alpha_i)$ per $\tilde{w}$ bin to vary the shape of the Δm distributions expected in data. The parameters are not class dependent. Similarly as for the parameters k_i of the $\cos\theta_{\mathrm{BY}}$ PDFs, the $\tilde{w}$ dependence of each of these three parameters will be expressed by a first-order polynomial in $\tilde{w}$ (see section 5.2.5). A validation of this is given in section 7.6.

5.2.4 Description of the Expectation Function on Data for one $\tilde{w}$ Bin

Up to this point there is only one item left on the roadmap of page 70: The assembly of the fit function. This section gives the full expression for $F_i^{\mathrm{Exp}}\left(\Delta m, \cos\theta_{\mathrm{BY}}\right)$, the function describing the expectation on data within one $\tilde{w}$ bin, and the next section gives the full expression for the total fit function $F^{\mathrm{Exp}}\left(\Delta m, \cos\theta_{\mathrm{BY}}, \tilde{w}\right)$.

Using the expressions defined in the previous sections $F_i^{\mathrm{Exp}}\left(\Delta m, \cos\theta_{\mathrm{BY}}\right)$ is given by

$$F_i^{\mathrm{Exp}}\left(\Delta m, \cos\theta_{\mathrm{BY}}|\vec{p}^{\mathrm{rew}}, \vec{p}_i^{\mathrm{shape}}, \vec{S}_i\right) = \sum_{j=1}^{24} S_{ij}^* \cdot N_{ij}^{\mathrm{Exp}}(\vec{p}^{\mathrm{rew}}) \cdot \hat{P}_{ij}^{\mathrm{Exp}}\left(\Delta m, \cos\theta_{\mathrm{BY}}|\vec{p}_i^{\mathrm{shape}}\right). \tag{5.45}$$

The parameters of this function are

$$\vec{p}^{\,\mathrm{rew}} = \left(V, \rho^2, \rho_D^2\right), \tag{5.46}$$

$$\vec{p}_i^{\,\mathrm{shape}} = \left(k_i, \Delta\mu_i^{\mathrm{Exp}}, \xi_i, \alpha_i\right) \quad \text{and} \tag{5.47}$$

$$\vec{S}_i = \left(S_{i\,\mathrm{Sig}}, S_{i\,D^{**}}, S_{i\,\mathrm{Cor}}, S_{i\,\mathrm{Uncor}}, S_{i\,\mathrm{Sig\,rel}}, S_{i\,D^0 e\nu}, S_{i\,\mathrm{Comb}\,D^{*0}}, S_{i\,c\bar{c}}\right). \tag{5.48}$$

The reweighting parameters V and ρ^2 are defined in equation 5.1, the reweighting parameter ρ_D^2 is defined in section 5.3.2.1. The reweighting parameters $\vec{p}^{\,\mathrm{rew}}$ feed the formulas derived in section 5.3. The shape parameters $\vec{p}_i^{\,\mathrm{shape}}$ were already defined in section 5.2.3. The scaler parameters $S_{i\,\mathrm{Sig}}$ till $S_{i\,c\bar{c}}$ simultaneously scale the expected number of reconstructed Y candidates (N_{ij}^{Exp}) belonging to a group of candidate classes,

$$\vec{S}_i^* = (S_{i1}^*, \ldots, S_{i24}^*) \qquad S_{ij}^* = \begin{cases} S_{i\,\mathrm{Sig}} & j = 1 \\ S_{i\,D^{**}} & j = 2, 15, 16 \\ S_{i\,\mathrm{Cor}} & j = 3 \\ S_{i\,\mathrm{Uncor}} & j = 4 \\ S_{i\,\mathrm{Sig\,rel}} & j = 5 - 12 \\ S_{i\,D^0 e\nu} & j = 13, 14 \\ S_{i\,\mathrm{Comb}\,D^{*0}} & j = 17 - 22 \\ S_{i\,c\bar{c}} & j = 23, 24 \end{cases}. \tag{5.49}$$

As one can see from the latter equation, there are eight scalers for the 24 candidate classes. Three of these scalers are fixed to one,

$$S_{i\,\mathrm{Sig}} = 1 \qquad\qquad S_{i\,\mathrm{Cor}} = 1 \qquad\qquad S_{i\,c\bar{c}} = 1. \tag{5.50}$$

The signal scaler ($S_{i\,\mathrm{Sig}}$) is fixed to one because the variation of the amount of Δm-peaking signal is already controlled by the parameters V and ρ^2; the scaler of the correlated background ($S_{i\,\mathrm{Cor}}$) is fixed to one because (i) correlated background is difficultly to distinguish from D^{**} background by the fit and (ii) its expected number of candidates (N_{i3}^{Exp}) is very small[5]; the scaler of the $c\bar{c}$ background ($S_{i\,c\bar{c}}$) is fixed to one because the expectation was determined on off-peak data. The number of expected D^{**} events is varied by one single scaler ($S_{i\,D^{**}} = S_{i2}^* = S_{i15}^* = S_{i16}^*$), independent of D^{*0} meson being correctly or wrongly reconstructed. The numbers of wrongly reconstructed signal candidates ($N_{i5}^{\mathrm{Exp}}, N_{i6}^{\mathrm{Exp}}, N_{i7}^{\mathrm{Exp}}, N_{i8}^{\mathrm{Exp}}$) are scaled by one common scaler $S_{i\,\mathrm{Sig\,rel}}$ since the simulation of the reconstruction process is good enough and makes no separate treatment of the commonly scaled candidate classes necessary[6]. $S_{i\,\mathrm{Sig\,rel}}$ also scales the expected numbers of candidate classes 9, 10, 11 and 12 since there is a strong similarity between the true decays of these classes and the signal decay.

At this point all symbols of equation 5.45 are already defined. For completeness the references of the definitions are given here or the definitions are retyped. The PDFs $\hat{P}_{ij}^{\mathrm{Exp}}\left(\Delta m, \cos\theta_{\mathrm{BY}}\right)$ were defined in the equation 5.8 as

$$\hat{P}_{ij}^{\mathrm{Exp}}\left(\Delta m, \cos\theta_{\mathrm{BY}} | \vec{p}_i^{\,\mathrm{shape}}\right) = \hat{D}_{ij}^{\mathrm{Exp}}\left(\Delta m | \Delta\mu_i^{\mathrm{Exp}}, \xi_i, \alpha_i\right) \hat{C}_{ij}^{\mathrm{Exp}}\left(\cos\theta_{\mathrm{BY}} | k_i\right). \tag{5.51}$$

---

[5]The systematic uncertainty due to fixing $S_{i\,\mathrm{Cor}}$ to one is discussed in section 7.6.

[6]E.g., if the discrepancy between the low-energetic photon spectrum in data and MC (see figure 4.12) would be much worse than one could expect that a separate scaling of candidate classes 5/6 and 7 is necessary.

The normalization factors N_{ij}^{Exp} were defined in equation 5.9. Some of them depend directly on the parameters V and ρ^2, or ρ_D^2. The PDFs $\hat{C}_{ij}^{\text{Exp}} (\cos\theta_{\text{BY}})$ and $\hat{D}_{ij}^{\text{Exp}} (\Delta m)$ are given in equations 5.40, 5.42 and 5.43.

5.2.5 The Final Fit Function

The final fit function $F^{\text{Exp}} (\Delta m, \cos\theta_{\text{BY}}, \tilde{w})$ describes the expectation of the three-dimensional distribution in Δm, $\cos\theta_{\text{BY}}$ and $\tilde{w}$ for data. It is given by

$$
F^{\text{Exp}} (\Delta m, \cos\theta_{\text{BY}}, \tilde{w} | \vec{p}^{\text{rew}}, S_{tu}, q_{xy}) = \begin{cases} F_1^{\text{Exp}} (\Delta m, \cos\theta_{\text{BY}} | \vec{p}_1) & \text{if } \tilde{w} \, \epsilon \text{ first } \tilde{w} \text{ bin} \\ \vdots \\ F_i^{\text{Exp}} (\Delta m, \cos\theta_{\text{BY}} | \vec{p}_i) & \text{if } \tilde{w} \, \epsilon \, i \, \text{th } \tilde{w} \text{ bin} \\ \vdots \\ F_{10}^{\text{Exp}} (\Delta m, \cos\theta_{\text{BY}} | \vec{p}_{10}) & \text{if } \tilde{w} \, \epsilon \text{ last } \tilde{w} \text{ bin} \end{cases}
$$
(5.52)

with

$$
\vec{p}^{\text{rew}} = \left(V, \rho_{A_1}^2, \rho_D^2 \right),
$$
(5.53)

$$
\left(S_{tu} \right) = \begin{pmatrix} S_{1\,\text{Sig}} & \dots & S_{1\,c\bar{c}} \\ \vdots & \ddots & \vdots \\ S_{10\,\text{Sig}} & \dots & S_{10\,c\bar{c}} \end{pmatrix} \quad \text{and}
$$
(5.54)

$$
\left(q_{xy} \right) = \begin{pmatrix} q_{0(\Delta\mu^{\text{Da}})} & q_{0(\xi)} & q_{0(\alpha)} & q_{0(k)} \\ q_{1(\Delta\mu^{\text{Da}})} & q_{1(\xi)} & q_{1(\alpha)} & q_{1(k)} \end{pmatrix}.
$$
(5.55)

The parameter vector $\vec{p}^{\text{rew}}$ was already defined in equation 5.46 and its definition is only retyped. Its third component is fixed to a value taken from a previous measurement [81], $\rho_D^2 = 1.12$. The parameter matrix S_{tu}[7] contains 80 elements. Because $S_{t\,\text{Sig}}$, $S_{t\,\text{Cor}}$ and $S_{t\,c\bar{c}}$ have been fixed to one for $t = 1, \dots, 10$ (see equations 5.50) the number of free parameters in S_{tu} is decreased to 50. Furthermore the ten parameters $S_{t\,D^0e\nu}$ scaling the number of candidates reconstructed in events with a $B^- \to D^0 e^- \overline{\nu}_e$ decay are reduced to one single parameter $S_{D^0e\nu}$,

$$
S_{t\,D^0e\nu} = S_{D^0e\nu} \qquad (t = 1, \dots, 10),
$$
(5.56)

which decreases the number of free parameters in S_{tu} down to 41. Since the number of expected candidates for the uncorrelated background ($N_{i\,\text{Uncor}}^{\text{Exp}}$) gets very small at high $\tilde{w}$ values[8] the fit is confused by free parameters $S_{9\,\text{Uncor}}$ and $S_{10\,\text{Uncor}}$. Therefore it is necessary to fix these to values to one,

$$
S_{9\,\text{Uncor}} = 1 \qquad\qquad S_{10\,\text{Uncor}} = 1,
$$
(5.57)

which reduces the number of free parameters in S_{tu} down to 39. From the eight parameters q_{xy} one can calculate the shape parameters $\vec{p}_i^{\text{shape}}$ of each of the ten $\tilde{w}$-bin functions $F_i^{\text{Exp}} (\Delta m, \cos\theta_{\text{BY}})$

---

[7]Instead of S_{iu} the notation S_{tu} has been used because the index i is already used in the right side of equation 5.52.

[8]compared to the other candidates with correctly reconstructed D^{*0} meson

by simple first-order polynomials,

$$\Delta\mu_i^{\text{Exp}} = q_{0(\Delta\mu^{\text{Exp}})} + q_{1(\Delta\mu^{\text{Exp}})}(\tilde{w}_i - 1) \qquad \xi_i = q_{0(\xi)} + q_{1(\xi)}(\tilde{w}_i - 1)$$

$$\alpha_i = q_{0(\alpha)} + q_{1(\alpha)}(\tilde{w}_i - 1) \qquad k_i = q_{0(k)} + q_{1(k)}(\tilde{w}_i - 1), \tag{5.58}$$

where $\tilde{w}_i$ is the centers of the ith $\tilde{w}$ bin $(i = 1, \ldots, 10)$.

As one can see now, the function $F^{\text{Exp}}(\Delta m, \cos\theta_{\text{BY}}, \tilde{w})$ has $2 + 39 + 8 = 49$ free parameters. The parameters of $F^{\text{Exp}}(\Delta m, \cos\theta_{\text{BY}}, \tilde{w})$ are converted to a parameter vector $\vec{p}_i$ of function $F_i^{\text{Exp}}(\Delta m, \cos\theta_{\text{BY}})$ by

$$\vec{p}_i = \left(\vec{p}^{\text{rew}}, \vec{p}_i^{\text{shape}}, \vec{S}_i\right). \tag{5.59}$$

5.3 The Reweighting Technique

The following two subsections (5.3.1 and 5.3.2) derive expressions used for the reweighting of $B^- \to D^{*0}e^-\bar{\nu}_e$ events and $B^- \to D^0e^-\bar{\nu}_e$ events. The results of the two subsections are the reweighting factors $W_k^{\text{Phy,Sig}}$ and $W_k^{\text{Phy,D}^0 e\nu}$ used in equation 5.15.

5.3.1 The Reweighting Technique for $B^- \to D^{*0}e^-\bar{\nu}_e$

Following [32] the differential decay rate of $B^- \to D^{*0}e^-\bar{\nu}_e$, after integration over all decay angles, is given by

$$\begin{aligned}
\frac{d\Gamma\left(B^- \to D^{*0}e^-\bar{\nu}_e\right)}{dw} &= \frac{G_F^2|V_{cb}|^2}{48\pi^3}(m_B - m_{D^*})^2 m_{D^*}^3 \sqrt{w^2 - 1}(w+1)^2 \\
&\times \left[1 + \frac{4w}{w+1}\frac{m_B^2 - 2wm_Bm_{D^*} + m_{D^*}^2}{(m_B - m_{D^*})^2}\right] F(w)^2,
\end{aligned} \tag{5.60}$$

where w is the product of the true four-velocities of the D^* meson and the B meson

$$w = v_B \cdot v_{D^*}. \tag{5.61}$$

These two equations were already discussed in section 2.2.3.

The aim of sections 5.3.1.1 and 5.3.1.2 is to give expressions for $d\Gamma\left(B^- \to D^{*0}e^-\bar{\nu}_e\right)/dw\big|_t$ where $t = \text{BMC}$ for the *BABAR* MC simulation and $t = \text{CLN}$ for the form factor model of Caprini, Lellouch and Neubert [32]. Section 5.3.1.3 derives the expression for the weights $W_k^{\text{Phy,Sig}}$ that are given to the kth $B^- \to D^{*0}e^-\bar{\nu}_e$ event (compare with equation 5.15),

$$W_k^{\text{Phy,Sig}} = \frac{d\Gamma\left(B^- \to D^{*0}e^-\bar{\nu}_e\right)(w_k)\big|_{\text{CLN}}}{d\Gamma\left(B^- \to D^{*0}e^-\bar{\nu}_e\right)(w_k)\big|_{\text{BMC}}}. \tag{5.62}$$

The reweighting of each $B^- \to D^{*0}e^-\bar{\nu}_e$ event changes the actual inflexible MC simulation into a flexible one depending on the parameters of the weights $W_k^{\text{Phy,Sig}}$. Two very important parameters are V and ρ^2, as defined in the introduction of this chapter (see equation 5.1). By varying V and ρ^2 one varies the BMC simulation. A fit to the data (section 5.4) determines the best values of V and ρ^2 and their statistical errors. Important to say is that the weights depend only on w but they do not depend on decay angles.

5.3.1.1   Hadronic Form Factor $F_{\mathrm{CLN}}(w)$ in the CLN Theory

In [32] $F_{\mathrm{CLN}}(w)$ is expressed by

$$
F_{\mathrm{CLN}}(w)^2 = \left[1 + \frac{4w}{w+1} \frac{m_B^2 - 2wm_Bm_{D^*} + m_{D^*}^2}{(m_B - m_{D^*})^2}\right]^{-1}
$$
$$
\times \left\{ 2\frac{1 - 2wr + r^2}{(1-r)^2}\left[1 + \frac{w-1}{w+1}R_1(w)^2\right] + \left[1 + \frac{w-1}{1-r}\left(1 - R_2(w)\right)\right]^2 \right\} h_{A_1}^2(w),
$$

$$(5.63)$$

where r is an abbreviation for the meson mass ratio, $r = m_{D^*}/m_B$. The w dependence of the only form factor h_{A_1} is is given by

$$
\frac{h_{A_1}(w)}{h_{A_1}(1)} = 1 - 8\rho^2 z + \left(53\rho^2 - 15\right)z^2 - \left(231\rho^2 - 91\right)z^3,
$$
$$
\text{where} \qquad z = \frac{\sqrt{w+1} - \sqrt{2}}{\sqrt{w+1} + \sqrt{2}}.
$$

$$(5.64)$$

The form factor ratios R_1 and R_2 are given by

$$
R_1(w) = R_1(1) - 0.12(w-1) + 0.05(w-1)^2 \quad \text{and} \tag{5.65}
$$
$$
R_2(w) = R_2(1) + 0.11(w-1) - 0.06(w-1)^2. \tag{5.66}
$$

So the only parameters entering $\mathrm{d}\Gamma\left(B^- \to D^{*0}e^-\overline{\nu}_e\right)/\mathrm{d}w\big|_{\mathrm{CLN}}$ are

- the form factor ratios at zero D^{*0} recoil, $R_1(1)$ and $R_2(1)$, whose values are taken from a recently published *BABAR* measurement [33],

$$
R_1(1) = 1.396 \pm 0.075 \qquad\qquad R_2(1) = 0.885 \pm 0.047, \tag{5.67}
$$

  and

- V and ρ^2 which will be estimated in the final fit to the data.

5.3.1.2   Hadronic Form Factor $F_{\mathrm{BMC}}(w)$ in the *BABAR* MC Simulation

In the *BABAR* MC simulation $F_{\mathrm{BMC}}(w)$ is expressed very similarly,

$$
F_{\mathrm{BMC}}(w)^2 = \left[1 + \frac{4w}{w+1} \frac{m_B^2 - 2wm_Bm_{D^*} + m_{D^*}^2}{(m_B - m_{D^*})^2}\right]^{-1}
$$
$$
\times \left\{ 2\frac{1 - 2wr + r^2}{(1-r)^2}\left[1 + \frac{w-1}{w+1}R_{1,\mathrm{BMC}}^2\right] + \left[1 + \frac{w-1}{1-r}\left(1 - R_{2,\mathrm{BMC}}\right)\right]^2 \right\} h_{A_1,\mathrm{BMC}}^2(w),
$$

$$(5.68)$$

with

$$
h_{A_1,\mathrm{BMC}}(w) = 1 - \rho_{\mathrm{BMC}}^2 (w-1). \tag{5.69}
$$

Differences to $F_{\mathrm{CLN}}(w)$ are:

- There is no w dependence in the form factor ratios R_1 and R_2.

- $h_{A_1,\text{BMC}}(w)$ is parametrized using a linear $h_{A_1,\text{BMC}}$ expansion around $w = 1$ in contrast to $h_{A_1}(w)$ which is parametrized as given in equation 5.64.

The parameter values of the *BABAR* MC define $\mathrm{d}\Gamma\left(B^- \to D^{*0}e^-\bar{\nu}_e\right)/\mathrm{d}w\big|_{\text{BMC}}$ completely:

$$
\begin{aligned}
R_{1,\text{BMC}} &= 1.18, \\
R_{2,\text{BMC}} &= 0.72, \\
\rho^2_{\text{BMC}} &= 0.92, \\
\mathcal{B}_{\text{BMC}}\left(B^- \to D^{*0}e^-\bar{\nu}_e\right) &= 0.056, \\
\tau_{B^-,\text{BMC}} &= 0.502\,\text{mm}/c.
\end{aligned}
\tag{5.70}
$$

Using these values and resolving the equation

$$
\mathcal{B}_{\text{BMC}}\left(B^- \to D^{*0}e^-\bar{\nu}_e\right) = \tau_{B^-,\text{BMC}} \cdot \int\limits_1^{w_{\max}} \frac{\mathrm{d}\Gamma\left(B^- \to D^{*0}e^-\bar{\nu}_e\right)}{\mathrm{d}w}\bigg|_{\text{BMC}} \mathrm{d}w
\tag{5.71}
$$

for $|V_{cb}|_{\text{BMC}}$ gives the value of $|V_{cb}|$ used in the BMC simulation,

$$
|V_{cb}|_{\text{BMC}} = 3.514 \cdot 10^{-2}.
\tag{5.72}
$$

5.3.1.3 The Event Weights $W_k^{\text{Phy,Sig}}$

The event weight $W_k^{\text{Phy,Sig}}$ depends directly on the variables

$$
\begin{aligned}
V &= h_{A_1}(1) \cdot |V_{cb}| \qquad \text{and} \\
\rho^2 &= \rho^2_{A_1}
\end{aligned}
$$

which will be varied in the fit. That means

$$
W_k^{\text{Phy,Sig}} = W_k^{\text{Phy,Sig}}(w_k | V, \rho^2),
\tag{5.73}
$$

where w_k is just w of the k th event. The full expression $W_k^{\text{Phy,Sig}}$ is given by[9]:

$$
\begin{aligned}
W_k^{\text{Phy,Sig}} &= \frac{\left.\frac{\mathrm{d}\Gamma\left(B^- \to D^{*0} e^- \bar{\nu}_e\right)}{\mathrm{d}w}(w)\right|_{\text{CLN}}}{\left.\frac{\mathrm{d}\Gamma\left(B^- \to D^{*0} e^- \bar{\nu}_e\right)}{\mathrm{d}w}(w)\right|_{\text{BMC}}} \\[2mm]
&= \frac{|V_{cb}|^2}{|V_{cb}|^2_{\text{BMC}}} \cdot \frac{F_{\text{CLN}}(w)^2}{F_{\text{BMC}}(w)^2} \\[2mm]
&= \frac{|V_{cb}|^2}{|V_{cb}|^2_{\text{BMC}}} \cdot \frac{h_{A_1}^2(w)}{h_{A_1,\text{BMC}}^2(w)} \\[2mm]
&\quad \times \frac{2\frac{1-2wr+r^2}{(1-r)^2}\left[1+\frac{w-1}{w+1}R_1(w)^2\right]+\left[1+\frac{w-1}{1-r}\left(1-R_2(w)\right)\right]^2}{2\frac{1-2wr+r^2}{(1-r)^2}\left[1+\frac{w-1}{w+1}R_{1,\text{BMC}}^2\right]+\left[1+\frac{w-1}{1-r}\left(1-R_{2,\text{BMC}}\right)\right]^2} \\[2mm]
&= \left\{\frac{V}{|V_{cb}|_{\text{BMC}}} \cdot \frac{1-8\rho^2 z+\left(53\rho^2-15\right)z^2-\left(231\rho^2-91\right)z^3}{1-\rho_{\text{BMC}}^2(w-1)}\right\}^2 \\[2mm]
&\quad \times \frac{2\frac{1-2wr+r^2}{(1-r)^2}\left[1+\frac{w-1}{w+1}R_1(w)^2\right]+\left[1+\frac{w-1}{1-r}\left(1-R_2(w)\right)\right]^2}{2\frac{1-2wr+r^2}{(1-r)^2}\left[1+\frac{w-1}{w+1}R_{1,\text{BMC}}^2\right]+\left[1+\frac{w-1}{1-r}\left(1-R_{2,\text{BMC}}\right)\right]^2}.
\end{aligned}
\tag{5.74}
$$

5.3.2 The Reweighting Technique for $B \to D^0 e\nu$

The aim of this section is to derive a reweighting expression that allows to change the decay model of $B \to D^0 e\nu$ events from the ISGW2[10] model [53] to the CLN[11] model [32]. The reason for the change to the CLN model is the possibility to vary the w distribution of $B \to D^0 e\nu$ events by an extra parameter, the later defined ρ_D^2. That possibility is not there in the ISGW2 model. The ISGW2 model is used in the *BABAR* MC simulation and the CLN model is what one would like to use in this analysis. Thus one has to give the weight

$$
R_{\text{ISGW2}}^{\text{CLN}} = \frac{\mathrm{d}\Gamma_{\text{CLN}}\left(B \to D^0 e\nu\right)}{\mathrm{d}\Gamma_{\text{ISGW2}}\left(B \to D^0 e\nu\right)}
\tag{5.75}
$$

to each $B \to D^0 e\nu$ event of the *BABAR* MC. The differential decay widths $\mathrm{d}\Gamma_{\text{CLN}}$ and $\mathrm{d}\Gamma_{\text{ISGW2}}$ depend on only one kinematic quantity w, which is the relativistic boost of the D^0 meson within the B rest frame. It can be calculated as the product of the true four-velocities of the D^0 meson and the B meson,

$$
w = v_B \cdot v_{D^0}.
\tag{5.76}
$$

In contrast to that what has been done in the reweighting of $B^- \to D^{*0} e^- \bar{\nu}_e$ events no direct comparison of the *BABAR* MC model (ISGW2) to the new model (CLN) is performed. Instead

---

[9]To make the $W_k^{\text{Phy,Sig}}$ expression better readable the event index k is omitted at w — read w_k instead of the written w.

[10]ISGW2 is an abbreviation for an updated version of a decay model of N. Isgur, D. Scora, B. Grinstein and M.B. Wise.

[11]CLN is an abbreviation for I. Caprini, L. Lellouch and M. Neubert.

of this one compares both models to a third model, called HQET, and determines the two ratios $R_{\text{HQET}}^{\text{CLN}}$ and $R_{\text{ISGW2}}^{\text{HQET}}$, defined by

$$R_v^u = \frac{\mathrm{d}\Gamma_u \left(B \to D^0 e\nu\right)}{\mathrm{d}\Gamma_v \left(B \to D^0 e\nu\right)} \qquad u\,,v = \text{CLN}\,, \text{ISGW2}\,, \text{HQET}. \tag{5.77}$$

The searched weight $R_{\text{ISGW2}}^{\text{CLN}}$ is, like the differential decay widths dΓ of all three models, w-dependent and it is given by

$$R_{\text{ISGW2}}^{\text{CLN}} = R_{\text{HQET}}^{\text{CLN}} \cdot R_{\text{ISGW2}}^{\text{HQET}} \tag{5.78}$$

In the next two subsections it is explained how the ratios $R_{\text{HQET}}^{\text{CLN}}$ and $R_{\text{ISGW2}}^{\text{HQET}}$ are derived. Subsection 5.3.2.3 gives the expression for the weights of $B \to D^0 e\nu$ events.

The reason for the HQET model detour is the following. As you see later the CLN model has one single parameter called ρ_D^2. Thus the searched weight is ρ_D^2 dependent. Now it is much easier to express the ratio $R_{\text{HQET}}^{\text{CLN}}$ by a mathematical term with ρ_D^2 than to do this for the ratio $R_{\text{ISGW2}}^{\text{CLN}}$. The ratio of the non-parametric models HQET and ISGW2 is extracted by a simple MC study.

5.3.2.1   Relation between the CLN Model and the HQET Model

The differential decay rate of $B \to D^0 e\nu$ events in the CLN model [32] and in the HQET model [46] is given by

$$\frac{\mathrm{d}\Gamma \left(B \to D^0 e\nu\right)}{\mathrm{d}w}\bigg|_u = \frac{G_F^2 |V_{cb}|^2}{48\pi^3} (m_B + m_{D^0})^2\, m_{D^0}^3 (w^2 - 1)^{3/2} |V_1^u(w)|^2 \tag{5.79}$$

$$u = \text{CLN}\,, \text{HQET}$$

where w is defined in equation 5.76 and $V_1^u(w)$ is a form factor with one single parameter ρ_D^2 in the case of CLN model. The differential decay widths of the two models differ only in their form factors. The definition of the form factors $V_1^{\text{CLN}}(w)$ and $V_1^{\text{HQET}}(w)$ is

$$V_1^{\text{CLN}}(w) = V_1(1) \left(1 - 8\rho_D^2 z + \left(51\rho_D^2 - 10\right) z^2 - \left(252\rho_D^2 - 84\right) z^3\right) \quad \text{and} \tag{5.80}$$

$$V_1^{\text{HQET}}(w) = 1 - 1.12 \left(w - 1\right) \tag{5.81}$$

with

$$z = \frac{\sqrt{w+1} - \sqrt{2}}{\sqrt{w+1} + \sqrt{2}} \quad . \tag{5.82}$$

Important to say is that the constant $V_1(1)$ is approximately one [32]. The ratio $R_{\text{HQET}}^{\text{CLN}}$ follows from the previous definitions and is

$$R_{\text{HQET}}^{\text{CLN}} = \left(V_1(1)\right)^2 \left(\frac{1 - 8\rho_D^2 z + \left(51\rho_D^2 - 10\right) z^2 - \left(252\rho_D^2 - 84\right) z^3}{1 - 1.12 \left(w - 1\right)}\right)^2 . \tag{5.83}$$

5.3.2.2   Relation between the ISGW2 Model and the HQET Model

200 million events of HQET MC and 200 million events of ISGW2 MC have been produced for the extraction of $R_{\text{ISGW2}}^{\text{HQET}}$.[12] In both cases the *BABAR* software package EvtGen [46] generated B

---

[12]The MC has been produced on generator level without detector simulation.
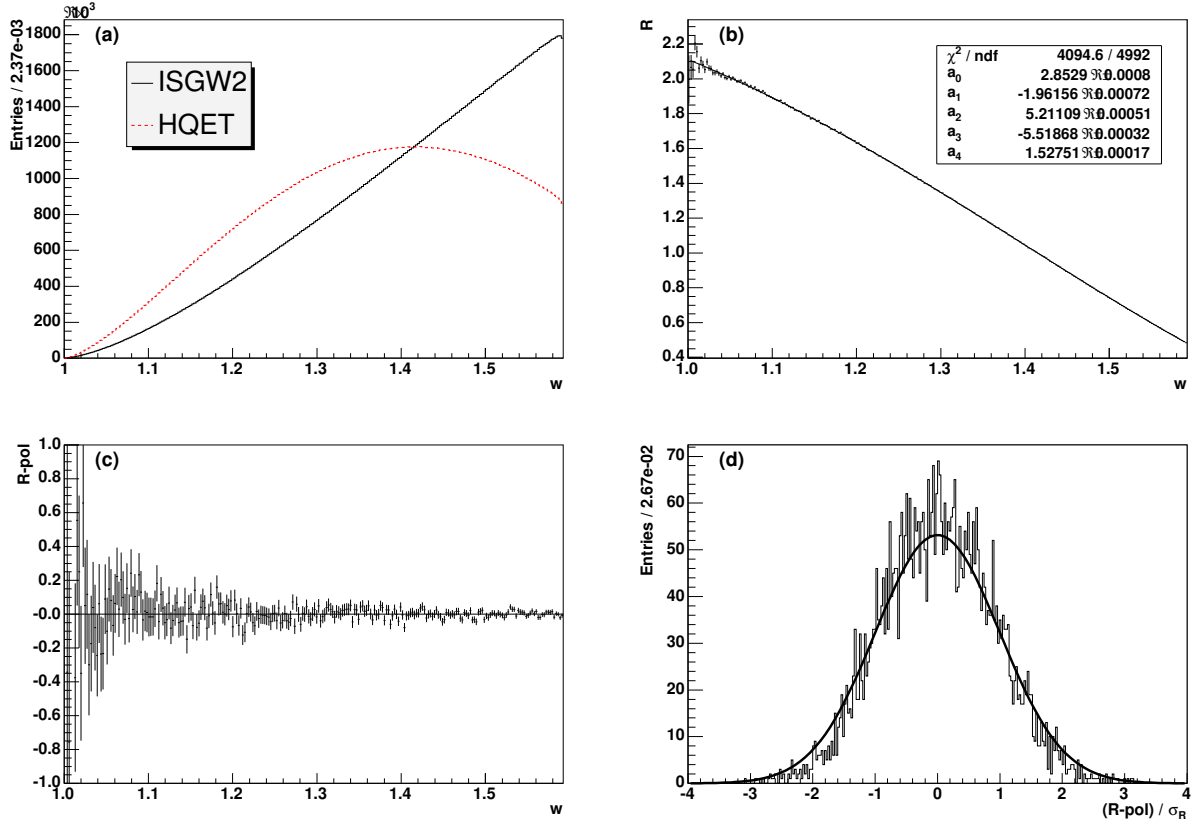
Figure 5.5: Plot **(a)** shows the w distribution of the HQET model and the ISGW2 model. The ratio R of these distributions and the result of a fit with the fourth order polynomial pol (see equation 5.84) are shown in plot **(b)**. The goodness of this fit is verified by plots (c) and (d). Plot **(c)** shows the difference between the fit result and the histogram from plot (b). Plot **(d)** shows the strength of deviations of $R - \text{pol}$ from zero. In plot (d) there is also drawn the expected distribution, a gauss function with mean=0 and sigma=1.

decay events with the decay chain $B^- \to D^0 e^- \overline{\nu}_e; D^0 \to K^- \pi^+$. The HQET model was taken as B decay model in the HQET MC and the ISGW2 model was taken as B decay model in the ISGW2 MC. The w distributions of both types of MC and their ratio are shown in figure 5.5a. To describe the w dependence of $R_{\text{ISGW2}}^{\text{HQET}}$ the ratio between the two w distributions has been fitted using a fourth-order polynomial $\text{pol}(w)$,

$$R_{\text{ISGW2}}^{\text{HQET}} = \text{pol}(w) = \sum_{l=0}^{4} a_l \, (w - 1)^l. \tag{5.84}$$

The fit and its quality are shown in the figures 5.5b-5.5d.

89

5.3.2.3 The Weights for $B \to D^0 e\nu$ Events

The quantity $R_{\text{ISGW2}}^{\text{CLN}}$ can be determined using the equations 5.78, 5.83 and 5.84. From this quantity one can define the weight $W_k^{\text{Phy,D}^0\text{e}\nu}$ for the kth $B^- \to D^0 e^- \bar{\nu}_e$ event,

$$
\begin{aligned}
W_k^{\text{Phy,D}^0\text{e}\nu} &= \frac{R_{\text{ISGW2}}^{\text{CLN}}}{V_1^2(1)} \\
&= \left(\frac{1 - 8\rho_D^2 z + \left(51\rho_D^2 - 10\right) z^2 - \left(252\rho_D^2 - 84\right) z^3}{1 - 1.12\,(w - 1)} \right)^2 \cdot \left(\sum_{l=0}^{4} a_l\,(w_k - 1)^l \right).
\end{aligned}
\tag{5.85}
$$

The coefficients a_l are given in figure 5.5b. The CLN model parameter ρ_D^2 remains a parameter of $W^{\text{Phy,D}^0\text{e}\nu}$. By weighting each simulated $B \to D^0 e\nu$ event of the BMC with $W_k^{\text{Phy,D}^0\text{e}\nu}$ one switches from a w distribution following the ISGW2 model to a w distribution following the CLN model.

5.4 The Fit to the Data

A fit of the function $F^{\text{Exp}}\left(\Delta m, \cos\theta_{\text{BY}}, \tilde{w}\right)$ defined in equation 5.52 extracts values for V and ρ^2. It is a log-likelihood fit minimizing the following sum,

$$
\text{NLL} = -2 \log \mathcal{L} = 2 \sum_{i=1}^{10} \sum_{j=1}^{14} \sum_{k=1}^{41} \Big(f_{ijk} \; - \; h_{ijk} \log f_{ijk} \; + \; \log h_{ijk}! \Big).
\tag{5.86}
$$

The indices i, j and k run over the $\tilde{w}$-, the $\cos\theta_{\text{BY}}$-, and the Δm-bin numbers of the fit range of the three dimensional data histogram, respectively. The bins are equally sized over the fit range. The ranges along $\tilde{w}$, $\cos\theta_{\text{BY}}$ and Δm are $\{1.000, 1.505\}$, $\{-4, 3\}$ and $\{0.135\,\text{GeV}/c^2, 0.153\,\text{GeV}/c^2\}$. The bin contents of the data histogram are named h_{ijk}. The integrals of the fit function over the (ijk)th bins are named f_{ijk}.

The fit relies on the *Minuit* package [82] which has been converted into a C++ class to be used in the ROOT frame work [39]. The best parameters of the fit function $F^{\text{Exp}}\left(\Delta m, \cos\theta_{\text{BY}}, \tilde{w}\right)$ are determined by the MIGRAD algorithm provided by Minuit. The corresponding error matrix is obtained by calling the HESSE algorithm also provided by Minuit.

To help the fit to converge the range of the scaler parameters is limited by loose boarders. The allowed range for the free scaler parameters is limited to the range $0.3 < S_{ix} < 3.0$ for $x =$'D^{**}', 'Uncor' and 'Sig rel'. For the combinatorial D^{*0} background the scalers are limited by $0.5 < S_{i\,\text{Comb}\,D^{*0}} < 2.0$ for $i = 2, \ldots, 10$; in the first $\tilde{w}$ bin a looser limitation, $0.3 < S_{1\,\text{Comb}\,D^{*0}} < 2.0$, was necessary.[13]

---

[13]See the explanation to the fitted value of $S_{1\,\text{Comb}\,D^{*0}}$ in section 6.2.2. The allowed range of $S_{1\,\text{Comb}\,D^{*0}}$ had to be relaxed since the value of $S_{1\,\text{Comb}\,D^{*0}}$ was running against its lower limit.

Chapter 6

Fit Result

The set of abbreviations defined at the beginning of chapter 5 is extended,

$$V = F(1)|V_{cb}|, \qquad (6.1a)$$

$$\rho^2 = \rho_{A_1}^2 \quad \text{and} \qquad (6.1b)$$

$$\mathcal{B}_{\text{Sig}} = \mathcal{B}\left(B^- \to D^{*0}e^-\overline{\nu}_e\right), \qquad (6.1c)$$

to keep the text and the formulas of this chapter and the following chapters better readable.

6.1   Monte Carlo Validation

Method
The MC validation is performed in order to check whether the analysis is able to extract the desired parameters V, ρ^2 and $\mathcal{B}_{\text{Sig}}$ from the data sample. The basic idea of the test is to split the full MC sample in two parts, where one part is used as pseudo data (PDA) and the other part is used as pseudo MC (PMC). With these two samples the entire procedure is repeated. This includes (i) the candidate selection, (ii) the extraction of MC shapes for $\cos\theta_{\text{BY}}$- and Δm-distributions for each $\tilde{w}$ bin and (iii) the final three-dimensional fit extracting the desired parameters.

In data we expect the $B^- \to D^{*0}e^-\overline{\nu}_e$ events and the $\overline{B}^0 \to D^{*+}e^-\overline{\nu}_e$ events to have a w distribution as given by equation 5.60 and section 5.3.1.1[1]. Therefore we should assign this w distribution also to the $B^- \to D^{*0}e^-\overline{\nu}_e$ events and the $\overline{B}^0 \to D^{*+}e^-\overline{\nu}_e$ events of the PDA sample. This is done in the MC validation. But this times the reweighting is not the suitable technique because the final fit is a maximum-likelihood fit and therefore requires non-weighted events. The usage of weighted events would destroy the basis of the maximum-likelihood fit, it would destroy the Poisson distribution of the bin contents of the finally fitted PDA histogram. To create the PDA sample correctly one has to use a 'killing' technique. If one wants the parameters $(\hat{V}, \hat{\rho}^2)$ to describe the signal w-distribution of the PDA sample then one has to remove each event assigned to the PDA sample with the probability

$$P_{\text{Sig kill}}(w|\hat{V}, \hat{\rho}^2) = 1 - W^{\text{Phy,Sig}}(w|\hat{V}, \hat{\rho}^2). \qquad (6.2)$$

$W^{\text{Phy,Sig}}(w|\hat{V}, \hat{\rho}^2)$ is defined in equation 5.74, w is defined in equation 5.61, and $\hat{V}$ has to be chosen small enough, so that $P_{\text{Sig kill}} \geq 0$ for all allowed w. The removing is performed in dependence on the true value of w, the value of the reconstructed $\tilde{w}$ is not needed.

---

[1]The parametrization should describe nature's true form factor shape with an accuracy of better then 2% [32].
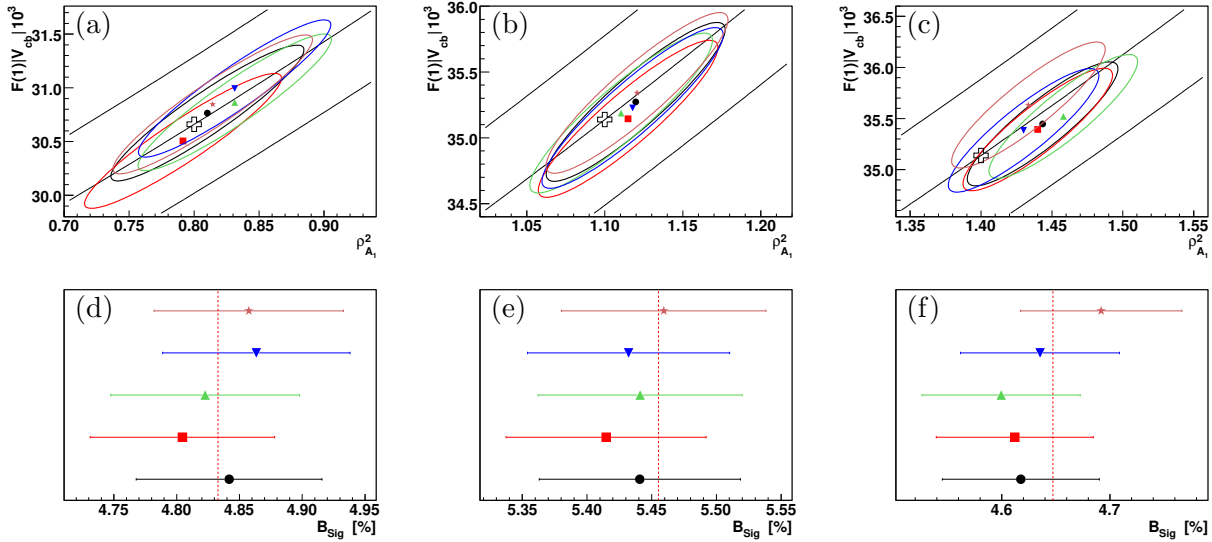
Figure 6.1: Subfigures **(a)** and **(d)** show the fit results of the five fits on PDA correspond-
ing to $(\hat{V}, \hat{\rho}^2) = (0.03066, 0.8)$. The subfigures of the second and the third column correspond to
$(\hat{V}, \hat{\rho}^2) = (0.03514, 1.1)$ and $(\hat{V}, \hat{\rho}^2) = (0.03514, 1.4)$, respectively. The three hollow crosses in the first
row show these true values of V and ρ^2 in the PDA samples. The corresponding true branching fractions
$(\hat{\mathcal{B}}_{\text{Sig}})$ are shown by the dashed lines in the plots of the lower row and by the middle diagonal lines in the
plots of the upper row. The two other diagonal lines in the biplots are lines of constant branching fraction
with $\mathcal{B}_{\text{Sig}} = \hat{\mathcal{B}}_{\text{Sig}} + 0.2\%$ and $\mathcal{B}_{\text{Sig}} = \hat{\mathcal{B}}_{\text{Sig}} - 0.2\%$. The ellipses in the upper row show the 1σ range ($\Delta\chi^2 = 1$).
One can see that the fit procedure is able to extract the true parameters. One could suppose that the fit
procedure gives a little bias to higher values, in particular for higher values of ρ^2. However, if there is really
a bias then it can be neglected because it is much smaller than the systematic uncertainties on V, ρ^2 and
$\mathcal{B}_{\text{Sig}}$ (see chapter 7).

As next, let me explain how the $B\bar{B}$ parts assigned to PDA and PMC are defined. The full
MC sample has been divided into five parts of nearly equal size. One of these parts is used to build
the PDA sample and the other four parts are used to define the PMC sample. The PDA sample
size is a quarter of the PMC sample size, that is also the approximate situation for the true data-
and MC-sample. Concerning the $c\bar{c}$ part of PDA and PMC I just used one half of the full MC $c\bar{c}$
sample for the PDA and the other half for the PMC.

Result
The five-fold division of the full MC sample was done to perform five statistically independent tests
for one $(\hat{V}, \hat{\rho}^2)$ parameter pair, each test using a different fifth for the PDA. Fifteen different PDA
samples obtained by three different $(\hat{V}, \hat{\rho}^2)$ pairs have been fitted by the nominal fit procedure
described in chapter 5. The results of the fits are shortly summarized in figure 6.1 comparing
the fitted values of V, ρ^2 and $\mathcal{B}_{\text{Sig}}$ with the true values. The figure shows that the fit behaves
as expected. A more detailed check is to look at the values of the background scalers. This has
been done for all fifteen fits. The background scalers of a typical fit are shown in figure 6.2. One
can see that there is a good agreement between the expectation and the fitted values. The fitted
polynomials $q_{0(x)} + q_{1(x)}(\tilde{w} - 1)$ for $x = k$, $\Delta\mu^{\text{Exp}}$, ξ and α describe the fitted shape of the Δm and
the $\cos\theta_{\text{BY}}$ distribution (compare equation 5.58); these polynomials are shown in figure 6.3 and do
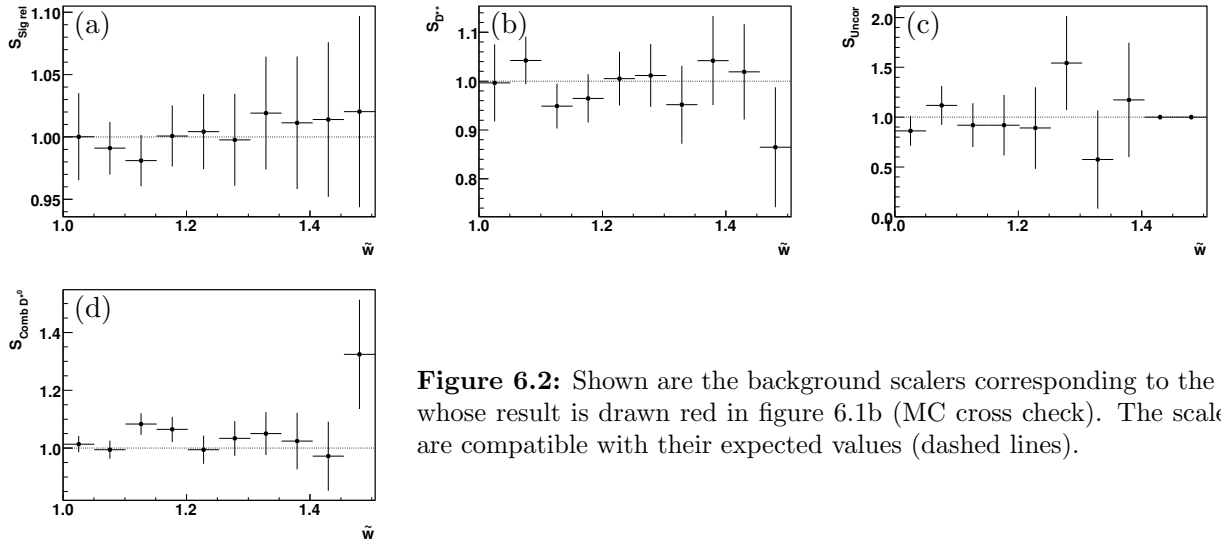
Figure 6.2: Shown are the background scalers corresponding to the fit whose result is drawn red in figure 6.1b (MC cross check). The scalers are compatible with their expected values (dashed lines).

also agree with the expectation.

Discussion of χ^2 Values of the Fits

It is also interesting to look at the χ^2 values from the fifteen fits.[2] The definition of χ^2 is given by

$$\chi^2 = \sum_{ijk\,*} \left(\frac{f_{ijk} - h_{ijk}}{\sqrt{f_{ijk}}} \right)^2, \tag{6.3}$$

where the notation of equation 5.86 has been used.[3] Let's assume the fit function $F^{\mathrm{Exp}}(\Delta m, \cos\theta_{\mathrm{BY}}, \tilde{w})$ would really be a parametrization of the true distribution function of the fitted sample. In this case one would expect a mean value $\langle \chi^2 \rangle = n$ where n is the number of degrees of freedom of the fit. The latter equation is not exactly true but a very good approximation for big values of n, such as $n > 100$. In this case the fitted χ^2 values approximately follow a Gaussian distribution with mean $\langle \chi^2 \rangle = n$ and standard deviation $\sigma_{\chi^2} = \sqrt{2n}$. But the distribution of p,

$$p = p\left(\chi^2, n\right) = \frac{\chi^2 - n}{\sqrt{2 \cdot n}}, \tag{6.4}$$

of the fifteen fits of the MC cross check has a mean value $\overline{p} = 2.0$ and a root mean square of $RMS_p = \sqrt{\overline{p^2} - \overline{p}^2} = 1.3$. Why are the expected values, $\overline{p} = 0$ and $RMS_p = 1$, so far away from the obtained values? The answer is that the assumption is not true; $F^{\mathrm{Exp}}(\Delta m, \cos\theta_{\mathrm{BY}}, \tilde{w})$ is not able to describe the true distribution function of the fitted sample with arbitrary precision. It is only an approximation of the true distribution function ($F^{\mathrm{true}}(\Delta m, \cos\theta_{\mathrm{BY}}, \tilde{w})$). With a growing

---

[2]The minimization has been performed using a log-likelihood fit (see equation 5.86). The χ^2 value is obtained from the fitted parameters.

[3]The star at the sum sign indicates that bins with less than five entries ($h_{ijk} < 5$) are merged with neighboring bins until $h_{ijk} \geq 5$. Thus, the description of the frequency distribution in these merged bins can be approximated by a Gaussian.
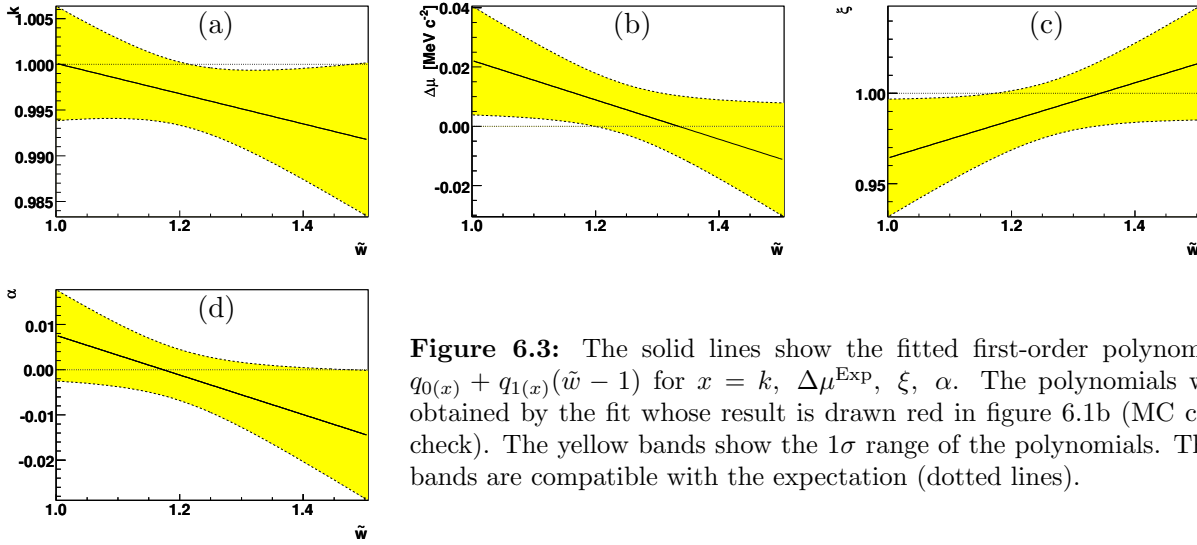
Figure 6.3: The solid lines show the fitted first-order polynomials $q_{0(x)} + q_{1(x)}(\tilde{w} - 1)$ for $x = k$, $\Delta\mu^{\mathrm{Exp}}$, ξ, α. The polynomials were obtained by the fit whose result is drawn red in figure 6.1b (MC cross check). The yellow bands show the 1σ range of the polynomials. These bands are compatible with the expectation (dotted lines).

statistic of the fitted sample the difference between the obtained χ^2 values and the expected χ^2 values[4] becomes arbitrary high, the strength of the deviation is only a question of the size of the fitted sample.

Conclusion

As shown in figure 6.1, the fit method described in chapter 5 extracts the true values of V, ρ^2 and $\mathcal{B}_{\mathrm{Sig}}$ with a sufficient precision.

6.2 The Fit Result

6.2.1 Central Values and Statistical Uncertainties

The values of V, ρ^2 and $\mathcal{B}_{\mathrm{Sig}}$ obtained by the fit described in section 5.4 are: $V = (36.32 \pm 0.51) \cdot 10^{-3}$, $\rho^2 = (1.083 \pm 0.046)$ and $\mathcal{B}_{\mathrm{Sig}} = (5.752 \pm 0.083) \cdot 10^{-2}$. Table C.1 shows the values and the statistical uncertainties of all parameters of $F^{\mathrm{Exp}}(\Delta m, \cos\theta_{\mathrm{BY}}, \tilde{w})$ determined in the fit. After the values of V, ρ^2 and $\mathcal{B}_{\mathrm{Sig}}$ have been corrected for differences between x ($x = \tau_{B^+}$, $\mathcal{B}(\Upsilon(4S) \to B^+B^-)$, $\mathcal{B}(D^{*0} \to D^0\pi^0)$, $\mathcal{B}(D^0 \to K^-\pi^+)$, $\mathcal{B}(\pi^0 \to \gamma\gamma)$) in the simulation and the currently best known value of x [8] [5] one obtains:

$$V = (35.8 \pm 0.5) \cdot 10^{-3} \tag{6.5a}$$

$$\rho^2 = 1.08 \pm 0.05 \tag{6.5b}$$

$$\mathcal{B}_{\mathrm{Sig}} = (5.60 \pm 0.08)\,\%. \tag{6.5c}$$

The value of $\mathcal{B}_{\mathrm{Sig}}$ is not a direct output of the fit but it is calculated from V and ρ^2 using equation 2.52. The uncertainty on $\mathcal{B}_{\mathrm{Sig}}$ follows from the partial derivatives $\partial\mathcal{B}_{\mathrm{Sig}}/\partial V$ and $\partial\mathcal{B}_{\mathrm{Sig}}/\partial\rho^2$, from

---

[4]The expectation assumes that $F^{\mathrm{Exp}}(\Delta m, \cos\theta_{\mathrm{BY}}, \tilde{w})$ can describe the true distribution $F^{\mathrm{true}}(\Delta m, \cos\theta_{\mathrm{BY}}, \tilde{w})$.

[5]See appendix C.2 for this correction.
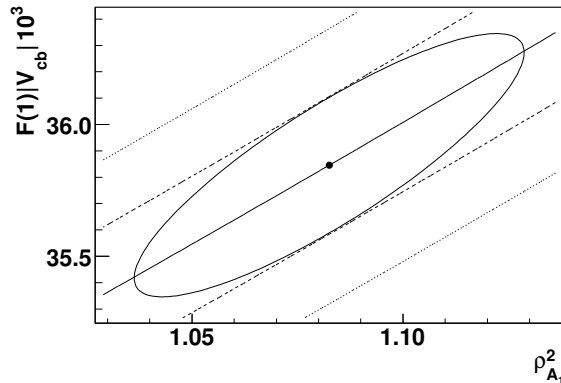
Figure 6.4: Shown is the fit result numerically presented in equations 6.5. The ellipse gives the 1σ uncertainties on V and ρ^2. The diagonal lines are lines of constant branching fraction $\mathcal{B}_{\mathrm{Sig}}$. The solid line corresponds to the value found by the fit and the dashed (dotted) line corresponds to the 1σ-band (2σ-band) of the fitted $\mathcal{B}_{\mathrm{Sig}}$ value.

Table 6.1: The result of the fit presented in equations 6.5 uses the currently best known values [8] of the input parameters listed in this table.

Input Parameter	Value
$\mathcal{B}\left(\Upsilon(4S) \to B^+ B^-\right)$	$(50.6 \pm 0.8)\%$
$\mathcal{B}\left(D^{*0} \to D^0 \pi^0\right)$	$(61.9 \pm 2.9)\%$
$\mathcal{B}\left(D^0 \to K^- \pi^+\right)$	$(3.80 \pm 0.07)\%$
$\mathcal{B}\left(\pi^0 \to \gamma\gamma\right)$	$(98.798 \pm 0.032)\%$
τ_{B^+}	$(1.638 \pm 0.011)\,\mathrm{ps}$
R_1	1.396 ± 0.075
R_2	0.885 ± 0.047

the uncertainties of V and ρ^2, and from the correlation ϱ_{stat} between V and ρ^2. The correlation between V and ρ^2 determined by the fit is

$$\varrho_{\mathrm{stat}} = 0.86. \tag{6.5d}$$

The values stated in equations 6.5 are graphically presented in figure 6.4. Table 6.1 lists the values of the input parameters used for the numbers in equations 6.5.

6.2.2 Comparison Plots between Data and the Fit Function

Comparison plots between the data and the fit show how well the function $F^{\mathrm{Exp}}\left(\Delta m, \cos\theta_{\mathrm{BY}}, \tilde{w}\right)$ describes the data. The largest set of check plots is given on a web page [40] which enables the visitor to get each of the nearly 100 comparison plots by one mouse click on a control panel.

Δm and $\cos\theta_{\mathrm{BY}}$ Distribution
Figure 6.5 shows the Δm distributions ($\cos\theta_{\mathrm{BY}}$ distributions) in the signal region and in the
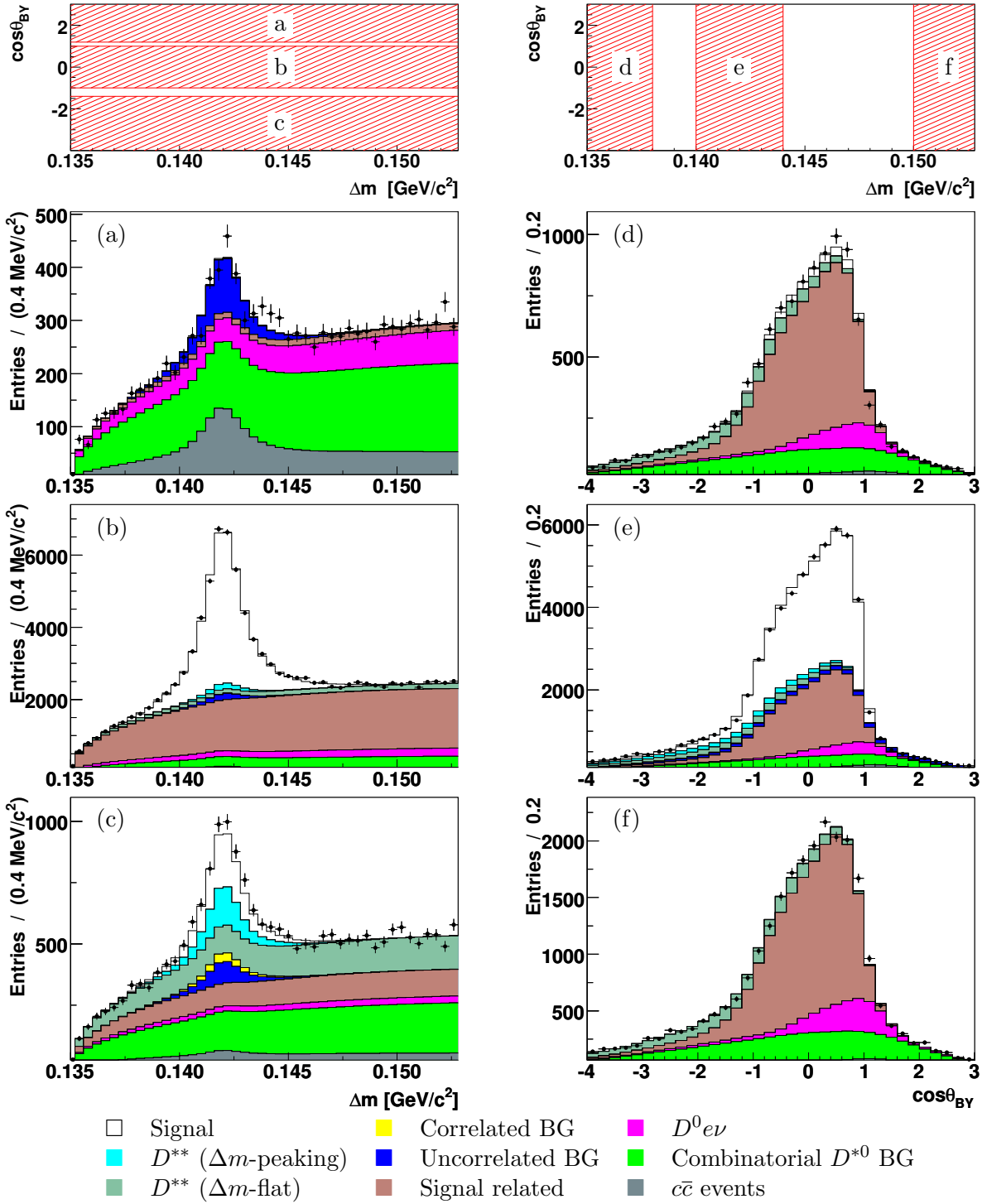
Figure 6.5: The Δm and the $\cos\theta_{BY}$ distribution of the data (points) are compared to the distributions modeled by the fitted function $F^{Exp}(\Delta m, \cos\theta_{BY}, \tilde{w})$ (stacked histograms, color code follows the classification of equation 5.49). The subfigures show the distributions in the signal bands (b,e) and in the side bands (a,c,d,f). The distributions are created using the entire $\tilde{w}$ signal range, for limited $\tilde{w}$ ranges see figures C.1, C.2 and C.3 in the appendix. The corresponding Δm and $\cos\theta_{BY}$ distributions of any $\tilde{w}$ bin are visible in [40]. The discrepancy at $\cos\theta_{BY} \approx 1$ (visible in the subfigures (d) and (e)) is caused by the product ansatz (see section 5.2.1.1) ignoring the mild correlation between $\cos\theta_{BY}$ and Δm.
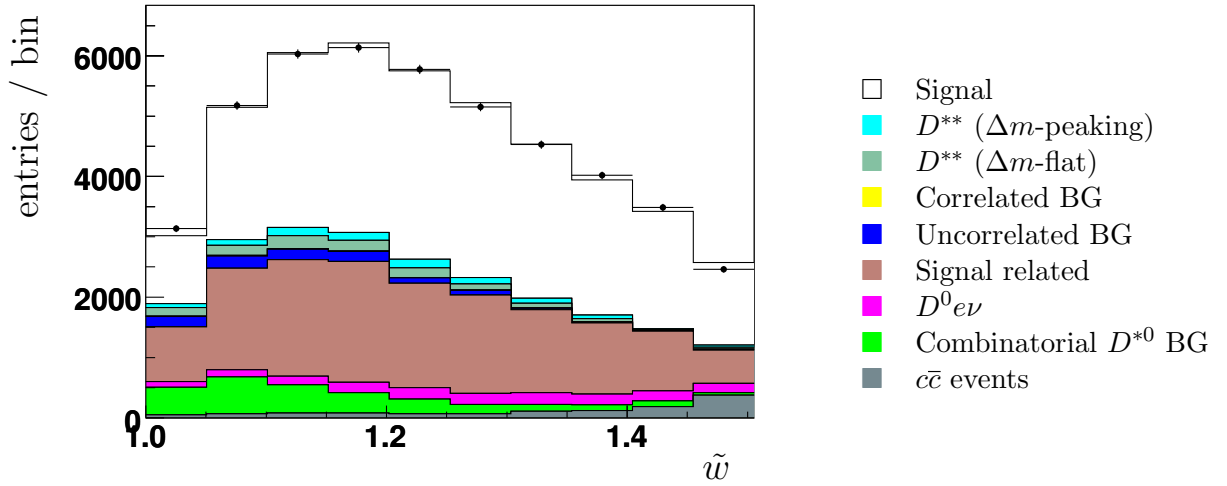
Figure 6.6: The $\tilde{w}$ distribution of the data (points) is compared to the distribution modeled by the fitted function $F^{\mathrm{Exp}}(\Delta m, \cos\theta_{\mathrm{BY}}, \tilde{w})$ (stacked histograms, color code follows the classification of equation 5.49). The distributions are plotted for the $\Delta m \cos\theta_{\mathrm{BY}}$ signal-range ($0.140\,\mathrm{GeV}/c^2 < \Delta m < 0.144\,\mathrm{GeV}/c^2$ and $-1 < \cos\theta_{\mathrm{BY}} < 1$).

sideband regions of $\cos\theta_{\mathrm{BY}}$ (Δm). The distributions in these plots are created using the entire $\tilde{w}$ signal range ($1 < \tilde{w} < 1.505$). Appendix C.3 also contains plots for limited $\tilde{w}$ ranges. There is a good agreement between the distributions obtained from the fitted function and the distributions obtained from data.

The discrepancy at $\cos\theta_{\mathrm{BY}} \approx 1$, visible in the figures 6.5d and 6.5e, is caused by the product ansatz (see section 5.2.1.1). Since there is a weak correlation between Δm and $\cos\theta_{\mathrm{BY}}$ (see table B.1) the steep edge at $\cos\theta_{\mathrm{BY}} \approx 1$ should be shifted to higher values of $\cos\theta_{\mathrm{BY}}$ with increasing Δm values. Since that is the case in data (and BMC) but not described by the PDFs $\hat{P}_{ij}(\Delta m, \cos\theta_{\mathrm{BY}})$ the steep edge of the fitted $\cos\theta_{\mathrm{BY}}$ distribution in the left Δm sideband (figure 6.5d) is shifted to a higher value with respect to the data. Accordingly, in the right Δm sideband (figure 6.5f) the edge is described at a $\cos\theta_{\mathrm{BY}}$ value lower than in data.

$\tilde{w}$ Distribution

Figure 6.6 compares the $\tilde{w}$ distribution of the data and the fitted function in the $\Delta m \cos\theta_{\mathrm{BY}}$ signal-range. The deviations in the ten $\tilde{w}$ bins are well compatible with statistical fluctuations.

Figure 6.7 shows the fitted values for the scaler parameters S_{ix} (i=1,...,10; x=D^{**}, Uncor, Sig rel [6], Comb D^{*0}) and the resulting numbers of fitted background candidates N_{ix},

$$N_{ix} = S_{ix} \cdot N_{ix}^{\mathrm{Exp}}, \tag{6.6}$$

where N_{ix}^{Exp} is the sum of all expected background candidates scaled by S_{ix} (see equation 5.49 and table 5.1). The most precisely determined scalers are the scalers $S_{i\,\mathrm{Sig\,rel}}$. The fit result $S_{i\,\mathrm{Sig\,rel}} < 1$ confirms that there are more low-energetic photon candidates in the simulation than in data.

A significant discrepancy between the data and the simulation is given in the first $\tilde{w}$ bin with $S_{1\,\mathrm{Comb}\,D^{*0}} = 0.471 \pm 0.022$. Figure C.1a shows that the fit has no other choice, the low value of

---
[6]The values of $S_{i\,\mathrm{Sig\,rel}}$ are those after the translation described in appendix C.2.
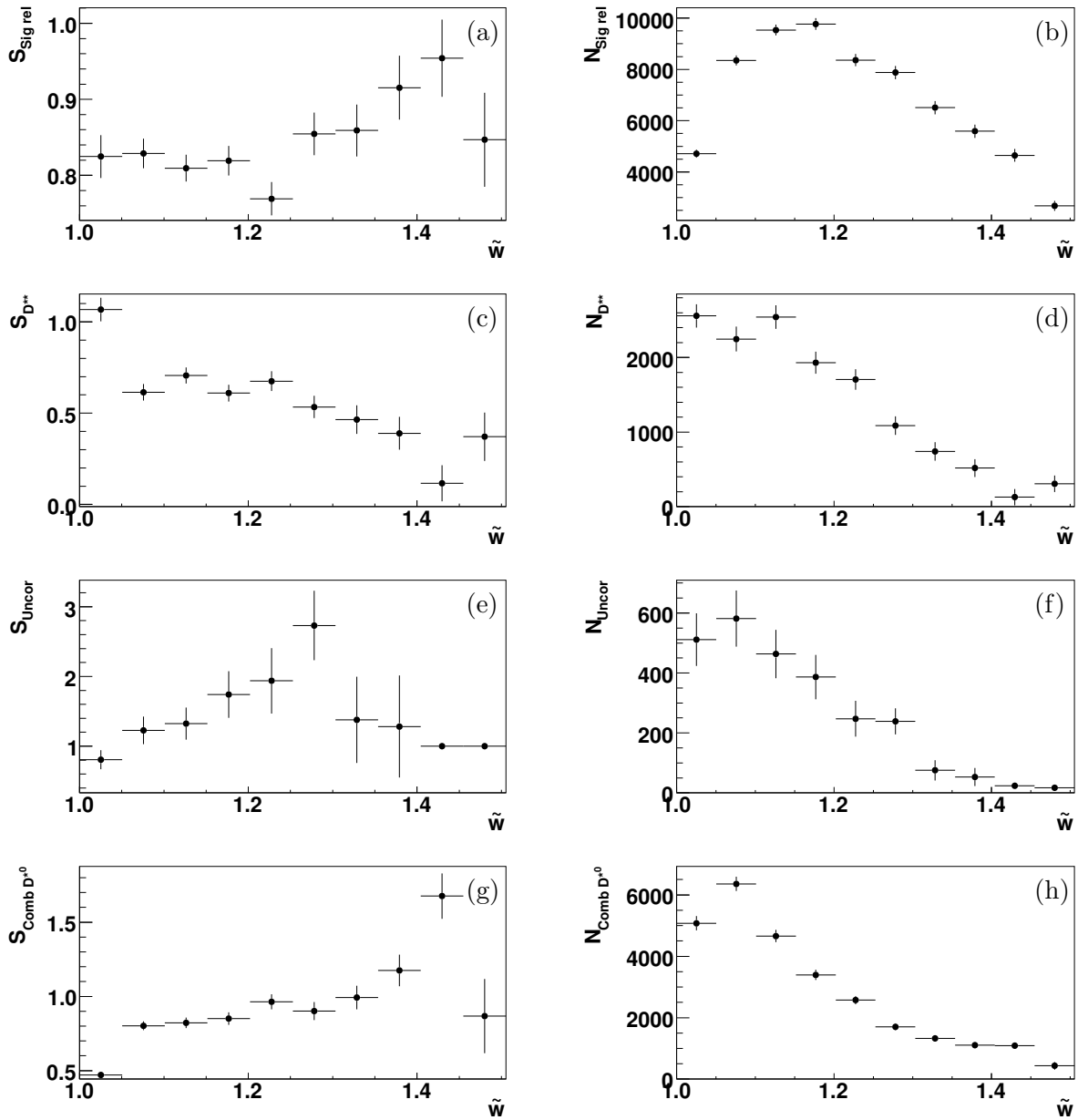
Figure 6.7: The left column shows the fitted values of the scaler variables as a function of $\tilde{w}$. The right column shows the amount of fitted background resulting from these scalers also as a function of $\tilde{w}$.
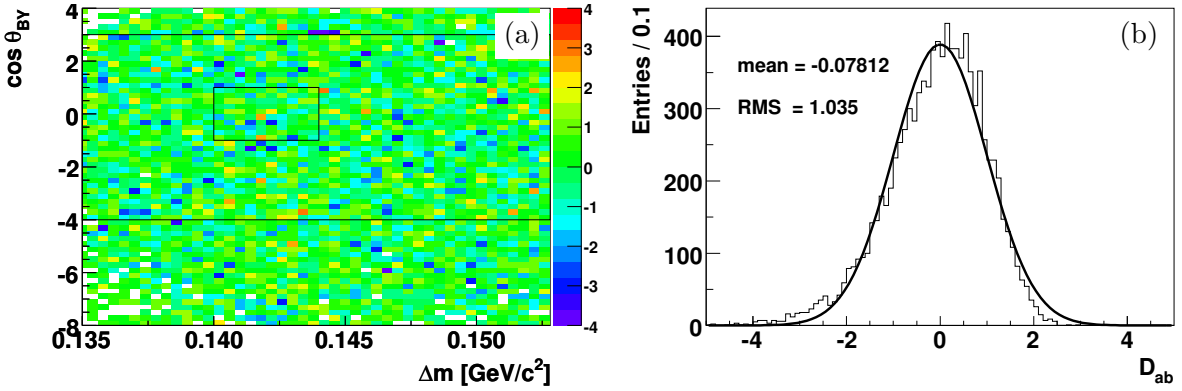
Figure 6.8: The left plot shows the bin-by-bin deviations D_{ab} between the fitted function and the data in the $\Delta m \cos\theta_{BY}$ plane for the entire $\tilde{w}$ fit-range. Since each color is homogeneously distributed over the entire plane the fit function is a good description of the data. The values of D_{ab} in the left plot are filled into a histogram shown in the right plot. If the data histogram contains less than 5 entries in a bin ($H_{ab} < 5$) than this bin is merged with neighboring bins until $H_{ab} \geq 5$. The shape of the right histogram is close to the expected shape (standard normal distribution which is also plotted) which means that the fitted function describes the data well.
The big and the small rectangles in (a) show the fit range and the approximate signal range. The numbers shown in (b) are the mean and the root mean square (RMS) of the D_{ab} frequency histogram.

$S_{1\,\mathrm{Comb}\,D^{*0}}$ results from a data MC discrepancy. In the MC validation the fit was able to find the correct values of the scalers (see figure 6.2). This gives confidence on the small value of $S_{1\,\mathrm{Comb}\,D^{*0}}$ – one has to accept that the scalers can show significant steps as a function of $\tilde{w}$. That is the reason for using non-smoothed scalers. The technique used for the smoothing of the shape parameters $\vec{p}_i^{\,\mathrm{shape}}$ is not allowed for the scaler parameters.

Deviation Plots in $\Delta m \cos\theta_{\mathrm{BY}}$ Plane

Another visualization of the difference between the data distributions and the distributions governed by the fitted function are two-dimensional deviation plots showing the bin-by-bin deviations D_{ab} in the $\Delta m \cos\theta_{\mathrm{BY}}$ plane,

$$D_{ab} = \frac{H_{ab} - I_{ab}}{\sqrt{H_{ab}}}. \tag{6.7}$$

Here, (ab) is the bin number in the $\Delta m \cos\theta_{\mathrm{BY}}$ histogram, H_{ab} is the bin content of the data histogram, and I_{ab} is the integral of the fitted function over the bin range. Figure 6.8a shows D_{ab} for the entire $\tilde{w}$ fit-range, appendix C.3 shows the plots for the first, the fifth and the tenth $\tilde{w}$ bin. If there are regions where the fitted function is a bad description for the data then the colors of the deviation plot are more reddish (underestimation) or more bluish (overestimation) in this region. The homogeneously distribution of each color over the $\Delta m \cos\theta_{\mathrm{BY}}$ plane of the deviation plot means that the fitted function describes the data well. In addition, figure 6.8b shows the frequency distribution of the deviations D_{ab}. As expected, this distribution relies in good approximation on a standard normal distribution.

6.2.3 Value of χ^2

The quantity NLL defined in equation 5.86 is minimized in the fit. But there is also the quantity χ^2 defined by equation 6.3.[7] The value of χ^2 is a simple check for the goodness of the fit and was already discussed at the end of section 6.1. The nominal fit on data yields $\chi^2 = 4435.5$ with 4095 degrees of freedom. This translates into a value $p = 3.8$ (see equation 6.4) which is compatible with the expectation from the fifteen MC cross checks ($\overline{p} = 2.0$ and $RMS_p = 1.3$).

---

[7]In contrast to NLL there is not only a meaning of the difference between two χ^2 values calculated from different parameter values, there is also a meaning of the absolute value of χ^2.

Chapter 7

Systematics

The equations 6.5 report the fitted values of V, $\rho^2_{A_1}$ and $\mathcal{B}_{\mathrm{Sig}}$ [1] with their statistic uncertainties as obtained by the fit method described in chapter 5. Since there are not only statistical but also systematic uncertainties, these equations do not give the final result of this analysis. Various systematic uncertainties have been identified and quantitatively determined. With respect to its source each of these uncertainties can be grouped either into the analysis-internal or into the analysis-external category of uncertainties:

- The category of analysis-internal uncertainties comprises everything specific to the *BABAR* experiment, e.g. uncertainties due to imperfect simulation of the detector like reconstruction and identification efficiencies of particles.

- The category of analysis-external uncertainties accounts for the uncertainties on input parameters taken from other measurements, e.g. branching fractions of decay channels used in the reconstruction.

This classification indicates that the result can be redetermined at a later time with more precise input parameters. E.g., there is hope that the uncertainty on $F(1)$ will decrease in the next years and therefore the value of $|V_{cb}|$ can be redetermined giving a more precise value of $|V_{cb}|$. Another classification groups the systematic uncertainties into two categories depending on their property

- to influence the shape of the $\tilde{w}$ distribution or

- to let it unchanged.

If a regarded uncertainty belongs to the latter category then it does not contribute to the uncertainty of $\rho^2_{A_1}$. Otherwise it is a source for uncertainties on $\mathcal{B}_{\mathrm{Sig}}$, V and $\rho^2_{A_1}$.

A summary of all evaluated uncertainties is given in table 7.3 at the end of section 7.5. The details are discussed in the subsections.

7.1 Efficiencies

Section 4.4 describes how the efficiency ratios R_i ($i = e, K, \pi, \pi^0$) between data and MC are obtained. Discussed are the track finding efficiency, the particle identification efficiency and the

---

[1]Following the notation introduced in equations 6.1, V and $\mathcal{B}_{\mathrm{Sig}}$ are abbreviations for $F(1)|V_{cb}|$ and $\mathcal{B}\left(B^- \to D^{*0}e^-\bar{\nu}_e\right)$, respectively.

neutral pion reconstruction efficiency. The selected MC candidates of this analysis are weighted with the data-MC-ratios of these three efficiencies as can be seen by equations 5.13 and 5.14. However, the efficiency ratios have an uncertainty themselves and this contributes to the uncertainty of the final result.

7.1.1 Tracking Efficiency

The tracking efficiency dependents on transverse momentum p_T and polar angle θ of the track as well as on the track multiplicity M of the event (see section 4.4.1 and [65]). The systematic uncertainty on the tracking correction factors is $\Delta R_i^{\text{Track}} = 0.8\%$ per reconstructed track ($i = e, K, \pi$) [65].

No Drift of R_i^{Track} with $\tilde{w}$

In the first instance it is assumed that this uncertainty has no influence on the shape of the $\tilde{w}$ spectrum of the fitted signal. In this case it only effects an uncertainty in V and $\mathcal{B}_{\text{Sig}}$, but the resulting uncertainty on $\rho_{A_1}^2$ is zero. Because the candidate reconstruction uses three tracks this results in a total systematic uncertainty of $(\Delta \mathcal{B}_{\text{Sig}})/\mathcal{B}_{\text{Sig}} = 2.4\%$. Due to $\mathcal{B}_{\text{Sig}} \propto V^2$ the resulting uncertainty on V is only the half of the latter value, $(\Delta V)/V = 1.2\%$. (Since the biases of R_e^{Track}, R_K^{Track} and R_π^{Track} have the same (unknown) value a quadratic addition of the uncertainties would not be correct.)

Drift of R_i^{Track} with $\tilde{w}$

Is there a possibility that the uncertainty on the tracking efficiency leads to an uncertainty on $\rho_{A_1}^2$? As mentioned at the beginning of this section, the tracking correction factor R_i^{Track} of the i-track depends on p_{Ti} and θ_i of the i-track and on the track multiplicity M of the event ($i = e, K, \pi$). If variable x ($x = p_{Ti}, \theta_i, M$) shows different distributions for different $\tilde{w}$ ranges then an x dependence of the unknown bias $\Delta R_i^{\text{Track}}$ would result in a no-zero uncertainty on $\rho_{A_1}^2$. As shown in figure 7.1, the only variables with $\tilde{w}$ dependence are the transverse momenta p_{Ti}. The polar angles θ_i and the track multiplicity M are nearly independent to $\tilde{w}$ (see also figure 7.1). The entire analysis has been repeated with alternative correction factors

$$^1R^{\text{Track}} = R^{\text{Track}} \cdot \left[1 + \frac{0.008}{1.25}\left(\frac{p_T}{\text{GeV}/c} - 1.25\right)\right] \quad \text{and} \tag{7.1a}$$

$$^2R^{\text{Track}} = R^{\text{Track}} \cdot \left[1 - \frac{0.008}{1.25}\left(\frac{p_T}{\text{GeV}/c} - 1.25\right)\right], \tag{7.1b}$$

where the number 1.25 is obtained from figure 7.1a and the number 0.008 is the uncertainty on R_i^{Track}. (The tracking efficiencies are independent to the particle type i.) The differences between the fitted values of the nominal fit and the fitted values using modification 7.1a are $\Delta(\rho_{A_1}^2)/\rho_{A_1}^2 = 0.5\%$, $\Delta(V)/V = 0.3\%$ and $\Delta(\mathcal{B}_{\text{Sig}})/\mathcal{B}_{\text{Sig}} = 0.2\%$. The corresponding differences using modification 7.1b are $\Delta(\rho_{A_1}^2)/\rho_{A_1}^2 = -0.5\%$, $\Delta(V)/V = -0.3\%$ and $\Delta(\mathcal{B}_{\text{Sig}})/\mathcal{B}_{\text{Sig}} = -0.2\%$. Since these uncertainties on V and $\mathcal{B}_{\text{Sig}}$ are negligible compared to $(\Delta V)/V = 1.2\%$ and $(\Delta \mathcal{B}_{\text{Sig}})/\mathcal{B}_{\text{Sig}} = 2.4\%$ the uncertainties due to a possible drift of R_i^{Track} with $\tilde{w}$ are listed separately in table 7.3.

7.1.2 PID Efficiency

Electrons

The detector MC simulations predicts a total electron efficiency $\check{\varepsilon}_{e\,\text{sig}}$. That means from $\check{N}_{\text{tot}}$ reconstructed electron tracks $\check{N}_{\text{sel}}$ tracks were selected by the electron selector, and $\check{\varepsilon}_{e\,\text{sig}} = \check{N}_{\text{sel}}/\check{N}_{\text{tot}}$. To
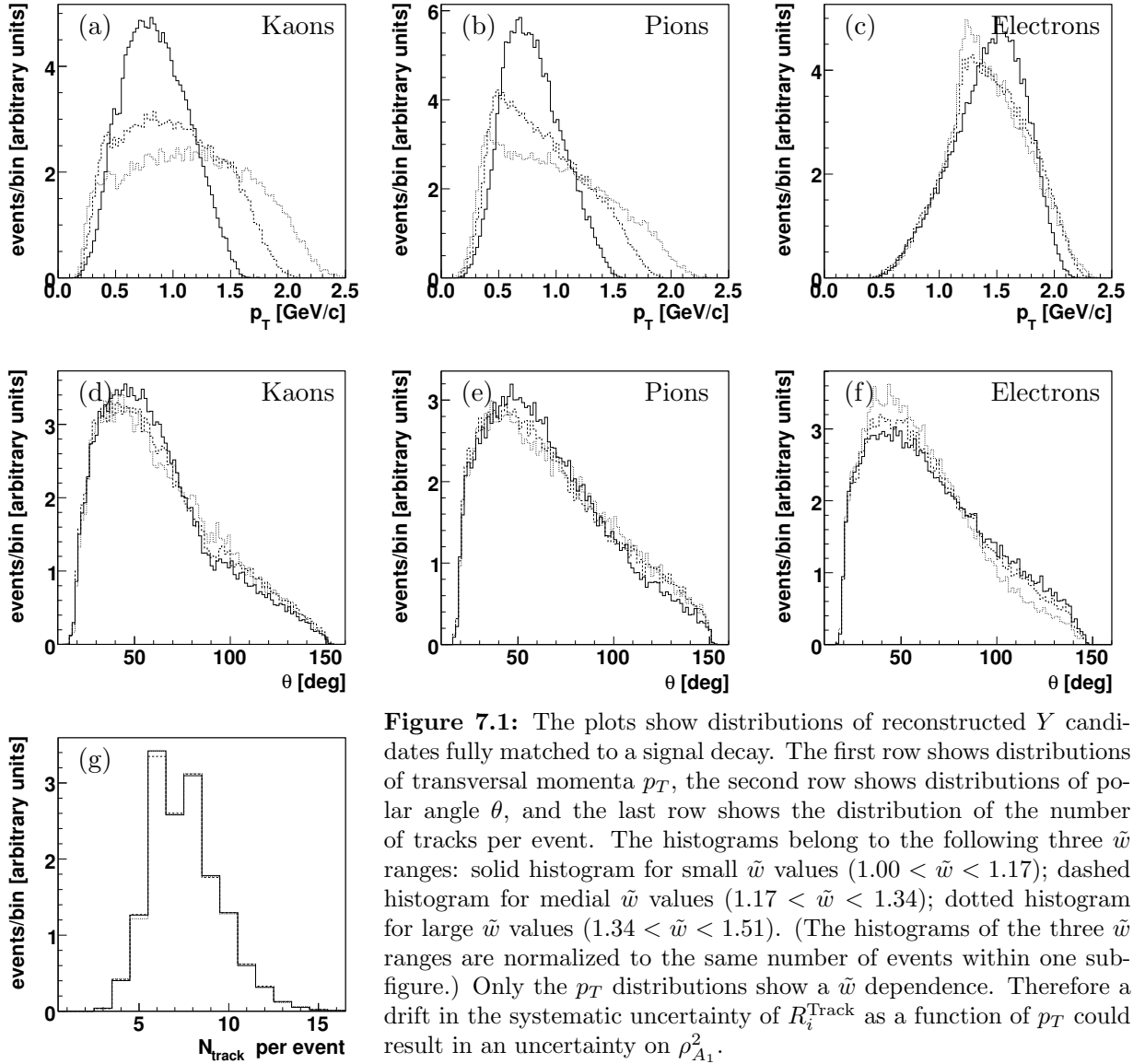
Figure 7.1: The plots show distributions of reconstructed Y candidates fully matched to a signal decay. The first row shows distributions of transversal momenta p_T, the second row shows distributions of polar angle θ, and the last row shows the distribution of the number of tracks per event. The histograms belong to the following three $\tilde{w}$ ranges: solid histogram for small $\tilde{w}$ values ($1.00 < \tilde{w} < 1.17$); dashed histogram for medial $\tilde{w}$ values ($1.17 < \tilde{w} < 1.34$); dotted histogram for large $\tilde{w}$ values ($1.34 < \tilde{w} < 1.51$). (The histograms of the three $\tilde{w}$ ranges are normalized to the same number of events within one subfigure.) Only the p_T distributions show a $\tilde{w}$ dependence. Therefore a drift in the systematic uncertainty of R_i^{Track} as a function of p_T could result in an uncertainty on $\rho_{A_1}^2$.

get an estimate of the electron efficiency $\varepsilon_{e\,\mathrm{sig}}$ in signal events of true data, $\check{\varepsilon}_{e\,\mathrm{sig}}$ has been weighted by the data MC ratio R_e^{Pid} of electron efficiencies obtained in radiative Bhabha events ($\varepsilon_{e\,\mathrm{bha}}$ and $\check{\varepsilon}_{e\,\mathrm{bha}}$). Therefore, the electron efficiency effectively used for the final result is

$$\varepsilon_e = \check{\varepsilon}_{e\,\mathrm{sig}} R_e^{\mathrm{Pid}} = \check{\varepsilon}_{e\,\mathrm{sig}} \frac{\varepsilon_{e\,\mathrm{bha}}}{\check{\varepsilon}_{e\,\mathrm{bha}}}. \tag{7.2}$$

ε_e is an estimate for the true value $\varepsilon_{e\,\mathrm{sig}}$. The systematic uncertainty $\Delta\varepsilon_{e\,\mathrm{sig}} = \varepsilon_e - \varepsilon_{e\,\mathrm{sig}}$ is difficult to estimate. However the most reliable value of $\Delta\varepsilon_{e\,\mathrm{sig}}$ is given by [83]

$$\Delta\varepsilon_{e\,\mathrm{sig}} = \varepsilon_e - \varepsilon_{e\,\mathrm{bha}}, \tag{7.3}$$

because (i) $\varepsilon_{e\,\mathrm{bha}}$ is the only value obtained from true data and (ii) one expects that the electron efficiency depends only very mildly on the environment given by the event type ($B\bar{B}$ event versus radiative Bhabha event). To estimate the uncertainties caused by $\Delta\varepsilon_{e\,\mathrm{sig}}$ the entire analysis has been repeated using $\varepsilon_{e\,\mathrm{bha}}$ instead of ε_e for the electron efficiency. The resulting differences to the result obtained by the nominal fit are taken as systematic uncertainties. They are listed in table 7.3.

Kaons

The same strategy that has been used for electrons is also used for kaons. The kaon efficiency effectively used for the final result is given by

$$\varepsilon_K = \check{\varepsilon}_{K\,\mathrm{sig}} R_K^{\mathrm{Pid}} = \check{\varepsilon}_{K\,\mathrm{sig}} \frac{\varepsilon_{K\,D^*}}{\check{\varepsilon}_{K\,D^*}}. \tag{7.4}$$

where $\varepsilon_{K\,D^*}$ and $\check{\varepsilon}_{K\,D^*}$ are the kaon efficiencies obtained from the D^* data sample and the D^* MC sample [58], respectively. $\check{\varepsilon}_{K\,\mathrm{sig}}$ is the selection efficiency of the kaon selector for kaons from the signal decay in MC. To estimate the uncertainties introduced into the analysis by using ε_K instead of $\varepsilon_{K\,\mathrm{sig}}$ the entire analysis has been repeated using $\varepsilon_{K\,D^*}$ instead of ε_K for the kaon efficiency. The differences to the result obtained by the nominal fit are taken as systematic uncertainties. They are listed in table 7.3.

7.1.3 π^0 Reconstruction Efficiency

No Drift of R_{π^0} with $\tilde{w}$

The authors of [61] state a total systematic uncertainty of $\Delta R_{\pi^0} = 3\%$. This results in an uncertainty of $(\Delta\mathcal{B}_{\mathrm{Sig}})/\mathcal{B}_{\mathrm{Sig}} = 3\%$ and $(\Delta V)/V = 1.5\%$.

Drift of R_{π^0} with $\tilde{w}$

But of course, the uncertainty on R_{π^0} also affects $\rho_{A_1}^2$. If the function that describes R_{π^0} in dependence on the π^0 momentum has a wrong shape (see figure 4.10 and equation 4.15) then this spoils the $\tilde{w}$ spectrum of the fitted signal yields. The reason is (similar to the situation described in section 7.1.1) that for signal decays there is a correlation between $\tilde{w}$ and p_{π^0}. The D^{*0} mesons with lower recoil relative to the B meson produce softer p_{π^0} spectra (see figure 7.2 and appendix D.1). To check whether the uncertainty ΔR_{π^0} has a systematic drift affecting the $\tilde{w}$ spectrum of fitted signal yields the entire analysis is repeated with different cuts on p_{π^0}. The fitted values of $\mathcal{B}_{\mathrm{Sig}}$, V and $\rho_{A_1}^2$ are shown as a function of the p_{π^0} cut in figure 7.3. Half of the difference between the maximal and the minimal value of x ($x = V$, $\rho_{A_1}^2$, $\mathcal{B}_{\mathrm{Sig}}$) is taken as systematic uncertainty on
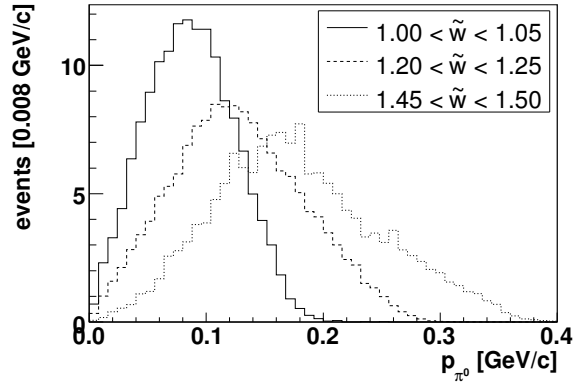
Figure 7.2: The plot shows the π^0 momentum spectrum of Y candidates fully matched to a signal candidate (unweighted *BABAR* MC). The histograms show that there is a correlation between $\tilde{w}$ and π^0 momentum.
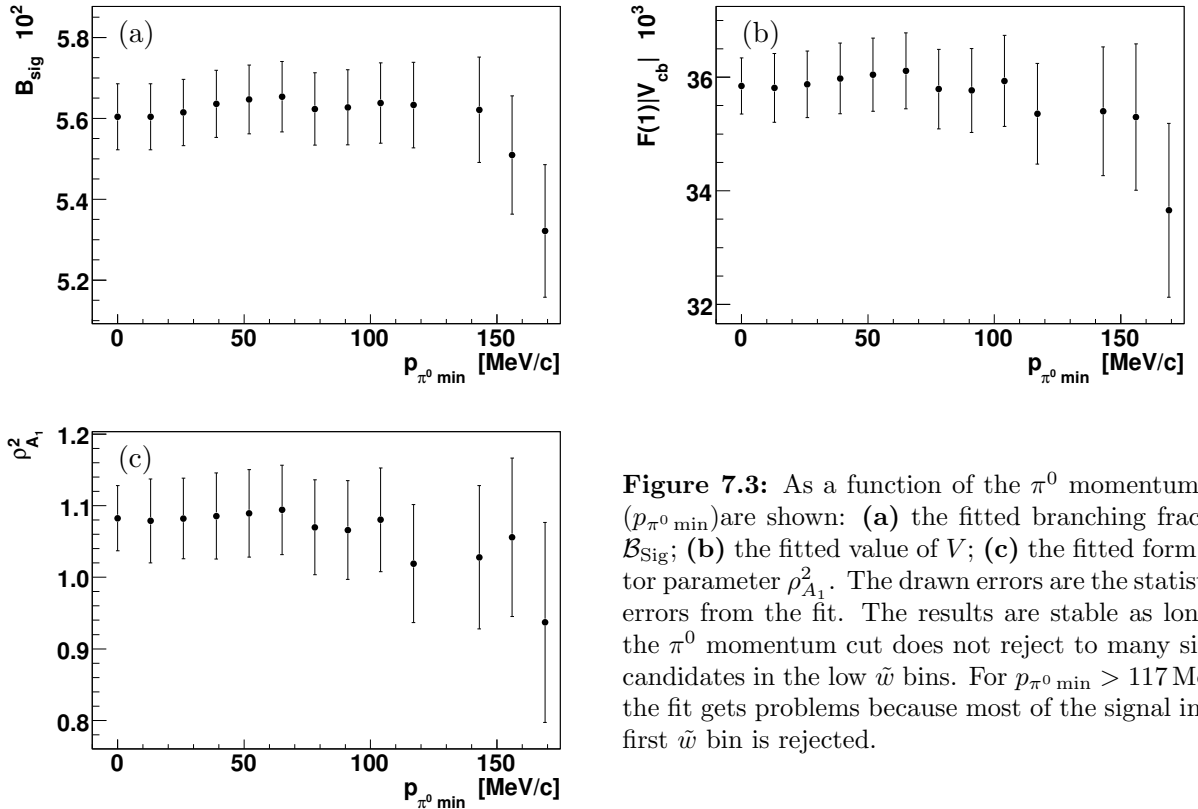
Figure 7.3: As a function of the π^0 momentum cut ($p_{\pi^0\,\mathrm{min}}$)are shown: **(a)** the fitted branching fraction $\mathcal{B}_{\mathrm{Sig}}$; **(b)** the fitted value of V; **(c)** the fitted form factor parameter $\rho^2_{A_1}$. The drawn errors are the statistical errors from the fit. The results are stable as long as the π^0 momentum cut does not reject to many signal candidates in the low $\tilde{w}$ bins. For $p_{\pi^0\,\mathrm{min}} > 117\,\mathrm{MeV}/c$ the fit gets problems because most of the signal in the first $\tilde{w}$ bin is rejected.

x arising from the uncertainties of describing the π^0 efficiency as a function of p_{π^0}. Since the fit results are only stable as long as the cut on the π^0 momentum does not reject to many signal candidates (especially in the low $\tilde{w}$ bins) only fits with cuts $p_{\pi^0\,\mathrm{min}} \leq 117\,\mathrm{MeV}/c$ are used within this procedure. The resulting uncertainties on V, $\rho^2_{A_1}$ and $\mathcal{B}_{\mathrm{Sig}}$ are listed in table 7.3. Since the statistics of the sample is changed by cutting on p_{π^0} the estimated uncertainties are not only due to systematic effects but do also contain a little fraction of statistic uncertainty.
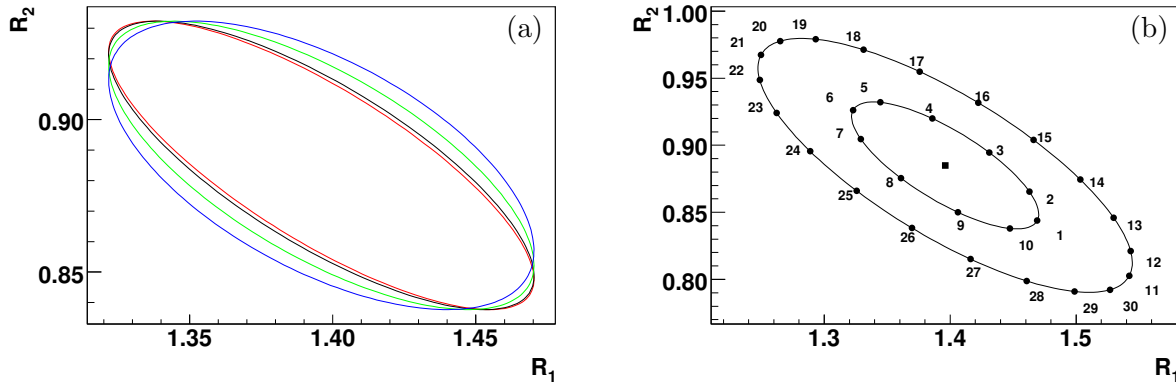
Figure 7.4: Subfigure **(a)** shows the R_1 R_2 error ellipses for four assumptions on the correlation of the *systematic part* of the covariance matrix of the used R_1 R_2 measurement [33]. The three colored ellipses assume this correlation to be equal to -1 (red), 0 (green) or 1 (blue). The black ellipse assumes that the correlation of the systematic part and the statistical part are equal, this case is used to derive the uncertainties on the result of this analysis. The difference between the four ellipses is small because the statistical uncertainties dominate. Since the correlation of R_1 and R_2 is due to the nature of the definition of R_1 and R_2 the blue ellipse is rather unlikely. Subfigure **(b)** defines thirty points on the 1σ- and the 2σ-ellipse of the R_1 R_2 measurement. The fit results for these thirty points in the R_1 R_2 plane are shown in table 7.1.

7.2 The Form Factor Ratios R_1 and R_2

The used form factor ratios R_1 and R_2 are taken from a *BABAR* measurement [33]. Reference [33] states the statistical part of the full covariance matrix but for the systematic part only the total uncertainties on R_1 and R_2 were determined. The correlation between R_1 and R_2 has not been determined.[2] But this correlation is needed to define an R_1 R_2 error ellipse. Figure 7.4a shows the 1σ-ellipses for four different assumptions about this correlation. For the determination of the systematic uncertainties of this analysis it is assumed that the statistical correlation and the systematic correlation of R_1 and R_2 are equal (black ellipse in figure 7.4a).

From the central values (see [33] or equation 2.66) and the corresponding covariance matrix of R_1 and R_2 one can draw the 1σ-ellipse and the 2σ-ellipse. The two ellipses are shown in figure 7.4b. To estimate the uncertainty on the fitted values arising from the uncertainty of the form factor ratios the entire analysis has been repeated thirty times, ten times with R_1-R_2 input values on the 1σ-ellipse and twenty times with R_1-R_2 input values on the 2σ-ellipse. The used points in the R_1-R_2 plane are marked in figure 7.4b. The fit results of the thirty fits are listed in table 7.1. Regarding the ten fits belonging to the 1σ-ellipse, the maximal deviation of x ($x = V, \rho_{A_1}^2, \mathcal{B}_{\mathrm{Sig}}$) from the value of the nominal fit is $\Delta x_{1\sigma}$. Regarding the twenty fits belonging to the 2σ-ellipse one can similarly define $\Delta x_{2\sigma}$. As expected, it turns out that $\Delta x_{1\sigma} \approx \frac{1}{2}\Delta x_{2\sigma}$ for all three numbers $(V, \rho_{A_1}^2, \mathcal{B}_{\mathrm{Sig}})$. The uncertainty on x is defined by $\Delta x = \max(\Delta x_{1\sigma}, \frac{1}{2}\Delta x_{2\sigma})$. The values of the uncertainties are $\Delta(V)/V = 0.4\%$, $\Delta(\mathcal{B}_{\mathrm{Sig}})/\mathcal{B}_{\mathrm{Sig}} = 3.0\%$ and $\Delta(\rho_{A_1}^2)/\rho_{A_1}^2 = 6.2\%$.

---

[2]The primary author of the analysis [33] was contacted and asked for the correlation of R_1 and R_2 due to the systematic uncertainties. He advised to use the correlation from the statistical part of the covariance matrix. [84]

Table 7.1: The table shows the fitted values of V and $\rho^2_{A_1}$ using various R_1 and R_2 input values. Also shown is the resulting value of $\mathcal{B}_{\mathrm{Sig}}$. The numbers are already translated to the parameter values listed in table 6.1. The form factor ratios R_1 and R_2 corresponding to the code number i are visualized in figure 7.4.

i	R_1	R_2	$V \cdot 10^3$	$\rho^2_{A_1}$	$\mathcal{B}_{\mathrm{Sig}} \cdot 10^2$	i	R_1	R_2	$V \cdot 10^3$	$\rho^2_{A_1}$	$\mathcal{B}_{\mathrm{Sig}} \cdot 10^2$
1	1.469	0.843	35.86	1.136	5.456	16	1.422	0.931	35.59	1.018	5.709
2	1.462	0.865	35.79	1.108	5.513	17	1.375	0.954	35.56	0.984	5.801
3	1.431	0.894	35.74	1.070	5.606	18	1.331	0.971	35.58	0.961	5.874
4	1.385	0.919	35.70	1.034	5.701	19	1.293	0.979	35.60	0.948	5.921
5	1.344	0.932	35.73	1.016	5.759	20	1.265	0.977	35.65	0.948	5.935
6	1.322	0.926	35.80	1.025	5.756	21	1.249	0.967	35.73	0.965	5.915
7	1.329	0.904	35.88	1.055	5.694	22	1.248	0.948	35.81	0.991	5.863
8	1.36	0.875	35.94	1.094	5.600	23	1.262	0.924	35.91	1.027	5.787
9	1.406	0.850	35.96	1.128	5.509	24	1.288	0.895	35.98	1.066	5.694
10	1.447	0.837	35.93	1.144	5.455	25	1.325	0.865	36.05	1.107	5.596
11	1.542	0.802	35.88	1.188	5.314	26	1.369	0.838	36.08	1.143	5.501
12	1.543	0.821	35.81	1.165	5.357	27	1.416	0.815	36.07	1.171	5.418
13	1.529	0.845	35.74	1.134	5.424	28	1.460	0.798	36.05	1.192	5.353
14	1.503	0.874	35.68	1.097	5.510	29	1.498	0.790	36.00	1.201	5.313
15	1.466	0.904	35.63	1.057	5.608	30	1.526	0.792	35.94	1.199	5.299

7.3 D^{**} Background

In this analysis, events with decays of type $B \to D^{**} e \nu_e$ are called D^{**} events if D^{**} is a charmed hadronic state $D^{**} = D_1, D_1', D_2^*, D^* \pi, \ldots$ but $D^{**} \neq D, D^*$. The Y candidates belonging to class 2, 15 or 16 of the list in table 5.1 contribute to the reconstructed D^{**} events. There are two uncertainties on the final result which are both introduced by D^{**} events. They are discussed in the two following paragraphs.

Unknown Branching Fractions of $B \to D^{**} e \nu_e$ Decays
The properties of Y candidates reconstructed in D^{**} events are very similar to the properties of Y signal candidates. This analysis discriminates D^{**} events and signal events by exploiting the different shapes in the $\cos\theta_{\mathrm{BY}}$ distribution (see figure 4.20). Since the knowledge about the branching fractions of the $B \to D^{**} e \nu_e$ decays is poor the shape of the $\cos\theta_{\mathrm{BY}}$ distribution of D^{**} events has an uncertainty. This uncertainty propagates to the fitted values of $F(1)|V_{cb}|$ and $\rho^2_{A_1}$. To evaluate this uncertainty, the entire analysis has been repeated 100 times. In each of the 100 tests the branching fractions $\mathcal{B}_i$ have been replaced by $\mathcal{B}_i'$,

$$\mathcal{B}_i' = r_i \, \mathcal{B}_i \qquad (i = 1, \ldots, 6), \tag{7.5}$$

where i indicates a group of decay modes of type $B \to D^{**} e \nu_e$ (see table 7.2) and $\mathcal{B}_i$ is the branching fraction of a decay from group i in the MC. The numbers r_i are random numbers basing on a Gauss distribution with mean $\mu = 1$ and standard deviation $\sigma = 0.3$. In total there are $6 \times 100 = 600$ random numbers. For V, $\rho^2_{A_1}$ and $\mathcal{B}_{\mathrm{Sig}}$, the maximal deviation from the value of the

Table 7.2: The generator's branching fractions of the decays $B^0 \to D^{**+}e^-\bar{\nu}_e$ and $B^- \to D^{**0}e^-\bar{\nu}_e$ are varied in six independent groups. Due to isospin symmetry the ratios between the branching fractions within one single group remain unchanged.

i	D^{**+}	D^{**0}
1	D_1^+	D_1^0
2	D_0^{*+}	D_0^{*0}
3	$D_1'^+$	$D_1'^0$
4	D_2^{*+}	D_2^{*0}
5	$D^{*+}\pi^0, D^{*0}\pi^+$	$D^{*+}\pi^-, D^{*0}\pi^0$
6	$D^+\pi^0, D^0\pi^+$	$D^+\pi^-, D^0\pi^0$

nominal fit is taken as systematic uncertainty. This gives $\Delta(V)/V = 0.3\%$, $\Delta(\rho_{A_1}^2)/\rho_{A_1}^2 = 0.7\%$ and $\Delta(\mathcal{B}_{\text{Sig}})/\mathcal{B}_{\text{Sig}} = 0.3\%$.

Δm Distribution of $B \to D^{**}e\nu_e$ Decays

There are Y candidates from D^{**} events with correctly reconstructed D^{*0} mesons, and there are Y candidates from D^{**} events with incorrectly reconstructed D^{*0} mesons. The fit procedure described in chapter 5 estimates their contribution to the fitted histogram without varying the ratio between both. Only the total amount of Y candidates from D^{**} events is varied, the ratio between these candidates with correctly and incorrectly reconstructed D^{*0} mesons is fixed to the expectation of the MC (efficiency corrected). Since we know that there are too many background photons in the simulated MC events we expect that the ratio is slightly shifted to values enhancing Y candidates with incorrectly reconstructed D^{*0} mesons. However, this could be slightly compensated by the fitted contribution of other candidate groups (e.g. combinatorial D^{*0} background). To see the influence on V, $\rho_{A_1}^2$ and $\mathcal{B}_{\text{Sig}}$ the expected ratio between the numbers of D^{*0} mesons correctly and wrongly reconstructed is varied. The fit has been repeated two times, one time with a higher and one time with a lower ratio, compared to the expectation from the simulation. To vary the ratio the expected number of correctly reconstructed D^{*0} mesons ($N_{i\,2}^{\text{Exp}}$) remains unchanged and the expected number of wrongly reconstructed D^{*0} mesons ($N_{i\,15}^{\text{Exp}} + N_{i\,16}^{\text{Exp}}$) is increased or decreased by 10%. The shift of the fitted values compared to the nominal fit is taken as systematic uncertainty. It has the same absolute values: $\Delta(V)/V = 0.1\%$, $\Delta(\rho_{A_1}^2)/\rho_{A_1}^2 = 0.1\%$ and $\Delta(\mathcal{B}_{\text{Sig}})/\mathcal{B}_{\text{Sig}} = 0.2\%$.

Why was the uncertainty determined by using a variation on $N_{i\,15}^{\text{Exp}} + N_{i\,16}^{\text{Exp}}$ of 10% instead of 20% or 30%? The answer is given by the nominal fit itself. The fit found that there is a variation of the scalers $S_{i\,\text{Sig rel}}$ ranging from a minimum of $S_{i\,\text{Sig rel}} = 0.9$ to a maximum of $S_{i\,\text{Sig rel}} = 1.1$. These values reflect the uncertainty on the expected ratio of correctly reconstructed D^{*0} mesons to wrongly reconstructed D^{*0} mesons in signal decays. Since this uncertainty should be the same in $B \to D^{**}e\nu_e$ decays the 10% variation of $N_{i\,15}^{\text{Exp}} + N_{i\,16}^{\text{Exp}}$ is reasonable.

7.4 $\tilde{w}$ Dependence of Shape Parameters of Δm- and $\cos\theta_{\text{BY}}$-PDF

Proper Extraction of Polynomials

It has been checked whether the polynomials $q_{0(y)} + q_{1(y)}(\tilde{w} - 1)$ defined in equation 5.58 behave in a way they are expected to behave ($y = k$, $\Delta\mu^{\text{Exp}}$, ξ, α). The polynomials have the task to
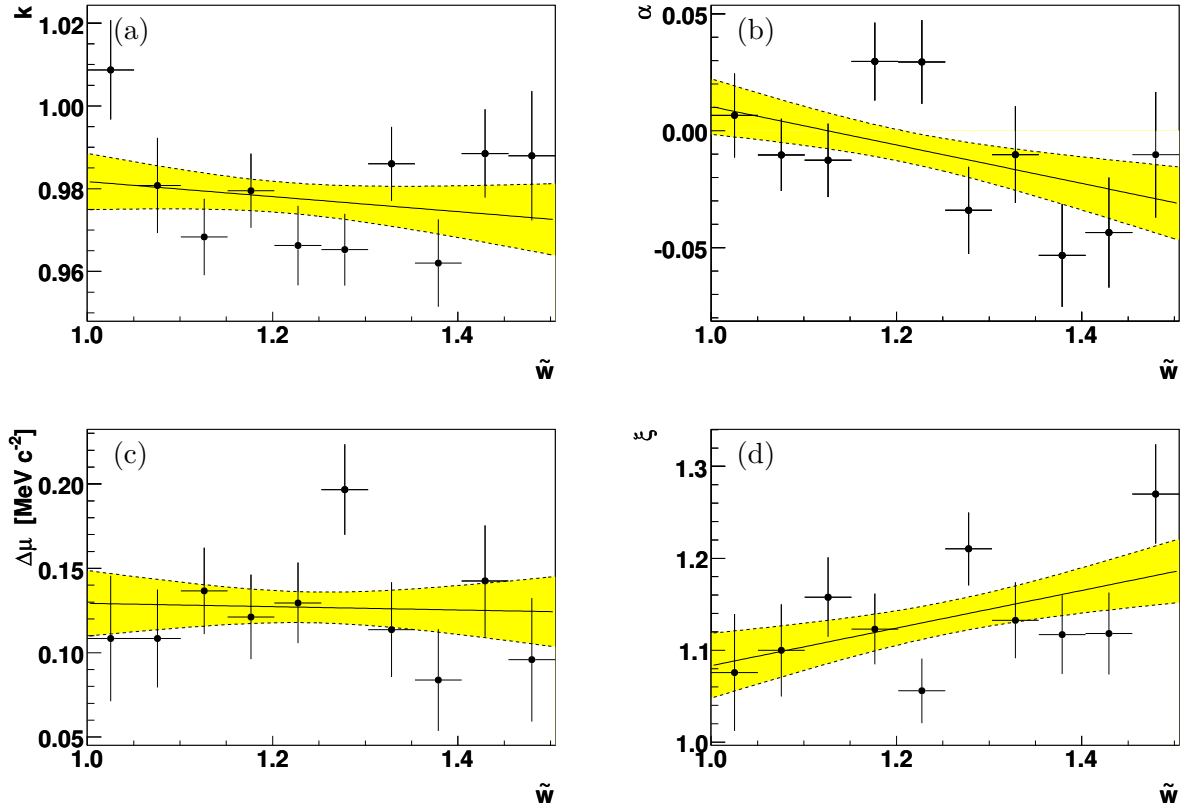
Figure 7.5: The figure illustrates the $\tilde{w}$ dependence of the four polynomials $q_{0(y)} + q_{1(y)}(\tilde{w} - 1)$ defined in equation 5.58 for $y = k$, $\Delta\mu^{\mathrm{Exp}}$, ξ and α. The solid lines and the yellow bands show the fitted polynomials and their statistical uncertainties from the nominal fit. Subfigure **(a)** shows the result of a fit where the individual parameters k_i were varied independently instead of being constrained to the polynomial's values $q_{0(k)} + q_{1(k)}(\tilde{w}_i - 1)$. Similarly, the fit was repeated for each of the other three shown parameters **(b-d)**. In each of the four alternative fits there is agreement between the ten parameters y_i and the polynomial.

smooth the individual parameters y_i in order to reduce the number of free parameters. The nominal fit has been repeated varying the individual parameters k_i ($i = 1, \ldots, 10$) independently to each other instead of constraining them to the polynomial's values $q_{0(k)} + q_{1(k)}(\tilde{w}_i - 1)$. Similarly, the fit was repeated three times corresponding to $y = \Delta\mu^{\mathrm{Exp}}$, ξ and α. The nominal fit and the four alternative fits show agreement between the polynomials and the parameters y_i (see figure 7.5). However, more important than to look at the polynomials is to check whether the values of V, ρ^2 or $\mathcal{B}_{\mathrm{Sig}}$ have changed significantly. In the four alternative fits the maximal deviation of $\mathcal{B}_{\mathrm{Sig}}$ to the value of the nominal fit is $\Delta(\mathcal{B}_{\mathrm{Sig}})/\mathcal{B}_{\mathrm{Sig}} = 0.1\%$. The corresponding maximal deviations of V and ρ^2 are $\Delta(V)/V = 0.4\%$ and $\Delta(\rho^2_{A_1})/\rho^2_{A_1} = 1.2\%$. But these deviations should not be taken as the uncertainties introduced by the description of the $\tilde{w}$ dependence of $F^{\mathrm{Exp}}(\Delta m, \cos\theta_{BY}, \tilde{w})$. This paragraph only demonstrates the proper extraction of the polynomials.

Constants instead of First-Order Polynomials
A rigorous way to determine the uncertainties arising from the description of the $\tilde{w}$ dependence of
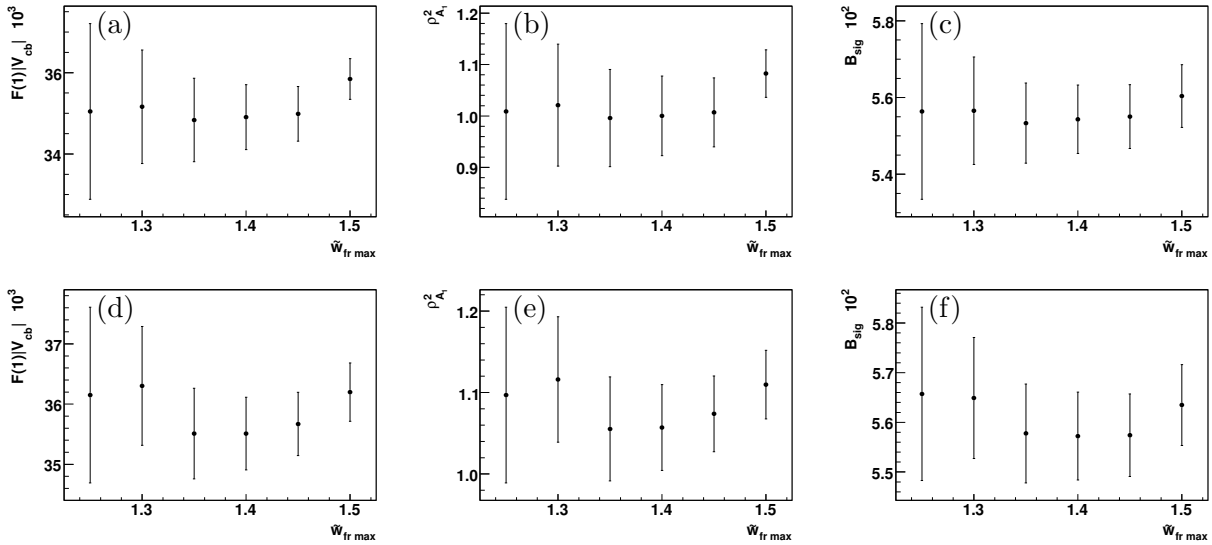
Figure 7.6: As a function of a maximal $\tilde{w}$ are shown: **(a,d)** the fitted value of $F(1)|V_{cb}|$; **(b,e)** the fitted form factor parameter $\rho^2_{A_1}$; **(c,f)** the fitted branching fraction $\mathcal{B}_{\text{Sig}}$. $\tilde{w}_{\text{fr max}}$ restricts the fit range to candidates with $\tilde{w} < \tilde{w}_{\text{fr max}}$. The upper row shows the fitted values for the nominal fit using first-order polynomials for the $\tilde{w}$ dependence of y ($y = k$, $\Delta\mu^{\text{Exp}}$, ξ, α), and the lower row shows the fitted values using constants for the four shape parameters. All fit results are stable within their statistical uncertainties.

$F^{\text{Exp}}(\Delta m, \cos\theta_{\text{BY}}, \tilde{w})$ is to repeat the nominal fit with $q_{1(k)}$, $q_{1(\Delta\mu^{\text{Exp}})}$, $q_{1(\xi)}$ and $q_{1(\alpha)}$ fixed to zero, allowing only for constant Δm and $\cos\theta_{\text{BY}}$ shape parameters. Half of the deviations between the fitted x ($x = V, \rho^2_{A_1}, \mathcal{B}_{\text{Sig}}$) and its value from the nominal fit are taken as systematic uncertainty on x (see table 7.3).

Limited $\tilde{w}$ Range

This simplification of the nominal fit does not only estimate uncertainties. It is also interesting to compare the results of this simplified fit with the results of the nominal fit after limiting the $\tilde{w}$ fit range. This is shown in figures 7.6 and 7.7. If one limits the $\tilde{w}$ fit range by a maximal allowed $\tilde{w}$ value ($\tilde{w} < \tilde{w}_{\text{fr max}}$) then the fitted values of x ($x = V, \rho^2_{A_1}, \mathcal{B}_{\text{Sig}}$) are stable as a function of $\tilde{w}_{\text{fr max}}$ within their statistical uncertainties. But if one limits the $\tilde{w}$ fit range by a minimal allowed $\tilde{w}$ value ($\tilde{w} > \tilde{w}_{\text{fr min}}$) then the fitted values of x are not stable as a function of $\tilde{w}_{\text{fr min}}$. However, the $\tilde{w}$ dependence of the fitted values of x is drastically reduced when using constants for the shape parameter y instead of using polynomials ($y = k$, $\Delta\mu^{\text{Exp}}$, ξ, α). This is a good reason for using the difference between the two fits (y modeled by $\tilde{w}$ independent constants, and y modeled by polynomials) as systematic uncertainty on V, $\rho^2_{A_1}$ and $\mathcal{B}_{\text{Sig}}$.

7.5 Other Systematic Uncertainties

7.5.1 Branching Fractions

The signal reconstruction is performed using only one decay channel for each intermediate state (see equation 4.1). Therefore, $\mathcal{B}_{\text{Sig}}$ and V^2 are proportional to the used branching fractions of
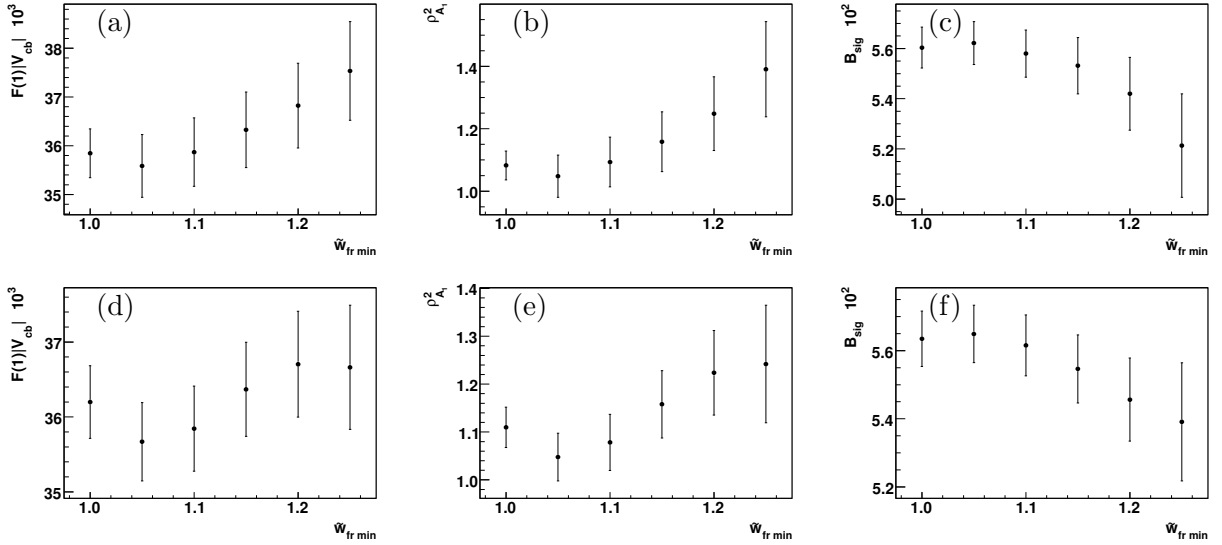
Figure 7.7: As a function of a minimal $\tilde{w}$ are shown: **(a,d)** the fitted value of $F(1)|V_{cb}|$; **(b,e)** the fitted form factor parameter $\rho^2_{A_1}$; **(c,f)** the fitted branching fraction $\mathcal{B}_{\text{Sig}}$. $\tilde{w}_{\text{fr min}}$ restricts the fit range to candidates with $\tilde{w} > \tilde{w}_{\text{fr min}}$. The upper row shows the fitted values for the nominal fit using first-order polynomials for the $\tilde{w}$ dependence of y ($y = k$, $\Delta\mu^{\text{Exp}}$, ξ, α), and the lower row shows the fitted values using constants for the four shape parameters. In contrast to reducing the $\tilde{w}$ fit-range by a maximal allowed $\tilde{w}$ value (see figure 7.6), the results presented in this figure are stable as a function of $\tilde{w}_{\text{fr min}}$ for the fits shown in the lower plots but not for the fits shown in the upper plots.

these channels (see equation C.1). Since a drift of these branching fractions with $\tilde{w}$ is not possible (branching fractions are constant numbers, independent to $\tilde{w}$) the uncertainties on these branching fractions propagate only to V and $\mathcal{B}_{\text{Sig}}$ but not to $\rho^2_{A_1}$. The uncertainties are listed in table 7.3. The largest contribution comes from the decay $D^{*0} \to D^0\pi^0$ which is nearly three times of the uncertainty coming from the decay $D^0 \to K^-\pi^+$. The uncertainty of $\mathcal{B}(\pi^0 \to \gamma\gamma)$ can be neglected.

7.5.2 Number of Charged B Meson Pairs

In order to determine the values of V and $\mathcal{B}_{\text{Sig}}$ it is not enough to know how many Y candidates have bee correctly reconstructed but one also needs to know N_{B^c},the number of charged B mesons in the data sample. $N^{\text{Data}}_{B^+B^-}$, the number of charged B meson pairs in the data sample is given by

$$
\begin{aligned}
N^{\text{Data}}_{B^+B^-} &= 2N_{B^c} \\
&= \mathcal{B}\left(\Upsilon(4S) \to B^+B^-\right) N^{\text{Data}}_{B\bar{B}}
\end{aligned}
\tag{7.6}
$$

where $N^{\text{Data}}_{B\bar{B}}$ is the number of neutral and charged B meson pairs in the data sample. $N^{\text{Data}}_{B\bar{B}}$ enters the analysis in formula 5.12 and $\mathcal{B}\left(\Upsilon(4S) \to B^+B^-\right)$ enters the analysis in formula C.1. Both contributions are briefly commented in the following two paragraphs.

$\mathcal{B}\left(\Upsilon(4S) \to B^+B^-\right)$
The discussion of $\mathcal{B}\left(\Upsilon(4S) \to B^+B^-\right)$ is completely the same as in 7.5.1. The uncertainties resulting

from $\mathcal{B}\left(\Upsilon(4S) \to B^+B^-\right)$ are listed in table 7.3.

B Counting

The total number of B meson pairs ($N_{B\bar{B}}^{\text{Data}}$) is determined as already mentioned in section 4.1. The basic idea is to subtract the luminosity scaled number of loosely selected multi-hadron events in subsamples of on-peak and off-peak data. The *BABAR* database-tool *BbkLumi* [42] reports

$$N_{B\bar{B}}^{\text{Data}} = (226.03 \pm 0.08 \pm 2.49)\, 10^6 \tag{7.7}$$

where the first uncertainty is statistical and the second one systematic. Adding the two uncertainties in quadrature gives the total uncertainty, $\Delta(N_{B\bar{B}}^{\text{Data}})/N_{B\bar{B}}^{\text{Data}} = 1.1\%$. The affect on the result is $\Delta(\mathcal{B}_{\text{Sig}})/\mathcal{B}_{\text{Sig}} = 1.1\%$ and $\Delta(V)/V = 0.6\%$. There is no resulting uncertainty on the form factor parameter $\rho_{A_1}^2$ because $N_{B\bar{B}}^{\text{Data}}$ scales the entire number of observed events, a drift of $N_{B\bar{B}}^{\text{Data}}$ with $\tilde{w}$ is not expected.

7.5.3   B Lifetime

The true B life time (τ_{B^+}) is needed in the translation C.1. Its uncertainty propagates to the fitted value of V but it has no influence on $\mathcal{B}_{\text{Sig}}$. The used value for τ_{B^+} is stated by the PDG [8] with

$$\tau_{B^+} = (1.638 \pm 0.011)\, 10^{-12} s \tag{7.8}$$

The resulting uncertainty on V is $\Delta(V)/V = 0.3\%$

7.5.4 $e^+e^- \to c\bar{c}$ Events

In the nominal fit, the number of Y candidates from $e^+e^- \to c\bar{c}$ events is fixed to a number obtained from off-peak data (see equation 5.20). The number measured in off-peak data has been scaled by the luminosity ratio between on-peak and off-peak data. In addition, there is a correction due to the different cross sections at the different center-of-mass energies (off-peak data: $10.54\,\text{GeV}/c^2$, on-peak data: $10.58\,\text{GeV}/c^2$).

Luminosity Scaling
The number of Y candidates reconstructed and selected in one $\tilde{w}$ bin in off-peak data is small[3] and has a statistical uncertainty of about 12%. But the scaling factor to the on-peak data is about 13. That means statistical fluctuations could become important. The statistical uncertainty on the numbers of expected Y candidates, $N_{i\,23}^{\text{Exp}}$ and $N_{i\,24}^{\text{Exp}}$, is approximately given by (compare with equation 5.20)

$$\Delta N_{ij}^{\text{Exp}} = k_{ij}\,\Delta\left(\sum_{r=1}^{4} N_i^{c\bar{c}\,\text{off},r}\frac{\mathcal{L}^{\text{on},r}}{\mathcal{L}^{\text{off},r}}\right)$$

$$\approx k_{ij}\frac{\mathcal{L}^{\text{on,tot}}}{\mathcal{L}^{\text{off,tot}}}\,\Delta\left(\sum_{r=1}^{4} N_i^{c\bar{c}\,\text{off},r}\right) = k_{ij}\overbrace{\frac{\mathcal{L}^{\text{on,tot}}}{\mathcal{L}^{\text{off,tot}}}\sqrt{\sum_{r=1}^{4} N_i^{c\bar{c}\,\text{off},r}}}^{=\Delta N_i^{c\bar{c}\,\text{Exp}}} = k_{ij}\,\Delta N_i^{c\bar{c}\,\text{Exp}} \tag{7.9}$$

$$(j = 23, 24;\ i = 1, \ldots, 10),$$

---

[3]numbers from the first to the last $\tilde{w}$ bin: 76, 93, 72, 68, 57, 51, 64, 71, 97, 220
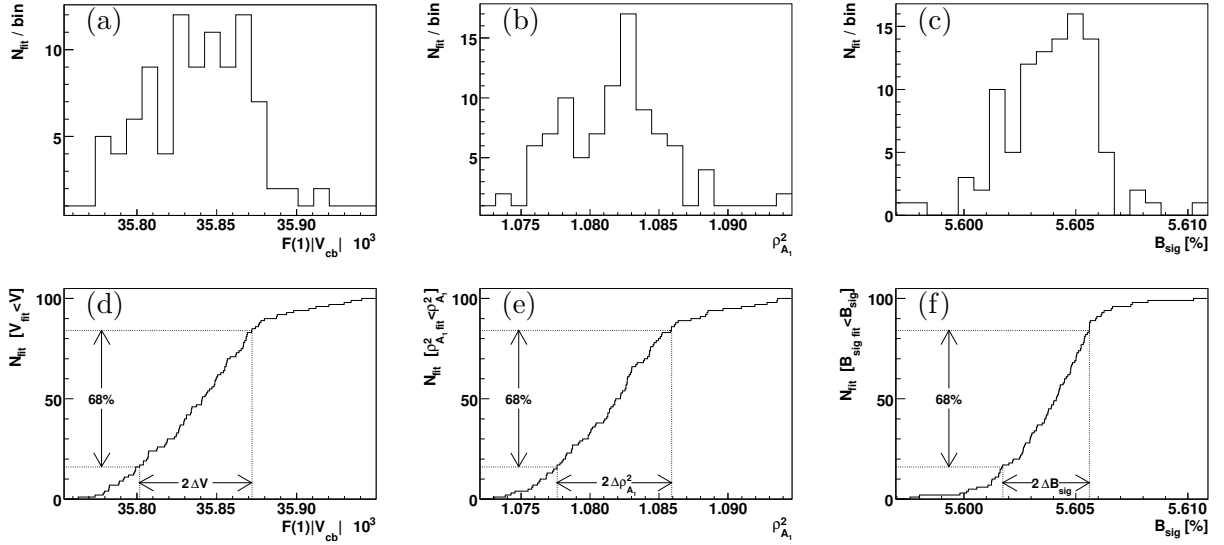
Figure 7.8: Shown are the results of 100 fits where each fit was performed with a varied number of $c\bar{c}$ events ($N'^{\mathrm{Exp}}_{i\,23}$ and $N'^{\mathrm{Exp}}_{i\,24}$, see equation 7.10). The upper row shows the fitted values. The lower row shows the cumulative distributions of the 100 fits. It also illustrates how the uncertainties are determined.

where k_{ij} is an abbreviation for $\dfrac{N^{\mathrm{RMC}}_{ij}}{N^{\mathrm{RMC}}_{i\,23}+N^{\mathrm{RMC}}_{i\,24}}\dfrac{\sigma^{\mathrm{on}}}{\sigma^{\mathrm{off}}}$. To check for uncertainties on the fitted values of V, $\rho^2_{A_1}$ and $\mathcal{B}_{\mathrm{Sig}}$ the fit has been repeated 100 times. Each time the numbers of expected Y candidates, $N^{\mathrm{Exp}}_{i\,23}$ and $N^{\mathrm{Exp}}_{i\,24}$, are replaced by $N'^{\mathrm{Exp}}_{i\,23}$ and $N'^{\mathrm{Exp}}_{i\,24}$,

$$N^{\mathrm{Exp}}_{ij} \mapsto N'^{\mathrm{Exp}}_{ij} = N^{\mathrm{Exp}}_{ij} + k_{ij}G_i \qquad (j = 23, 24; \; i = 1, \dots, 10), \qquad (7.10)$$

where G_i are ten random numbers basing on a Gauss distribution with mean $\mu = 0$ and standard deviation $\sigma = \Delta N^{c\bar{c}\,\mathrm{Exp}}_i$. The results of the hundred fits are shown in figure 7.8. The systematic uncertainty Δx ($x = V, \rho^2_{A_1}, \mathcal{B}_{\mathrm{Sig}}$) is determined by $\Delta x = (x_{84} - x_{16})/2$, where x_i are the 100 fitted values of x after sorting them ($x_i < x_{i+1}$ with $i = 1, \dots, 99$). The resulting uncertainties are $\Delta(V)/V = 0.1\%$, $\Delta(\rho^2_{A_1})/\rho^2_{A_1} = 0.4\%$ and $\Delta(\mathcal{B}_{\mathrm{Sig}})/\mathcal{B}_{\mathrm{Sig}} = 0.03\%$.

Number of Generated D^{*0} Mesons

As can bee seen in equation 5.20, the ratio between Y candidates with correctly reconstructed D^{*0} mesons and Y candidates with wrongly reconstructed D^{*0} mesons is taken from the MC. This has been done due to the low statistic of the off-peak data in the interesting kinematic range. What is the uncertainty on the fitted value of x ($x = V, \rho^2_{A_1}, \mathcal{B}_{\mathrm{Sig}}$) due to taking this ratio from MC? If there is a deviation between the number of generated D^{*0} mesons in simulation and data then this deviation contributes to the systematic uncertainties of the fitted parameters. An overlay of the Δm distribution for data and MC is shown in figure 7.9. To check the influence of the ratio the fit has been repeated two times, one time with a number of Y candidates with correctly reconstructed D^{*0} meson scaled by a factor 1.1 ($N^{\mathrm{RMC}}_{i\,23} \mapsto 1.1 \cdot N^{\mathrm{RMC}}_{i\,23}$), and a second time with a scaling factor 0.9 ($N^{\mathrm{RMC}}_{i\,23} \mapsto 0.9 \cdot N^{\mathrm{RMC}}_{i\,23}$). The deviation from the fitted values of the nominal fit are taken as systematic uncertainties: $\Delta(V)/V = 0.2\%$, $\Delta(\rho^2_{A_1})/\rho^2_{A_1} = 0.7\%$ and $\Delta(\mathcal{B}_{\mathrm{Sig}})/\mathcal{B}_{\mathrm{Sig}} = 0.01\%$. The deviations using a scaling of 1.1 have the same absolute values like the deviations using a scaling of 0.9, but they have opposite sign. The performed variation of the ratio by $\pm 10\%$ leads to a very
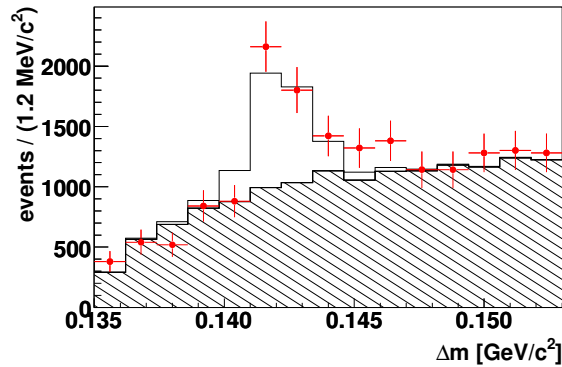
Figure 7.9: Shown is the Δm distribution of all reconstructed Y candidates for $1.0 < \tilde{w} < \tilde{w}_{\max}$. The histograms origin from $e^+e^- \rightarrow c\bar{c}$ MC events (open histogram: correctly reconstructed D^{*0}; hatched histogram: no correctly reconstructed D^{*0}). They are overlayed on the off-peak data (red dots) which has been scaled to the number of $e^+e^- \rightarrow c\bar{c}$ MC events using the luminosity of the off-peak data and the cross section $\sigma(e^+e^- \rightarrow c\bar{c}) = 1.3\,\text{nb}$. If there is a deviation between the number of generated D^{*0} mesons in simulation and data then this deviation contributes to the systematic uncertainties of the fitted parameters. Due to the low statistics of off-peak data it is difficult to say (i) if there is a deviation between simulation and data and (ii) how big this deviation is. (Error bars are statistical only.)

conservative uncertainty estimation. However, the procedure is suitable since the ratio is only a source of minor contribution to the final uncertainty.

7.6 Additional Cross Checks

Alternative π^0 Selector
As a further check, the entire analysis has been repeated using the *pi0SoftLoose* selector instead of the *pi0SoftDefaultMass* selector. The only difference between both selectors is the looser selection criterion on the $\gamma\gamma$ mass ($m_{\gamma\gamma}$) required by the *pi0SoftLoose* selector ($0.100\,\text{GeV}/c^2 < m_{\gamma\gamma} < 0.160\,\text{GeV}/c^2$ instead of $0.115\,\text{GeV}/c^2 < m_{\gamma\gamma} < 0.150\,\text{GeV}/c^2$). The parameter values of the parametrization R_{π^0} (equation 4.15) were replaced according to the selector replacement [61]:

$$a = 0.9735 \qquad \text{and} \qquad b = 6.236 \cdot 10^{-3}. \tag{7.11}$$

The result of the analysis remains unchanged when using the pi0SoftLoose selector instead of the pi0SoftDefaultMass selector.

Multiple Candidate Selection
In case of multiple candidate-groups in the event the candidate group with the best D^0 mass is selected and the others are rejected (see section 4.5.3). To check whether this selection of a best candidate group introduces an uncertainty in the analysis the entire analysis has been repeated selecting a random candidate-group instead of the candidate group with the best D^0 mass. The fit result remains unchanged.

Table 7.3: The table gives a summary of all systematic uncertainties on $F(1)|V_{cb}|$, $\rho_{A_1}^2$ and $\mathcal{B}\left(B^- \to D^{*0}e^-\overline{\nu}_e\right)$ $(= \mathcal{B}_{\text{Sig}})$. All uncertainties are given as numbers relative to the fitted values. The first block of systematic uncertainties lists the analysis-internal contributions, the second block lists the analysis-external contributions.

Category	$\frac{\Delta(F(1)|V_{cb}|)}{F(1)|V_{cb}|}[\%]$	$\frac{\Delta\rho_{A_1}^2}{\rho_{A_1}^2}[\%]$	$\frac{\Delta\mathcal{B}_{\text{Sig}}}{\mathcal{B}_{\text{Sig}}}[\%]$
total systematic analysis-internal	**3.2**	**4.8**	**4.4**
tracking efficiency (no drift with $\tilde{w}$)	1.2	-	2.4
drift of tracking efficiency with $\tilde{w}$	0.3	0.5	0.2
PID efficiency ($e^\pm$)	0.7	0.2	1.6
PID efficiency ($K^\pm$)	0.6	2.0	<0.1
π^0 reconstruction efficiency (no drift with $\tilde{w}$)	1.5	-	3.0
drift of π^0 reconstruction efficiency with $\tilde{w}$	2.1	3.5	0.9
Δm distribution of D^{**} background	0.1	0.1	0.2
$\tilde{w}$ dependence of shape parameters	1.0	2.5	0.6
number of $B\overline{B}$ events	0.6	-	1.1
luminosity scaling of off-peak data	0.1	0.4	-
total systematic analysis-external	**2.7**	**6.3**	**6.1**
$R_1(1)$ and $R_2(1)$	0.4	6.2	3.0
branching fractions of D^{**} background	0.3	0.7	0.3
number of generated D^{*0} mesons in $c\bar{c}$ events	0.2	0.7	-
$\mathcal{B}\left(\Upsilon(4S) \to B^+B^-\right)$	0.8	-	1.6
$\mathcal{B}\left(D^{*0} \to D^0\pi^0\right)$	2.3	-	4.7
$\mathcal{B}\left(D^0 \to K^-\pi^+\right)$	0.9	-	1.8
B life time	0.3	-	-
total systematic	**4.2**	**7.9**	**7.5**

Correlated Background

In the nominal fit the amount of correlated background is fixed to the MC expectation. (The scalers $S_{i\,\mathrm{Cor}}$ are fixed to one in equation 5.50.) In principle, this is a source of systematic uncertainty on the fitted values. However, since the fraction of correlated background candidates within the candidates with correctly reconstructed D^{*0} meson is very small ($1.0\%\ldots1.5\%$) the influence of correlated background to the fitted values must be very small too. The nominal fit has been repeated two times, one time with $S_{i\,\mathrm{Cor}} = 0.67$ and a second time with $S_{i\,\mathrm{Cor}} = 1.5$. The relative deviations from the results obtained with $S_{i\,\mathrm{Cor}} = 1.0$ are smaller than 0.1%.

MINOS

To get more confidence to the obtained values the minimization of the fit procedure has been checked by using the MINOS algorithm also provided by the MINUIT package [82]. As described in [82] the MINOS algorithm provides a much more reliable way to estimate errors on parameters of the fitted function, but it needs much more computing time. The best values of V and ρ^2 found by MIGRAD remain unchanged after having used MINOS. In a good approximation the MINOS-errors on V and ρ^2 are symmetric. The parabolic errors given by the MINOS algorithm ($\Delta V = 0.48, \Delta(\rho^2) = 0.043$) are somewhat smaller than the errors given by the HESSE algorithm ($\Delta V = 0.51, \Delta(\rho^2) = 0.046$).

7.7 Systematic Correlation

The aim of this subsection is to give a value for the total systematic correlation ϱ_{sys} between V and $\rho^2_{A_1}$. For a correct determination of ϱ_{sys} one would need to determine the correlations $\varrho_{\mathrm{sys}i}$ ($i = 1, \ldots, 17$) of each of the seventeen contributions listed in table 7.3. This would give an additional column of correlations between V and $\rho^2_{A_1}$ in this table. However, the determination of these correlations is very complex. It is not enough to determine σ_{Vi} and $\sigma_{\rho i}$, the individual systematic uncertainties on V and $\rho^2_{A_1}$. One also needs to determine the shift of the mean value of the one parameter (say V) when fixing the other (say $\rho^2_{A_1}$) at various values.

An approximation for the calculation of ϱ_{sys} is given in the following lines. The covariance matrices C_i of the individual contributions listed in table 7.3 have to be added to obtain the total systematic covariance matrix C,

$$C = \sum_i C_i \tag{7.12}$$

with

$$C = \begin{pmatrix} \sigma_V^2 & \varrho_{\mathrm{sys}}\,\sigma_V\,\sigma_\rho \\ \varrho_{\mathrm{sys}}\,\sigma_V\,\sigma_\rho & \sigma_\rho^2 \end{pmatrix} \qquad C_i = \begin{pmatrix} \sigma_{Vi}^2 & \varrho_{\mathrm{sys}i}\,\sigma_{Vi}\,\sigma_{\rho i} \\ \varrho_{\mathrm{sys}i}\,\sigma_{Vi}\,\sigma_{\rho i} & \sigma_{\rho i}^2 \end{pmatrix} \tag{7.13}$$

and

$$\sigma_V^2 = \sum_i \sigma_{Vi}^2 \qquad\qquad \sigma_\rho^2 = \sum_i \sigma_{\rho i}^2. \tag{7.14}$$

Therefore the total systematic correlation ϱ_{sys} is given by

$$\varrho_{\mathrm{sys}} = \frac{\sum_i \varrho_{\mathrm{sys}i}\,\sigma_{Vi}\,\sigma_{\rho i}}{\sigma_V\,\sigma_\rho}. \tag{7.15}$$

Let us regard the sum in the numerator of the latter equation. For all summands with $\sigma_{\rho i} = 0$ the value of $\varrho_{\text{sys}i}$ does not influence this numerator.[4] For all summands with $\sigma_{\rho i} \neq 0$ one can make the reasonable assumption $\varrho_{\text{sys}i} = 1$. This gives the value $\varrho_{\text{sys}} = 0.43$.

Another possibility to extract the systematic correlation ϱ_{sys} is to exploit the total systematic uncertainty $\sigma_{\mathcal{B}}$ on the branching fraction $\mathcal{B}_{\text{Sig}}$. Since the branching fraction is a function of V and $\rho_{A_1}^2$ (see equation 2.52) the uncertainty on $\mathcal{B}_{\text{Sig}}$ can be expressed by

$$\sigma_{\mathcal{B}}^2 = \left(\frac{\partial \mathcal{B}_{\text{Sig}}}{\partial V}\right)^2 \sigma_V^2 + \left(\frac{\partial \mathcal{B}_{\text{Sig}}}{\partial \rho_{A_1}^2}\right)^2 \sigma_\rho^2 + 2\left(\frac{\partial \mathcal{B}_{\text{Sig}}}{\partial \rho_{A_1}^2}\right)\left(\frac{\partial \mathcal{B}_{\text{Sig}}}{\partial V}\right)\varrho_{\text{sys}}\sigma_V\sigma_\rho. \tag{7.16}$$

Because all terms except ϱ_{sys} are known from the last row of table 7.3 and from equation 2.52 one can calculate ϱ_{sys} by resolving the equation 7.16 for ϱ_{sys},

$$\varrho_{\text{sys}} = \frac{\sigma_{\mathcal{B}}^2 - \left(\frac{\partial \mathcal{B}_{\text{Sig}}}{\partial V}\right)^2 \sigma_V^2 - \left(\frac{\partial \mathcal{B}_{\text{Sig}}}{\partial \rho_{A_1}^2}\right)^2 \sigma_\rho^2}{2\left(\frac{\partial \mathcal{B}_{\text{Sig}}}{\partial V}\right)\left(\frac{\partial \mathcal{B}_{\text{Sig}}}{\partial \rho_{A_1}^2}\right)\sigma_V\sigma_\rho}. \tag{7.17}$$

This yields a value of $\varrho_{\text{sys}} = 0.45$ which is close to 0.43, the value of the approximation using $\varrho_{\text{sys}i} = 1$. Since $\varrho_{\text{sys}} = 0.45$ does not need this assumption it is used as systematic correlation between V and $\rho_{A_1}^2$.

---

[4]In fact, the ith correlation is not defined if $\sigma_{\rho i} = 0$.

Chapter 8

Conclusion

8.1 Summary of the Analysis Method

The Standard Model of Particle Physics (SM) summarizes the present-day knowledge of fundamental particles and their interactions. It is a very successful model used as starting point of many predictions that have been confirmed in experiments of the last decades.

One of the experiments checking the SM predictions is the *BABAR* experiment whose detector is situated at the PEP-II storage rings at the Stanford Linear Accelerator Center in California. One of its major tasks is to perform measurements which give constraints to the SM parameters defining the CKM matrix. The high statistic data sample of pairs of B meson decays collected by the *BABAR* detector allows for very precise measurements which in turn gives a high sensitivity to the consistency between measurements and SM predictions.

The measurement of the decay $B^- \to D^{*0} e^- \overline{\nu}_e$ does not only give a value of the CKM matrix element $|V_{cb}|$. It also gives constraints for the description of hadrons, namely the form factor parameter $\rho_{A_1}^2$. In addition, the measurement of the branching fraction $\mathcal{B}\left(B^- \to D^{*0} e^- \overline{\nu}_e\right)$ is possible. All of this three numbers are determined in this analysis which is briefly summarized in the following lines.

The analysis is based on a data sample of 226 million B meson pairs whose decays were recorded by the *BABAR* detector. It is divided into the following two steps:

1. Reconstruction of $B^- \to D^{*0} e^- \overline{\nu}_e$ decays defining a sample of possible signal candidates,

2. Description of this sample by the result of a fit of an expectation function to this sample.

The main idea in the first part is the application of a set of selection criteria enhancing the fraction of correctly reconstructed $B^- \to D^{*0} e^- \overline{\nu}_e$ decays. Of high importance are the clean electron and kaon identification provided by the *BABAR* detector. The second step has two tasks. On the one hand it contains the determination of the background fraction in the sample of reconstructed signal candidates. This is done by exploiting the separation power of the two variables Δm and $\cos\theta_{\mathrm{BY}}$. On the other hand it also contains the determination of the product $F(1)|V_{cb}|$ and the form factor parameter $\rho_{A_1}^2$, where $F(w|\rho_{A_1}^2)$ is a form factor as a function of the relativistic boost w of the D^{*0} meson in the B rest frame. The sensitivity on $\rho_{A_1}^2$ is given by the variable $\tilde{w}$ estimating the true value of w. The branching fraction $\mathcal{B}\left(B^- \to D^{*0} e^- \overline{\nu}_e\right)$ is directly determined from the obtained values of $F(1)|V_{cb}|$ and $\rho_{A_1}^2$ by an integration of $d\Gamma/dw$ over the allowed values of w.

8.2 Results

The result depends on a set of input parameters whose values are given by [8, 33]:

$$\mathcal{B}\left(\Upsilon(4S) \to B^+B^-\right) = (50.6 \pm 0.8)\%$$
$$\mathcal{B}\left(D^{*0} \to D^0\pi^0\right) = (61.9 \pm 2.9)\%$$
$$\mathcal{B}\left(D^0 \to K^-\pi^+\right) = (3.80 \pm 0.07)\%$$
$$\mathcal{B}\left(\pi^0 \to \gamma\gamma\right) = (98.798 \pm 0.032)\% \qquad (8.1)$$
$$\tau_{B^+} = (1.638 \pm 0.011)\,\text{ps}$$
$$R_1 = 1.396 \pm 0.075$$
$$R_2 = 0.885 \pm 0.047$$

When using this set of input parameters the analysis yields

$$F(1)|V_{cb}| = (35.8 \pm 0.5 \pm 1.1 \pm 1.0) \cdot 10^{-3}$$
$$\rho_{A_1}^2 = (1.08 \pm 0.05 \pm 0.05 \pm 0.07) \qquad (8.2)$$
$$\mathcal{B}\left(B^- \to D^{*0}e^-\overline{\nu}_e\right) = (5.60 \pm 0.08 \pm 0.25 \pm 0.34)\%,$$

where the uncertainties are statistical, analysis-internal systematic and analysis-external systematic. The correlations from the statistical and the systematic covariance matrix between $F(1)|V_{cb}|$ and $\rho_{A_1}^2$ are found to be

$$\varrho_{\text{stat}} = 0.86 \quad \text{and}$$
$$\varrho_{\text{sys}} = 0.45, \qquad (8.3)$$

respectively. The addition of the covariance matrices gives a total correlation of

$$\varrho = 0.51 \qquad (8.4)$$

between $F(1)|V_{cb}|$ and $\rho_{A_1}^2$.

Using $F(1) = 0.914 \pm 0.026$ as stated in equation 2.59, the measured value of $F(1)|V_{cb}|$ can be translated into a value for the CKM matrix element $|V_{cb}|$,

$$|V_{cb}| = (39.2 \pm 0.5 \pm 1.6 \pm 1.1) \cdot 10^{-3}, \qquad (8.5)$$

where the uncertainties are statistical, total experimental systematic and total theoretical systematic, respectively.

8.3 Comparison with other Measurements

Interpretation of $\rho_{A_1}^2$

As mentioned before, the form factor ratios R_1 and R_2 are very important input parameters for this analysis. The two numbers were taken from a measurement [33] using reconstructed $\overline{B}^0 \to D^{*+}e^-\overline{\nu}_e$ decays. The authors of [33] did not only determine R_1 and R_2, simultaneously they also determined $\rho_{A_1}^2$.

By taking R_1 and R_2 from [33] one assumes that the decays $\overline{B}^0 \to D^{*+}e^-\overline{\nu}_e$ and $B^- \to D^{*0}e^-\overline{\nu}_e$ are governed by one and the same theory (described in section 2.2). This assumption is motivated by the isospin symmetry between the two decays. Since the value of $\rho_{A_1}^2$ stated in equation 8.2 is compatible with the value from [33] ($\rho_{A_1}^2 = 1.15 \pm 0.07$), the assumption that the same theory applies to both decays is confirmed.
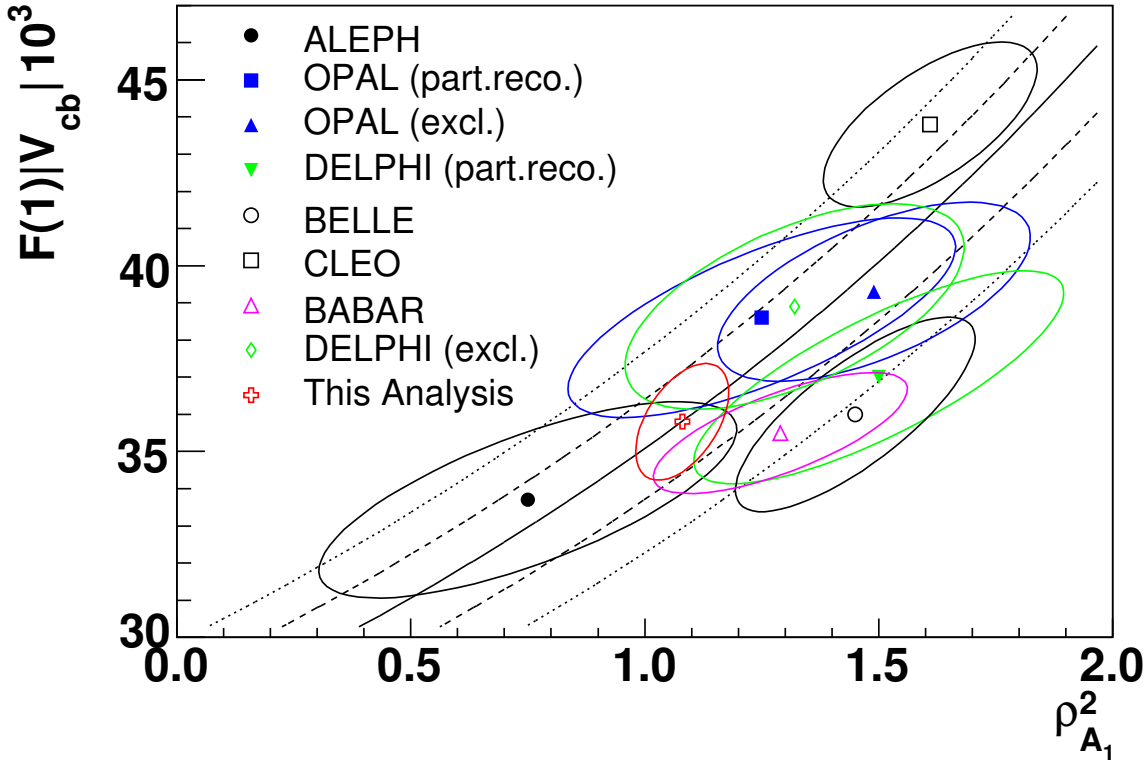
Figure 8.1: Shown is a comparison between $F(1)|V_{cb}|$ and $\rho^2_{A_1}$ with measurements obtained by ALEPH [87], OPAL [88], DELPHI [89, 90], CLEO [74], BABAR [73] and BELLE [91]. All measurements have been rescaled to a common set of input parameters (see equation 8.1) by the HFAG [85]. The diagonal lines are lines of constant branching fraction corresponding to the result of this analysis (solid: central value, dashed: $\pm 1\sigma$, dotted: $\pm 2\sigma$).

$F(1)|V_{cb}|$ and $\rho^2_{A_1}$

To compare the results of different measurements with each other one needs to translate these different measurements to one common set of input parameters. The *Heavy Flavor Averaging Group* (HFAG) [85] performs this translation for various measurements of $(F(1)|V_{cb}|, \rho^2_{A_1})$. The result of this translation for the parameter set called *Winter 2006*[1] is shown in figure 8.1. Within the uncertainties the values obtained in this analysis agree with the other measurements. Only the CLEO measurement [74] differs considerably.

It is very important to note that nearly all the values shown in the comparison plot rely on measurements of the decay $\overline{B}^0 \to D^{*+}e^-\overline{\nu}_e$. Only the CLEO experiment used both channels together, $\overline{B}^0 \to D^{*+}e^-\overline{\nu}_e$ and $B^- \to D^{*0}e^-\overline{\nu}_e$.[2]

The predominant uncertainty on $\rho^2_{A_1}$ comes from the uncertainty of the form factor ratios which could be improved recently [33, 86]. The measurements compared to the results of this analysis used R_1 R_2 input values with larger uncertainties, thus their error ellipses in figure 8.1 are broader.

---

[1]The parameter set *Winter 2006* is identical to the parameter set used in this analysis (see equations 8.1).

[2]The CLEO collaborators found nearly equal results when analyzing $\overline{B}^0 \to D^{*+}e^-\overline{\nu}_e$ decays and $B^- \to D^{*0}e^-\overline{\nu}_e$ decays separately.
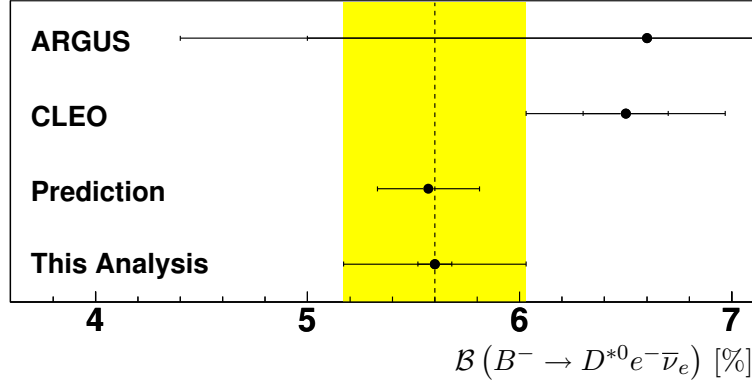
Figure 8.2: Comparison of the branching fraction $\mathcal{B}\left(B^- \to D^{*0}e^-\overline{\nu}_e\right)$ with two other measurements [93, 92] and a prediction from an average value of $\mathcal{B}\left(\overline{B}^0 \to D^{*+}e^-\overline{\nu}_e\right)$ [8] (see text). The inner error bars are statistical and the outer are statistical and systematic combined. (Instead of the original ARGUS value reported in [93] an rescaled value [8] is shown.)

$\mathcal{B}\left(B^- \to D^{*0}e^-\overline{\nu}_e\right)$

The branching fraction $\mathcal{B}\left(B^- \to D^{*0}e^-\overline{\nu}_e\right)$ has been measured before by the ARGUS collaboration [93] and the CLEO collaboration [92]. In addition it can be predicted from the averaged branching fraction $\mathcal{B}\left(\overline{B}^0 \to D^{*+}e^-\overline{\nu}_e\right) = 0.0520 \pm 0.0024$ [8] exploiting the isospin symmetry $(\Gamma(B^- \to D^{*0}e^-\overline{\nu}_e) = \Gamma(\overline{B}^0 \to D^{*+}e^-\overline{\nu}_e))$ and the B lifetime ratio $(\tau_{B+}/\tau_{B^0} = 1.071 \pm 0.009)$ [8]. Figure 8.2 compares these three values to the branching fraction measured in this analysis. The result of this analysis and the prediction are in good agreement. This agreement to the measurements in the channel $\overline{B}^0 \to D^{*+}e^-\overline{\nu}_e$ is also illustrated by the lines of constant branching fraction in figure 8.1.

Assuming consistency between the three measurements shown in figure 8.1 one can calculate the weighted mean $\overline{\mathcal{B}}(B^- \to D^{*0}e^-\overline{\nu}_e)$ which is in good approximation the mean between this measurement and the measurement of CLEO,

$$\overline{\mathcal{B}}(B^- \to D^{*0}e^-\overline{\nu}_e) = (6.02 \pm 0.48)\%. \tag{8.6}$$

However, the correct averaging procedure has also to take into account the correlation between the systematic uncertainties.

Appendix A

Reconstruction and Selection

A.1   Reconstruction and Selection in the τ analysis

The authors of the τ analysis [61] apply selection criteria which support the accumulation of $e^+e^- \to \tau^+\tau^-$ events. Roughly spoken, they select events with exactly two oppositely charged tracks where one of these tracks is very consistent with an electron hypothesis[1] (e track) and the other track is treated by the pion hypothesis (π track). Additionally taking into account the EMC bumps, each selected event is assigned to one of the following two categories:

1. If there are no (unmatched) EMC bumps in the event then the event is assigned to the $\tau \to \pi$ category.

2. An event is assigned to the $\tau \to \rho$ category if it contains a π^0 candidate with very loose selection criteria (mass lower than $0.250\,\mathrm{GeV}/c^2$, momentum greater than $0.1\,\mathrm{GeV}/c$). If there are additional EMC bumps beside the one[2] or two bumps necessary for the π^0 reconstruction then the event is not selected. The event also remains unselected if the reconstructed mass ($m_{\pi\pi^0}$) of the π track and the π^0 does not satisfy $0.55\,\mathrm{GeV}/c^2 < m_{\pi\pi^0} < 1.00\,\mathrm{GeV}/c^2$. This criteria supports the '$\tau \to \rho\nu, \rho \to \pi\pi^0$' hypothesis of the π-track associated τ decay.

There are some further selection criteria applied in the τ analysis, all aiming at purer samples of events with $\tau \to \rho\nu$ decays and $\tau \to \pi\nu$ decays. Important to note is that only one PID selection criteria has been applied to the π tracks: The energy-momentum-ratio E/p oft the charged π candidate has to be lower than 0.8 to suppress $\tau \to e\nu\bar{\nu}$ decays[3]. Waiving additional PID selection criteria for the π tracks reduces the final systematic uncertainties. Consequently, in the $\tau \to \pi$ category there are more events then only $\tau \to \pi\nu$ events included, e.g. there are also the similar $\tau \to K\nu$ and $\tau \to \mu\nu\bar{\nu}$ events included. But also events that should have been sorted into the category 2 contribute to the category 1, e.g. the π^0 of the $\rho \to \pi\pi^0$ decay could be missed entirely as a function of EMC acceptance. To complete the thoughts, the events contributing to the $\tau \to \rho$ category contain not only $\tau \to \rho\nu$ decays but also, e.g. $\tau \to K^*\nu, K^* \to \pi\pi^0$ decays, or

---

[1]The electron is selected by PidLHElectrons selector.

[2]The τ analysis takes also into account so-called merged π^0 candidates reconstructed from only one single EMC bump. Within the laboratory system, the two photons of a high-energetic π^0 meson mostly form a small angle leading to non-separable electromagnetic showers in the EMC, leading to one single bump after the reconstruction. Due to coming from D^{*0} mesons, the π^0 mesons reconstructed in the semileptonic analysis are very low-energetic and produce two separate bumps. Thus, merged π^0 mesons are not interesting at this point.

[3]In this case the 'π track' was caused by the electron.

$\tau \to a_1\nu, a_1 \to \pi\pi^0\pi^0$ decays where one of the neutral a_1-daughters flew into an EMC acceptance hole. Summarizing, if one would be more correct then equation 4.24 would have to be replaced by

$$\frac{N^\rho}{N^\pi} \propto \frac{\varepsilon_{\pi^0}\left[\varepsilon_\pi\mathcal{B}\left(\tau\to\rho\nu\right) + \varepsilon_K\mathcal{B}\left(\begin{smallmatrix}\tau\to K^*\nu,\\K^*\to K\pi\end{smallmatrix}\right) + \varepsilon_\pi(1-\varepsilon_{\pi^0})\mathcal{B}\left(\begin{smallmatrix}\tau\to a_1\nu\\a_1\to\pi\pi^0\pi^0\end{smallmatrix}\right)\right]\varepsilon_e\mathcal{B}\left(\tau\to e\nu\bar\nu\right)}{\left[\varepsilon_\pi\mathcal{B}\left(\tau\to\pi\nu\right) + \varepsilon_\mu\mathcal{B}\left(\tau\to\mu\nu\bar\nu\right) + \varepsilon_K\mathcal{B}\left(\tau\to K\nu\right) + \varepsilon_\pi(1-\varepsilon_{\pi^0})\mathcal{B}\left(\tau\to\rho\nu\right)\right]\varepsilon_e\mathcal{B}\left(\tau\to e\nu\bar\nu\right)},$$
(A.1)

but even that would only be an approximation.

After the events have been assigned to $\tau \to \rho$ and $\tau \to \pi$ categories, two corrections are applied (for more detailed description see [61]):

Low-Energy Background Photons There are events which should have been assigned to the $\tau \to \pi$ category but due to the presence of background photons the event was assigned to the $\tau \to \rho$ category. The following correction is performed: Events with exactly one bump are shifted from the $\tau \to \rho$ category into the $\tau \to \pi$ category if the bump energy is less than $0.1\,\mathrm{GeV}$. Events with two bumps are shifted from the $\tau \to \rho$ category into the $\tau \to \pi$ category if the sum of the two bump energies is less than $0.135\,\mathrm{GeV}$.

Hadronic Split-offs A hadron (e.g. a pion) interacts with the EMC material by electromagnetic and hadronic interaction processes. As a result of the hadronic interaction, secondary hadrons can be generated. If these secondary particles have (i) a large enough life time and (ii) a very small probability to deposit energy in the EMC, then they can produce second EMC cluster, separated from the primary EMC cluster. Such a cluster is called *hadronic split-off*. The τ analysis performs a correction due to these split-offs.

A.2 Values of the Variable $\cos\theta_{\mathrm{BY}}$ for Non-Signal Decays

Assume that one reconstructs the true decay $B \to D^{*0}Xe^-\bar\nu_e$ in the channel $B^- \to D^{*0}e^-\bar\nu_e$ and the reconstructed D^{*0} (electron) is matched to the true D^{*0} (electron). In other words, the D^{*0} meson and the electron come from the same true B meson but the neutrino is not the only non-reconstructed particle. What happens to the value of $\cos\theta_{\mathrm{BY}}$? Let's start from four-momentum conservation of the true decay,

$$p_B = p_\nu + p_Y + p_X.$$
(A.2)

The equation can be transformed like this (The four four-momentum vectors are taken from the truth-side of the event.):

$$p_B - p_Y = p_\nu + p_X$$
(A.3a)

$$m_B^2 + m_Y^2 - 2E_BE_Y + 2\vec{p}_B\vec{p}_Y = m_\nu^2 + m_X^2 + 2E_\nu E_X - 2\vec{p}_\nu\vec{p}_X$$
(A.3b)

$$-m_B^2 - m_y^2 + 2E_BE_Y = -m_\nu^2 - m_X^2 - 2E_\nu E_X + 2\vec{p}_\nu\vec{p}_X + 2\vec{p}_B\vec{p}_Y$$
(A.3c)

$$\underbrace{\frac{-m_B^2 - m_Y^2 + 2E_BE_Y}{2\,|\vec{p}_B|\,|\vec{p}_Y|}}_{=(\cos\theta_{\mathrm{BY}})_{\mathrm{rec}}} = \underbrace{-\frac{m_X^2 + 2E_\nu(E_X - p_X\cos\sphericalangle(\nu,X))}{2\,|\vec{p}_B|\,|\vec{p}_Y|}}_{=\Delta_X} + \underbrace{\frac{2\vec{p}_B\vec{p}_Y}{2\,|\vec{p}_B|\,|\vec{p}_Y|}}_{=(\cos\theta_{\mathrm{BY}})_{\mathrm{true}}}$$
(A.3d)

$$(\cos\theta_{\mathrm{BY}})_{\mathrm{rec}} = \Delta_X + (\cos\theta_{\mathrm{BY}})_{\mathrm{true}}$$
(A.3e)

The term $(\cos\theta_{\mathrm{BY}})_{\mathrm{true}}$ must have values between -1 and $+1$. Due to $p_X \le E_X$ the first term on the right side always satisfies $\Delta_X \le 0$. Now it should be clear: If a particle X is missing in the

reconstruction of the B decay then the reconstructed value of $\cos\theta_{\mathrm{BY}}$ $(= (\cos\theta_{\mathrm{BY}})_{\mathrm{rec}})$ can have values below -1 but not above $+1$. For low-energetic photons $(X = \gamma)$ additionally created in the B decay the the effect is not so drastic. But for $X = \pi$ the distribution of $= (\cos\theta_{\mathrm{BY}})_{\mathrm{rec}}$ gets a long tail to values below -1. This is helpful to discriminate against decays like $B \to D^{**}e\nu, D^{**} \to D^{*0}\pi$.

Appendix B

Fit Method

B.1 Correlations between Δm and $\cos\theta_{\mathrm{BY}}$

Table B.1: The table lists the correlation for each of the 24 candidate classes defined in table 5.1. The correlations are determined from the selected MC candidates. They are given in percent and as a function of $\tilde{w}$. The uncertainties are calculated using a method given in [78]. For candidate classes belonging to true signal decays the correlation trends to positive values, as expected. In general, the correlations are very small and the approximation of uncorrelated $\Delta m \cos\theta_{\mathrm{BY}}$ distributions is a good one.

j	Candidate Class	$1.00 < \tilde{w} < 1.15$			$1.15 < \tilde{w} < 1.30$			$1.30 < \tilde{w} < 1.51$		
1	Sig	0.99	$\pm$	0.49	0.25	$\pm$	0.41	0.08	$\pm$	0.45
2	$D^{**}e\nu\,(1)$	-0.81	$\pm$	1.08	0.86	$\pm$	1.11	2.36	$\pm$	1.24
3	Correlated	2.38	$\pm$	3.34	-4.55	$\pm$	3.58	0.48	$\pm$	3.45
4	Uncorrelated	-0.85	$\pm$	1.14	1.35	$\pm$	2.05	2.47	$\pm$	3.67
5	SemiSig (1)	0.21	$\pm$	0.64	0.62	$\pm$	0.52	0.92	$\pm$	0.57
6	SemiSig (2)	1.07	$\pm$	0.77	0.77	$\pm$	0.69	1.17	$\pm$	0.8
7	SemiSig (3)	1.32	$\pm$	0.5	0.42	$\pm$	0.48	0.58	$\pm$	0.62
8	SemiSig (4)	1.59	$\pm$	2.58	1.41	$\pm$	2.88	5.79	$\pm$	3.47
9	SigLike (1)	5.76	$\pm$	3.73	-8.22	$\pm$	3.34	-4.94	$\pm$	4.2
10	SigLike (2)	2.55	$\pm$	3.8	3.64	$\pm$	3.42	7.26	$\pm$	4.49
11	SigLike (3)	0.38	$\pm$	0.64	0.38	$\pm$	0.62	-0.35	$\pm$	0.8
12	$D^{*\pm}e\nu$	1.09	$\pm$	0.48	0.63	$\pm$	0.46	-0.05	$\pm$	0.6
13	$D^0 e\nu(1)$	-1.24	$\pm$	1.66	0.88	$\pm$	0.88	-3.5	$\pm$	0.65
14	$D^0 e\nu(2)$	-1.07	$\pm$	0.99	-0.4	$\pm$	1.5	-2.29	$\pm$	2.11
15	$D^0\pi e\nu$	0.84	$\pm$	0.96	2.6	$\pm$	1.4	-0.05	$\pm$	2.78
16	$D^{**}e\nu(2)$	0.37	$\pm$	0.51	0.48	$\pm$	0.57	1.33	$\pm$	0.7
17	CombD^{*0} (1)	-0.61	$\pm$	1.56	2.41	$\pm$	1.74	-1.15	$\pm$	1.64
18	CombD^{*0} (2)	-1.68	$\pm$	1.11	4.52	$\pm$	3.11	-14.21	$\pm$	6.18
19	CombD^{*0} (3)	-1.03	$\pm$	0.42	-0.67	$\pm$	1.02	3.48	$\pm$	2.23
20	CombD^{*0} (4)	-2.53	$\pm$	2.24	-1.76	$\pm$	2.77	0.43	$\pm$	3.3
21	CombD^{*0} (5)	2.96	$\pm$	1.02	9.08	$\pm$	1.36	8.88	$\pm$	2.04
22	CombD^{*0} (6)	-0.6	$\pm$	0.43	1.83	$\pm$	0.61	-0.16	$\pm$	0.96
23	$c\bar{c}$(peak)	7.33	$\pm$	8.94	-0.85	$\pm$	5.57	-0.11	$\pm$	2.23
24	$c\bar{c}$(flat)	-2.84	$\pm$	1.4	-1.84	$\pm$	1.82	0.85	$\pm$	1.25

B.2 Quality Check for the Product Ansatz

In the figures of this appendix there are plots showing the quality of the product ansatz from equation 5.8. For each of the 24 candidate classes there are two plots.

1. There is a deviation plot between two differently generated histograms of the Δm-$\cos\theta_{\mathrm{BY}}$-distribution. The bins (a,b) of the first histogram are filled with M_{ab}, the selected reweighted MC events in bin (a,b). The bins (a,b) of the second histogram are filled with I_{ab}, the integral of $\sum_{i=1}^{10} N_{ij}^{\mathrm{RMC}} \hat{P}_{ij}^{\mathrm{RMC}} (\Delta m, \cos\theta_{\mathrm{BY}})$ over the (a,b)-bin range. The deviation plot shows the quantity

$$D_{ab} = \frac{M_{ab} - I_{ab}}{\sigma_{M_{ab}}}, \tag{B.1}$$

where $\sigma_{M_{ab}}$ is the statistic uncertainty on M_{ab}. About 95.5% of all bins should have a deviation between -2 and 2. If there are regions where $\hat{P}_{ij}^{\mathrm{RMC}}$ is a bad description of the selected candidates, then the colors of the deviation plot are more reddish (underestimation) or more bluish (overestimation). If all colors are homogeneously distributed over the Δm-$\cos\theta_{\mathrm{BY}}$-plane of the deviation plot then $\hat{P}_{ij}^{\mathrm{RMC}}$ is a well-describing function. In this case the product ansatz from equation5.8 is a good ansatz.

2. The quantity shown in the first quality plot should be a deviation by chance. Therefore, the histogramming of the various deviations D_{ab} should result into a Gaussian distribution with mean=0 and sigma=1. The second quality plot shows this Gaussian-expected distribution together with the expected gauss function. Because the distribution is spoiled in case of low statistics I require at least five candidates per bin. If there are less candidates in a bin then the bin is merged with the next bins until there are five candidates.

The resulting $2 \cdot 24 = 48$ plots are shown in figures B.1 to B.8. Figure B.9 shows the two quality plots for the sum of all 24 candidate classes.
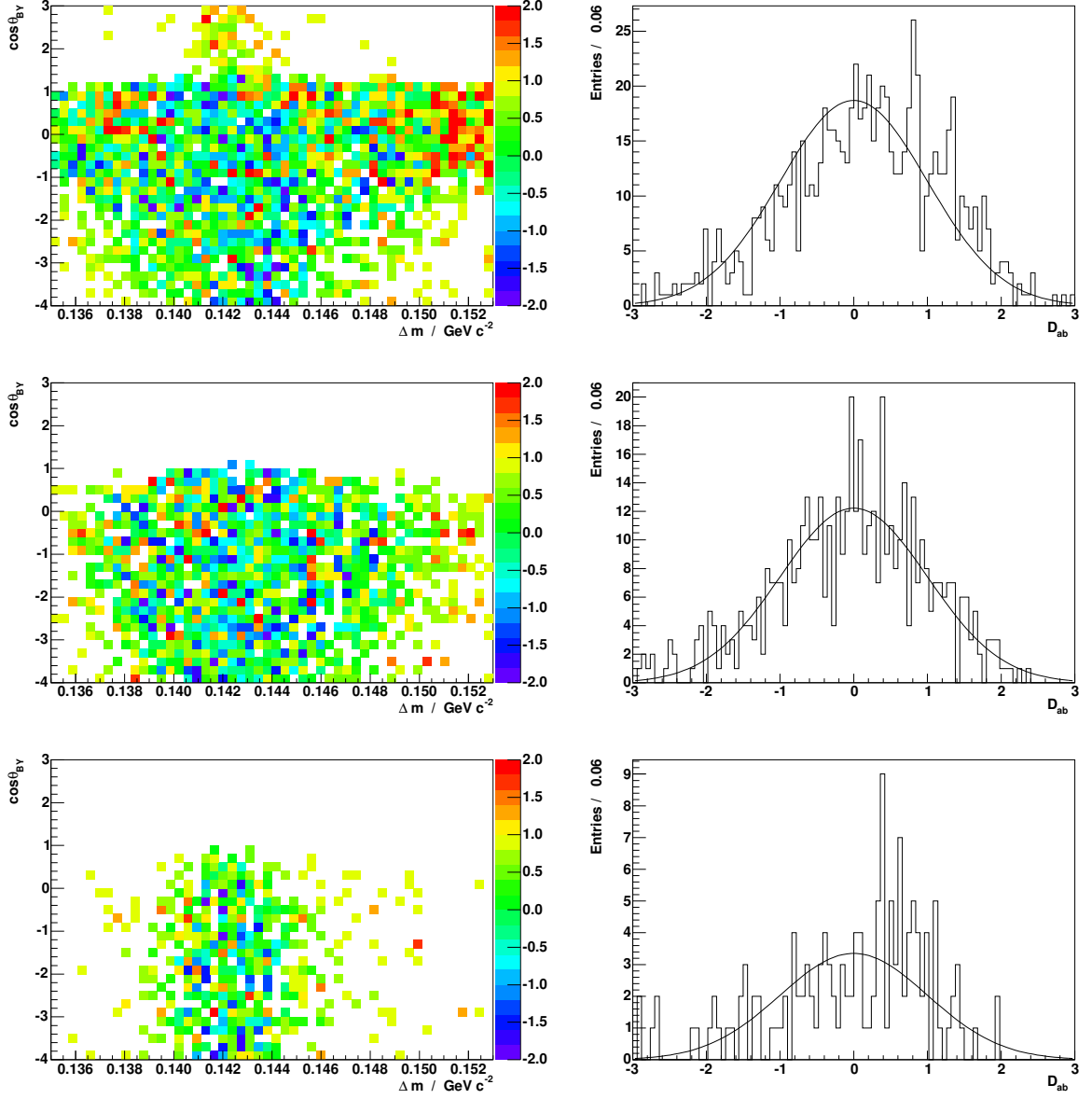
Figure B.1: From the top row to the bottom row there are plots for the candidate classes 'Sig', '$D^{**}e\nu\,(1)$', and 'Correlated' (see table 5.1). The left plots show deviations D_{ab} between the Δm-$\cos\theta_{\mathrm{BY}}$-distribution in RMC and its description by PDFs. The right plots show the frequency distribution of the deviations from the left plots. For more detailed description see page 126.
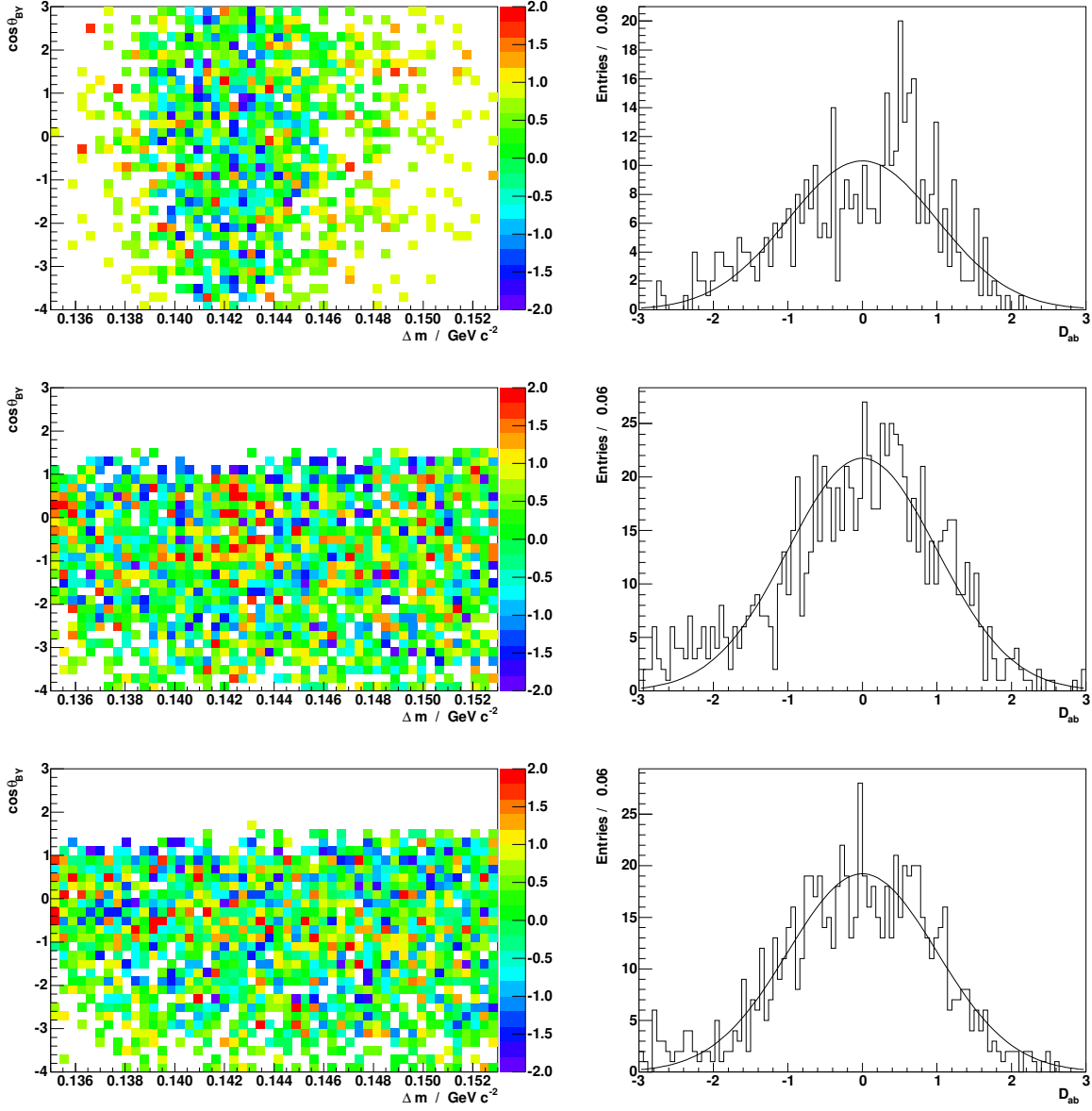
Figure B.2: From the top row to the bottom row there are plots for the candidate classes 'Uncorrelated', 'SemiSig (1)', and 'SemiSig (2)' (see table 5.1). The left plots show deviations D_{ab} between the Δm-$\cos \theta_{\mathrm{BY}}$-distribution in RMC and its description by PDFs. The right plots show the frequency distribution of the deviations from the left plots. For more detailed description see page 126.
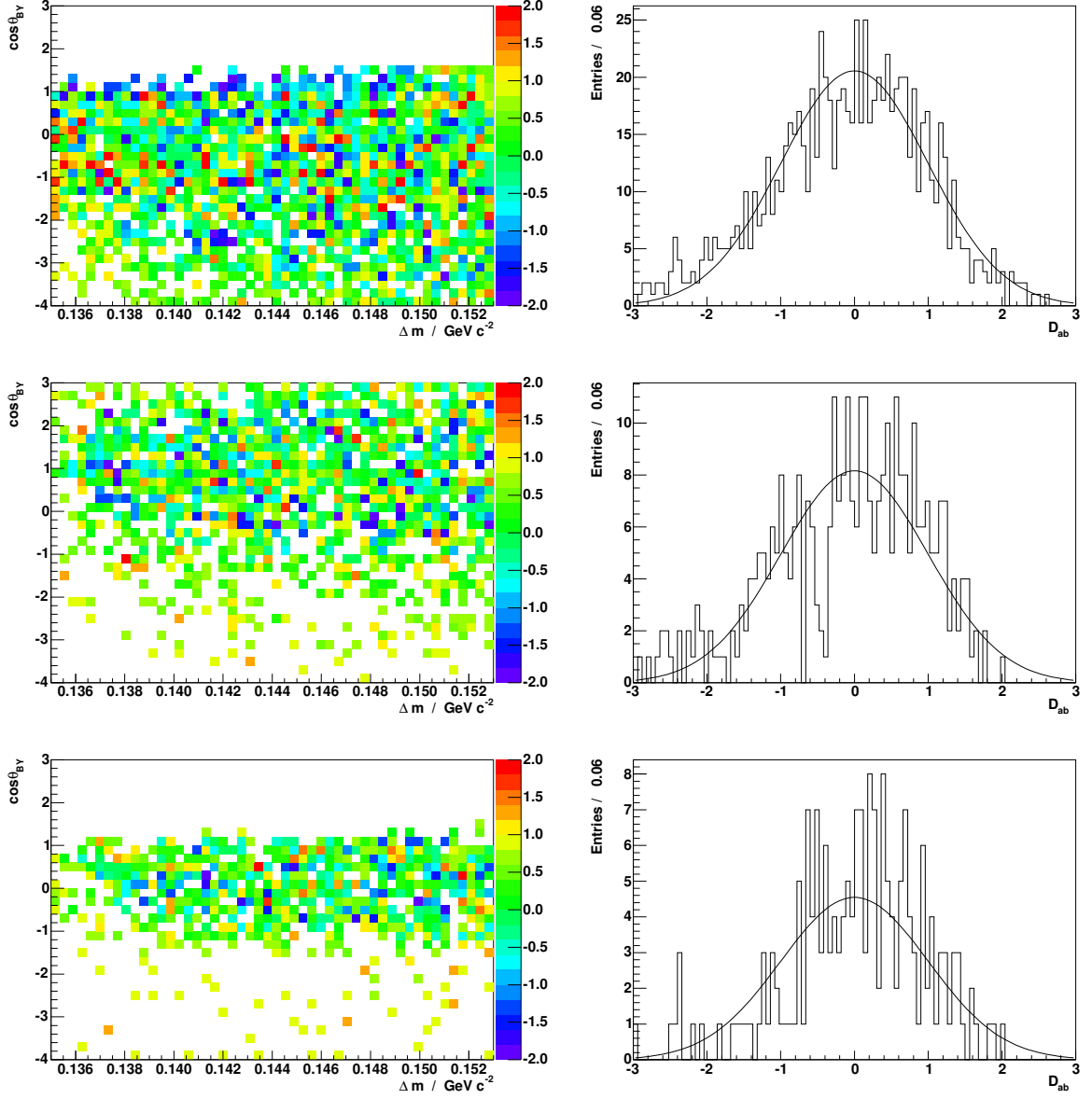
Figure B.3: From the top row to the bottom row there are plots for the candidate classes 'SemiSig (3)', 'SemiSig (4)', and 'SigLike (1)' (see table 5.1). The left plots show deviations D_{ab} between the Δm-$\cos\theta_{\mathrm{BY}}$-distribution in RMC and its description by PDFs. The right plots show the frequency distribution of the deviations from the left plots. For more detailed description see page 126.

129
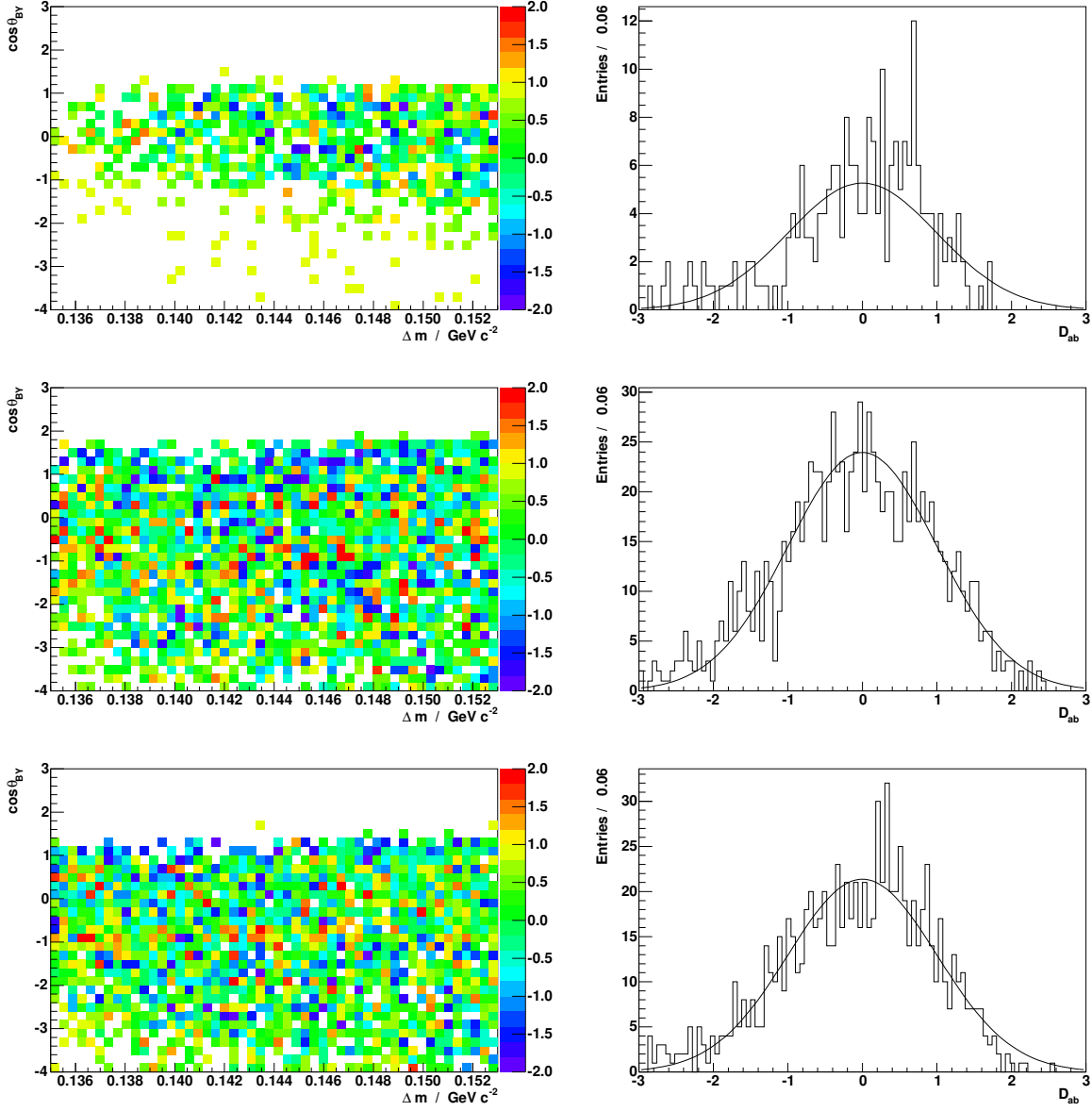
Figure B.4: From the top row to the bottom row there are plots for the candidate classes 'SigLike (2)', 'SigLike (3)', and 'D*$^{\pm}$eν' (see table 5.1). The left plots show deviations D_{ab} between the Δm-cos θ_{BY}-distribution in RMC and its description by PDFs. The right plots show the frequency distribution of the deviations from the left plots. For more detailed description see page 126.
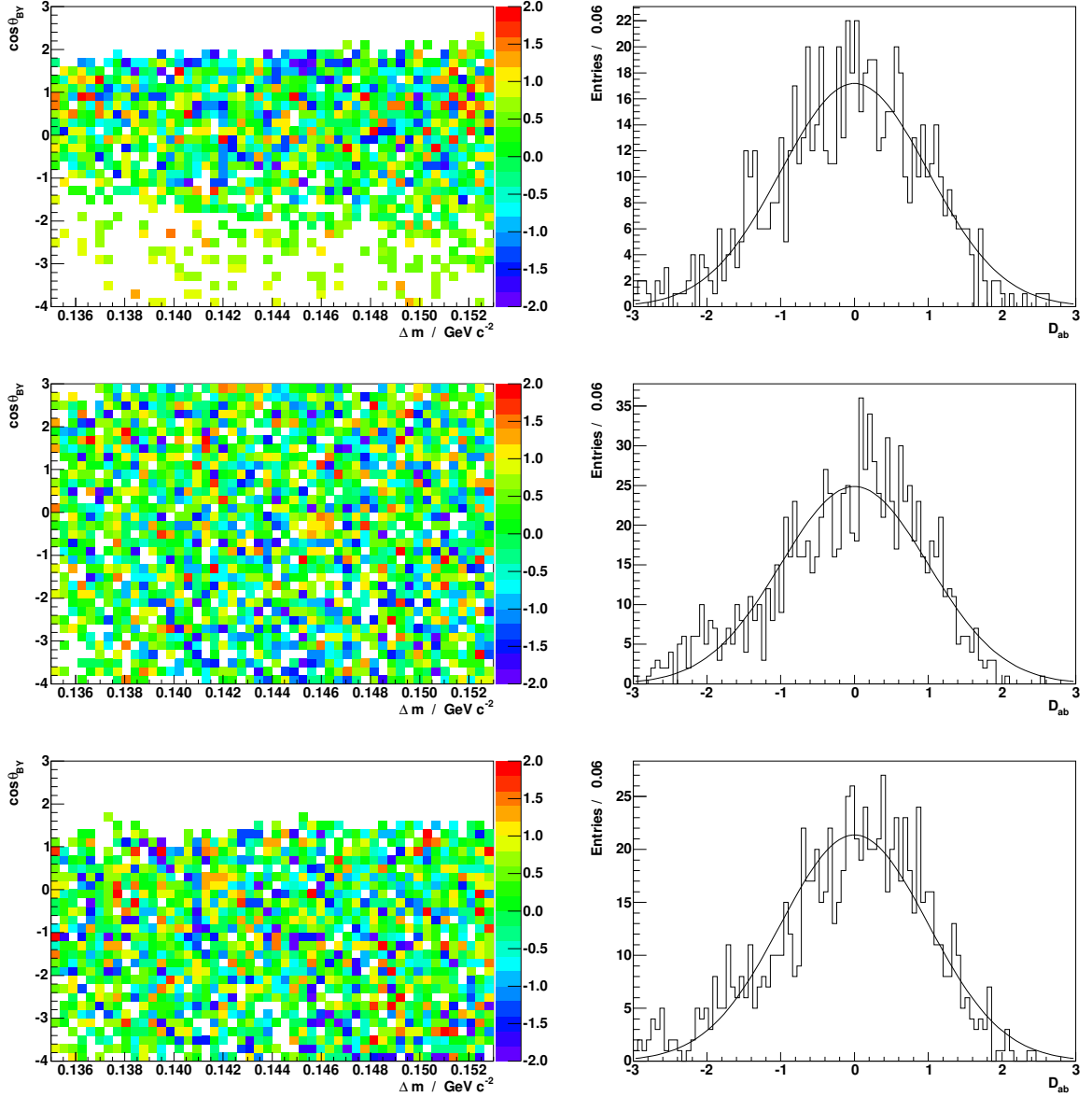
Figure B.5: From the top row to the bottom row there are plots for the candidate classes '$D^0 e\nu(1)$', '$D^0 e\nu(2)$', and '$D^0 \pi e\nu$' (see table 5.1). The left plots show deviations D_{ab} between the Δm-$\cos\theta_{\mathrm{BY}}$-distribution in RMC and its description by PDFs. The right plots show the frequency distribution of the deviations from the left plots. For more detailed description see page 126.
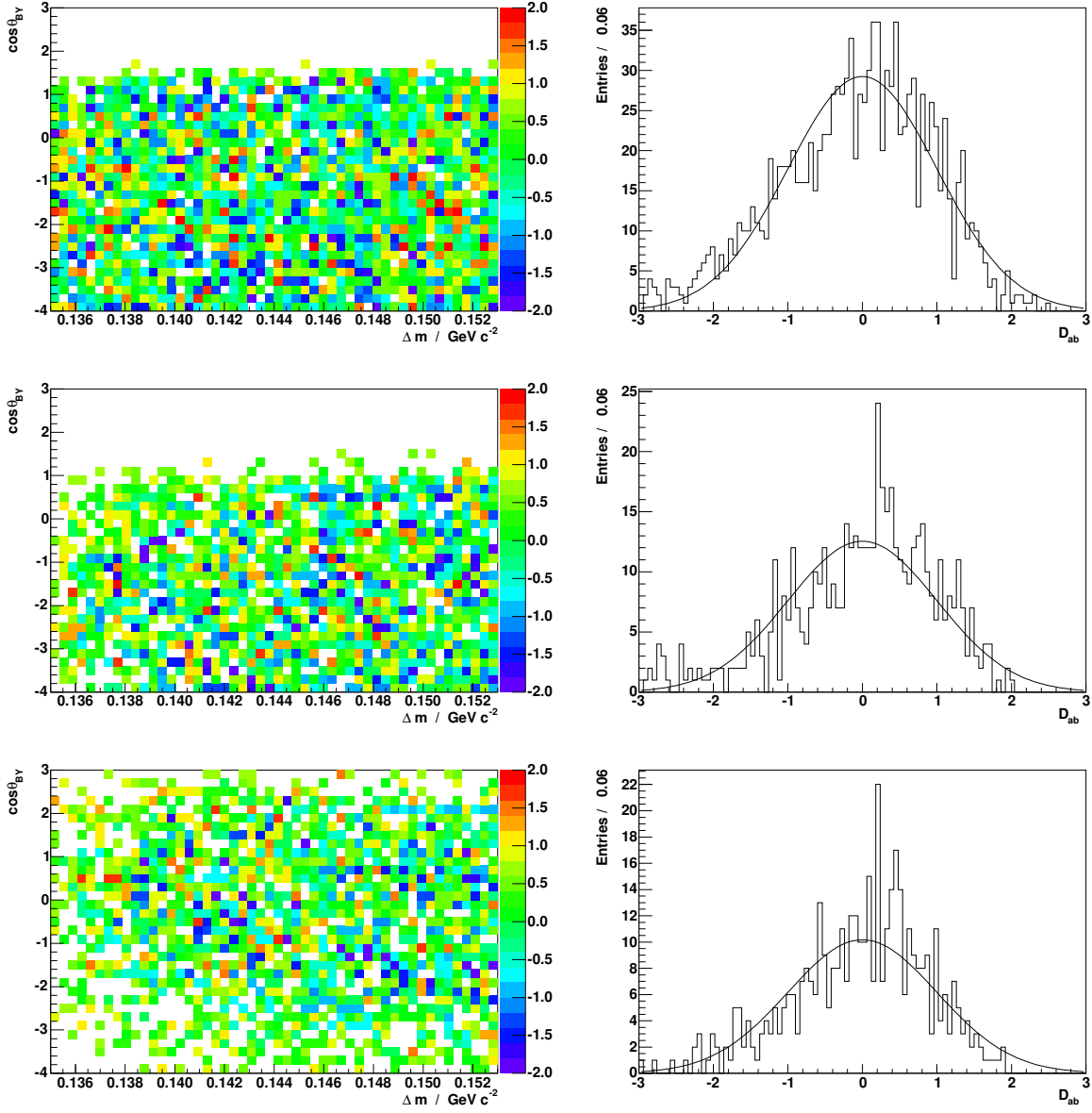
Figure B.6: From the top row to the bottom row there are plots for the candidate classes '$D^{**}e\nu(2)$', 'Comb$D^{*0}(1)$', and 'Comb$D^{*0}(2)$' (see table 5.1). The left plots show deviations D_{ab} between the Δm-$\cos\theta_{\mathrm{BY}}$-distribution in RMC and its description by PDFs. The right plots show the frequency distribution of the deviations from the left plots. For more detailed description see page 126.
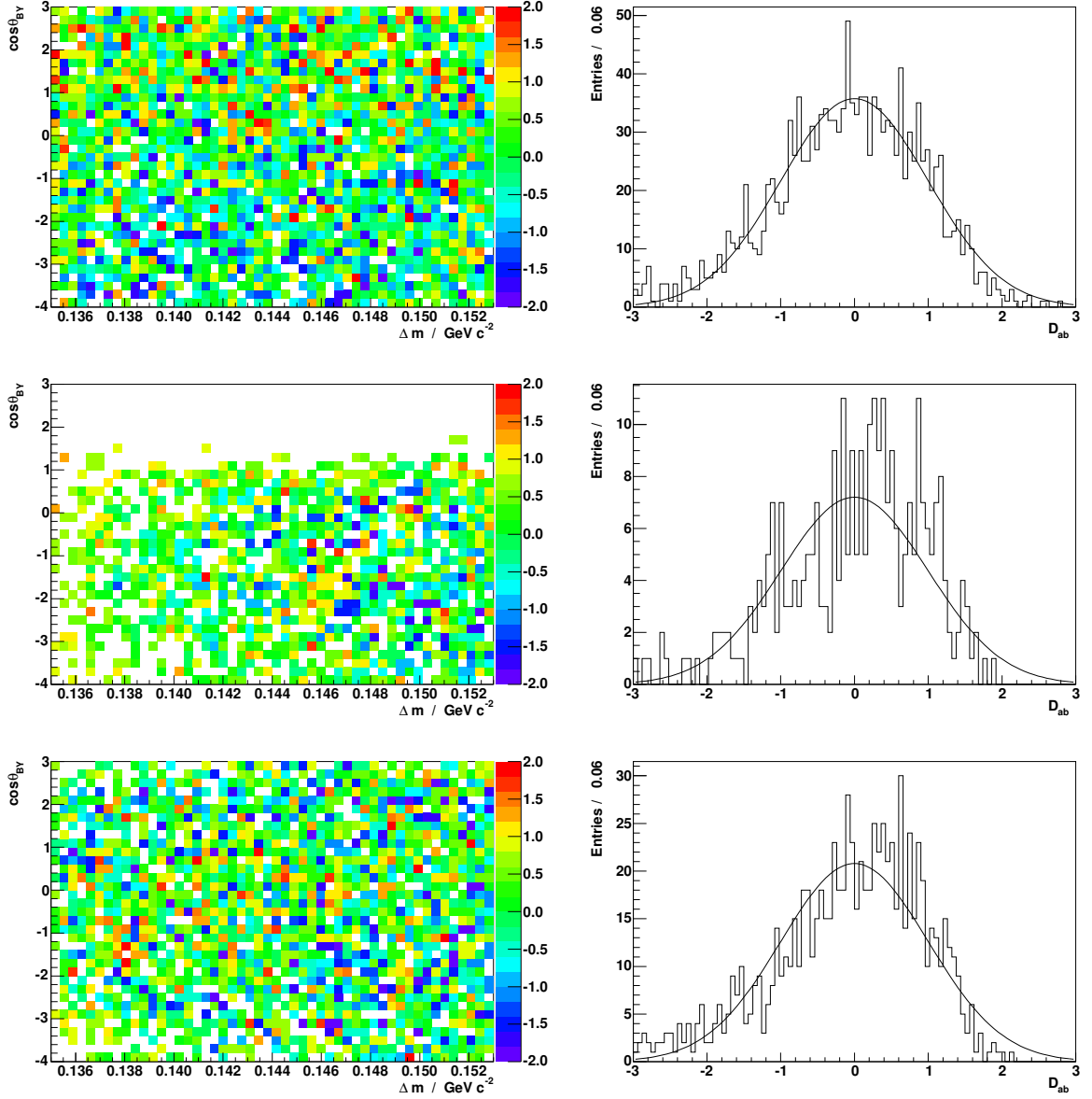
Figure B.7: From the top row to the bottom row there are plots for the candidate classes 'CombD^{*0} (3)', 'CombD^{*0} (4)', and 'CombD^{*0} (5)' (see table 5.1). The left plots show deviations D_{ab} between the Δm-cos θ_{BY}-distribution in RMC and its description by PDFs. The right plots show the frequency distribution of the deviations from the left plots. For more detailed description see page 126.
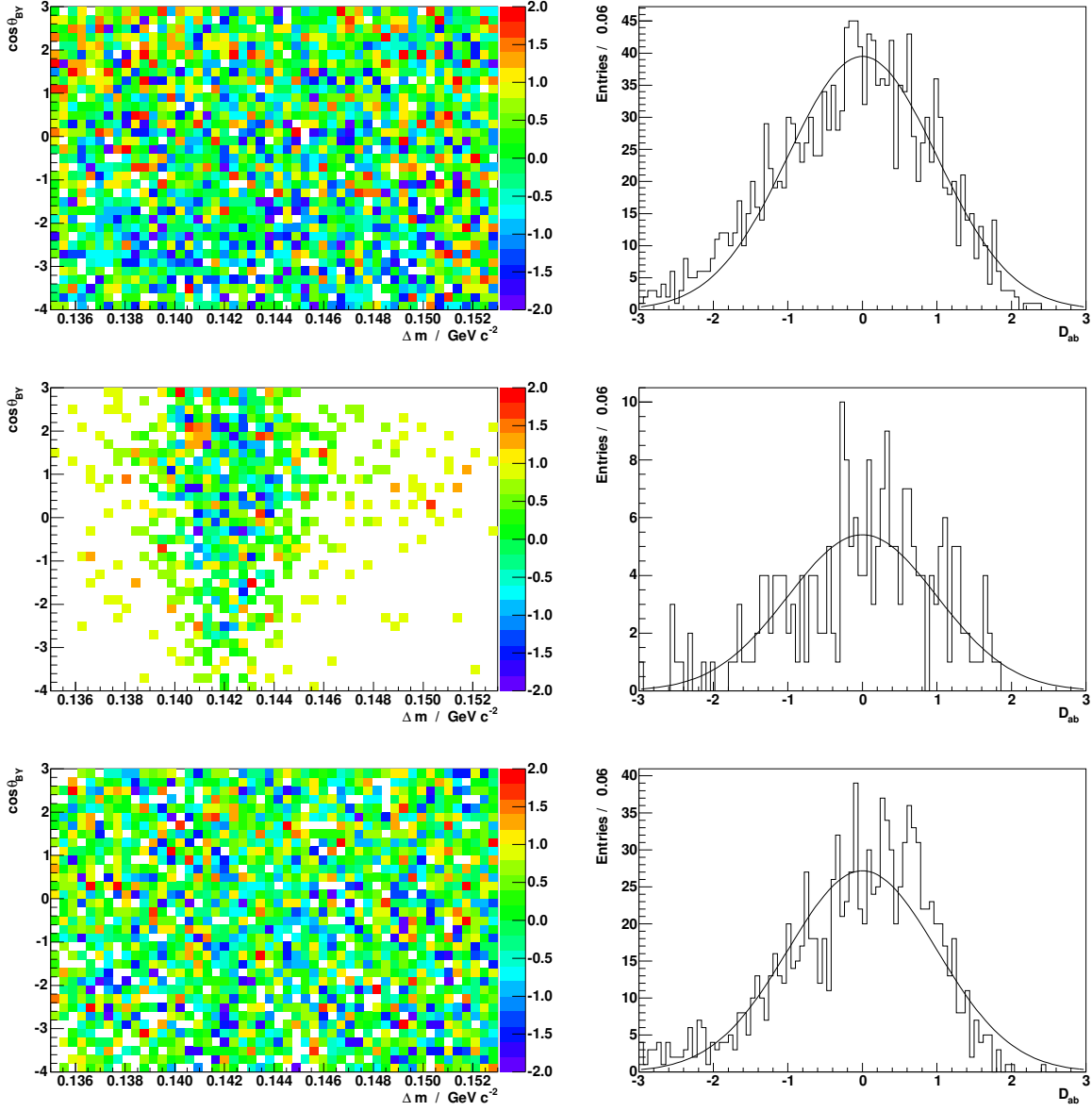
Figure B.8: From the top row to the bottom row there are plots for the candidate classes 'CombD^{*0} (6)', '$c\bar{c}$(peak)', and '$c\bar{c}$(flat)' (see table 5.1). The left plots show deviations D_{ab} between the Δm-$\cos\theta_{\mathrm{BY}}$-distribution in RMC and its description by PDFs. The right plots show the frequency distribution of the deviations from the left plots. For more detailed description see page 126.
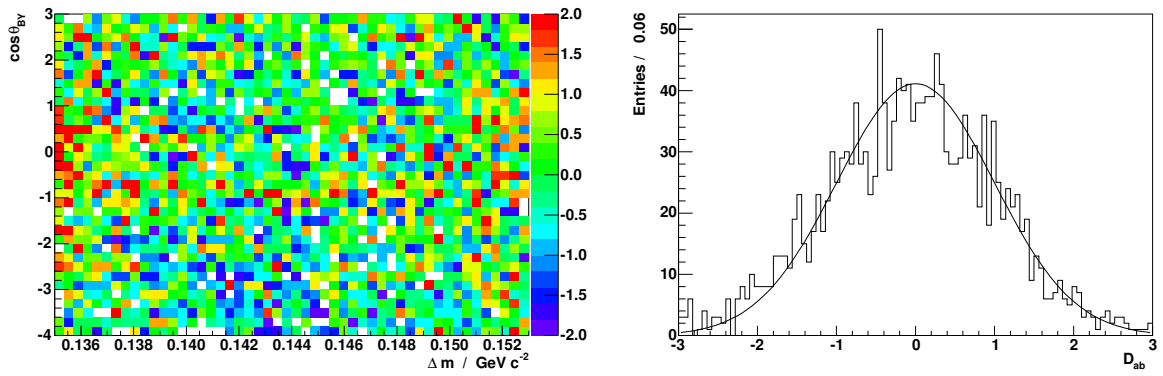
Figure B.9: The left plot shows deviations D_{ab} between the Δm-$\cos\theta_{\mathrm{BY}}$-distribution of all candidates in RMC and its description by PDFs. The right plot shows the frequency distribution of the deviations from the left plot. For more detailed description see page 126.

Appendix C

Fit Result

C.1 Fitted Parameters of $F^{\mathrm{Exp}}\left(\Delta m, \cos\theta_{\mathrm{BY}}, \tilde{w}\right)$

Table C.1 lists the values and the statistical uncertainties of all parameters of $F^{\mathrm{Exp}}\left(\Delta m, \cos\theta_{\mathrm{BY}}, \tilde{w}\right)$ determined by the fit. The listed values correspond to values of branching fractions and B life time assumed in the *BABAR* MC simulation (see table C.2). Appendix C.2 shows how the fitted values are translated to the currently best known values of analysis input parameters.

C.2 Translation of Fit Result from Simulation's Parameters to PDG Values

The expectation values $N_{i\,\mathrm{Sig}}^{\mathrm{Exp}}$ $(i = 1, \ldots, 10)$ for the numbers of correctly reconstructed signal candidates rely on input parameters of the *BABAR* MC simulation. These parameters are listed in table C.2. The input parameter in the simulation is indirect proportional to V^2 in case of branching fractions, and it is direct proportional to V^2 in case of the B life time.

Thus, to translate the fitted value V from a value using the input parameters x_i^{BMC} to a value using the input parameters x_i^{PDG} ($x =$ one of the parameters listed in table C.2) one has to scale the fitted value V in the following way

$$V \longmapsto V \times \sqrt{\frac{\tau_{B^+}^{\mathrm{PDG}}}{\tau_{B^+}^{\mathrm{BMC}}} \prod_m \frac{\mathcal{B}_m^{\mathrm{BMC}}}{\mathcal{B}_m^{\mathrm{PDG}}}}, \tag{C.1}$$

where the modi in the product are $m = \Upsilon(4S) \to B^+B^-,\ D^{*0} \to D^0\pi^0,\ D^0 \to K^-\pi^+,\ \pi^0 \to \gamma\gamma$. The less interesting parameters $S_{i\,\mathrm{Sig\,rel}}$ $(i = 1, \ldots, 10)$ have to be rescaled by the quadrature of the number used to rescale V to obtain a correct value for $N_{i\,\mathrm{Sig\,rel}}^{\mathrm{Data}} = S_{i\,\mathrm{Sig\,rel}} \cdot N_{i\,\mathrm{Sig\,rel}}^{\mathrm{Exp}}$

C.3 Comparison Plots between Data and Fitted Function

Figures C.1, C.2 and C.3 contain comparison plots of Δm and $\cos\theta_{\mathrm{BY}}$ distributions. Figure C.4 shows deviation plots between the fitted function and the data in the $\Delta m \cos\theta_{\mathrm{BY}}$ plane.

Table C.1: Fitted parameters of $F^{\mathrm{Exp}}\left(\Delta m, \cos\theta_{\mathrm{BY}}, \tilde{w}\right)$ corresponding to analysis input parameters as assumed in the *BABAR* MC simulation. The fitted parameters are translated as described in appendix C.2.

Parameter	Value			Parameter	Value		
$F(1)\lvert V_{cb}\rvert \cdot 10^3$	36.32	$\pm$	0.51	$S_{6\,D^{**}}$	0.534	$\pm$	0.061
$\rho^2_{A_1}$	1.083	$\pm$	0.046	$S_{7\,D^{**}}$	0.464	$\pm$	0.078
$q_{0(\Delta\mu^{\mathrm{Exp}})}/(\mathrm{MeV}/c^2)$	0.129	$\pm$	0.019	$S_{8\,D^{**}}$	0.389	$\pm$	0.090
$q_{1(\Delta\mu^{\mathrm{Exp}})}/(\mathrm{MeV}/c^2)$	-0.009	$\pm$	0.071	$S_{9\,D^{**}}$	0.116	$\pm$	0.099
$q_{0(\xi)}$	1.083	$\pm$	0.035	$S_{10\,D^{**}}$	0.37	$\pm$	0.13
$q_{1(\xi)}$	0.20	$\pm$	0.12	$S_{1\,\mathrm{Uncor}}$	0.81	$\pm$	0.14
$q_{0(\alpha)}$	0.010	$\pm$	0.012	$S_{2\,\mathrm{Uncor}}$	1.23	$\pm$	0.20
$q_{1(\alpha)}$	-0.081	$\pm$	0.048	$S_{3\,\mathrm{Uncor}}$	1.32	$\pm$	0.23
$q_{0(k)}$	0.9817	$\pm$	0.0068	$S_{4\,\mathrm{Uncor}}$	1.74	$\pm$	0.33
$q_{1(k)}$	-0.017	$\pm$	0.027	$S_{5\,\mathrm{Uncor}}$	1.94	$\pm$	0.47
$S_{1\,\mathrm{Sig\,rel}}$	0.804	$\pm$	0.027	$S_{6\,\mathrm{Uncor}}$	2.73	$\pm$	0.50
$S_{2\,\mathrm{Sig\,rel}}$	0.807	$\pm$	0.019	$S_{7\,\mathrm{Uncor}}$	1.38	$\pm$	0.62
$S_{3\,\mathrm{Sig\,rel}}$	0.789	$\pm$	0.017	$S_{8\,\mathrm{Uncor}}$	1.28	$\pm$	0.73
$S_{4\,\mathrm{Sig\,rel}}$	0.798	$\pm$	0.019	$S_{1\,\mathrm{Comb}\,D^{*0}}$	0.471	$\pm$	0.022
$S_{5\,\mathrm{Sig\,rel}}$	0.749	$\pm$	0.021	$S_{2\,\mathrm{Comb}\,D^{*0}}$	0.802	$\pm$	0.030
$S_{6\,\mathrm{Sig\,rel}}$	0.833	$\pm$	0.027	$S_{3\,\mathrm{Comb}\,D^{*0}}$	0.822	$\pm$	0.035
$S_{7\,\mathrm{Sig\,rel}}$	0.837	$\pm$	0.033	$S_{4\,\mathrm{Comb}\,D^{*0}}$	0.850	$\pm$	0.042
$S_{8\,\mathrm{Sig\,rel}}$	0.892	$\pm$	0.041	$S_{5\,\mathrm{Comb}\,D^{*0}}$	0.963	$\pm$	0.051
$S_{9\,\mathrm{Sig\,rel}}$	0.930	$\pm$	0.049	$S_{6\,\mathrm{Comb}\,D^{*0}}$	0.901	$\pm$	0.061
$S_{10\,\mathrm{Sig\,rel}}$	0.825	$\pm$	0.060	$S_{7\,\mathrm{Comb}\,D^{*0}}$	0.992	$\pm$	0.079
$S_{1\,D^{**}}$	1.068	$\pm$	0.065	$S_{8\,\mathrm{Comb}\,D^{*0}}$	1.18	$\pm$	0.11
$S_{2\,D^{**}}$	0.615	$\pm$	0.046	$S_{9\,\mathrm{Comb}\,D^{*0}}$	1.68	$\pm$	0.15
$S_{3\,D^{**}}$	0.707	$\pm$	0.044	$S_{10\,\mathrm{Comb}\,D^{*0}}$	0.87	$\pm$	0.25
$S_{4\,D^{**}}$	0.610	$\pm$	0.047	$S_{D^0 e\nu}$	0.539	$\pm$	0.029
$S_{5\,D^{**}}$	0.675	$\pm$	0.054				

Table C.2: The *BABAR* MC simulation (BMC) uses the input parameters listed in the second column. For the final result the fitted values of $F(1)\lvert V_{cb}\rvert$, $\rho^2_{A_1}$ and $\mathcal{B}_{\mathrm{Sig}}$ are translated to the currently best known values of input parameters (PDG [8]).

Input Parameter	BMC	PDG [8]
$\mathcal{B}\left(\Upsilon(4S) \to B^+B^-\right)$	50.0%	$(50.6 \pm 0.8)\%$
$\mathcal{B}\left(D^{*0} \to D^0\pi^0\right)$	61.9%	$(61.9 \pm 2.9)\%$
$\mathcal{B}\left(D^0 \to K^-\pi^+\right)$	3.83%	$(3.80 \pm 0.07)\%$
$\mathcal{B}\left(\pi^0 \to \gamma\gamma\right)$	98.8%	$(98.798 \pm 0.032)\%$
τ_{B^+}	1.674 ps	$(1.638 \pm 0.011)\,\mathrm{ps}$
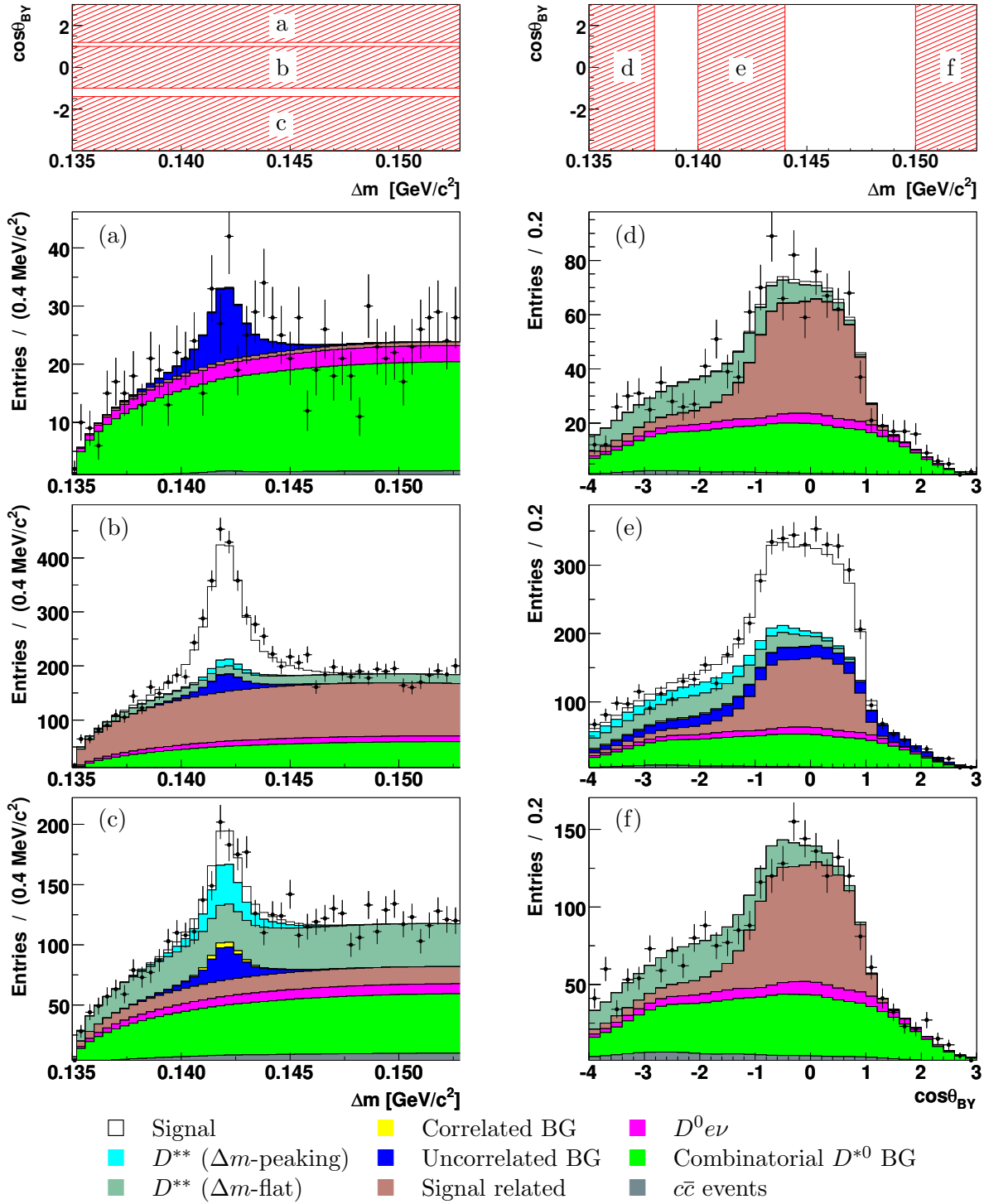
Figure C.1: The Δm and the $\cos\theta_{\mathrm{BY}}$ distribution of the data (points) are compared to the distributions modeled by the fitted function $F^{\mathrm{Exp}}(\Delta m, \cos\theta_{\mathrm{BY}}, \tilde{w})$ (stacked histograms, color code follows the classification of equation 5.49). The subfigures show the distributions in the signal bands (b,e) and in the side bands (a,c,d,f). The distributions are created using the lowest $\tilde{w}$ bin of the fit ($1.00 < \tilde{w} < 1.05$).
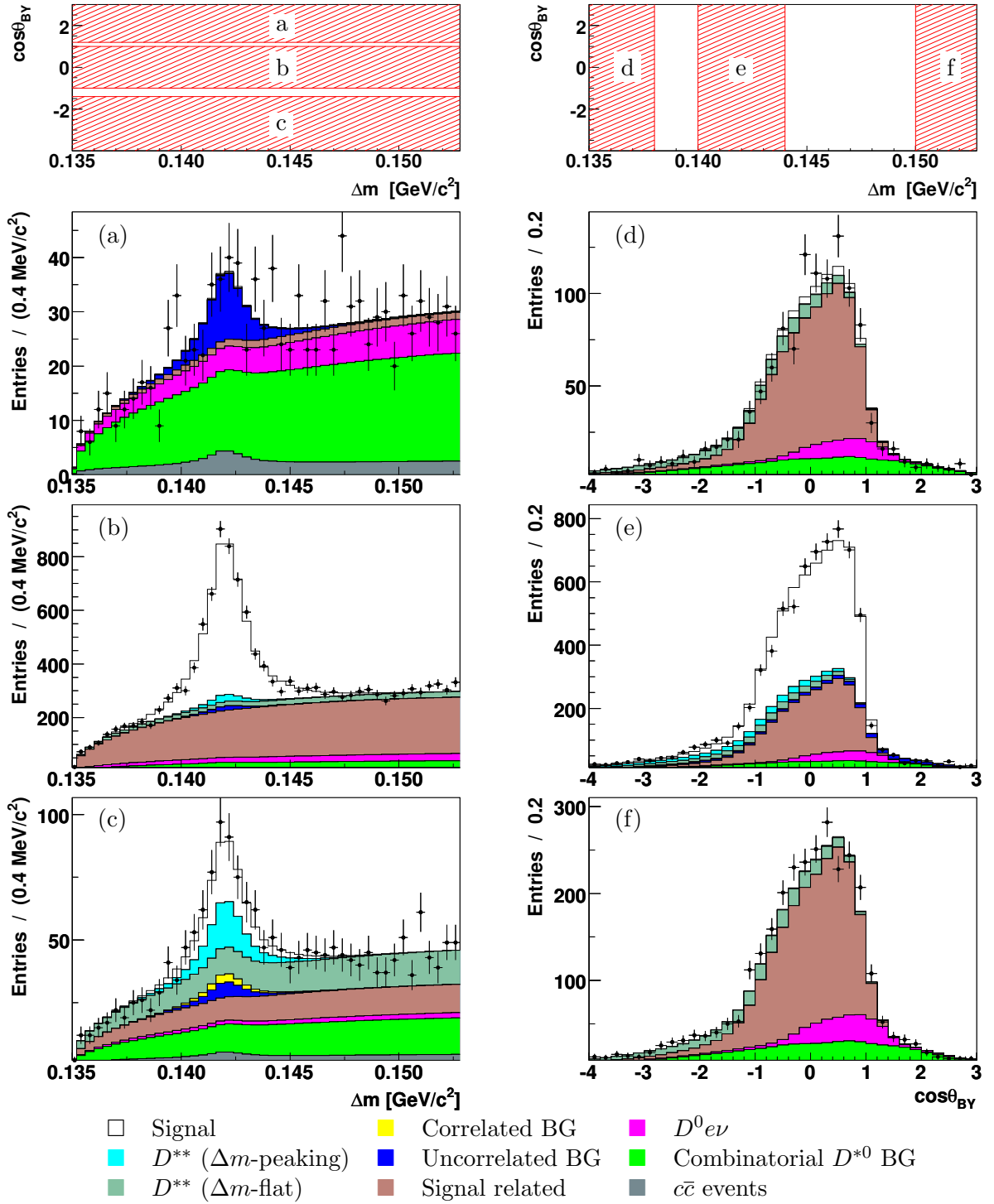
Figure C.2: The Δm and the $\cos\theta_{BY}$ distribution of the data (points) are compared to the distributions modeled by the fitted function $F^{Exp}(\Delta m, \cos\theta_{BY}, \tilde{w})$ (stacked histograms, color code follows the classification of equation 5.49). The subfigures show the distributions in the signal bands (b,e) and in the side bands (a,c,d,f). The distributions are created using the fifth $\tilde{w}$ bin of the fit ($1.20 < \tilde{w} < 1.25$).
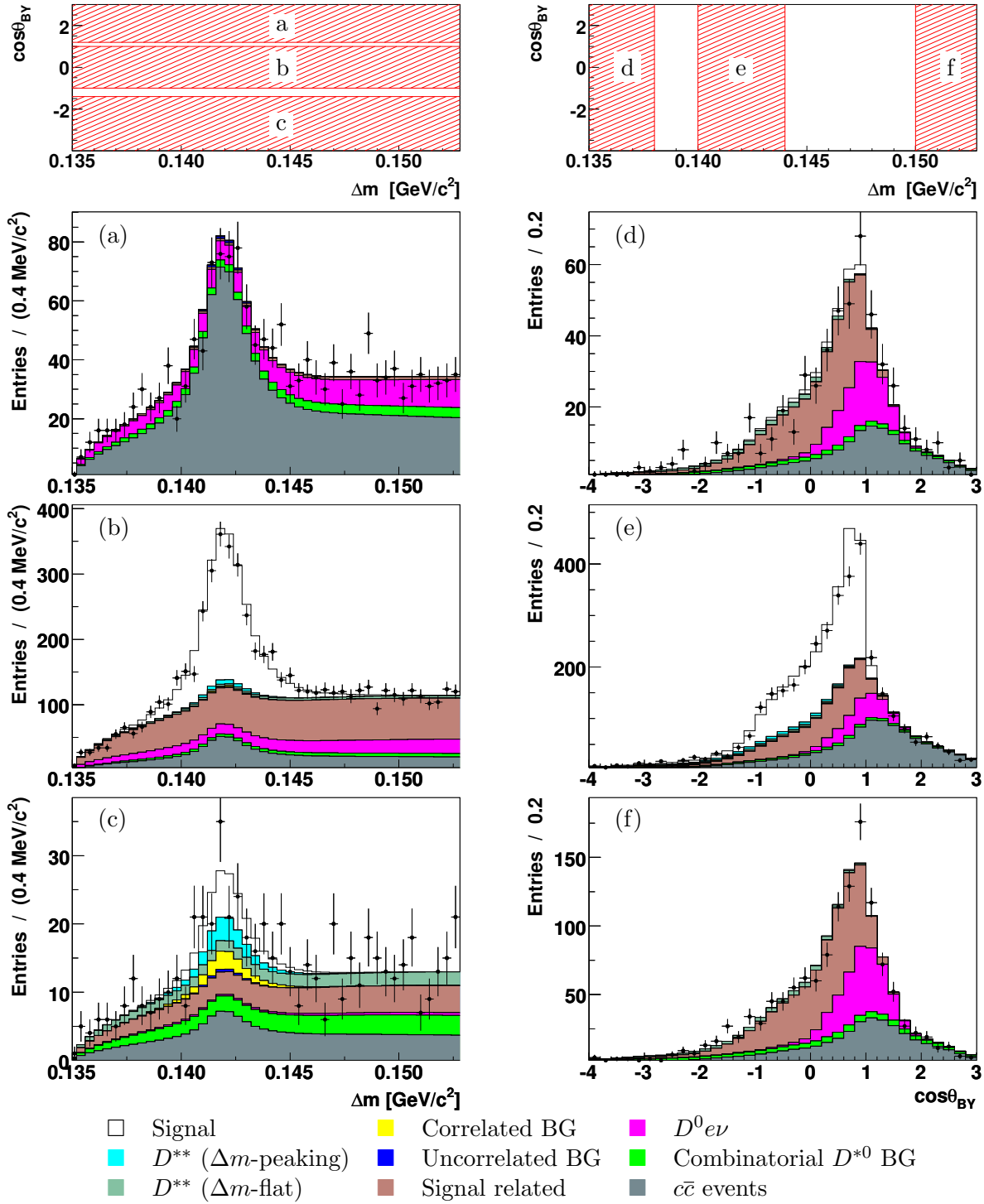
Figure C.3: The Δm and the $\cos\theta_{\mathrm{BY}}$ distribution of the data (points) are compared to the distributions modeled by the fitted function $F^{\mathrm{Exp}}(\Delta m, \cos\theta_{\mathrm{BY}}, \tilde{w})$ (stacked histograms, color code follows the classification of equation 5.49). The subfigures show the distributions in the signal bands (b,e) and in the side bands (a,c,d,f). The distributions are created using the highest $\tilde{w}$ bin of the fit ($1.45 < \tilde{w} < 1.51$).
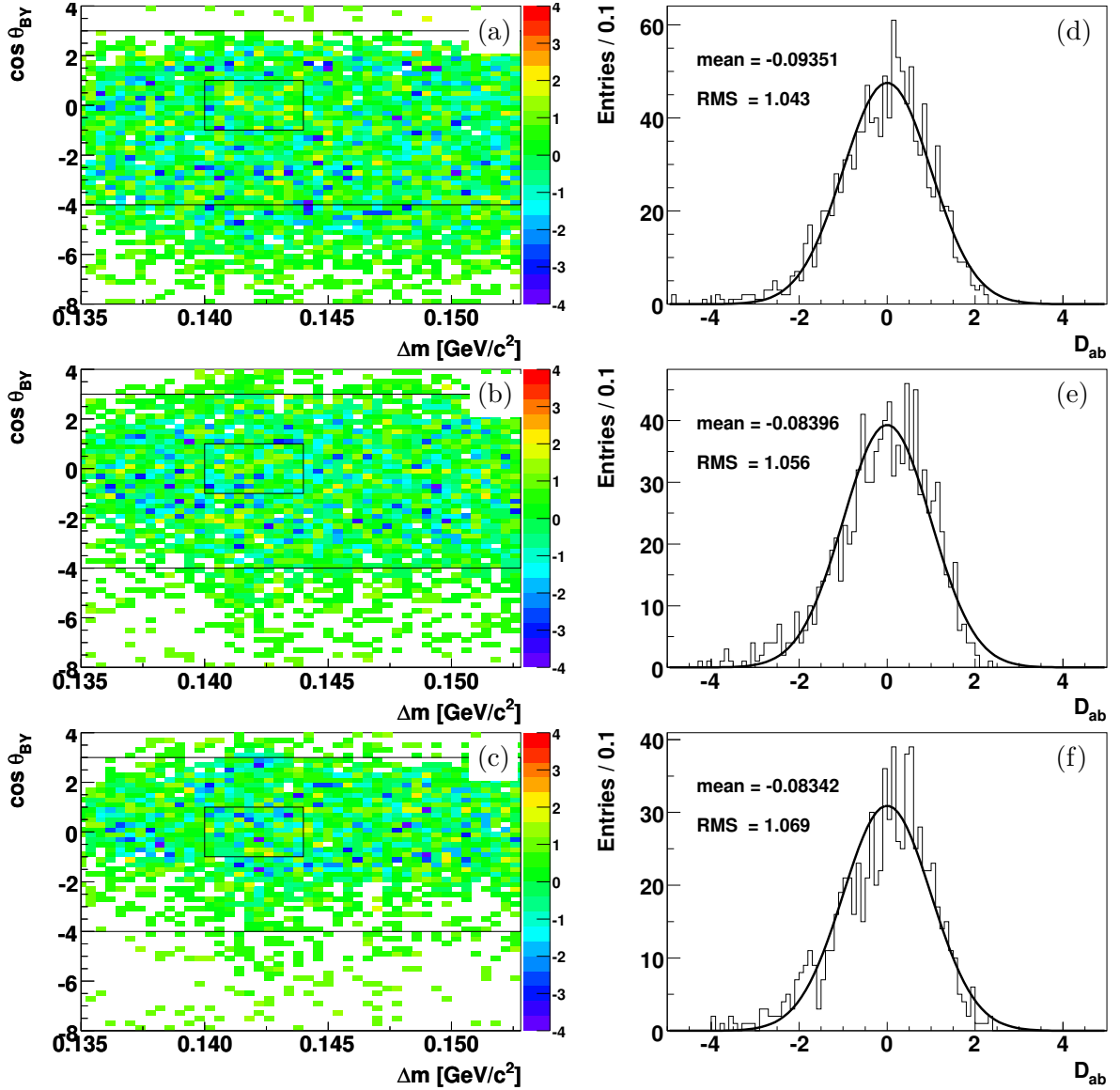
Figure C.4: The left plots show the bin-by-bin deviations D_{ab} (see equation 6.7) between the fitted function and the data in the Δm $\cos\theta_{BY}$ plane for **(a)** the first $\tilde{w}$ bin ($1.00 < \tilde{w} < 1.05$), **(b)** the fifth $\tilde{w}$ bin ($1.20 < \tilde{w} < 1.25$) and **(c)** the tenth $\tilde{w}$ bin ($1.45 < \tilde{w} < 1.51$). Since each color is homogeneously distributed over the three planes the fit function is a good description of the data. The values of D_{ab} shown in subfigure (a) are filled into a histogram shown in (d). If a bin content H_{ab} of the data histogram used to calculate D_{ab} is lower than 5 then the bin is merged with one of its neighbor bins until $H_{ab} \geq 5$ before the bin is filled into the histogram shown in (d). Analogously, subfigures (e) and (f) are created from subfigures (b) and (c), respectively. The shape of the right histograms is close to the expected shape (standard normal distribution which is also plotted) which means that the fitted function describes the data well.

The big and the small rectangles in the left plots show the fit range and the approximate signal range. The numbers shown in the left plots are the mean and the root mean square (RMS) of the D_{ab} frequency histogram.

Appendix D

Sytematics

D.1 π^0 Momentum Spectra in ten $\tilde{w}$ Bins
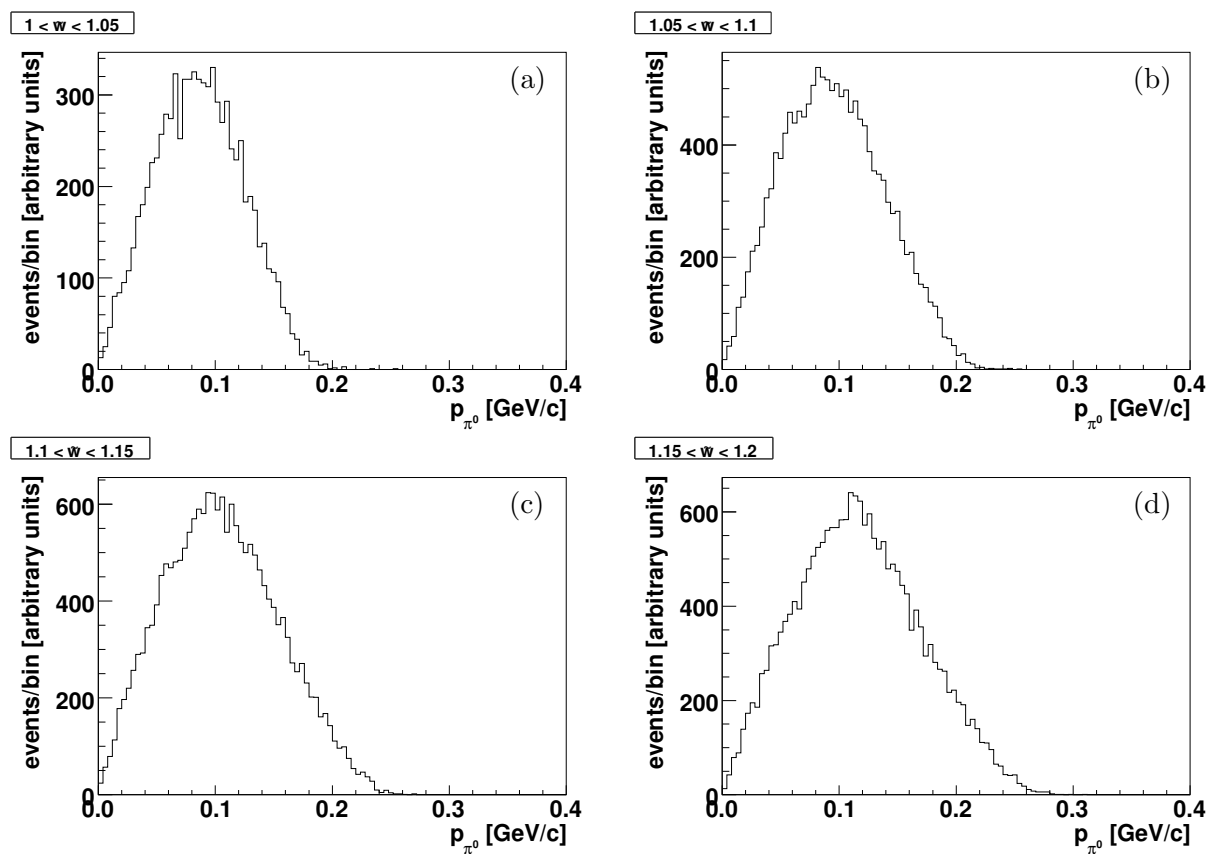
Figure D.1: The plots show the π^0 momentum spectra for Y candidates fully matched to a signal decay. The plots show unweighted *BABAR* MC.
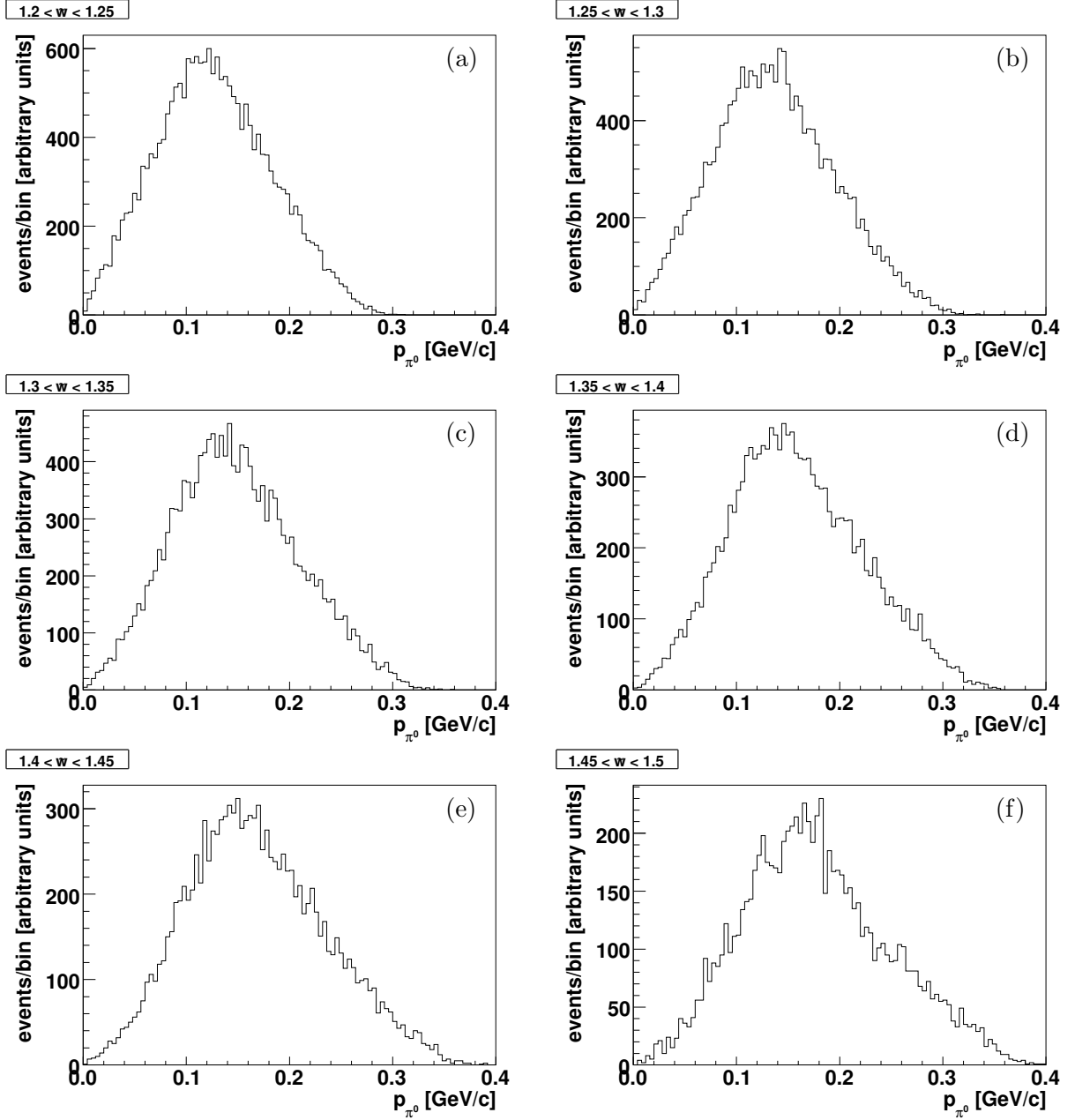
Figure D.2: The plots show the π^0 momentum spectra for Y candidates fully matched to a signal decay. The plots show unweighted *BABAR* MC.

List of Figures

List of Tables

Bibliography

[1] R. Davis, Prog. Part. Nucl. Phys. **32**, 13 (1994).

[2] Y. Fukuda *et al.* [Super-Kamiokande Collaboration], Phys. Rev. Lett. **81**, 1562 (1998) [arXiv:hep-ex/9807003].

[3] D. N. Spergel *et al.* [WMAP Collaboration], Astrophys. J. Suppl. **148**, 175 (2003) [arXiv:astro-ph/0302209].

[4] P. W. Higgs, Phys. Lett. **12**, 132 (1964).

[5] S. L. Glashow, Rev. Mod. Phys. **52**, 539 (1980) [Science **210**, 1319 (1980)].

[6] S. Weinberg, Rev. Mod. Phys. **52**, 515 (1980) [Science **210**, 1212 (1980)].

[7] A. Salam, Rev. Mod. Phys. **52**, 525 (1980) [Science **210**, 723 (1980)].

[8] W.-M. Yao *et al.* [Particle Data Group], J. Phys. G 33, 1 (2006)

[9] M. Kobayashi and T. Maskawa, Prog. Theor. Phys. **49**, 652 (1973).

[10] N. Cabibbo, Phys. Rev. Lett. **10**, 531 (1963).

[11] J. H. Christenson, J. W. Cronin, V. L. Fitch and R. Turlay, Phys. Rev. Lett. **13**, 138 (1964).

[12] L. Wolfenstein, Phys. Rev. Lett. **51**, 1945 (1983).

[13] J. Charles *et al.* [CKMfitter Group], Eur. Phys. J. C **41**, 1 (2005) [arXiv:hep-ph/0406184].

[14] P. F. Harrison and H. R. Quinn [BABAR Collaboration], SLAC-R-0504 *Papers from Workshop on Physics at an Asymmetric B Factory (BaBar Collaboration Meeting), Rome, Italy, 11-14 Nov 1996, Princeton, NJ, 17-20 Mar 1997, Orsay, France, 16-19 Jun 1997 and Pasadena, CA, 22-24 Sep 1997*

[15] N. Isgur and M. B. Wise, Phys. Lett. B **232**, 113 (1989).

[16] N. Isgur and M. B. Wise, Phys. Lett. B **237**, 527 (1990).

[17] M. Wirbel, B. Stech and M. Bauer, Z. Phys. C **29**, 637 (1985).

[18] M. Neubert, Phys. Rept. **245**, 259 (1994) [arXiv:hep-ph/9306320].

[19] J. D. Richman and P. R. Burchat, Rev. Mod. Phys. **67**, 893 (1995) [arXiv:hep-ph/9508250].

[20] A. Sirlin, Nucl. Phys. B **196**, 83 (1982).

[21] A. Czarnecki, Phys. Rev. Lett. **76**, 4124 (1996) [arXiv:hep-ph/9603261].

[22] M. Neubert, Phys. Lett. B **338**, 84 (1994) [arXiv:hep-ph/9408290].

[23] S. Hashimoto, A. S. Kronfeld, P. B. Mackenzie, S. M. Ryan and J. N. Simone, Phys. Rev. D **66**, 014503 (2002) [arXiv:hep-ph/0110253].

[24] M. E. Luke, Phys. Lett. B **252**, 447 (1990).

[25] S. Okubo, Phys. Rev. D **3**, 2807 (1971).

[26] S. Okubo and I. F. Shih, Phys. Rev. D **4**, 2020 (1971).

[27] E. de Rafael and J. Taron, Phys. Lett. B **282**, 215 (1992).

[28] E. de Rafael and J. Taron, "Analyticity properties and unitarity constraints of heavy meson Phys. Rev. D **50**, 373 (1994) [arXiv:hep-ph/9306214].

[29] C. G. Boyd, B. Grinstein and R. F. Lebed, Phys. Lett. B **353**, 306 (1995) [arXiv:hep-ph/9504235].

[30] C. G. Boyd, B. Grinstein and R. F. Lebed, Nucl. Phys. B **461**, 493 (1996) [arXiv:hep-ph/9508211].

[31] C. G. Boyd, B. Grinstein and R. F. Lebed, Phys. Rev. D **56**, 6895 (1997) [arXiv:hep-ph/9705252].

[32] I. Caprini, L. Lellouch and M. Neubert, Nucl. Phys. B **530** (1998) 153 [arXiv:hep-ph/9712417].

[33] B. Aubert *et al.* [BABAR Collaboration], arXiv:hep-ex/0602023.

[34] B. Aubert *et al.* [BABAR Collaboration], Nucl. Instrum. Meth. A **479**, 1 (2002) [arXiv:hep-ex/0105044].

[35] B. Aubert *et al.* [BABAR Collaboration], Phys. Rev. Lett. **89**, 201802 (2002) [arXiv:hep-ex/0207042].

[36] *Illustrating material from the main page of BABAR's publication board,*
http://www.slac.stanford.edu/BFROOT/www/Organization/PubBoard/OfficialPlots/. . .
. . . index.html

[37] R. Santonico and R. Cardarelli, Nucl. Instrum. Meth. **187**, 377 (1981).

[38] C. Lu [BABAR LST Group], SLAC-PUB-11521 *Prepared for 32nd International Conference on High-Energy Physics (ICHEP 04), Beijing, China, 16-22 Aug 2004*

[39] The ROOT system homepage, http://root.cern.ch/

[40] Automatically generated output of the fit program for the nominal fit
http://iktp.tu-dresden.de/Vcb_Fit_Doc/

[41] C.Hearty, "Measurement of the Number of $\Upsilon(4S)$ Mesons Produced in Run 1 (B Counting)", *BABAR* Analysis Document **134**

[42] D. Hutchcroft, *one of the BABAR bookkeeping documentation web pages,* http://www.slac.stanford.edu/BFROOT/www/Computing/Distributed/Bookkeeping/... ...Documentation/package_docs/BbkLumi_help.html

[43] B. Barish *et al.* [CLEO Collaboration], Phys. Rev. Lett. **76**, 1570 (1996).

[44] R. Gamet and C. Touramanis., "Luminosity Measurement for the Runs 1,2 and 3 data sample using Release 12 and SP5 Simulation", *BABAR* Analysis Document **1312**

[45] R. Gamet, "Run 4 luminosity using Release 16 and SP6", a *BABAR* hypernews posting in the luminosity hypernews at http://babar-hn.slac.stanford.edu:5090/HyperNews/get/luminosity/169.html

[46] A. Ryd *et al.*, "EvtGen – A Monte Carlo Generator for B-Physics", *BABAR* Analysis Document **522**

[47] T. Sjostrand, Comput. Phys. Commun. **82**, 74 (1994).

[48] S. Agostinelli *et al.* [GEANT4 Collaboration], Nucl. Instrum. Meth. A **506**, 250 (2003).

[49] *BABAR* Simulation Production Group, http://www.slac.stanford.edu/BFROOT/www/Computing/Offline/Production/index.html

[50] S. Robertson, Talk on the *BABAR* collaboration meeting for the Simulation Development Group on December 6th 2004, http://www.slac.stanford.edu/BFROOT/www/Organization/CollabMtgs/2004/detDec04/... .../Mon3/robertson.pdf

[51] E. Barberio and Z. Was, "PHOTOS: A Universal Monte Carlo for QED radiative corrections. Version 2.0," Comput. Phys. Commun. **79**, 291 (1994).

[52] J. L. Goity and W. Roberts, Phys. Rev. D **51**, 3459 (1995) [arXiv:hep-ph/9406236].

[53] D. Scora and N. Isgur, Phys. Rev. D **52**, 2783 (1995) [arXiv:hep-ph/9503486].

[54] N. Isgur, D. Scora, B. Grinstein and M. B. Wise, Phys. Rev. D **39**, 799 (1989).

[55] P. Billoir, Nucl. Instrum. Meth. A **225**, 352 (1984).

[56] T. Brandt, "Likelihood Based Electron Identification", *BABAR* Analysis Document **396**

[57] T. Brandt (representing the *BABAR* collaboration), "Semileptonic *B* Decays at *BABAR*", babar-talk-0187, *Talk given by Thorsten Brandt on the 9th International Symposium on Heavy Flavour Physics (2001)*

[58] S. Mclachlin (for the particle identification group of *BABAR*), "PID Control Samples at *BABAR*", *BABAR* Analysis Document **1056**

[59] G. Mancinelli and S. Spanier, "Kaon Selection at BaBar", *BABAR* Analysis Document **116**

[60] S. Sekula *et al.*, "The NetTagger", *BABAR* Analysis Document **103**

[61] Mark Allen *et al.*, "A Measurement of π^0 Efficiency Using $\tau \to \rho\nu$ and $\tau \to \pi\nu$ Decays" *BABAR* Analysis Document **870**

[62] J. Back, P. Harrison and G. Mohanty , "A new track-bump matching algorithm for the *BABAR* Electromagnetic Calorimeter", *BABAR* Analysis Document **812**

[63] J. Back, "Track-cluster matching for the electromagnetic calorimeter using Detector Model", *BABAR* Note#440
J. Back, "Track-cluster matching for the electromagnetic calorimeter using a simple model", *BABAR* Note#439

[64] S.J. Gowdy and P. Strother, "*BABAR* EMC Reconstruction Code", *BABAR* Note#475

[65] T. Allmendinger, "Tracking Efficiency Studies in Release 12 and 14", *BABAR* Analysis Document **867**

[66] *BABAR* PID Working Group,
http://www.slac.stanford.edu/BFROOT/www/Physics/Tools/Pid/pid.html

[67] J. Hollar, K. Mishra and T. Brandt, "ROOT based PID tables", available on the home page of the *BABAR* PID group at
http://www.slac.stanford.edu/BFROOT/www/Physics/Tools/Pid/Utils/BetaPidUser/...
.../BetaPidUser.ps

[68] *BABAR* Neutrals Working Group,
http://www.slac.stanford.edu/BFROOT/www/Physics/Analysis/AWG/Neutrals/

[69] V. Klose, "A measurement of the π^0 efficiency using D^0 decays into $K\pi\pi^0$", *BABAR* Analysis Document **1194**

[70] Skimming home page "Skims at *BABAR*",
http://www.slac.stanford.edu/BFROOT/www/Physics/skims/

[71] P.D. Jackson and R.V. Kowalewski, "Tagging using $B \to Dl\nu(X)$ decays", *BABAR* Analysis Document **537**, *The appendix contains information about the BToDlnu skim.*

[72] G. C. Fox and S. Wolfram, Nucl. Phys. B **149**, 413 (1979) [Erratum-ibid. B **157**, 543 (1979)].

[73] B. Aubert [BABAR Collaboration], Phys. Rev. D **71**, 051502 (2005) [arXiv:hep-ex/0408027].

[74] R. A. Briere *et al.* [CLEO Collaboration], Phys. Rev. Lett. **89**, 081803 (2002) [arXiv:hep-ex/0203032].

[75] R. S. Dubitzky, "Measurement $|V_{cb}|$ using $B \to D^*e\nu$ Semileptonic Decays", *BABAR* Analysis Document **527**

[76] [BABAR Collaboration], arXiv:hep-ex/0602023.

[77] J. E. Duboscq *et al.* [CLEO Collaboration], Phys. Rev. Lett. **76** (1996) 3898.

[78] Glen Cowan, "Statistical Data Analysis", Oxford Univerity Press (1998), Section 9.2 of this reference describes a method how to estimate the covariance of a correlation coefficient.

[79] K. S. Cranmer, Comput. Phys. Commun. **136**, 198 (2001) [arXiv:hep-ex/0011057].

[80] R. Gamet, "Run 4 luminosity using Release 16 and SP6", a *BABAR* hypernews posting in the luminosity hypernews at
http://babar-hn.slac.stanford.edu:5090/HyperNews/RETIRED/get/physAnal/2271.html

[81] K. Abe *et al.* [Belle Collaboration], Phys. Lett. B **526**, 258 (2002) [arXiv:hep-ex/0111082].

[82] http://wwwasdoc.web.cern.ch/wwwasdoc/minuit/minmain.html

[83] Private communication with Thorsten Brandt, former convener of the *BABAR* PID working group

[84] Private communication with Arthur E. Snyder, primary author [33]

[85] http://www.slac.stanford.edu/xorg/hfag/

[86] B. Aubert [BABAR Collaboration], arXiv:hep-ex/0607076.

[87] D. Buskulic *et al.* [ALEPH Collaboration], Phys. Lett. B **395**, 373 (1997).

[88] G. Abbiendi *et al.* [OPAL Collaboration], Phys. Lett. B **482**, 15 (2000) [arXiv:hep-ex/0003013].

[89] P. Abreu *et al.* [DELPHI Collaboration], Phys. Lett. B **510**, 55 (2001) [arXiv:hep-ex/0104026].

[90] J. Abdallah *et al.* [DELPHI Collaboration], Eur. Phys. J. C **33**, 213 (2004) [arXiv:hep-ex/0401023].

[91] K. Abe *et al.* [BELLE Collaboration], Phys. Lett. B **526**, 247 (2002) [arXiv:hep-ex/0111060].

[92] N. E. Adam *et al.* [CLEO collaboration], Phys. Rev. D **67**, 032001 (2003) [arXiv:hep-ex/0210040].

[93] H. Albrecht *et al.* [ARGUS Collaboration], Phys. Lett. B **275**, 195 (1992).

Acknowledgments

Erklärung und Versicherung gemäß §5 (1) Punkt 5, Anlage 1 der Promotionsordnung der Fakultät Mathematik und Naturwissenschaften an der Technischen Universität Dresden vom 20. März 2000

Erklärung

Die Dissertation wurde am Institut für Kern- und Teilchenphysik der Technischen Universität Dresden unter der Betreuung von Prof. Dr. Klaus R. Schubert angefertigt.

Versicherung

Hiermit versichere ich, daß ich die vorliegende Arbeit ohne unzulässige Hilfe Dritter und ohne Benutzung anderer als der angegebenen Hilfsmittel angefertigt habe; die aus fremden Quellen direkt oder indirekt übernommenen Gedanken sind als solche kenntlich gemacht. Die Arbeit wurde bisher weder im Inland noch im Ausland in gleicher oder ähnlicher Form einer anderen Prüfungsbehörde vorgelegt.

Dresden, den 30.11.2006

Jens Schubert